

THÈSE

Pour obtenir le grade de

DOCTEUR DE L'UNIVERSITÉ DE GRENOBLE

Spécialité : **Physique des matériaux**

Arrêté ministériel : 7 août 2006

Présentée par

Jan KUNC

Thèse dirigée par **Marek POTEMSKI** et
codirigée par **Roman GRILL**

préparée au sein du **Laboratoire National des Champs
Magnétiques Intenses, CNRS, Grenoble, France** dans l'**École
Doctorale de Physique de Grenoble** et au sein du **Institute of
Physics, Charles University, Prague, République Tchèque.**

Gaz électronique bidimensionnel de haute mobilité dans des puits quantiques de CdTe: Etudes en champ magnétique intense

Thèse soutenue publiquement le **14^{ème} Février 2011**,
devant le jury composé de :

Dr. Marek POTEMSKI, docteur habilité

Directeur de recherche, LNCMI-CNRS, Grenoble, France,
Membre de jury

Doc., RNDr. Roman GRILL, CSc.

Directeur de groupe de semiconducteurs, FUUK, Prague, Rép. Tchèque,
Membre de jury

Dr. Wojciech KNAP, docteur habilité

Directeur de recherche, GES, Université Montpellier II, France,
rapporteur

Ing. Ludvík SMRČKA, DrSc.

Directeur de recherche, Institute of Physics, AS CR, Rép. Tchèque,
rapporteur

Ing. Petr VAŠEK, CSc.

Chercheur, Institute of Physics, AS CR, Rép. Tchèque, Membre de jury

Dr. Anne-Laure BARRA

Chercheur, LNCMI-CNRS, Grenoble, France, Membre de jury





UNIVERSITÉ DE GRENOBLE

CHARLES UNIVERSITY PRAGUE

faculty of mathematics and physics



High mobility two-dimensional electron gas in CdTe quantum wells: High magnetic field studies

THESIS SUBMITTED TO THE CHARLES UNIVERSITY
AND UNIVERSITÉ DE GRENOBLE
FOR THE DEGREE OF DOCTOR OF PHILOSOPHY

Jan KUNC

This thesis was submitted by:

Jan KUNC

ENROLLED IN PHD STUDY PROGRAM: PHYSICS, QUANTUM OPTICS AND OPTOELECTRONICS (F-6) SINCE 2006 AT THE CHARLES UNIVERSITY, PRAGUE AND ENROLLED IN PHD STUDY PROGRAM: PHYSIQUE, PHYSIQUE DES MATERIAUX SINCE 2007 AT UNIVERSITÉ DE GRENOBLE, FRANCE.

Address:

Charles University in Prague
Faculty of Mathematics and Physics
Institute of Physics
Department of semiconductors and semiconductor optoelectronics
Ke Karlovu 5
CZ-121 16 Prague 2
Czech Republic

Email address:

kunc@karlov.mff.cuni.cz

This thesis was co-supervised by:

Doc. RNDr. Roman GRILL, CSc.

Address:

Charles University in Prague
Faculty of Mathematics and Physics
Institute of Physics
Department of semiconductors and semiconductor optoelectronics
Ke Karlovu 5
CZ-121 16 Prague 2
Czech Republic

Email address:

grill@karlov.mff.cuni.cz

and by:

Dr. Marek POTEMSKI

Address:

Centre National de la Recherche Scientifique
Laboratoire National des Champs Magnétiques Intenses
25 rue des Martyrs
F-38 042 Cedex 9
France

Email address:

marek.potemski@lncmi.cnrs.fr

Acknowledgement

I would like to thank here all the people, who helped and supported me during my doctoral study. First of all, I would like to thank Jan Franc who suggested me the possibility to spend part of the doctoral study in Prague, at the Charles University, and part in the Grenoble High Magnetic Field Laboratory. I highly appreciate and thank my supervisors Marek Potemski and Roman Grill for their help, suggestions and encouragement. I appreciate their patience and endurance in guiding my thesis. In particular, I thank Marek Potemski for the hospitality in the Grenoble High Magnetic Field Laboratory and discussing the data interpretation with Roman Grill. I would like to thank Milan Orlita for the helpful discussions of the experimental data and answering my never-ending questions on the apparent basics of solid state physics. It is a pleasure for me to thank Tomasz Wojtowicz from the Institute of Physics of Polish Academy of Sciences who provided us the unique set of samples studied in this work. The experimental work would be hardly feasible without considerable help of Duncan Maude, Ivan Breslavetz, Robert Pankow and Claude Mollard. I also thank Paulina Płochocka for her help at the beginning of my work. I appreciate the help and cooperation with Clément Faugeras and Benjamin Piot, with whom I had the opportunity to become acquainted with the experiments of the far-infrared absorption and magneto-transport experiments in tilted magnetic field. I thank Nicolas Brefuel who helped me many times with the French administration and translations into French. Last, but not least, I would like to thank Petr Vašek and Anne-Laure Barra who have agreed to be members of the jury during the defense of this thesis and especially I would like to thank Wojciech Knap and Ludvík Smrčka who are the referees of the presented work. I would like to thank also the direction and the staff of the Grenoble High Magnetic Field Laboratory and of the Institute of Physics of the Charles University in Prague. It would be impossible to make the presented work without them.

Because the doctoral study does not consist only of the world within the walls of the laboratory, I would like to thank also my parents and my sister Iva. Another important acknowledgement is devoted to all my friends, with whom I had the opportunity to spend this great time both in Grenoble and in Prague.

In the end, I acknowledge the financial support of the French government. The scholarship (dossier No. 20072492), which allowed me to spend part of my co-tutelle study in the Grenoble High Magnetic Field Laboratory and I acknowledge the acceptance of the project: “Fractional Quantum Hall Effect in CdTe/CdMgTe Quantum Wells - tilted field experiments”, which was financed within The 7th Framework Program - EuroMagNET II.

List of Latin symbols

a_0^*	effective Bohr radius
B	magnetic field
d	degeneracy of Landau levels
d_{QW}	width of quantum well
e	elementary charge ($e = 1.602 \times 10^{-19}$ C)
E_C	energy of bottom of conduction band
E_F	Fermi energy
E_g	energy of forbidden gap
$E_{n,e}$	energy of the bottom of n^{th} electronic subband
$E_{n,hh}$	energy of the top of n^{th} heavy hole subband
$E_{n,lh}$	energy of the top of n^{th} light hole subband
E_V	energy of top of valence band
g	Landé g-factor
G	Density of states at arbitrary magnetic field
G_0	Density of states at $B = 0$ T
g_e	Landé g-factor of electrons
g_h	Landé g-factor of heavy holes
h	Planck constant ($h = 6.626 \times 10^{-34}$ Js)
\hbar	reduced Planck constant $\hbar = h/2\pi = 1.055 \times 10^{-34}$ Js
j_z	projection of angular momentum $l = 3/2$ in the quantization axis, hole spin state
k_B	Boltzmann constant ($k_B = 1.38 \times 10^{-23}$ J/K)
k_F	Fermi wave vector
m_0	free-electron mass ($m_0 = 9.1 \times 10^{-31}$ kg)
m	effective mass
m_e	effective mass of electron
m_h	effective mass of heavy hole
m_l	effective mass of light hole
n	subband index
N	index of Landau level
n_e	concentration of electrons
N_e	index of electronic Landau level
n_D	concentration of donors
n_{FD}	Fermi-Dirac distribution
n_h	concentration of holes
N_h	index of hole Landau level
n_{ph}	concentration of photo-excited carriers
R_{xx}	Longitudinal resistance
R_{xy}	Hall resistance
s	projection of angular momentum $l = 1/2$ in the quantization axis, electron spin state
T	temperature
T_e	temperature of electrons

T_h	temperature of holes
V_{conf}	confinement potential
V_H	Hartree electrostatic potential
V_{xc}	exchange and correlation potential
x, y	coordinates in the plane of quantum well
z	coordinate perpendicular on the quantum well, growth direction, quantization axis

List of Greek symbols

ΔE_Z	Zeeman spin splitting
Δ_s	spin splitting of electronic Landau level
ϵ	unit vector of the polarization of light
ϵ_0	permittivity of vacuum ($\epsilon_0 = 8.85 \times 10^{-12}$ F/m)
ϵ_r	relative permittivity
Γ_e	broadening of electronic Landau level
Γ_h	broadening of hole Landau level
μ	mobility
μ_B	Bohr magneton ($\mu_B = 9.27 \times 10^{-24}$ J/T)
ν_m, ν_n	band index
σ_0	Longitudinal conductivity at $B = 0$ T
σ_{xx}	Longitudinal conductivity
σ_{xy}	Hall conductivity
σ^+	left-handed circular polarization
σ^-	right-handed circular polarization
τ_q	quantum lifetime
τ_{tr}	transport lifetime
ω_c	cyclotron angular frequency
ω_e	cyclotron angular frequency of electrons
ω_h	cyclotron angular frequency of heavy holes

Used abbreviations

2D, 3D	Two and three dimensions
2DEG	Two-dimensional electron gas
AF	Anti-ferromagnetic
ARB.U.	Arbitrary units
CB	Conduction band
CF	Composite fermion
CCD	Charge coupled device
DFA	Density function approximation
DOS	Density of states
EFA	Envelope function approximation
Eq.	Equation
FIG.	Figure
FIR	Far infrared
FQHE(S)	Fractional quantum Hall effect (state)
FWHM	Full width at half maximum
GZS	Giant Zeeman splitting
HWHM	Half width at half maximum
IQHE(S)	Integer quantum Hall effect (state)
LED	Light emitting diode
LL	Landau level
MBE	Molecular beam epitaxy
MIT	Metal insulator transition
ML	Monolayer
PL	Photoluminescence
PLE	Photoluminescence excitation
QW	Quantum well
QHE	Quantum Hall effect
RS	Raman scattering
TAB.	Table
SL	Superlattice
VB	Valence band

Contents

1	Preface	1
1.1	Preface (English)	1
1.2	Préface (En français)	3
1.3	Úvod (Česky)	5
2	Theoretical overview	7
2.1	Solution of the Schrödinger equation in periodic crystals	7
2.2	Quantum confinement	8
2.3	Motion of confined carriers in perpendicular magnetic fields	9
2.4	Density of states	10
2.5	Fermi golden rule	11
2.6	Inter-band matrix elements	13
3	Samples	14
4	Band structure calculations	16
4.1	Introduction	16
4.2	Self-consistent solution of Schrödinger and Poisson equation	16
4.3	Results	18
4.4	In-plane dispersion	21
5	Basic characterization of the samples	24
5.1	Raman scattering	24
5.2	Far infrared studies	29
6	Magneto-transport	32
6.1	Low-field magneto-transport in CdTe QW	32
6.1.1	Analysis of the conductivity	33
6.1.2	Analysis of the resistivity	37
6.1.3	Comments on various formulas of SdH oscillations	48
6.2	Low-field magneto-resistance in CdMnTe QW	50
6.2.1	Base temperature measurements	50
6.2.2	Temperature dependence	54
6.3	High-field magneto-resistivity in CdTe QW	59
6.3.1	Magneto-resistivity in perpendicular field	59
6.4	Magneto-resistivity in tilted field	62

7	Magneto-photoluminescence	71
7.1	Spectral properties of zero field PL	71
7.1.1	Introduction	71
7.1.2	Description of the PL spectrum	72
7.1.3	Fitting procedure	74
7.1.4	Discussion	76
7.2	An overview of the experimental results in magnetic field	79
7.2.1	CdTe QWs	79
7.2.2	CdMnTe QWs	84
7.3	Spin gap enhancement	90
7.3.1	Introduction	90
7.3.2	Samples	92
7.3.3	Experimental results	92
7.3.4	Spin splitting of fully populated Landau levels	95
7.3.5	Data modelling	95
7.3.6	Discussion	98
7.3.7	Conclusions	100
7.4	Intensity changes of PL	101
7.4.1	Introduction	101
7.4.2	Relative strength of the radiative and non-radiative recombination channel	101
7.4.3	Effect of occupancy, degeneracy and selection rules	102
7.4.4	Screening	104
7.4.5	Field-induced optical spin pumping	105
7.4.6	Lattice relaxation	108
7.4.7	Comparison with CdMnTe QWs	109
8	Photoluminescence excitation	113
8.1	Brief introduction	113
8.2	Zero field photoluminescence excitation	114
8.3	Field evolution of PLE	117
9	Conclusions	120
9.1	Conclusions (English)	120
9.2	Résumé (En français)	123
9.3	Závěr (Česky)	126
10	List of publications	128

Chapter 1

Preface

1.1 Preface (English)

Many-body quantum mechanical systems of identical interacting particles are of perpetual interest in the solid state physics. An electron gas is a good example of such a system. At high magnetic fields, the manifestation of electron-electron interaction is enhanced in two-dimensional systems and the striking properties of interacting particles are experimentally accessible. Confinement of the motion into two dimensions helps to strengthen many-body interactions as well. Since its first experimental observation on the surface of liquid helium [1] two-dimensional electron gas (2DEG) has profited interest in wide variety of materials and types of quantum confinement. Especially its confinement into a semiconductor heterojunction in silicon inversion layer [2] has attracted attention at the beginning of its discovery and later on many investigations have been performed in such devices like Field Effect Transistors (FET) and Metal Oxide Semiconductor FET (MOSFET). Remote doping in High Electron Mobility Transistors (HEMT) allowed to significantly increase mobilities of a 2DEG and the technological progress in the methods of the Molecular Beam Epitaxy (MBE) growth like Atomic Layer Epitaxy (ALE) has highly improved the quality of confined electron gas. In former geometries, confinement in the heterojunction of two materials was usually used, which led to the confinement in a triangular-like potential. However, two heterojunctions can be placed close to each other in order to construct quantum well (QW), where potential shape is variable and many shapes has been investigated like rectangular, parabolic or graded potential QWs, symmetrically and asymmetrically n-doped, p-doped and undoped QWs. The progress in the understanding of the properties of a 2DEG has not been connected only to the special geometries of quantum confinement, but also to the choice of the material. After early studies based on silicon (Si), there has been an extensive interest in III-V semiconductor compounds of gallium (Ga), arsenic (As), indium (In), phosphorus (P) and nitrogen (N) and especially QWs of GaAs, GaInAs, InP and GaN has been studied in 1970's and 1980's. Among others, considerable amount of attention has been paid also to the diluted magnetic semiconductor heterostructures based on doping the QWs by magnetic ions of manganese (Mn). New challenges appeared in 1990's by using II-VI compounds of cadmium (Cd), tellurium (Te) and mercury (Hg) like CdTe, CdHgTe and HgTe and by recent investigations of QWs based on lead (Pb) and tellurium (PbTe).

Experimental investigation of a 2DEG has led in past to many fundamental discoveries. Let's mention especially the integer quantum Hall effect (QHE) discovered in 1980 by Klaus von Klitzing *et al.* [3] in Si MOSFET and the discovery of the Fractional quantum Hall effect (FQHE) two years later by D. C. Tsui *et al.* [4]. The unceasing experimental effort can be traced in order to understand properties of 2DEG in these striking integer and fractional quantum Hall states until these days. Interaction of 2DEG with a lattice vibrations (polarons and magneto-polarons), vibrational modes of 2DEG (plasmons), magnons, rotons and other quasiparticles inherent to the electron gas has led also to deeper understanding of processes in many-body systems.

Throughout this work, we will present the experimental study of a two-dimensional electron gas confined in semiconductor, asymmetrically modulation doped quantum wells based on II-VI compound of CdTe and part of the work will deal with a diluted magnetic semiconductor of CdMnTe. Our motivation to study 2DEG in CdTe QW is mainly of fundamental interest. We will focus on the properties of strongly correlated electron gas in integer and fractional quantum Hall states and experimental manifestation of many-body electron-electron interaction will be the pivotal goal of presented work. The experimental techniques, we have used, are especially measurements of magneto-photoluminescence and longitudinal and Hall magneto-resistance. As the complementary techniques, Far Infrared (FIR) magneto-absorption, Raman scattering and photoluminescence excitation has been used too.

In chapter 2, we introduce briefly a theoretical background, necessary to understand basics of an electron motion in a periodic crystal, confined potential and perpendicular magnetic field. The chapter 3 describes the structure of the investigated MBE grown samples and basics of the samples growth are mentioned. In chapter 4 we present our calculations of the confined states. Their energies are calculated in the Local Density Approximation (LDA) including a many-body electron-electron interaction. Short introduction of the complementary FIR cyclotron resonance absorption and Raman scattering experiments is presented in the following chapter. We provide detailed analysis of the low field magneto-resistivity in the chapter 6.1 and survey of high field experiments in perpendicular magnetic field is presented. The comprehensive, magneto-optical study of 2DEG is presented in the chapter 7. First, we present basic analysis of magneto-PL of CdTe and magnetic CdMnTe QWs and then, particular attention is paid to the detailed analysis of the spin gap enhancement of fully populated Landau levels. In the following section the interpretation of the magnetic field induced intensity changes of PL emission is presented. Last chapter 8 is devoted to the photoluminescence excitation, comparison is done between quasi-absorption spectra and calculations presented in chapter 4. At the end, we summarize the main results obtained during this work, list of publications is provided and future perspectives are suggested.

1.2 Préface (En français)

Les systèmes quantiques constitués de plusieurs particules indiscernables en interaction sont d'un intérêt majeur dans le domaine de la physique des solides. Le gaz d'électrons est un bon exemple d'un tel système. Dans le régime des champs magnétiques intenses, la manifestation de l'interaction électron-électron est amplifiée et les propriétés de cette interaction sont plus facilement accessibles par l'expérience. Le confinement du mouvement dans deux dimensions renforce de plus les interactions multi-corps. Depuis sa première observation expérimentale sur la surface de l'Hélium liquide, le gaz bidimensionnel d'électrons (GE-2D) a suscité de l'intérêt pour de nombreux systèmes de matériaux et des types de confinement quantique différents. En particulier, le confinement électronique dans une hétérojonction semi-conductrice dans des couches de silicium en inversion a suscité beaucoup d'intérêt et de nombreuses études ont été réalisées dans de tels systèmes, comme des FET (Field Effect Transistor) et MOSFET (Metal Oxide Semiconductor FET). La technique du dopage hors du puits quantique dans les structures HEMT (High Electron Mobility Transistors) a permis d'augmenter de manière significative les mobilités des GE-2D et les progrès technologiques des méthodes d'épitaxie par jets moléculaires MBE (Molecular Beam Epitaxy) ont permis une forte amélioration de leur qualité. Dans les premières études, le confinement électronique était habituellement obtenu à l'interface entre deux matériaux et présentait un potentiel de forme triangulaire. Cependant, deux hétérojonctions peuvent être également réalisées près l'une de l'autre, et constituent un nouveau type de confinement, le puits quantique (QW; quantum well), où la forme du potentiel de confinement est variable et offre de nombreuses possibilités d'études, comme des potentiels rectangulaires ou paraboliques. La possibilité d'étudier des puits non-dopés ou dopés de manière symétrique ou non, dopage de type n- ou p- a été particulièrement intéressante et instructive. Les progrès dans la compréhension des propriétés d'un GE-2D n'ont pas été dus seulement aux géométries de confinement, mais également au choix des matériaux utilisés. Après les premières études, basées essentiellement sur le silicium (Si), il y a eu un intérêt considérable pour les alliages semi-conducteurs des groupes III et V, basés sur le gallium (Ga), l'arsenic (As), l'indium (In), le phosphore (P) et l'azote (N). En particulier, les puits quantiques de GaAs, GaInAs et de GaN ont été énormément étudiés dans les années 1970 et 1980. De plus, un intérêt considérable a été prêté aux semi-conducteurs magnétiques dilués, basés sur un dopage avec des ions magnétiques comme le manganèse (Mn). De nouveaux défis sont apparus dans les années 1990, où l'on a commencé à employer des composés des groupes II et VI, comme le cadmium (Cd), le tellure (Te) et le mercure (Hg), comme CdTe, CdHgTe et HgTe et, plus récemment encore, par des études portant sur des puits quantiques à base de plomb (Pb) et de tellure (PbTe). La recherche expérimentale sur les gaz électroniques bidimensionnels a permis de découvrir beaucoup de principes de physique quantique fondamentale. Ainsi, l'effet Hall quantique (Quantum Hall Effect - QHE) a été découvert en 1980 par Klaus von Klitzing dans un transistor MOSFET de silicium. La découverte de l'effet Hall quantique fractionnel (Fractional Quantum Hall Effect - FQHE) deux ans après par Dan Tsui en est un autre exemple. Ce type de recherche expérimentale visant à comprendre les propriétés d'un GE-2D dans les régimes de l'effet Hall quantique entier ou fractionnaire se perpétue encore aujourd'hui. L'interaction d'un GE-2D avec les vibrations du réseau cristallin (polarons et les magnéto-polarons), les modes vibratoires de 2DEG (plasmons),

les magnons, les rotons et d'autres quasi-particules inhérentes au gaz d'électrons, ont également permis une meilleure compréhension des systèmes multi-corps. Dans ce travail, nous présentons l'étude expérimentale de gaz d'électrons bidimensionnels confinés dans un puits quantique semi-conducteur, asymétriquement n-dopé, à base de composés II-VI, CdTe. Une partie du travail traitera de puits quantiques magnétiques de semi-conducteurs dilués CdMnTe. Notre motivation pour étudier GE-2D dans CdTe QW est principalement d'intérêt fondamental. Nous nous concentrerons sur les propriétés du gaz d'électrons fortement corrélés dans le régime de Hall quantique et sur la manifestation expérimentale des interactions multi-corps. Les techniques expérimentales que nous avons employées, sont en particulier la magnéto-photoluminescence et la mesure du magnéto-transport longitudinal et transverse (magnéto-résistivité de Hall). Nous avons aussi employé des techniques complémentaires, comme la magneto-absorption infrarouge (Far infrared - FIR), la diffusion Raman et l'excitation de la photoluminescence (Photoluminescence excitation - PLE). Dans le deuxième chapitre, nous présentons brièvement un fond théorique, nécessaire pour comprendre les principes du mouvement électronique dans un cristal périodique, dans un potentiel confiné, en présence d'un champ magnétique perpendiculaire. Le troisième chapitre décrit la structure des échantillons élaborés par MBE et nous expliquons brièvement les techniques de croissance. Dans le chapitre 4 nous présentons nos calculs des états confinés et leurs énergies. Nous avons considéré les interactions électron-électron dans l'Approximation de densité locale (Local Density Approximation - LDA). Une brève description des expériences complémentaires d'absorption infrarouge et de diffusion Raman est présentée dans le chapitre suivant. Nous présentons l'analyse détaillée de la magnéto-résistivité à faible champ magnétique dans le chapitre 6.1 puis nous étendons ces résultats au régime de champ magnétique intense. L'étude magnéto-optique du gaz bidimensionnel est présentée dans la chapitre 7. Nous présentons d'abord l'analyse élémentaire de magnéto-PL de puits quantiques de CdTe et de CdMnTe et puis, une attention particulière est prêtée à l'analyse détaillée du spin splitting des niveaux de Landau entièrement peuplés. Dans la section suivante, l'interprétation de la modulation de l'intensité de la PL en fonction du champ magnétique est présentée. Le chapitre 8 est dédié à la spectroscopie d'excitation de la photoluminescence (PLE). Nous faisons une comparaison entre les spectres de quasi-absorption et les calculs présentés dans le chapitre ???. Finalement, nous récapitulons les résultats principaux obtenus pendant ce travail, la liste des publications issues de ce travail et les perspectives à donner à ce travail.

1.3 Úvod (Česky)

Mnoha-částicové kvantové systémy identických interagujících částic jsou předmětem neuctahajícího zájmu ve fyzice pevných látek. Jedním z příkladů takového systému je elektronový plyn. Ve vysokých magnetických polích, stejně tak omezením prostorových stupňů volnosti elektronového plynu do dvou dimenzí, jsou projevy mnoha - částicových interakcí dále zvýrazněny a vlastnosti interagujících částic se stávají experimentálně lépe dostupné. Od svého objevení na povrchu kapalného helia byl dvou-dimenzionální elektronový plyn (2DEP) studován v široké řadě materiálů a typech kvantového omezení. Zpočátku, zejména jeho studium v heterostrukturách na bázi křemíku vyvolalo širokou vlnu zájmu a později byla řada studií provedena taktéž v takových strukturách, jako jsou polem řízený tranzistor (Field Effect Transistor - FET) a polem řízený tranzistor typu MOSFET (Metal Oxide FET). Dopování v oblasti mimo aktivní část heterostrukury přispělo k vytvoření tranzistoru s vysokými pohyblivostmi elektronů (High Electron Mobility Transistor - HEMT) a stejně tak vývoj v oblasti technologie růstu výrazně přispěl ke zlepšení kvality 2DEP. Kvantové omezení 2DEP na rozhraní dvou materiálů bylo zpočátku nejčastější používanou geometrií. Avšak další možností je umístit dvě taková rozhraní blízko vedle sebe, což vede k vytvoření tzv. kvantové jámy, kde tvar potenciálu kvantového omezení může být libovolně měněn a takové potenciály jako je pravoúhlý, parabolický, či stupňovitý byly studovány, stejně tak jako různé způsoby symetrického a asymetrického dopování. Porozumění chování 2DEP však nebylo spojeno jen s různými geometriemi kvantového omezení, ale také s volbou materiálů. Po počátečních studiích ve strukturách na bázi křemíku se zájem obrátil na polovodiče typu III-V, jako jsou galium (Ga), arsen (As), indium (In), fosfor (P) a dusík (N) a zejména kvantové jámy na bázi GaAs, GaInAs, InP a GaN byly studovány v sedmdesátých a osmdesátých letech 20. století. Mezi jinými, značná pozornost byla věnována též zředěným magnetickým polovodičům (Diluted Magnetic Semiconductors - DMS) na bázi manganu (Mn). Nové oživení zájmu o tuto problematiku přišlo počátkem devadesátých let minulého století s příchodem rozvíjející se technologie II-VI polovodičů jako jsou kadmium (Cd), telur (Te), rtuť (Hg) a především heterostrukury CdTe, CdHgTe a HgTe byly studovány, stejně tak jako užití olova (Pb) v PbTe v posledních letech. Experimentální studium 2DEP vedlo v minulosti k mnoha objevům fundamentálního charakteru. Zmíňme především celočíselný kvantový Hallův jev (integer quantum Hall effect - IQHE) objevený v roce 1980 Klausem von Klitzingem *et al.* [3] v křemíkové heterostruktuře typu MOSFET a objev zlomkového kvantového Hallova jevu o dva roky později [4] a intenzivní experimentální úsilí ve studiu nevšedních vlastností 2DEP v režimu celočíselného a zlomkového kvantového Hallova jevu lze vystopovat do dnešních dnů. Studium interakcí 2DEP s mřížkovými vibracemi (polarony a magnetopolarony), vibračních modů 2DEP (plasmonů), magnonů, rotonů a dalších kvazičástic inherentních elektronovému plynu vedlo taktéž k hlubšímu porozumění procesů v mnoha-částicových systémech. Tato práce je souhrnem zejména experimentálního studia dvou-dimenzionálního elektronového plynu omezeného v asymetricky dopovaných kvantových jamách na bázi II-VI materiálu, CdTe. Část práce je pro srovnání věnována též kvantovým jamám na bázi CdMnTe. Naší hlavní motivací je základní výzkum vlastností 2DEP. Zaměříme se na vlastnosti silně korelovaného elektronového plynu v celočíselných a zlomkových kvantových Hallových stavech a na projevy mnoha-částicových interakcí. Mezi zde použité experimentální techniky patří především měření magneto-fotoluminiscence,

podélného a Hallova odporu a jako doplňkové techniky bylo použito měření infračervené absorpce, Ramanova rozptylu a excitační fotoluminiscence.

V kapitole č. 2 nastíníme teoretické základy pohybu elektronu v periodickém krystalovém potenciálu, kvantových jamách a magnetickém poli. V kapitole č. 3 popíšeme detailně strukturu použitých vzorků a v kapitole č. 4 uvedeme kvantově-mechanické výpočty pásové struktury ve dvou studovaných vzorcích. Výpočty jsou provedeny v aproximaci lokální elektronové hustoty (Local Density Approximation - LDA) včetně zahrnutí mnohačástečkové elektron-elektronové interakce. Následující kapitola je úvodem do doplňkových měření infračervené absorpce a Ramanova rozptylu. Detailní analýza měření magneto-rezistivity se nachází v kapitole č. 6.1. Analýza magneto-fotoluminiscence je prezentována v kapitole č. 7, kde nejdříve seznámíme čtenáře se základy fotoluminiscence v kvantových jamách CdTe a magnetických kvantových jamách CdMnTe a poté je zvláštní pozornost věnována spinovému štěpení plně obsazených Landauových hladin a vlivu elektron-elektronové interakce. Další podkapitola se detailně zabývá intenzitními změnami luminiscence v magnetickém poli. Poslední kapitola je věnována excitační luminiscenci, kde jsou, mimo jiné, výpočty energetických hladin prezentované v kapitole č. 4 srovnány s experimentem. Na samotném konci shrneme stěžejní výsledky této dizertační práce a nastíníme perspektivy dalšího vývoje studia 2DEP.

Chapter 2

Theoretical overview

In the first chapter, theoretical basics used throughout the presented thesis are introduced. The theoretical overview here is not intended to be comprehensive introduction into the solid state physics, what can be found elsewhere [5, 6]

2.1 Solution of the Schrödinger equation in periodic crystals

Stationary solution of the Schrödinger equation in ideal, infinitely large, periodic crystal is given in a single-particle approximation according to the Bloch theorem, Eq. (2.1)

$$\Psi_{\mathbf{k}}(\mathbf{r}) = e^{i\mathbf{k}\cdot\mathbf{r}} u_{\mathbf{k}}(\mathbf{r}) \quad (2.1)$$

by plane wave $e^{i\mathbf{k}\cdot\mathbf{r}}$ determined by the vector \mathbf{k} and function $u_{\mathbf{k}}(\mathbf{r})$ periodic with a period of the lattice. Having hamiltonian of the crystal \hat{H} , Eq. (2.2), given by the crystal potential $V(\mathbf{r})$,

$$\hat{H} = -\frac{\hbar^2}{2m_0} \Delta + V(\mathbf{r}) \quad (2.2)$$

and solving Schrödinger stationary equation (2.3)

$$\hat{H}\Psi_{\mathbf{k}}(\mathbf{r}) = E_{\mathbf{k}}\Psi_{\mathbf{k}}(\mathbf{r}) \quad (2.3)$$

by using wave functions (2.1) as an ansatz, one can find equation (2.4) for the unknown functions $u_{\mathbf{k}}(\mathbf{r})$.

$$-\frac{\hbar^2}{2m} [-k^2 u_{\mathbf{k}}(\mathbf{r}) + 2i\mathbf{k} \cdot \nabla u_{\mathbf{k}}(\mathbf{r}) + \Delta u_{\mathbf{k}}(\mathbf{r})] + V u_{\mathbf{k}}(\mathbf{r}) = E_{\mathbf{k}} u_{\mathbf{k}}(\mathbf{r}) \quad (2.4)$$

Equation (2.4) has several solutions for every \mathbf{k} vector. Every solution corresponds to one band in the band structure of the crystal and will be specified by additional index ν_m , $u_{\nu_m, \mathbf{k}}(\mathbf{r})$. Solving first equation (2.4) at $\mathbf{k}=0$, obtaining solutions $u_{\nu_m, \mathbf{0}}(\mathbf{r})$ and then expanding solutions $u_{\nu_m, \mathbf{k}}(\mathbf{r})$ at non-zero \mathbf{k} vectors into the basis of the solutions $u_{\nu_m, \mathbf{0}}(\mathbf{r})$

$$u_{\nu_n, \mathbf{k}}(\mathbf{r}) = \sum_{\nu_m} c_{\nu_m}(\mathbf{k}) u_{\nu_m, \mathbf{0}}(\mathbf{r}) \quad (2.5)$$

leads to the set of equations for expansion coefficients $c_{\nu_m}(\mathbf{k})$. This is well-known kp-approximation of the band structure in the vicinity of given \mathbf{k} vector. Considering solutions around Γ point, it can be shown [6], that energy $\epsilon_{n\mathbf{k}}$ of the band ν_m can be described as

$$\epsilon_{\nu_n, \mathbf{k}} = \epsilon_{\nu_n \mathbf{0}} + \frac{\hbar^2}{2} \sum_{\alpha, \beta} k_\alpha \frac{1}{\mu_{\nu_n}^{\alpha\beta}} k_\beta \quad (2.6)$$

where $1/\mu_{\nu_n}^{\alpha\beta}$ is an effective mass tensor. This is a so called effective mass approximation of the electronic band structure. A resulting motion of the electron in the periodic crystal can be seen as a motion of a free electron with an effective mass, which is different from the free electron mass m_0 . It can be shown, that in CdTe, which has a zinc-blende crystallographic structure, the effective mass tensor reduces to a scalar for the conduction band¹ and its mass is positive, however, for the valence band², the effective mass can not be replaced by a scalar, the effective mass is anisotropic and negative. Usually, for the sake of simplicity, spherically averaged value for effective mass of holes in the valence band is taken.

2.2 Quantum confinement

Let's consider confinement of the electron motion in the z-direction described by the confinement potential $V_{conf}(z)$. Electron motion is usually described here in the envelope function approximation (EFA), neglecting the part $u_{\nu_m, \mathbf{k}}(\mathbf{r})$ of the Bloch wave function (2.1) periodic with the lattice constant of host material. Hamiltonian (2.7) in EFA and effective mass approximation

$$\hat{H}_{conf} = -\frac{\hbar^2}{2m} \Delta + V_{conf}(z) \quad (2.7)$$

leads to the separable Schrödinger equation and its solution can be written as (2.8),

$$\psi_{k_x, k_y, n}(\mathbf{r}) = \frac{1}{\sqrt{\Omega}} e^{i\mathbf{k}_\perp \cdot \mathbf{r}_\perp} \chi_n(z) \quad (2.8)$$

Wave function (2.8) is a product of the in-plane solution $\frac{1}{\sqrt{\Omega}} e^{i\mathbf{k}_\perp \cdot \mathbf{r}_\perp}$ and envelope wave function $\chi_n(z)$ of the n^{th} subband in the z-direction, where $\mathbf{k}_\perp = (k_x, k_y)$, $\mathbf{r}_\perp = (x, y)$ are in-plane wave-vector and position. Ω is an area of the sample in order to normalize the in-plane part of the total envelope wave function.

Energy dispersion (2.9) of carriers confined in z-direction, but free in the x-y plane,

$$E_n(k_x, k_y) = \frac{\hbar^2 k_\perp^2}{2m} + E_{n\mathbf{0}} \quad (2.9)$$

in two dimensions is in the vicinity of $\mathbf{k}_\perp = 0$ (Γ point) parabolic in the plane of quantum well. Confinement energy $E_{n\mathbf{0}}$ of the bottom (top) of n^{th} subband in the conduction (valence) band depends on many factors like a width and height of the confining potential, shape of the quantum well, presence of electron or hole gas or electron-hole plasma. In order to obtain the values of confinement energy comparable with an experiment, numerical solutions are usually necessary, as will be shown in the case of our QWs in the chapter 4.

¹Conduction band is the lowest energy band, which is unoccupied or only partially occupied. Electrons are free to move in the atomic lattice.

²Valence band is the highest energy band, fully or nearly fully occupied.

2.3 Motion of confined carriers in perpendicular magnetic fields

Motion of the confined carriers with an effective mass m in the presence of magnetic field $\mathbf{B} = (0, 0, B)$ perpendicular to the plane of the QW is solved by replacing momentum operator \mathbf{p} by $\mathbf{p} - q\mathbf{A}$, where q is a charge of the investigated particle and \mathbf{A} is a vector potential. In the Landau gauge $\mathbf{A} = (0, Bx, 0)$ the Hamiltonian (spin is not taken into account) in the effective mass and envelope function approximation reads:

$$\hat{H}_{field} = -\frac{\hbar^2}{2m} \frac{\partial^2}{\partial x^2} + \frac{1}{2m} \left[-i\hbar \frac{\partial}{\partial y} - qBx \right]^2 - \frac{\hbar^2}{2m} \frac{\partial^2}{\partial z^2} + V_{conf}(z) \quad (2.10)$$

Since hamiltonian \hat{H}_{field} commutes with k_y , one can separate variables, so as the solution of the stationary Schrödinger equation is

$$\psi_{k_y}(\mathbf{r}) = \frac{1}{\sqrt{\Omega}} e^{ik_y y} \varphi(x, z) \quad (2.11)$$

in the form of the plane wave $\frac{1}{\sqrt{\Omega}} e^{ik_y y}$ and the part $\varphi(x, z)$ depending on x and z coordinates. Substituting (2.11) into (2.10) allows to separate also x and z coordinates,

$$\varphi_{n,N}(x, z) = \chi_n(z) \phi_N(x) \quad (2.12)$$

where $\chi_n(z)$ is given by

$$\left(-\frac{\hbar^2}{2m} \frac{\partial^2}{\partial z^2} + V_{conf} \right) \chi_n(z) = E_{n0} \chi_n(z)$$

and $\phi_N(x)$ is a wave function of linear harmonic oscillator expressed in terms of Hermite polynomials \mathcal{H}_N

$$\phi_N(x) = \frac{1}{\sqrt{l_B}} \frac{1}{\sqrt{2^N N! \sqrt{\pi}}} e^{-\frac{(x-x_0)^2}{2l_B^2}} \mathcal{H}_N \left(\frac{x-x_0}{l_B} \right) \quad (2.13)$$

at the position

$$x_0 = -l_B^2 k_y \quad (2.14)$$

where

$$l_B = \sqrt{\frac{\hbar}{eB}} \quad (2.15)$$

is a magnetic length and the energies

$$E_N = \hbar\omega_c \left(N + \frac{1}{2} \right) \quad (2.16)$$

denote the energies of so called Landau levels, separated by $\hbar\omega_c = \hbar eB/m$, where ω_c is a cyclotron angular frequency. Total energy of the state $|n, N, k_y\rangle$ in \mathbf{r} -representation

$$\langle \mathbf{r} | k_y, n, N \rangle = \psi_{k_y, n, N} = \frac{1}{\sqrt{\Omega}} e^{ik_y y} \chi_n(z) \phi_N(x) \quad (2.17)$$

is given by

$$E_{nN} = E_{n0} + \hbar\omega_c \left(N + \frac{1}{2} \right) \quad (2.18)$$

and it is degenerated in the quantum number k_y . Degeneracy d does not depend on the material parameters and grows linearly with magnetic field, $d = 2eB/h$.

2.4 Density of states

Density of states $G(E)$ (spin is not taken into account) per unit area at the energy E can be calculated in 2D by

$$G(E) = \frac{1}{(2\pi)^2} \int \delta(E - E(\mathbf{k}_\perp)) d\mathbf{k}_\perp \quad (2.19)$$

giving in the quantum wells with parabolic dispersion step-like density of states $G(E)$ at zero magnetic field

$$G(E) = \frac{m}{\pi\hbar^2} \sum_n \theta(E - E_{n\mathbf{0}}) \quad (2.20)$$

and density of states in a form of sum of δ -functions

$$G(E) = \frac{eB}{h} \sum_{n,N} \delta(E - E_{nN}) \quad (2.21)$$

in the perpendicular magnetic field B . Formulas (2.20) and (2.21) are derived for ideal system, where energy levels are infinitely sharp. However, every physical systems manifest always certain degree of broadening of various origin (lifetime, disorder, etc.) which can be phenomenologically introduced describing energy levels by gaussian or lorentzian line shapes.

Assuming, that energy $E_{n\mathbf{0}}$ or E_{nN} has a statistical distribution $f(0, \Gamma)$, where first statistical moment is zero and second Γ , the convolution

$$G_\Gamma(E) = f(0, \Gamma) * G(E) \quad (2.22)$$

describes the density of states of broadened levels and broadening Γ . It is straightforward to show, that at zero magnetic field in the case of Gaussian

$$f_G(0, \Gamma) = \frac{1}{\sqrt{2\pi}\Gamma} e^{-\frac{E^2}{2\Gamma^2}} \quad (2.23)$$

and Lorentzian broadening

$$f_L(0, \Gamma) = \frac{1}{\pi\Gamma} \frac{1}{1 + \left(\frac{E}{\Gamma}\right)^2} \quad (2.24)$$

the density of states is given by

$$G_\Gamma^{gauss}(E - \epsilon_{mn}) = \frac{m}{\pi\hbar^2} \frac{1}{2} \left(1 + \operatorname{erf} \left(\frac{E - E_{n\mathbf{0}}}{\Gamma\sqrt{2}} \right) \right) \quad (2.25)$$

and,

$$G_\Gamma^{lorentz}(E - \epsilon_{mn}) = \frac{m}{\pi\hbar^2} \frac{1}{2} \left(1 + \frac{2}{\pi} \arctan \left(\frac{E - E_{n\mathbf{0}}}{\Gamma} \right) \right) \quad (2.26)$$

respectively. The density of states in the magnetic field can be obtained by substitution of distribution functions (2.23) or (2.24) on place of δ -functions in idealized density of states (2.21).

2.5 Fermi golden rule

So far, we have introduced the energy levels alone. In optical experiments, which are a pivotal part of the presented work, the probabilities of the transitions between particular energy levels are important. Assuming classically described electro-magnetic radiation

$$\mathbf{E} = \mathbf{e}_0 E_0 e^{-i(\omega t - \mathbf{k} \cdot \mathbf{r})} \quad (2.27)$$

with amplitude of the electrical intensity E_0 oscillating with a angular frequency ω , polarization \mathbf{e}_0 and wave vector \mathbf{k} . It interacts with a matter in a single photon, semi-classical approximation³ by interaction hamiltonian,

$$\hat{H}_{int} = \frac{e}{2m_0} [\mathbf{p} \cdot \mathbf{A} + \mathbf{A} \cdot \mathbf{p}] \quad (2.28)$$

where m_0 is electron mass and \mathbf{A} is a vector potential of the incident electromagnetic radiation \mathbf{E} . The probability p_{ij} of the absorption between the initial, fully occupied $|i\rangle$ (energy E_i) and final, completely empty $|j\rangle$ (energy E_j) state is given by Fermi Golden rule,

$$p_{ij} = \frac{2\pi}{\hbar} |\langle f|V|i\rangle|^2 \delta(E_f - E_i - \hbar\omega) \quad (2.29)$$

where V is in the electric dipole approximation,

$$V = \frac{ieE_0}{2m_0\omega} \mathbf{e}_0 \cdot \mathbf{p} \quad (2.30)$$

and the intensity of the transition is determined by matrix element $|V_{ij}|^2 = |\langle f|V|i\rangle|^2$. Set of transitions with non-zero matrix element $|V_{ij}|^2$ determines selection rules. Selection rules for inter-band transitions in CdTe and CdMnTe in the magnetic field are depicted in Fig. 2.1 and Fig. 2.2. The hole levels $j_z = \pm 3/2$ are ordered in both materials in the same way, but electronic levels $s = \pm 1/2$ have opposite ordering (electronic level $s = +1/2$ is at higher energy than level $s = -1/2$ in CdMnTe, in contrast to CdTe). This is caused by electron-manganese sd -interaction, which inverts the ordering of the electronic levels $s = \pm 1/2$ with respect to CdTe. The convention of σ^+ (left-handed) and σ^- (right-handed) circular polarization follows convention of Born, Wolf [7]. σ^+ (σ^-) polarized photons have projection of the angular momentum into quantization z -axis $L_z = +\hbar$ ($L_z = -\hbar$).

If the initial (final) electronic state involved in the absorption process is only partially occupied (empty) one has to consider the fact, that electrons (resp. holes) are fermions and Pauli exclusion principle has to be taken into account. Then, the probability of absorption p_{ij}

$$p_{ij} = \frac{2\pi}{\hbar} |\langle f|V|i\rangle|^2 n_{FD}^i (1 - n_{FD}^f) \delta(\epsilon_f - \epsilon_i - \hbar\omega) \quad (2.31)$$

is determined also by the occupation factors $n_{FD}^{i(f)}$ of the initial and final states given in the thermal equilibrium by Fermi-Dirac distribution (2.32).

$$n_{FD} = \frac{1}{e^{\frac{E-E_F}{k_B T}} + 1} \quad (2.32)$$

³Semi-classical approximation reflects the fact, that the matter is described quantum mechanically, however, electro-magnetic radiation classically.

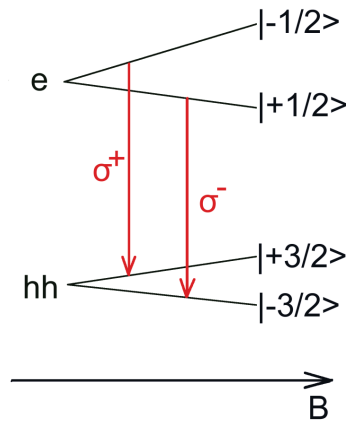


Figure 2.1: Selection rules for interband optical transition in CdTe as a function of magnetic field. Optical interband transitions accompanied by emission of σ^+ and σ^- circularly polarized photons are represented by red arrows.

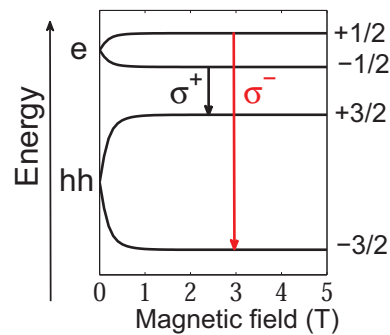


Figure 2.2: Selection rules in CdMnTe. The two upper(lower) levels correspond to the two spin-resolved electronic (hole) energy levels. Exchange sp-d interaction manifests itself in a typical field dependence, which is described by Brillouin function instead of a linear field dependence as expected in non-magnetic structures. Allowed optical transitions in σ^+ (σ^-) circular polarization are sketched out by black (red) arrows.

In contrast to the absorption, the spontaneous emission⁴ (photoluminescence) can not be described, until electro-magnetic radiation is described quantum mechanically. However, PL intensity can be related to that of the absorption by means of Einstein coefficients ([6], p. 272) and the same Fermi Golden rule (2.31) can be used to describe also spontaneous emission.

⁴In our case, we mean by spontaneous emission especially photoluminescence. Generally, it can be any kind of radiative recombination process which can take place without presence of other electromagnetic radiation, like electroluminescence, chemoluminescence, triboluminescence, etc.

2.6 Inter-band matrix elements

Evaluating matrix element $|V_{ij}|^2$ gives the information on the intensity of the transition. Full wave function (including Bloch part) of the initial and final state can be written at zero magnetic field in \mathbf{r} -representation as,

$$\langle \mathbf{r} | i(f) \rangle = \Psi_{i(f)}(\mathbf{r}) = u_{\nu_{i(f)}}(\mathbf{r}) \frac{1}{\sqrt{\Omega}} e^{i\mathbf{k}_\perp \cdot \mathbf{r}_\perp} \chi_{i(f)}(z) \quad (2.33)$$

where $u_{\nu_{i(f)}}(\mathbf{r})$ is the periodic part of the Bloch function in a center of the Brillouin zone, $\nu_{i(f)}$ is an index of the band and $\chi_{i(f)}(z)$ is an envelope wave function in the direction of quantum confinement. Neglecting integrals of mixed products of quickly oscillating functions $u_{\nu_{i(f)}}(\mathbf{r})$ and slowly varying envelope functions $\chi_{i(f)}(z)$, one gets

$$\langle f | V | i \rangle = \mathbf{e}_0 \cdot \mathbf{p}_{ij} \cong \mathbf{e}_0 \cdot \langle u_{\nu_i} | \mathbf{p} | u_{\nu_f} \rangle \langle \chi_i | \chi_f \rangle + \delta_{\nu_i \nu_f} \mathbf{e}_0 \cdot \langle \chi_i | \mathbf{p} | \chi_f \rangle \quad (2.34)$$

The second term in (2.34) is zero for inter-band ($\nu_i \neq \nu_f$) transitions, hence, within used approximation, the strength of inter-band transitions is given only by the overlap of the envelope functions $p_{ij} \propto |\langle \chi_i | \chi_f \rangle|^2$. This leads to the selection rule $i+j$ is even number in the symmetrical QWs and if the QW is rectangular and infinitely deep, only transitions $i = j$ are allowed. However, we are interested in the study of asymmetrically doped QWs, where these selection rules may be strongly violated. Therefore we will present the envelope function calculations in chapter 4 in order to properly determine selection rules between particular subbands.

In magnetic field, the envelope function is given by $\varphi_{n_i(f)N_i(f)}(x, z) = \chi_{n_i(f)}(z) \phi_{N_i(f)}(x)$, where $N_i(N_f)$ are quantum numbers of the Landau level in the initial and final state. Due to the orthogonality of linear harmonic oscillator functions $\langle \phi_{N_i} | \phi_{N_f} \rangle = \delta_{N_i, N_f}$, only inter-band transitions between Landau levels with the same quantum number $N_i = N_f$ are allowed within this approximation. Moreover, due to orthonormality of the functions $\phi_{N_i}(x)$ and $\phi_{N_j}(x)$, the oscillator strength does not depend on the index of the Landau levels between which the transition occurs.

Chapter 3

Samples

The samples used in the presented study are semiconductor modulation doped quantum wells based on II-VI material CdTe. The samples have been grown by molecular beam epitaxy (MBE) in the Institute of Physics, Polish Academy of Sciences (IFPAN). The growth method of high quality QWs containing 2DEG has been developed in IFPAN in 1990's [8]. Throughout the whole presented study, we have focused our main attention on non-magnetic modulation doped CdTe/Cd_{0.74}Mg_{0.26}Te quantum wells of the well width 20 and 30 nm. Part of the experimental work has been also devoted to the magnetic quantum wells based on diluted magnetic semiconductor CdMnTe with very low manganese concentration.

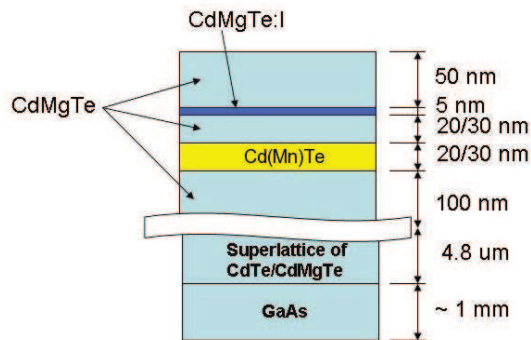


Figure 3.1: Structure of the samples.

The sample structure is sketched in the Fig. 3.1. The samples are grown on the (100)GaAs semi-insulating substrate which are nowadays of very high and reproducible quality with respect to the CdTe substrates. Different lattice constants of GaAs and CdTe cause the strain in the grown sample, which is relaxed by growing roughly 2 μm buffer layer of CdTe, $\approx 2 \mu\text{m}$ layer of CdMgTe followed 5 times by set of superlattice (SL) and 100 nm thick spacer of CdMgTe. The SL consists of 4 monolayers (ML) of CdTe and 4 ML of CdMgTe. The quantum well itself consists of 62 (sample No. 013008A) or 93 (sample No. 020108A) MLs of CdTe. In order to reduce the interface roughness between CdTe QW and CdMgTe barrier, the atomic layer epitaxy (ALE) technique¹ of growth has

¹Atomic layer epitaxy technique (ALE) has been introduced in 1970's by T. Suntola, Finland [9]. The ALE is used to grow 2 component materials of uniform structure, well aligned with the substrate. It is

been used for growing the initial 6 and final 6 ML of CdTe QW and other monolayers have been grown by standard MBE technique. The QW is followed by the spacer of the same width as the width of the QW, and followed by 5 nm wide iodine doped (CdMgTe:I) layer. The sample is terminated by 50 nm wide cap layer.

The sample based on diluted magnetic semiconductor CdMnTe (No. 013108A) has been grown in the similar way as the sample No. 013008A. The main difference is the width of the QW, which is here 21.1 nm and the content of digitally doped manganese inside the QW. Digitally doped CdTe:Mn QW consists of 8 ML of CdTe at the beginning and at the end of the QW, 1 ML of CdMnTe and 6 times set of 7 ML of CdTe and 1 ML of CdMnTe. The resulting manganese concentration was of about 0.5%.

As the main difference between the two non-magnetic samples No. 013008A and No. 020108A is the width of QW, for the sake of simpler formulation, we will use the notation 20 nm and 30 nm wide QW, respectively. In all references on CdMnTe QW, the sample No. 013108A will be considered.

We had few pieces of each type of introduced samples available. The set of samples used for resistivity measurements was equipped with indium electrical contacts as depicted in Fig. 3.2. Two current contacts and 4 smaller contacts (roughly square configuration) were placed on each side of the sample in order to measure both longitudinal and Hall resistivity.

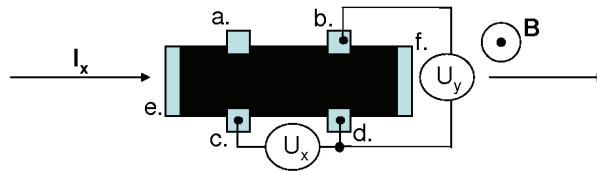


Figure 3.2: Configuration of the electrical contacts. Pairs of contacts a.-c. and b.-d. used to measure Hall resistivity $R_{xy} = U_y/I_x$, pairs of contacts a.-b. and c.-d. used to measure longitudinal resistivity $R_{xx} = U_x/I_x$. Two current contacts marked e. and f.

For purely optical experiments, we have used samples without electrical contacts. The samples used in far infrared experiments were polished under small angle in order to avoid interferences between plan parallel surfaces of the sample.

based on the growth of the two elements separately, 1 ML of the 1st and the 2nd compound, alternatively. This is in contrast to the standard, two or more component material growth, where all the components are grown simultaneously.

Chapter 4

Band structure calculations

4.1 Introduction

Basic knowledge of the energy structure of any experimentally studied physical system is of the fundamental importance for further data interpretation. We have calculated energies of confined states in the two, non-magnetic QWs in the density function approximation (DFA). Electronic and hole wave functions have been calculated in envelope function approximation (EFA). Beside more advanced, like tight binding methods [10, 11, 12] of heterostructure wave-function calculations, EFA represents a good approximation in QWs of such a width like 20 and 30 nm [13, 14]. Generally, EFA is restricted to high symmetry points in the heterostructure band structure, in contrast to tight-binding methods, which are capable to handle band structure in whole Brillouin zone [6]. For the sake of simplicity, we will restrict ourselves to the Γ point alone and zero temperature. In the discussion, we justify the validity of the parabolic approximation of the valence band structure in the vicinity of the Γ point.

4.2 Self-consistent solution of Schrödinger and Poisson equation

The hamiltonian (eq. 4.1) describes the structure of our QWs. It contains the kinetic energy $\mathcal{T} = -\frac{\hbar^2}{2} \frac{d}{dz} \frac{1}{m_e(z)} \frac{d}{dz}$, confinement potential V_{conf} , electro-static Hartree potential V_H and many-body contribution V_{xc} , which accounts for electron-electron interactions.

$$\hat{H} = -\frac{\hbar^2}{2} \frac{d}{dz} \frac{1}{m(z)} \frac{d}{dz} + V_{conf}(z) + V_H + V_{xc} \quad (4.1)$$

In the hamiltonian (4.1) $m(z)$ is the position dependent effective mass either of electrons or holes. In our calculations, we consider z as a growth direction. In the case of hole wave function calculations, the many-body exchange and correlation potential V_{xc} diminishes due to their very small concentration. Since we have used z -dependent material parameters (effective mass, permittivity), discontinuities of resulting envelope wave function $\chi_i(z)$ on the heterostructure interfaces have to be properly taken into account. The form of the kinetic operator \mathcal{T} leads to the continuous envelope wave function $\chi_i(z)$ and $\frac{1}{m_e(z)} \frac{d\chi_i(z)}{dz}$. However, $\frac{d\chi_i(z)}{dz}$ is discontinuous. Although there are other possibilities how to order

momentum operators [14], the form of kinetic operator used here is generally accepted and experimentally justified [15].

All z -dependent input parameters $p(z)$ ($p(z)$ stands for effective mass $m(z)$, relative permittivity $\epsilon_r(z)$ and confinement potential $V_{conf}(z)$) were described by shape function (4.2)

$$p(z) = (p_{out} - p_{in}) \left(\frac{1}{e^{\frac{z-z_1}{w}} + 1} + \frac{1}{e^{-\frac{z-z_2}{w}} + 1} \right) + p_{in} \quad (4.2)$$

determined by the value of a given parameter p_{in} inside and p_{out} outside QW and by the coordinates z_1, z_2 of the QW-barrier interface. Width w of the QW-barrier interface was chosen to be comparable to the lattice constant in CdTe ($w = 0.1 \text{ \AA}$). The shape function (4.2) has been chosen for the sake of simple numerical implementation.

Exchange and correlation term [16, 17, 18, 19, 20] are in DFA given by formula (4.3).

$$V_{xc} = -\frac{e^2}{8\pi\epsilon_0\epsilon_r(z)a_0^*(z)} \left\{ 1 + 0.0545r_s(z) \ln \left[1 + \frac{11.4}{r_s(z)} \right] \right\} \left[\frac{2}{\pi(4/9\pi)^{1/3}r_s(z)} \right] \quad (4.3)$$

Parameter $a_0^*(z)$ is an effective Bohr radius, Eq. (4.4),

$$a_0^*(z) = \frac{4\pi\epsilon_0\epsilon_r(z)\hbar^2}{m_e(z)e^2} \quad (4.4)$$

and r_s , Eq. (4.5), is a dimensionless electron density parameter.

$$r_s(z) = \left\{ \frac{4}{3}\pi[a_0^*(z)]^3 n_e(z) \right\}^{-1/3} \quad (4.5)$$

Electrostatic Hartree potential V_H is calculated by self-consistent solution of Poisson, Eq. (4.7), and stationary Schrödinger equation, Eq. (4.6), in order to obtain electronic envelope wave-functions $\chi_n(z)$ and subband energies E_n .

$$\hat{H}\chi_n(z) = E_n\chi_n(z) \quad (4.6)$$

$$\frac{d^2V_H}{dz^2} = \frac{e^2}{\epsilon_0\epsilon_r(z)} \left(n_D(z) - n_e \sum_{n \in \text{occupied}} |\chi_n(z)|^2 \right) \quad (4.7)$$

Concentration of donors $n_D(z)$ in the Poisson equation (4.7) is taken to be spatially distributed in the rectangular region (in z -direction) of the width 5 nm. Doping region is separated from the QW by the spacer of the same width as a width of the QW (Tab. 4.1).

As a second step, using self-consistently calculated electro-static potential of electrons, we have calculated energy spectrum of holes by solving hamiltonian (4.1) using effective mass of light or heavy holes and neglecting V_{xc} term.

We have implemented the simplest, although not the fastest, method of numerical solution of the set of Schrödinger and Poisson equations, which is based on discretization of the z -axis into intervals with nodes in z_k , where $k = \{1, \dots, N-1\}$ and N is number of equidistant interval of the length dz . Approximating the envelope wave function $\chi_n(z)$ by

Parameter	sample 013008A	sample 020108A
width of QW	20 nm	30 nm
spacer between QW and doping layer	20 nm	30 nm
concentration of 2DEG	$4.5 \times 10^{11} \text{ cm}^{-2}$	$2.9 \times 10^{11} \text{ cm}^{-2}$
effective mass of electrons in the QW	0.1 m_0 [this work]	
effective mass of electrons in the barrier	0.11 m_0 [21]	
effective mass of heavy holes in QW	0.5 m_0 [this work]	
effective mass of heavy holes in the barrier	0.58 m_0 [21]	
effective mass of light holes in QW	0.14 m_0 [21]	
effective mass of light holes in the barrier	0.16 m_0 [21]	
relative permittivity in the QW	$\epsilon_r=9.0$ [21]	
relative permittivity in the barrier	$\epsilon_r=8.5$ [21]	
valence band offset	30% [22]	
offset of the barrier for holes	$V_{barrier,h} = 125.4 \text{ meV}$	
offset of the barrier for electrons	$V_{barrier,e} = 293 \text{ meV}$	
gap of CdTe	$E_g(\text{CdTe})=1.605 \text{ eV}$ [23]	
gap of $\text{Cd}_{0.74}\text{Mg}_{0.26}\text{Te}$	$E_g(\text{Cd}_{0.74}\text{Mg}_{0.26}\text{Te})=2.023 \text{ eV}$ [23]	

Table 4.1: Parameters of the samples used in DFT calculations.

a vector $\chi_n(z_k)$ and derivative $\frac{d\chi_n(z)}{dz}$ by finite difference $(\chi_n(z_{k+1}) - \chi_n(z_k))/dz$ leads to the matrix representation (4.8) of the kinetic energy operator \mathcal{T} ,

$$\mathcal{T} = -\frac{\hbar^2}{2} \mathcal{D}_1 \frac{1}{m(z)} \mathcal{D}_2 \quad (4.8)$$

where an example of the numerical implementation of the operators \mathcal{D}_1 and \mathcal{D}_2 for the case of the z-axis discretization on four elements with $N = 5$ nodes at positions z_k is shown in matrices (4.9) and (4.10), respectively. Tests of the convergence of the solution has been done by refining the z-axis.

$$\mathcal{D}_1 = \frac{d}{dz} = \frac{1}{dz} \begin{pmatrix} -1 & 1 & 0 & 0 & 0 \\ 0 & -1 & 1 & 0 & 0 \\ 0 & 0 & -1 & 1 & 0 \\ 0 & 0 & 0 & -1 & 1 \\ 0 & 0 & 0 & 0 & -1 \end{pmatrix} \quad (4.9)$$

$$\mathcal{D}_2 = \frac{d}{dz} = \frac{1}{dz} \begin{pmatrix} 1 & 0 & 0 & 0 & 0 \\ -1 & 1 & 0 & 0 & 0 \\ 0 & -1 & 1 & 0 & 0 \\ 0 & 0 & -1 & 1 & 0 \\ 0 & 0 & 0 & -1 & 1 \end{pmatrix} \quad (4.10)$$

The material parameters used in the calculations [21] are summarized in the table 4.1.

4.3 Results

First, we compare the three potential contributions to the total potential of electrons in 20 nm wide QW, see Fig. 4.1. The negative sign of V_{xc} reflects the attractive character of

the electron-electron exchange interaction.

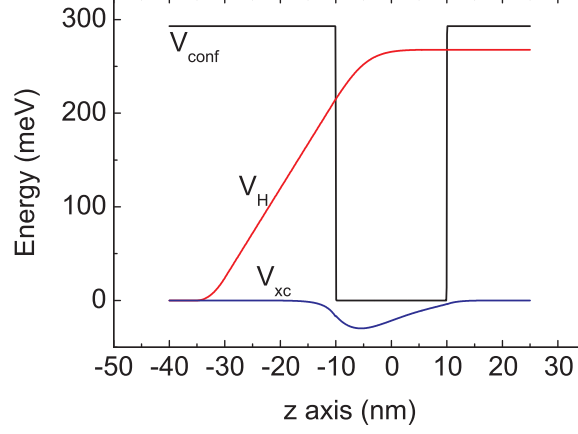


Figure 4.1: Three components of total effective potential in 20 nm wide QW containing 2DEG of concentration $4.5 \times 10^{11} \text{ cm}^{-2}$. Confinement V_{conf} , Hartree V_H and exchange and correlation V_{xc} potentials are depicted by black, red and blue curves, respectively.

Spatial evolution of the edge of the conduction and valence band, across the 20 and 30 nm wide QW, is depicted in Fig. 4.2 and Fig. 4.3, respectively. Due to asymmetric, single-side doping, positively charged donors in the doping layer attract (repel) electrons (holes) in the QW, and thus causing a spatial shift of the electronic (hole) envelope wave functions $\chi_n^e(z)$ ($\chi_n^h(z)$). This spatial shift changes selection rules in asymmetrically, with respect to symmetrically, doped QWs.

Diminishing of the confinement effect with growing width of the QW is apparent via squeezing of the inter-subband distance for both electronic and hole levels. The calculated electron, heavy and light hole energies for both QWs are summarized in the Tab. 4.2. The electron subband energies are related to the ground electronic state e_1 ($E_{1,e} = 0 \text{ meV}$), and both light and heavy holes are related to the ground state of heavy holes hh_1 ($E_{1,hh}$).

n	20 nm wide QW			30 nm wide QW		
	$E_{n,e}$	$E_{n,hh}$	$E_{n,lh}$	$E_{n,e}$	$E_{n,hh}$	$E_{n,lh}$
1	0	0	4.7	0	0	2.3
2	30.7	8.5	24.7	20.9	3.8	12.1
3	66.4	19.7	51.8	37.5	9.3	26.1

Table 4.2: Energies of the first three lowest lying electronic, heavy hole and light hole levels for both 20 and 30 nm wide QWs. Bottom of the conduction band is taken as a reference zero-energy for electrons. Zero-energy reference for holes is taken at the top of valence band of heavy holes.

We have found, that in 20 nm (30 nm) wide QW, the Fermi energy lies at 53.9 meV (75.7 meV) below the conduction band edge (measured from the bottom of the conduction band in the flat band region on the left hand side from the doping layer, see Fig. 4.2 and

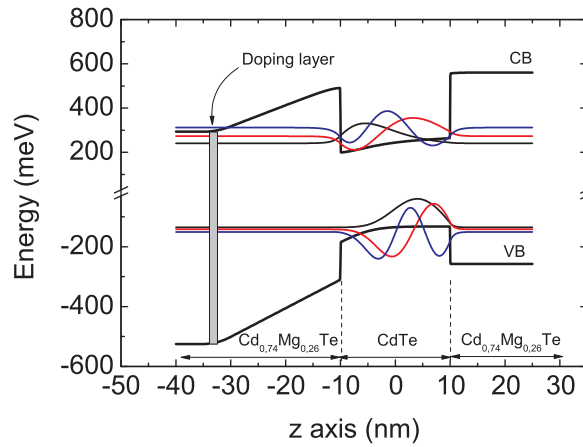


Figure 4.2: Resulting band structure (black solid lines) in 20 nm wide CdTe QW. Electron concentration $4.5 \times 10^{11} \text{ cm}^{-2}$. Upper(lower) black solid line corresponds to the spatial evolution of the bottom(top) of conduction(valence) band in z -direction. Calculated in Γ point of the reciprocal band structure. First electron and heavy hole wave-functions are plotted by thin black, blue and red colors in the corresponding band. Modulation doping is depicted by greyed rectangle in the left part of the figure.

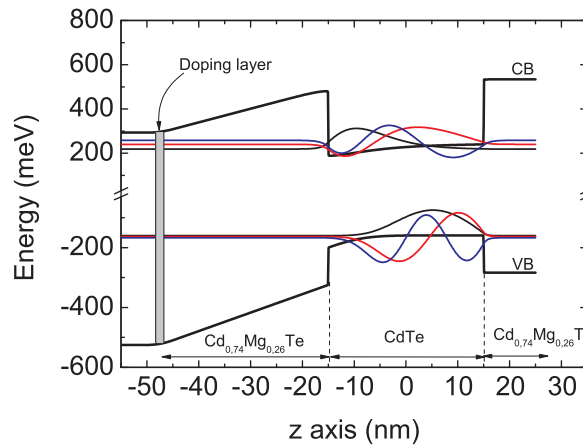


Figure 4.3: The same as Fig. 4.2, but calculated for 30 nm wide CdTe QW containing 2DEG of the concentration $2.9 \times 10^{11} \text{ cm}^{-2}$.

Fig. 4.3). According to the literature [24], donor binding energy in CdTe QWs at zero magnetic field is roughly 21 meV. Therefore we conclude, that donors are located well above the Fermi energy in both quantum wells, hence we expect that all of them are

fully ionized at zero temperature. The difference ≈ 22 meV between the Fermi energy of the 2DEG and the position of donors in the 20 nm wide QW could be a reason of possible reoccupation of donor states by electrons at the temperature higher than 40 K ($5k_B T = 22$ meV at ≈ 40 K). This could be therefore a reason of decreasing electron concentration of 2DEG inside the QW at so high temperatures. However, this effect will be accompanied by temperature induced lowering of the Fermi energy, which will occur already at roughly 25 K ($E_F = 5k_B T$ at ≈ 25 K).

4.4 In-plane dispersion

Although the majority of our experiments are sensitive only to the band structure in the vicinity of Γ point, in several cases, also band structure further apart the Γ point becomes important. These are, for example, correct interpretation of the photoluminescence excitation (PLE) spectra and description of the PL spectral line shape at zero magnetic field. For the sake of simplicity, we will use throughout this work a parabolic approximation for both conduction and valence bands. This simplified approach, although often used and valid especially for the conduction band, often fails in the description of the valence band. Therefore, we have calculated the structure of the valence band in order to verify the parabolic band approximation for holes. We have used 4×4 kp-Hamiltonian (4.11),

$$\mathcal{H}_{kp} = \begin{pmatrix} H_{hh} - H_{\perp}^{+} & c & b & 0 \\ c^{*} & H_{lh} - H_{\perp}^{-} & 0 & -b \\ b^{*} & 0 & H_{lh} - H_{\perp}^{-} & c \\ 0 & -b^{*} & c^{*} & H_{hh} - H_{\perp}^{+} \end{pmatrix} \quad (4.11)$$

where H_{hh} and H_{lh} are given by hamiltonian (4.1) for heavy and light holes, respectively. Terms H_{\perp}^{\pm} read

$$H_{\perp}^{\pm} = \frac{\hbar^2 k_{\perp}^2}{2m_0} (\gamma_1 \pm \gamma_2) \quad (4.12)$$

and terms b and c are given by

$$b = \frac{\sqrt{3}}{2} \frac{\hbar}{m_0} (k_x - ik_y) (\gamma_3 p_z + p_z \gamma_3) \quad (4.13)$$

and

$$c = \frac{\sqrt{3}}{2} \frac{\hbar^2}{m_0} [\gamma_2 (k_x^2 - k_y^2) - 2i\gamma_3 k_x k_y]. \quad (4.14)$$

Luttinger parameters γ_1 and γ_2 can be expressed in terms of the mass of heavy and light holes,

$$\gamma_1 = \frac{m_0}{2} \left(\frac{1}{m_l} + \frac{1}{m_h} \right) \quad (4.15)$$

and

$$\gamma_2 = \frac{m_0}{4} \left(\frac{1}{m_l} - \frac{1}{m_h} \right). \quad (4.16)$$

This is more convenient, since the effective masses, which can be directly determined from the experiment, are more intuitive parameters as compared to the Luttinger parameters.

The effective mass of the light hole $m_l = 0.14m_0$ and the Luttinger parameter $\gamma_3 = 1.6$ were taken from [21]¹. The solution of the Schrödinger equation

$$\mathcal{H}_{kp}\psi_{k_x,k_y,n}(\mathbf{r}) = E_{k_x,k_y,n}\psi_{k_x,k_y,n}(\mathbf{r}) \quad (4.17)$$

is, in general, anisotropic in reciprocal space. However, for the wave vectors of our interest, the anisotropy is small, hence we take the solution in the direction $\mathbf{k}_\perp = \frac{k_\perp}{\sqrt{2}}(1, 1)$. We have solved Schrödinger equation (4.17) in the basis of the envelope wave functions (2.8). The solution converged well when taking the basis of the ten lowest-energy heavy hole and the ten lowest-energy light hole states. The valence band structure of both 20 nm and 30 nm wide QWs are shown in Fig. 4.4 and Fig. 4.5, respectively. We plot the

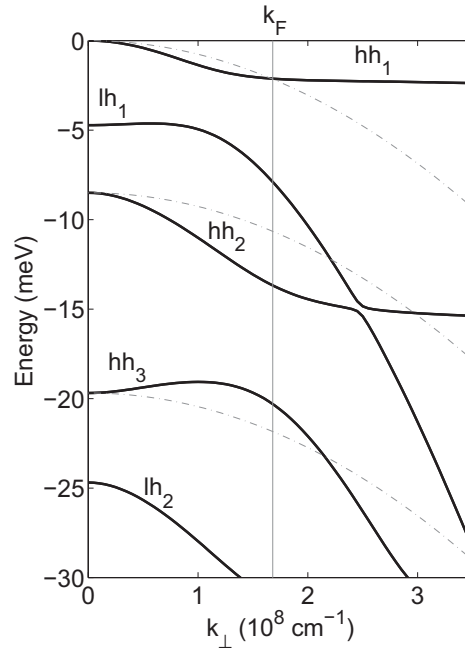


Figure 4.4: Dispersion of the lowest heavy and light hole valence band states in 20 nm wide QW. Vertical dashed line show Fermi wave vector corresponding to the electron concentration in the conduction band $n_e = 4.5 \times 10^{11} \text{ cm}^{-2}$. Approximative parabolic energy dispersion of heavy hole states is depicted for comparison by dash-dotted line.

energy dispersions of the first three heavy and first two light hole states. It should be noted that the terms “light” and “heavy” for holes are no longer correct when we talk about in-plane dispersion of valence band holes. The reason is twofold. Firstly, heavy holes are heavier than light holes only in the the z -direction (growth direction) of QWs. As a result, the energy of quantum confinement for the first heavy hole subband hh_1 is

¹In the literature, the mass of light holes ranges from $0.12m_0$ to $0.16m_0$ and the value of Luttinger parameter γ_3 from 1.6 to 2.5. We have found, that in our QWs, solutions of the valence band structure lead to non-physical valence band structure for any $\gamma_3 > 1.7$ and effective mass of light holes $m_l > 0.15$. Such solutions give increasing energy of holes (conduction band-like dispersion) at high wave vectors. Hence, we have chosen values $m_l = 0.14m_0$ and $\gamma_3 = 1.6$, which give correct $k_\perp \rightarrow \infty$ limit of valence bands.

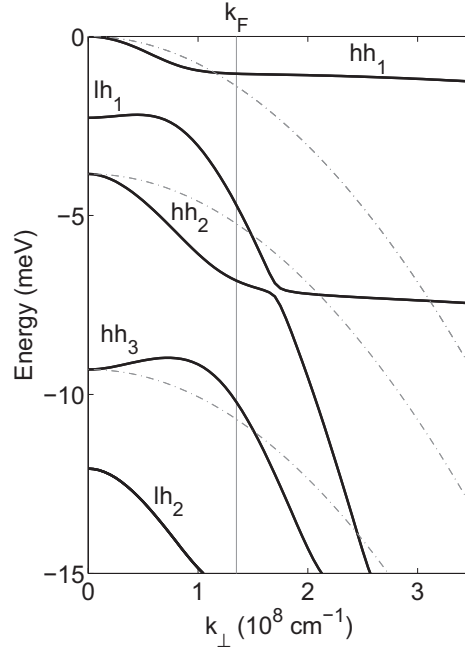


Figure 4.5: Dispersion of the lowest heavy and light hole valence band states in 30 nm wide QW. Vertical dashed line show Fermi wave vector corresponding to the electron concentration in the conduction band $n_e = 2.9 \times 10^{11} \text{ cm}^{-2}$. Approximative parabolic energy dispersion of heavy hole states is depicted for comparison by dash-dotted line.

smaller than for the first light hole subband lh_1 . However, in the in-plane direction (x, y directions), heavy holes hh_1 are always lighter than light holes lh_1 in the near surroundings of the Γ point. This property of the quantum confinement is in the literature called “mass reversal” and it is described by the k-p-Hamiltonian (4.11). The second reason is that light and heavy holes are generally mixed at $\mathbf{k} \neq 0$. This follows from the terms b and c in k-p-Hamiltonian (4.11). However, we follow terminology usually used in the literature (e.g. Ref. [6]), and call the bands according to their pure states in the z -direction and at the Γ point ($\mathbf{k} = 0$).

We compare the calculated valence band structure with the approximative parabolic dispersion of heavy hole states, see dispersions plotted by dash-dotted lines in Fig. 4.4 and Fig. 4.5. One can see that although the approximation is quite rough, it describes at least the lowest energy heavy hole band with the precision better than 1 meV up to the Fermi wave vector. Hence, for the sake of simplicity, we will use in our data analysis the parabolic approximation of the heavy hole energy dispersion.

Chapter 5

Basic characterization of the samples

5.1 Raman scattering

Raman scattering (RS) is an inelastic scattering of photons. It carries an information about low-energy excitations, which change the rotational, vibrational or electronic state of the investigated system. Our goal was to experimentally study mainly low-energy electronic properties of a 2DEG, determined by the spin splitting of electronic Landau levels and cyclotron resonance excitations.

The inelastic scattering is every scattering mechanism, during which the energy of the incident photon $h\nu_0$ is changed to some different, scattered energy $h\nu_1$. Energy difference $\Delta E = |h\nu_0 - h\nu_1|$ corresponds to a given excitation (vibrational, rotational or electronic) between certain ground $|0\rangle$ and excited $|1\rangle$ state with energies E_0 and E_1 , respectively. The Raman scattering signal consists of two main components, Stokes and anti-Stokes. They can be distinguished according to their position in the Raman spectra. The Stokes (anti-Stokes) component appears on the lower (higher) energy part of the Raman spectra with respect to the energy $h\nu_0$. These two components also differ by their relative intensity. The Stokes component is usually stronger. The relative strength of the two components is given mainly, beside the matrix elements of the transitions, by the degeneracy of the initial and final states and by the thermal distribution, which describes the occupation of the states $|0\rangle$ and $|1\rangle$ involved in the Raman scattering process. The energy of the incident photons $h\nu_0$ can be chosen arbitrarily. The intensity of the Raman scattering is generally very weak. However, it is possible to enhance its intensity by tuning the energy of either incoming or outgoing (scattered) photons in resonance with an energy E_{real} of certain, optically active excitation of the investigated system. If the energy of the photons $h\nu_0$ ($h\nu_1$) is in resonance with E_{real} , then we talk about incoming (outgoing) resonance.

We studied RS using the laser light generated by Ti:sapphire laser tunable in the spectral range from 700 – 900 nm. We employed the polarization resolved technique for both excitation and detection of RS (σ^+ or σ^- circular polarization). A preferable configuration for optimal excitation and detection of RS was when excitation and detection were set to opposite circular polarizations. In Figs. 5.1 and 5.2 we present Raman spectra obtained in resonant and non-resonant configurations, respectively. Non-resonant Raman scattering in Fig. 5.2 was measured by tuning the energy of incoming photons $h\nu_0$ well below the band gap energy of CdTe. Resonant Raman scattering was measured by tuning $h\nu_0$ roughly

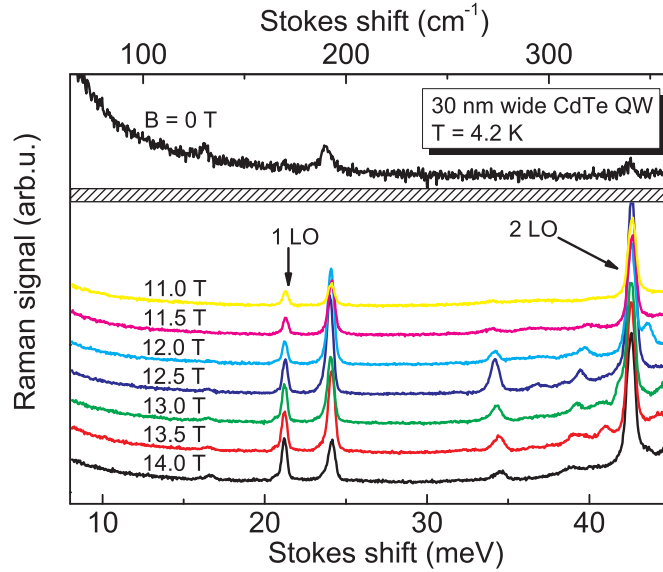


Figure 5.1: Raman signal measured at the temperature of $T = 4.2$ K. Energy of the incident laser was tuned 120 meV above main PL emission line (1.589 eV) and the laser power on the sample was of about $P_{exc} = 60 \mu\text{W}$. Raman scattering was generated by σ_{exc}^- circular polarization and emitted signal was collected in σ_{PL}^+ circular polarization. Laser spot size was estimated to be of about 200 – 600 μm in diameter.

60 meV above the edge of the forbidden gap. The intensity of the Raman signal is then enhanced by both incoming and outgoing resonances. Comparing both resonant and non-resonant Raman scattering spectra, one can clearly see that, as expected, the resonant Raman spectra are much richer. Moreover, although they are richer, they were excited also by the laser light of $\approx 5\times$ weaker intensity.

We have observed a set of 5 Raman lines in resonantly excited RS, see Fig. 5.1. These lines are observed at the energies of 16.7, 21.2, 24.1, 34.2 and 42.5 meV below the energy of the laser excitation. The Raman signals with the Stokes shift of 21.2 and 42.5 meV correspond to the first and second harmonics of LO-phonon in CdTe. The Raman shift of 16.7 meV is close to the energy of TO-phonon in bulk CdTe (≈ 17.5 meV) or this peak could be interpreted also as a LA-phonon in X and L point of a Brillouin zone, see Fig. 5.3.

Raman signal at the energy of 24.1 meV (Fig. 5.1) is interpreted as LO-phonon in the $\text{Cd}_{0.74}\text{Mg}_{0.26}\text{Te}$ barrier. The expected energy 24.7-26.4 meV was obtained by the linear interpolation between the energy of LO-phonon in CdTe (21.6 meV) and MgTe (36.5-40.0 meV) [21]. The origin of the signal at the energy of 34.2 meV is unknown. The Raman peak in non-resonantly induced RS at the energy of 36.5 meV is due to LO-phonon of GaAs substrate (see Fig. 5.2). This set of vibrational modes observed in the resonant and non-resonant RS was very similar in both 20 and 30 nm wide quantum wells. Therefore we present here only the data measured in 30 nm wide QW.

The intensity of the second LO-phonon replica marked by 2LO in Fig. 5.1 is stronger than than the intensity of the first replica (1LO). The reason is, that the second LO-

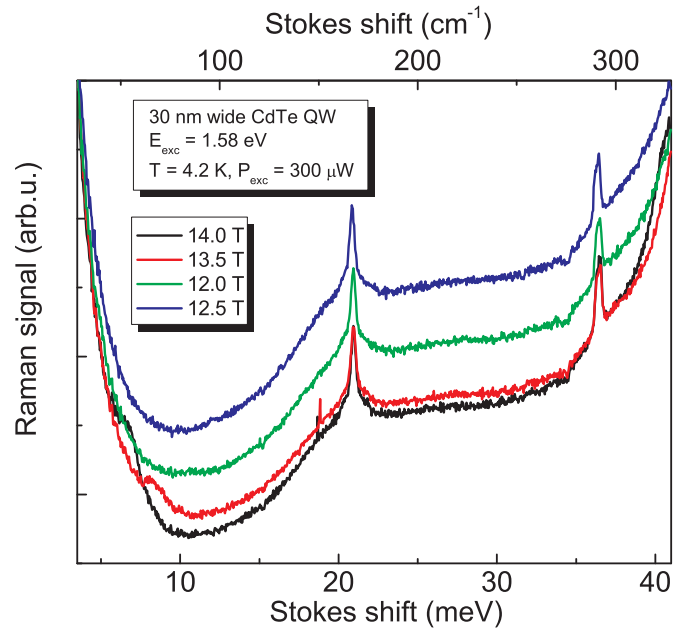


Figure 5.2: The same parameters of the experiment as in the Fig. 5.1, but the energy of the laser light was tuned below the energy of PL emission (≈ 13 meV) and the excitation power was $P_{exc} \approx 300$ μ W.

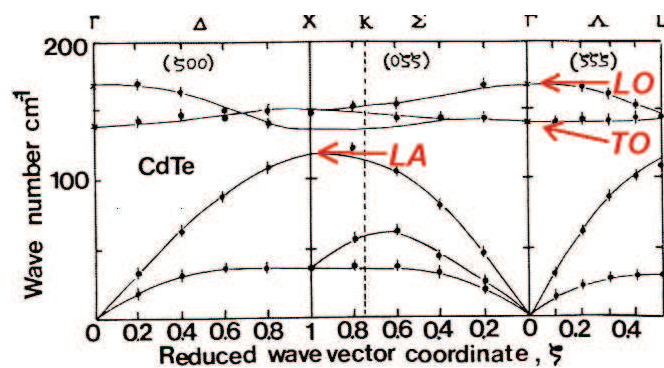


Figure 5.3: Dispersion of optical and acoustical phonons in CdTe according to [25]. Red arrows show phonons which are observed in the measured Raman scattering spectra (see Fig. 5.1 and Fig. 5.2).

phonon replica 2LO undergoes outgoing resonance with the energy levels, which take part in the photoluminescence radiative recombination, thus its intensity is more enhanced. We have found, that also the first LO-phonon replica can be enhanced when tuned in the resonance with the PL. Because the PL originates in the electron-hole recombination inside the QW, we assign also both 1LO and 2LO phonon replicas to have origin in the confined LO-phonon modes inside the QW. However, it should be noted that the signal from bulk LO-phonon modes will also contribute to both signals of 1LO and 2LO. This is because the energies of confined and bulk LO-phonons are in our samples very close to each other (much closer than the spectral resolution we have). This is caused by the fact, that the energy dispersion of LO-phonons is almost constant, or negligibly changes across the 1st Brillouin zone. The smallest z component of the quantized wave vector $k_{z,min} = \pi/d_{QW}$ (d_{QW} is a width of the QW) is roughly $40 - 50\times$ smaller than the size of the 1st Brillouin zone $k_{1.BZ} = \pi/a_0$ ($a_0 = 6.5 \text{ \AA}$ is a lattice constant of CdTe). The dispersion of the LO-phonon energy does not considerably change in the vicinity of the Γ point, up to the wave vectors of the order of $\approx k_{1.BZ}/5$, see Fig. 5.3. Therefore at least the first 10 ($k_{1.BZ}/5k_{z,min} \approx 10$) confined LO-phonons have the energy, which is very close to the energy of bulk LO-phonons.

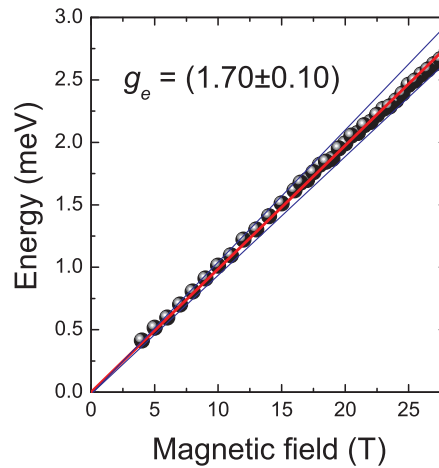


Figure 5.4: Magnetic field dependence of the energy of the electron spin flip excitation up to 28 T in 20 nm wide QW, measured at the temperature $T = 4.2 \text{ K}$, excitation power $P_{exc} = 32 \mu\text{W}$ (laser spot size $200 - 600 \mu\text{m}$). Energy of the excitation laser was tuned always from 1 to 5 meV above main PL emission energy. Electron spin flip was induced by σ^+ circular polarization and Raman signal was detected in σ^- circular polarization. The extracted electron g -factor is $g_e = (1.70 \pm 0.10)$. Two blue lines depict the high and low energy uncertainty bounds.

Beside vibrational excitations (LO, TO, LA phonons), which we have discussed so far, our main goal was to study electronic excitations. However, the only electronic excitation we were able to observe was the spin flip of electrons. We have measured the energy of the electron spin flip as a function of magnetic field in the range from 0 to 28 T for 20 nm wide QW (see Fig. 5.4) and 30 nm wide QW (see Fig. 5.5). Within a simple model, the energy of the electron spin flip excitation is given at $\mathbf{k} = 0$ by the Zeeman energy $g_e \mu_B B$, where

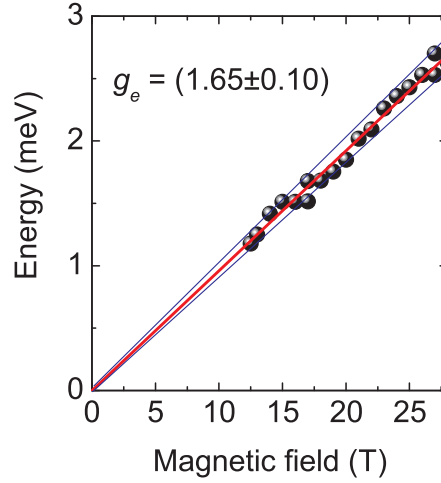


Figure 5.5: The same as in Fig. 5.4, but the data correspond to 30 nm wide QW and the excitation power was $P_{exc} = 220 \mu\text{W}$. The electron g -factor is $g_e = (1.65 \pm 0.10)$.

g_e is g -factor of electrons and μ_B is Bohr magneton ($\mu_B = 57.9 \mu\text{eV}\text{T}^{-1}$). Fitting the field dependence of the energy of the spin flip excitation gives the electronic g -factor $g_e = (1.70 \pm 0.10)$ and $g_e = (1.65 \pm 0.10)$ in 20 and 30 nm wide QW, respectively. Both values are equal within an experimental error and they well agree with values in the literature, e.g. Refs. [26, 27]. In the works [26, 27], the authors investigated CdTe/Cd_{0.75}Mg_{0.25}Te undoped QWs. The two samples of their interest had also similar widths 21 and 28.8 nm and corresponding electron g -factors were $|g_e| = 1.56$ and 1.602, respectively. Although an experimental error in our case is larger, our mean value of the g -factor in the narrower QW is larger than the mean value of the g -factor in the wider QW. This is in contrast to the results in Refs. [26, 27]. The reason of this discrepancy is probably due to the presence of the 2DEG in our QWs. Presence of the 2DEG causes that electronic spin flip excitations are not probed at the Γ point (center of the 1st Brillouin zone at $\mathbf{k} = 0$), but they are probed at $\mathbf{k} \neq 0$. It is well known that the spin gap of the electronic Landau levels can be influenced by electron-electron interaction at non-zero wave vectors [28] and therefore the scaling of the electronic g -factor with the width of the QW need not to be necessarily the same as in the undoped QWs. Since the experimental error of the g -factor determination in our samples is quite large and the mean values are not too distinct from the values of the electronic g -factor in the literature, we will use throughout this work the g -factor of electrons $|g_e| = 1.6$. This value is inside the 95% confidence interval of our experimentally measured electronic g -factors and is in agreement with the works of other authors [26, 27].

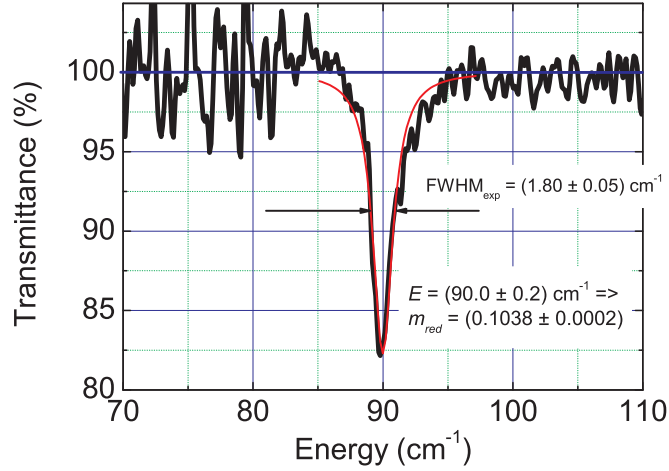


Figure 5.6: Transmission spectrum of 20 nm wide QW at 10 T and at the temperature of 2 K. Spectral resolution 0.25 cm^{-1} . Black curve is a data and red curve is a fit of the data with the Lorentz function. Width of the absorption peak was deduced directly from the experimental data.

5.2 Far infrared studies

Far infrared (FIR) spectroscopy deals with the part of the electromagnetic spectrum which ranges from energies of 10 to 1000 cm^{-1} . The magneto-spectroscopy in the FIR region is widely applied to 2DEG structures. It allows to probe the cyclotron resonance excitation, or in other words, inter-Landau level transitions of electrons in the vicinity of the Fermi energy. In the single particle picture, the energy of the cyclotron resonance in 2D system is given by the formula 5.1.

$$E_{CR} = \hbar\omega_c = \frac{\hbar eB}{m_e} \quad (5.1)$$

We have focused on the energy range from 50 to 170 cm^{-1} in the magnetic fields from ≈ 2 to 28 T , which corresponds to the spectral range, where cyclotron resonance of CdTe appears. All experiments were done in the transmission configuration, at the temperature of pumped helium ($T \approx 2 \text{ K}$). In order to avoid an interference of the light between the two plan-parallel surfaces of the samples, the substrate of the sample was polished under small angle, less than 5° . In Fig. 5.6 we show the spectrum of a cyclotron resonance measured at 10 T and at very high spectral resolution of 0.25 cm^{-1} . The width of the cyclotron resonance is here 1.80 cm^{-1} , which is roughly by an order of magnitude higher than the spectral resolution. Hence, we believe, that this is a real width of cyclotron resonance which is not influenced by the instrumental function of Far Infrared (FIR) spectrometer. For the sake of the time demands on the experiment, the rest of our FIR experiments was performed with much smaller spectral resolution of about 2 or 2.5 cm^{-1} , and measured width of cyclotron resonance was always of about $\approx 2.3 \text{ cm}^{-1}$. This value of the cyclotron resonance broadening does not correspond to the real value of broadening because its width is comparable to the spectral resolution of 2 cm^{-1} . Therefore, the difference between both widths 1.80 and 2.3 cm^{-1} measured with the spectral resolution of 0.25 and 2.0 cm^{-1} can

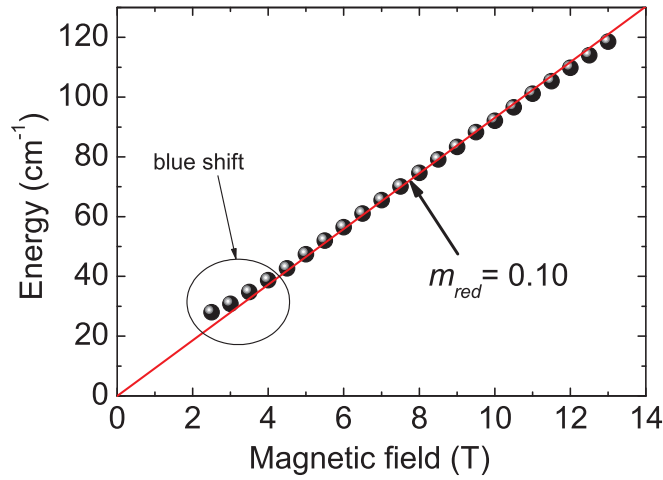


Figure 5.7: Energy position of the cyclotron resonance as a function of magnetic field at the temperature of 2 K for 20 nm wide QW. Black points are maxima of the absorption and red curve is a fit of the data with the expected single particle behavior given by the formula 5.1. The blue shift of the data with respect to the expected linear field dependence is labelled too.

be attributed to the instrumental function of the FIR spectrometer. For this reason, we have focused only on the analysis of the position of the cyclotron resonance absorption and not on the width neither on the intensity (intensity of the absorption also changes as a function of the spectral resolution - the worse spectral resolution the smallest intensity of the absorption). Detailed analysis of the cyclotron resonance absorption line shape (width and intensity) should thus contain a deconvolution of the experimental data by the instrumental function.

The main goal of our FIR study was to determine the effective mass of electrons. For this reason, we have measured cyclotron resonance absorption as a function of the magnetic field in the range from 2 to 14 T for both 20 and 30 nm wide QWs. An example of the magnetic field dependence of the energy of a cyclotron resonance absorption is depicted in Fig. 5.7 for 20 nm wide QW measured at the temperature of pumped helium $T = 2$ K. Effective mass of electrons was measured to be $0.10m_0$ in both QWs. This value is in agreement with the values published in literature, see for example [29].

More detailed inspection of the data of a cyclotron resonance in Fig. 5.7 reveals slight disagreement with strictly linear field dependence in the low-field limit with respect to the expected behavior given by the equation 5.1. The interpretation of this low-field blue shift is not clear so far.

In Fig. 5.8, we show the data of cyclotron resonance measured in 20 nm wide QW up to 28 T. The step-like structure of the data is caused by the step of the magnetic field 0.5-1 T used to measure the field dependence of the FIR absorption. Field dependence of the cyclotron resonance above Reststrahlenband consists of two principal contributions. A pinned mode (see Fig. 5.8), which only slowly grows in the energy and becomes pinned to the energy of LO-phonon at magnetic fields higher than 22 T. The second contribution

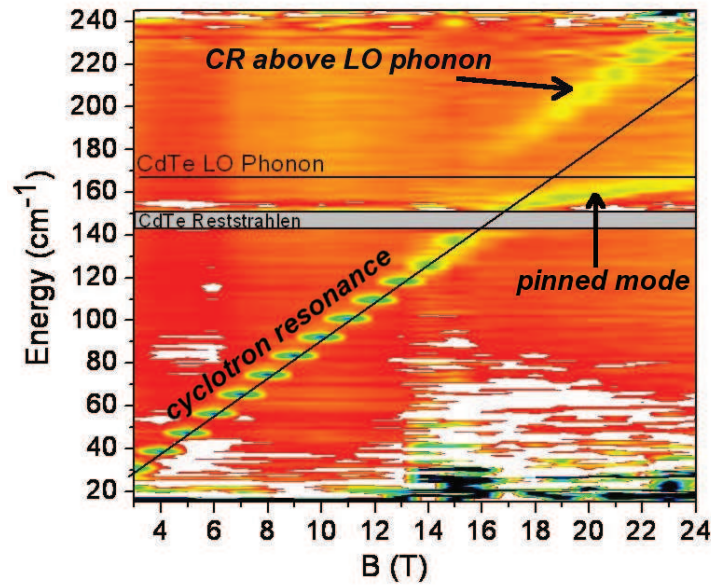


Figure 5.8: Far infrared spectra of 20 nm wide QW at the temperature of 2 K. Green and yellow marked features in the color scale correspond to the absorption of the cyclotron resonance. Pinned mode and blue shifted cyclotron resonance above Reststrahlen band are marked by arrows.

in the energy range above Reststrahlenband is the linearly growing energy of the cyclotron resonance absorption. This part of the cyclotron resonance is blue shifted with respect to the cyclotron resonance below Reststrahlenband. We attribute all these effects above Reststrahlenband to be of the coupled magneto-polaron and magneto-plasmon modes [30, 31, 32, 33, 34]. FIR magneto-absorption data measured in 30 nm wide QW do not show the pinned mode and the blue shift of a cyclotron resonance above Reststrahlenband was not so large as in 20 nm wide QW. More detailed analysis of this phenomenon is beyond the scope of this thesis and will be presented elsewhere.

Chapter 6

Magneto-transport

6.1 Low-field magneto-transport in CdTe QW

Magneto-transport deals with a study of transport of an electrical charge in a magnetic field. We will study magneto-transport properties of 2DEG via magneto-resistance and magneto-conductivity. The approach based on magneto-resistance is usually easier from the experimental point of view, however, the approach based on magneto-conductivity is better accessible from the theoretical point of view. Unfortunately, a connection between these two approaches is sometimes difficult due to unknown and/or complex geometrical factors. However, when assuming the homogeneous current distribution in the sample, the geometrical factors are quite easy to handle, as will be shown. The low field magneto-transport in 20 nm wide CdTe QW has been used to study such phenomena as, for example, weak localization, Shubnikov-de Haas oscillations, Landau level broadening, transport scattering time, quantum life-time and character of a dominant scattering mechanism.

We have measured both longitudinal (R_{xx}) and Hall (R_{xy}) magneto-resistance. An example of data measured at base temperature of 91 mK is shown in Fig. 6.1. The high quality of the studied 2DEG is reflected in the low field onset of Shubnikov-de Haas oscillations ($B_1 = 94$ mT) and the low field onset of spin splitting ($B_2 = 0.51$ T). The local minima in Hall resistance are caused by the contribution of longitudinal resistance R_{xx} . Hall resistivity is not influenced by R_{xx} at integer filling factors, because $R_{xx} = 0 \Omega$ at enough high magnetic fields (≈ 1 T and more). Hall resistivity can be influenced by longitudinal resistance only if R_{xx} is non-zero, hence in the plateaux-to-plateaux transition only. Because the plateaux-to-plateaux transitions correspond to the local minima of Hall resistivity, these minima are then caused by the contribution of R_{xx} . Another manifestation of R_{xx} in a data of R_{xy} is a shift of magnetic field, at which Hall resistance R_{xy} is zero. In an ideal case, R_{xy} should be zero at $B = 0$ T. However, adding some contribution of R_{xx} shifts the Hall resistance and thus causing, that experimentally measured Hall resistance is zero at non-zero magnetic field. The shift of the field, where $R_{xy} = 0 \Omega$ is in our experiment caused also by the remanent field ≈ 26 mT of the superconduction coil, in which the experiment was performed. The field, at which we have observed $R_{xy} = 0 \Omega$ was 32 mT. The real Hall resistance \tilde{R}_{xy} was found using an empirical formula (6.1),

$$\tilde{R}_{xy} = R_{xy} + \gamma_1 R_{xx} \quad (6.1)$$

where the parameter γ_1 represents the geometry of the electrical contacts on the sample.

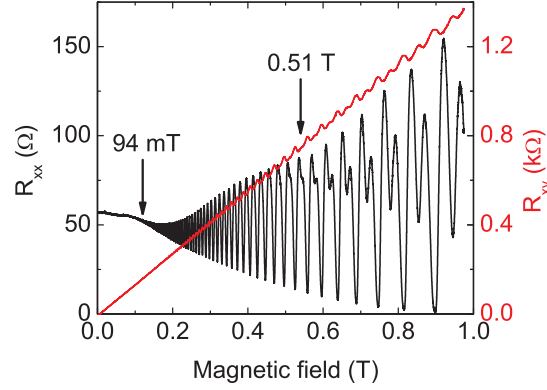


Figure 6.1: Longitudinal (black curve) and Hall (red curve) resistivity of 20 nm wide CdTe/CdMgTe QW at base temperature of 91 mK. Sample was illuminated by laser light at the energy $E_{exc} = 2.41$ eV (Ar^+), power on the sample $P_{illum} = 1.0$ μW and laser spot size ≈ 2 mm. Arrows at 94 mT and 0.54 T show magnetic fields at which Shubnikov-de Haas oscillations (B_1) and spin splitting (B_2) appear.

The deduced contribution of R_{xx} was of about $\gamma_1 = 16$ %. Such a correction well reduces the observed local minima in R_{xy} and at the same time it shifts the zero Hall resistance to the magnetic field of 25.8 mT, which is in good agreement with a remanent field of the superconduction coil used in these experiments.

The second geometrical factor is the ratio of distances between electrical contacts used for measuring R_{xx} and R_{xy} given by $\gamma_2 = l_x/l_y = 1.07$, where l_x (l_y) is a distance between longitudinal (Hall) contacts. Having these two geometrical factors (γ_1 and γ_2) and assumption of a homogeneous current in the sample, one can derive formulas (6.2) and (6.3) to calculate longitudinal (σ_{xx}) and Hall (σ_{xy}) conductivity.

$$\frac{\sigma_{xx}}{\sigma_0} = \frac{R_{xx}R_{xx,0}}{R_{xx}^2 + \gamma_2^2 \tilde{R}_{xy}^2} \quad (6.2)$$

$$\frac{\sigma_{xy}}{\sigma_0} = \frac{\tilde{R}_{xy}R_{xx,0}}{\frac{R_{xx}^2}{\gamma_2} + \gamma_2 \tilde{R}_{xy}^2} \quad (6.3)$$

The parameter σ_0 is the zero field conductivity given by equation (6.4),

$$\sigma_0 = \frac{n_e e^2 \tau_{tr}}{m_e} \quad (6.4)$$

where n_e is the concentration of 2DEG, e is an elementary charge, τ_{tr} is a transport life-time and m_e is an effective mass of electron.

6.1.1 Analysis of the conductivity

The conductivity calculated according to the formulas (6.2) and (6.3) is plotted in Fig. 6.2 (a). The data, normalized by conductivity σ_0 , Eq. (6.4), were fitted by the semi-classical Drude

model (Eq. (6.5) and (6.6)) normalized by the same parameter σ_0 .

$$\sigma_{xx}^{Drude} = \frac{\sigma_0}{1 + (\omega_e \tau_{tr})^2} \quad (6.5)$$

$$\sigma_{xy}^{Drude} = \frac{\sigma_0 \omega_e \tau_{tr}}{1 + (\omega_e \tau_{tr})^2} \quad (6.6)$$

Other two parameters in Eq. (6.5) and (6.6) are cyclotron angular frequency of electrons ω_e and transport lifetime τ_{tr} .

Fair agreement with the experimental data has been obtained. The transport life time is the only fitting parameter here, $\tau_{tr} = 15$ ps. The corresponding zero field conductivity is $\sigma_0 = 18.7$ mS/m and mobility

$$\mu = \frac{e}{m_e} \tau_{tr} \quad (6.7)$$

$\mu = 260000$ cm²V⁻¹s⁻¹. Subtracting the data and the Drude model, one can see systematic deviations from Drude model, Fig. 6.2 (b). These contributions are of the order of 0.5 % of the total conductivity. They are not taken into account in Boltzmann transport equation and they are usually of purely quantum mechanical origin. We suggest the interpretation of a dip in the conductivity in the vicinity of zero magnetic field as due to a contribution of a weak localization. Weak localization, suggested first by Abrahams at the end of 1970's [35], is caused by destructive interference of electrons in disordered media and thus reduces conductivity at zero magnetic field. It occurs at low temperatures, at which the phase of electrons is maintained for enough long time, so as they can interfere with each other. It is weaker in high quality samples, it strengthens in more disordered materials. When disorder is too extensive, the localization turn into strong Anderson localization [36]. Another typical feature of weak localization is that it rapidly disappears with increasing magnetic field, which is of the order of mT in high quality samples. There can be found an extensive amount of both theoretical and experimental works [37, 38, 39, 40, 41, 42, 43] dealing with this phenomenon. Review paper comparing various approaches of the weak localization description is provided by McPhail [40]. Our data exhibit qualitatively similar behavior as the one reported in several other works [44, 45, 40]. However, we have not been able to reach the satisfactory description of our data by any approximative description of weak localization, thus leaving the final conclusion open.

The second contribution to the total conductivity is usually explained in terms of electron-electron interaction. It is often called negative magneto-resistance in the literature [46, 47] and there had been long discussion, whether it can influence also field dependence of the conductivity. It has been shown recently, that it does [48, 49, 50]. Although principally correct approach, the data description by electron-electron interaction is not very transparent and hard to visualize. Instead, we prefer an alternative approach based on semi-classical picture, where many-body phenomena are described in a picture of non-interacting (or weakly interacting) single-particles. This is similar to quasi-particle approach¹. The idea has been sketched already at the end of 1970's [51], but we will follow the recent work of Dmitriev [52]. Although semi-classical, it goes beyond the frame

¹An extraordinary example of quasi-particle approach in a physics of interacting many-body systems is a description of Fractional quantum Hall effect, where complex electron-electron interactions are simplified by introducing single-particle picture of composite fermions, which do not, or very weakly, interact with each other.

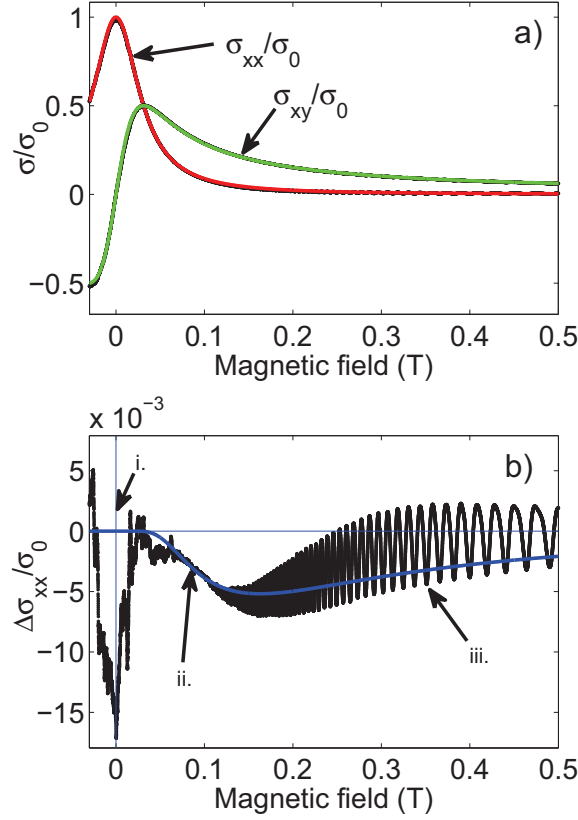


Figure 6.2: (a) Longitudinal (σ_{xx}) and Hall (σ_{xy}) electrical conductivity at base temperature of $T = 91$ mK, normalized by zero-field value σ_0 . Data (black points) are compared with Drude model, which is depicted by red (σ_{xx}) and green (σ_{xy}) curves. (b) Difference between data of longitudinal conductivity σ_{xx} and their fit by Drude model, normalized by σ_0 . Possible interpretation of (i) a dip in the vicinity of zero magnetic field as a weak localization effect and (ii) decrease of the conductivity as a contribution of either electron-electron interaction or localization of circling electrons. Blue curve is a fit using model of the localization of circling electrons. (iii) Schubnikov-de Haas oscillations.

of Boltzmann transport equation. The idea is based on classical picture of the electron motion in magnetic field. Such an electron moves on circular trajectories with a radius $R = v/\omega_e$, where v is velocity of the electron (Fermi velocity). The higher magnetic field is, the smaller is the radius R , and the more probable is the localization of such an electron. These electrons are called circling electrons, because since they are localized, they only circle around given scattering center or potential fluctuation and do not contribute to the conductivity. It has been shown [53], that the fraction of such electrons is given by Eq. (6.8)

$$P = e^{-\frac{2\pi}{\omega_e\tau_{tr}}} \quad (6.8)$$

and their negative contribution to the conductivity is given by Eq. (6.9).

$$\Delta\sigma_{circ} = -\sigma_0 \frac{P}{1 + (\omega_e\tau_{tr})^2} \quad (6.9)$$

Equation (6.9) is valid, if number of scatterers within one cyclotron orbit is much smaller than one. The comparison of the presented theory of circling electrons with a data is shown in Fig. 6.2 (b). The model is plotted by blue line. Although an agreement with data is satisfactory, we had to use time $\tau = 10$ ps in formula (6.8) instead of $\tau_{tr} = 15$ ps, as should be when following strictly Eq. (6.9). The reason is probably due to the fact that the assumption of the negligible concentration of scatterers per one cyclotron orbit is not fulfilled. Hence numerical modelling of the data following [52] could give more accurate results.

We inverted conductivity tensor considering Drude model and the model of circling electrons in order to deduce an influence of the circling electrons on the resistivity. The experimentally measured resistance was calculated with respect to the geometry of our sample as described above. The comparison is presented in Fig. 6.3. Drude model gives constant field dependence of resistance R_{xx} and its field dependence in Fig. 6.3 is thus a manifestation of circling electrons.

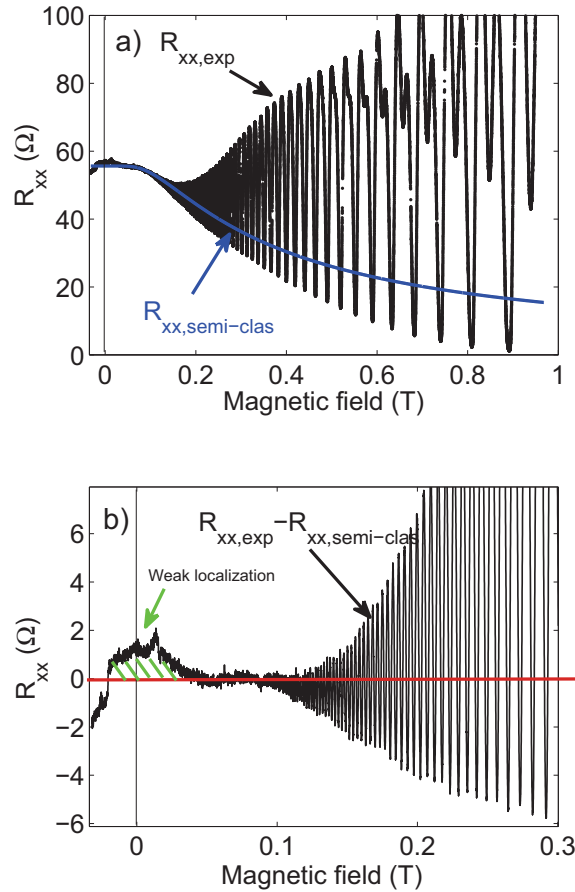


Figure 6.3: (a) Measured resistance R_{xx} (black points) compared with a background of the resistance given by the semi-classical contribution of localized circling electrons (blue curve). (b) Difference of data and the theory shown in part (a) gives the contributions of weak localization and Shubnikov-de Haas oscillations to the resistance R_{xx} .

Subtracting Drude and circling contribution to the resistivity from the data (subtracting black and blue curves in Fig. 6.3), one obtains the influence of a weak localization and Shubnikov-de Haas oscillations on the measured resistance. Weak localization is negligibly small and SdH oscillations are well-separated from all other contributions. Such a separation simplifies an analysis of particular phenomena, especially in the case of SdH oscillations it simplifies the processing of Fourier transform. Fourier transform of SdH oscillations is presented in Fig. 6.4. It clearly shows two pivotal frequencies. The stronger (weaker) one, at the frequency of $B_{\nu=1}/2$ ($B_{\nu=1}$) originates in spin unresolved (resolved) Landau levels. Field $B_{\nu=1}$ is a field at the filling factor $\nu = 1$. More detailed analysis of SdH oscillations will be provided in the following text, analyzing resistance R_{xx} .

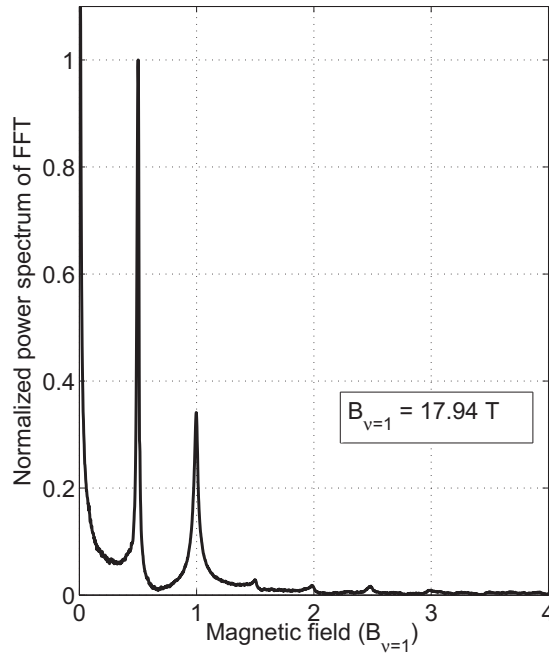


Figure 6.4: Normalized power spectrum of Fast Fourier Transform of the data presented in Fig. 6.3 (b). Data are plotted as a function of the magnetic field normalized by magnetic field at filling factor $\nu = 1$ ($B_{\nu=1} = 17.94 \text{ T}$).

6.1.2 Analysis of the resistivity

Basic theory

Here, we focus on the analysis of SdH oscillations measured in the temperatures from 91 mK to 1200 mK. Data at these two limiting temperatures are shown for illustration in Fig. 6.5. Clear dumping of the amplitude of SdH oscillations is observed.

In order to model such an experimental observation, we have used two standard models. The two models, which differ in the type of the broadening of electronic Landau levels, Gaussian or Lorentzian. The density of states in 2-dimensional systems will be then described by equation (6.10) for Lorentzian broadening and by equation (6.11) for Gaussian

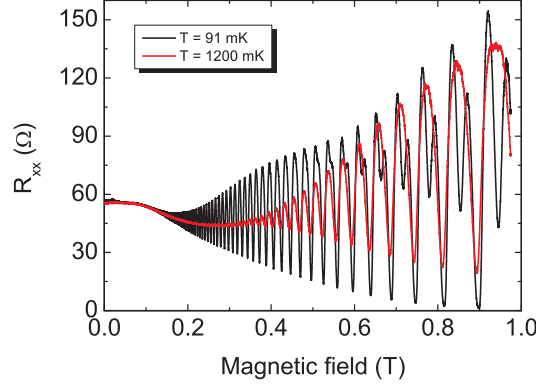


Figure 6.5: Longitudinal resistance R_{xx} at the lowest (black curve) and highest (red curve) temperature.

broadening. Normalization is done by zero-field density of states $m_e/\pi\hbar^2$.

$$g_1(E, B) = \frac{\hbar\omega_e}{\pi\Gamma_e} \sum_{N=0}^{\infty} \frac{1}{1 + \left(\frac{E-E_N}{\Gamma_e}\right)^2} \quad (6.10)$$

$$g_2(E, B) = \frac{\hbar\omega_e}{\sqrt{2\pi}\Gamma_e} \sum_{N=0}^{\infty} e^{-\frac{(E-E_N)^2}{2\Gamma_e^2}} \quad (6.11)$$

The resulting normalized conductivity at arbitrary temperature is calculated according to formula (6.12) (for example [54, 55])

$$\frac{\sigma_{xx}}{\sigma_0} = \int_{-\infty}^{\infty} g_l(E, B) \left(-\frac{\partial n_{FD}}{\partial E}\right) dE \quad (6.12)$$

and the conclusion follows Fourier series (6.13). The results for both Gaussian and Lorentzian broadening differ in fact only in the exponent l , see Eq. (6.13), where $l = 1$ for Lorentzian broadening and $l = 2$ for Gaussian broadening.

$$\left| \frac{\sigma_{xx}(B) - \sigma_0}{\sigma_0} \right| = 2 \sum_{s=1}^{\infty} (-1)^s \exp \left[-2 \left(\frac{\pi\Gamma_e s}{\hbar\omega_e} \right)^l \right] \frac{s 2\pi^2 k_B T / \hbar\omega_e}{\sinh(s 2\pi^2 k_B T / \hbar\omega_e)} \cos \left(\frac{2\pi E_F s}{\hbar\omega_e} \right) \quad (6.13)$$

Usually, for the sake of simplicity, only the first term in the Fourier series (6.13) is taken, hence the expression used to describe the oscillatory part of conductivity is (6.14).

$$\left| \frac{\sigma_{xx}(B) - \sigma_0}{\sigma_0} \right| = 2 \exp \left[-2 \left(\frac{\pi\Gamma_e}{\hbar\omega_e} \right)^l \right] \frac{2\pi^2 k_B T / \hbar\omega_e}{\sinh(2\pi^2 k_B T / \hbar\omega_e)} \cos \left(\frac{2\pi E_F}{\hbar\omega_e} \right) \quad (6.14)$$

The condition, which validates an approximation by the first term in Fourier series, is not always fulfilled. It assumes very small modulation of the density of states, hence very small magnetic fields. The approximation of Eq. (6.14) by the first term alone is applicable in our samples roughly up to 0.5 T as was deduced by modelling of DOS (Eq. (6.10), (6.11))

and comparing it with its Fourier series expansion. Though the Fast Fourier Transform of data in Fig. 6.4 clearly shows small contributions of higher order terms, these higher order terms are negligibly small. The applicability of this approximation will be revised also later in the text.

Another important assumption, used in the derivation of Eq. (6.13), is introduced by neglecting spin splitting of Landau levels. We have shown in the data, that spin splitting appears at the base temperature (91 mK) at about 0.5 T, what is the same limitation as given by assuming only the first term in Fourier expansion.

The relation between conductivity and resistivity is in the literature usually done by approximative equation:

$$\frac{\Delta\sigma_{xx}}{\sigma_0} \approx \frac{\Delta\rho_{xx}}{\rho_0} \approx \frac{\Delta R_{xx}}{R_{xx,0}} \quad (6.15)$$

We are aware of limits of this approximative formula, however, we have tried to analyze SdH by both conductivity and resistivity and both approaches provided the same results, hence, we will analyze preferably the directly measured data of R_{xx} .

In order to eliminate all possible background contributions to the resistance, for example, the discussed contribution of circling electrons, we analyze the amplitude of SdH oscillations $\Delta R_{xx} = |R_{xx,max} - R_{xx,min}|$. In order to subtract $R_{xx,max}$ and $R_{xx,min}$, the maximal values $R_{xx,max}$ at fields of the minimal values $R_{xx,min}$ were determined by the nearest-neighbor interpolation method. Amplitudes of SdH oscillations obtained with such a procedure are presented in Fig. 6.6, for a complete set of temperatures from 91 mK to 1200 mK. The manifestation of spin splitting is marked by dashed line. This is the part of the data, which is not taken into account in our analysis.

Approximative expressions

According to formulas (6.14) and (6.15) the amplitude of the resistance is given by Eq. (6.16), where cosine was replaced by a factor 2 in order to account for its maximum-to-minimum amplitude. We compare two approaches of analyzing data using the expression

$$|R_{max} - R_{min}| = 4R_{xx,0} \exp \left[-2 \left(\frac{\pi\Gamma_e}{\hbar\omega_e} \right)^l \right] \frac{2\pi^2 k_B T / \hbar\omega_e}{\sinh(2\pi^2 k_B T / \hbar\omega_e)}. \quad (6.16)$$

The first approach approximates the term $x/\sinh(x)$ by $2xe^{-x}$ and the second one treats the whole expression (6.16) without any approximations. In the literature, sometimes also an approximation $x/\sinh(x) \approx 1$ is used. It is valid at low temperatures and high magnetic fields when $x \ll 1$. Although it could be concluded at the first sight, that this approximation could be valid in our data, since the data looks temperature insensitive at low temperatures, the condition of its validity is not fulfilled; $x \cong 1.5T(K)/B(T)$ in CdTe. Hence the region of validity extends into the region of spin splitting already at the base temperature of 91 mK. A misleading conclusion of temperature independent data comes from the fact, that the low temperature data were measured with much smaller step in temperature than high temperature data. Hence, the data look temperature insensitive.

The approximation $x/\sinh(x) \approx 2xe^{-x}$ is valid in the limit $x \gg 1$ and it will be applied only for the case of Lorentzian Landau level broadening. We have found, comparing both expressions $x/\sinh(x)$ and $2xe^{-x}$, that the condition $x > 2.5$ is sufficient to keep an error

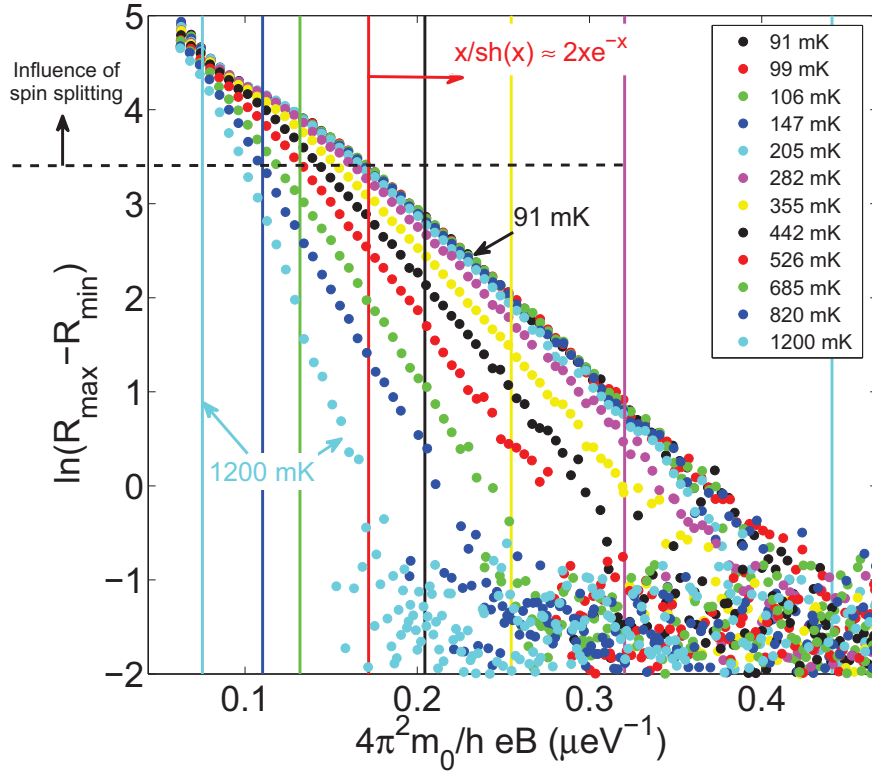


Figure 6.6: (Points) Natural logarithm of the amplitude of SdH oscillations plotted versus $4\pi^2 m_{e0}/h eB$ in the range of temperatures 91-1200 mK. Horizontal dashed line show the region of the data where influence of the spin splitting occurs. Vertical solid lines of a given color assign the maximal field where approximation $x/\sinh(x) = 2xe^{-x}$ holds for a given temperature (data plotted with the same color). Units of the x -axis are given by the prefactor of a parameter γ in Eq. (6.17).

of the approximation in the order of few percent. Intervals of the validity $x > 2.5$ are shown in Fig. 6.6 by vertical lines and the red arrow denotes the half-plane where the approximation holds. Multiplying the data by magnetic field and taking their natural logarithm leads to the final formula (6.17).

$$\ln(\Delta R_{xx} B) = \ln(16R_0 \pi^2 k_B T m_e / \hbar e) + \frac{4\pi^2}{\hbar e B} (-\pi k_B T m_e - \Gamma_e m_e) \quad (6.17)$$

The slope of $\ln((R_{xx,max} - R_{xx,min})B)$ versus $4\pi^2 m_0 / \hbar e B$ is described by parameter γ , Eq. (6.18), which is given by effective mass of electrons and broadening of Landau levels.

$$\gamma = -\pi k_B T m_e - \Gamma_e m_e \quad (6.18)$$

The slope γ is plotted in Fig. 6.7 together with two possible fits of its linear temperature dependence in the high temperature limit. The two fits are shown to underline the uncertainty of parameters m_e and Γ_e , obtained in this approximation. In the first case (blue fit in Fig. 6.7), the effective mass of electrons is twice larger than expected and Landau level broadening is too small. In the second case (red fit in Fig. 6.7), the effective mass is closer to the expected value of 0.1 and the broadening is also more realistic. However the

interval of data which was used to obtain these parameters is difficult to find unless we know the result.

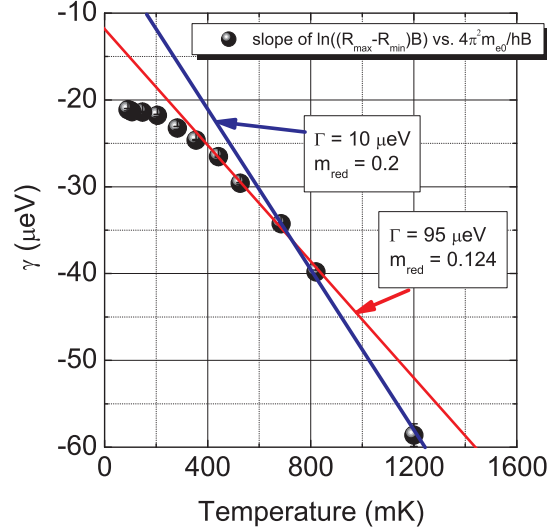


Figure 6.7: Slope $\gamma = -\pi k_B T m_e - m_e \Gamma_e$ of the $\ln((R_{xx,max} - R_{xx,min})B)$ versus $4\pi^2 m_0 / h e B$ as a function of temperature. Two possible fits of $\gamma = \gamma(T)$ (red and blue curve) are compared.

Another problem of this approximation is how well these parameters reproduce the absolute value of the SdH oscillations. The comparison is done in Fig. 6.8 by using formula (6.16) and parameters $\Gamma_e = 95 \mu\text{eV}$ and $m_e = 0.124 m_0$. One can see, that even though the slopes of the model well reproduce the slopes of the data, the discrepancy in the absolute values is too big.

We have shown here that the approximation $x/\sinh(x) \approx 2xe^{-x}$ of the formula (6.16) and using two fitting parameters (m_e, Γ_e) does not work well. Although the enhanced effective mass determined from SdH oscillations has been reported in the literature [56] p. 550, we will show in the following approach, that such a conclusion from the analysis of the slope of SdH oscillations alone might be wrong.

Temperature properties

In the second approach, we have used directly the formula (6.16) to fit the amplitudes of SdH oscillations. The unperturbed electron mass $m_e = 0.1 m_{e0}$ was used and only the broadening Γ_e was treated as a fitting parameter. The result for Lorentzian and Gaussian broadening of electronic Landau levels are shown in Fig. 6.9 (a) and Fig. 6.10 (a), respectively.

Very good agreement with data has been obtained in the case of Lorentzian broadening. The good agreement with a model is in fact at the expense of introducing a term of temperature dependent broadening, see Fig. 6.9 (b) and Fig. 6.10 (b). Broadening is in the range from 70 to 80 μeV for Gaussian and from 105 to 120 μeV for Lorentzian broadening. Even though one could conclude from temperature dependence of broadening on some tendency in the data (minimum of Γ_e at about 300 mK), the uncertainty of the

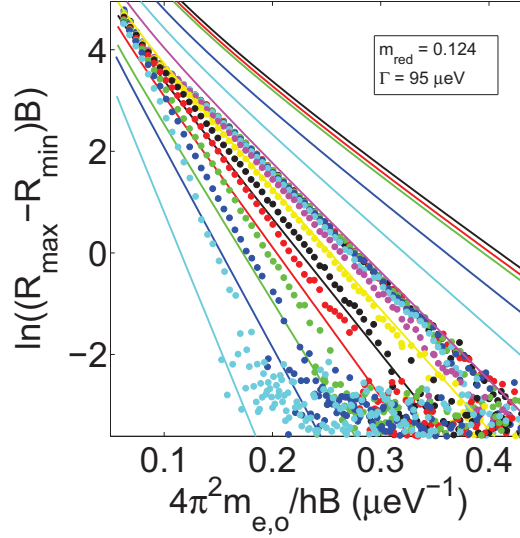


Figure 6.8: Comparison of the data (points) and model (lines) of the amplitude of SdH oscillations for temperatures 91-1200 mK. The values of fitting parameters are $\Gamma_e = 95 \mu\text{eV}$, $m_e = 0.124m_0$, as obtained by analyzing slopes of diminishing amplitude of SdH oscillations alone, without taking into account their absolute values.

fitting parameter of about $10 \mu\text{eV}$ makes it difficult to do further conclusion. Both types of broadening differ also in the zero field resistance $R_{xx,0}$, which is a scaling parameter of the amplitude of SdH oscillations, see Eq. (6.16). Its value is $R_{xx,0} = 25 \Omega$ and $R_{xx,0} = 65 \Omega$ in the case of Gaussian and Lorentzian broadening, respectively. The experimentally measured value is 58Ω in the Hall bar and 53Ω in the van der Pauw configurations. Comparing these values and the quality of the fit, we conclude, that the electronic Landau level have mainly Lorentzian line shape with small contribution of Gaussian broadening.

We have tried to improve the description of SdH oscillations in the case of Gaussian broadening taking into account more than the first term in the Fourier series expansion in Eq. (6.13). The result is shown in Fig. 6.11 where we have taken into account first 50 terms of the fourier expansion of conductivity. The result is not very distinct with respect to the one-term case presented in Fig. 6.10. The difference occurs in the high field region, where the data are better described by 50 terms. This is a natural conclusion, because at high fields the modulation of the density of states is no longer small. Landau levels can not be any more described simply by harmonic modulation, and therefore higher harmonics appear in the case of high-field deep density of states modulation.

Although the data has been successfully described, the question remains, why the fitting parameter Γ_e exhibits certain degree of the variation around the value $\Gamma_e \approx 110 \mu\text{eV}$. Because the temperature of electrons need not to correspond to the bath temperature, we fitted the data once more, using a constant Lorentzian broadening $\Gamma_e = 110 \mu\text{eV}$ and an effective mass of electron as in the first set of data analysis $m_e = 0.1m_0$ and the temperature was used as a fitting parameter. Another reason for using the temperature as a fitting parameter is that the temperature determined in the experiment is burdened

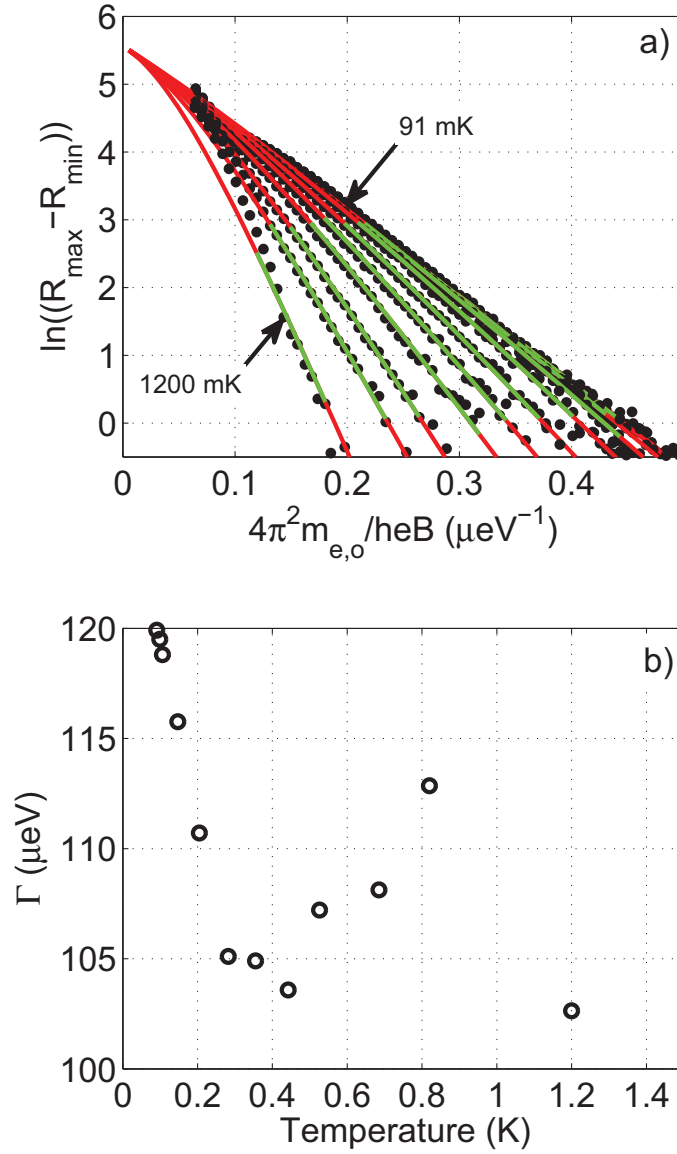


Figure 6.9: (a) Amplitude of SdH oscillations (black points) fitted by formula (6.16). Lorentzian broadening was assumed ($l=1$) and Γ_e was used as a fitting parameter. Fitted curves are plotted by red lines. Regions of the data which were used in fitting procedure are marked by green curves. (b) Fitting parameter Γ_e as a function of temperature.

by an experimental error², which can be, in principle, corrected by using temperature as a fitting parameter. The fitted temperature, see Fig. 6.12, which we call the carrier temperature, is roughly the same as the bath temperature (measured in experiment) at

²A cernox thermometer was used to measure the temperature of the sample. The distance between the thermometer and the sample was $\approx 3\text{-}5$ mm.

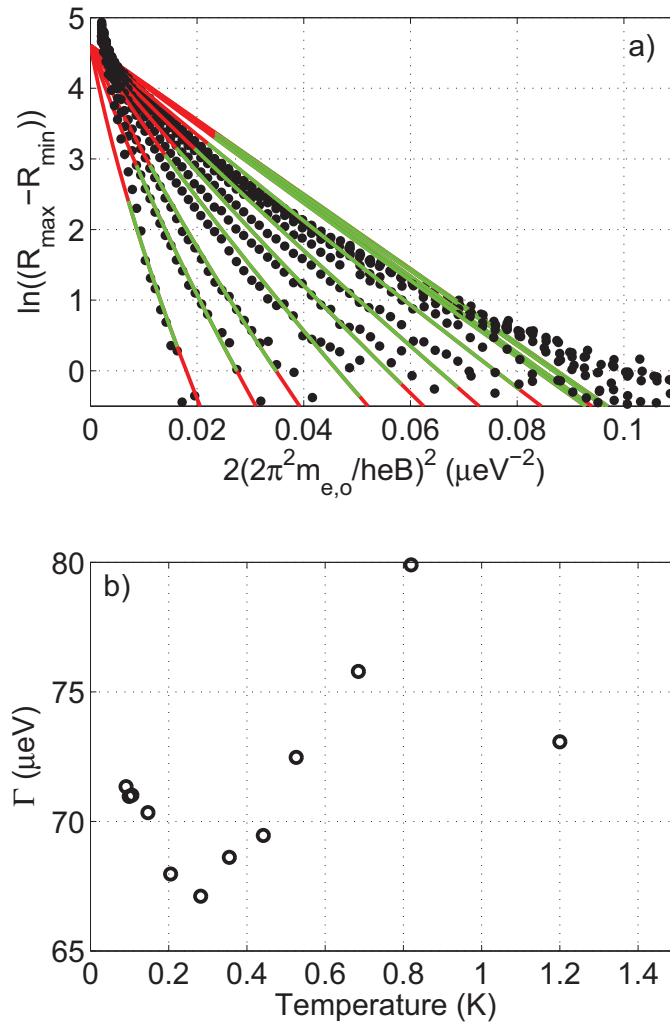


Figure 6.10: The same as in Fig. 6.9 but Gaussian broadening ($l=2$) used.

high temperatures above 200 mK. Slight deviations from the measured values are assigned to the experimental error of the temperature determination. However, the low temperature limit shows quite big discrepancy between both values. The carrier temperature saturates at the value of about 200 mK.

We exclude too large current used in the magneto-resistivity measurements as a reason for such a saturation, because the data were measured twice, using the current 20 and 100 nA and the amplitude of the SdH oscillations was the same in both cases. The reason of the saturation can be that we illuminate sample by the laser light, and thus we increase the carrier temperature with respect to the lattice temperature. If the cooling power is less efficient below 200 mK than the heating by the laser beam, the temperature saturates in such a case.

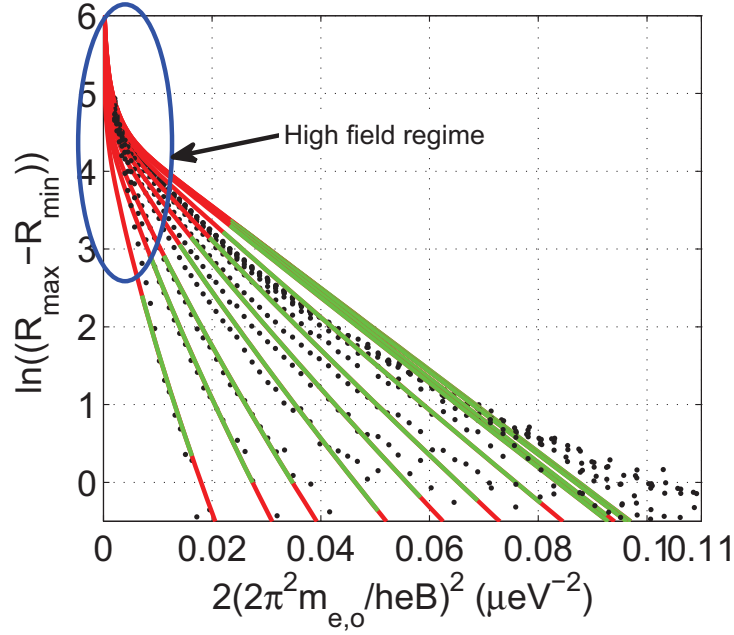


Figure 6.11: The same as in Fig. 6.10 but first 50 terms in Fourier expansion of the density of states used. The improvement with respect to one-term Fourier expansion in high field regime is marked by blue circle.

Field properties

So far, we have been studying the broadening and effective mass of electrons as a function of temperature. Here, we plot the data as a function of temperature for all magnetic fields, thus obtaining field dependence of broadening and electron effective mass. The same data as in Fig. 6.6 are plotted here versus temperature and shown in Fig. 6.13.

In contrast to the previous section, the analysis here can be done independently on the shape of the Landau level broadening. As follows from the full expression of the electrical conductivity, Eq. (6.13), the shape of the broadening enters only as an exponent l in the temperature independent part of Eq. (6.13). Hence, one can use a whole temperature independent part as a single fitting parameter which has a meaning of amplitude of SdH oscillations A at zero-temperature, Eq. (6.19).

$$A = 4R_0 e^{-2\left(\frac{\pi\Gamma_e}{\hbar\omega_e}\right)^l} \quad (6.19)$$

Thus, we use the formula (6.20) with two free parameters - amplitude A and electron effective mass m_e .

$$|R_{max} - R_{min}| = A \frac{2\pi^2 k_B m_e T / \hbar e B}{\sinh(2\pi^2 k_B m_e T / \hbar e B)} \quad (6.20)$$

The result of fitting is compared with data in Fig. 6.13 and field dependence of the amplitude and effective mass are depicted in Fig. 6.14 (a) and (c). The corresponding broadening of the Lorentzian or Gaussian line shape can be calculated according to the equation (6.19), and the field dependence of Lorentzian and Gaussian broadening Γ_e is

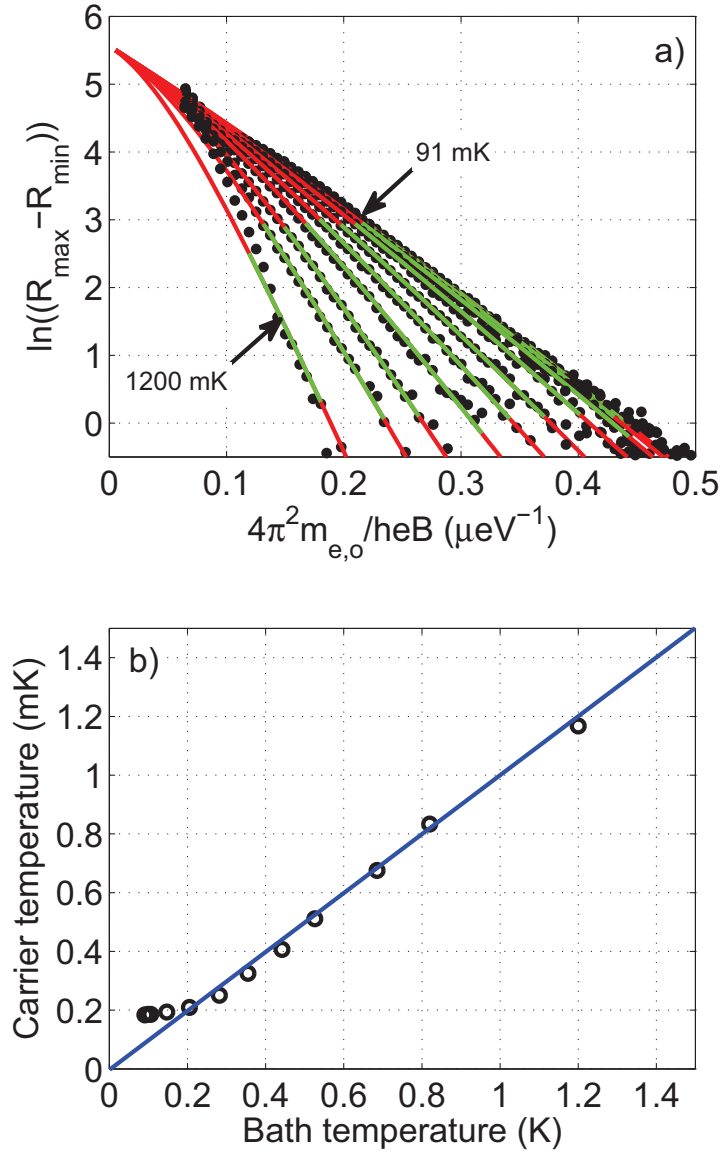


Figure 6.12: The same as in Fig. 6.9 but temperature of carriers was used as a fitting parameter. Lorentzian broadening with $\Gamma_e = 110 \mu\text{eV}$ used constant for all bath temperatures. Effective mass of electron $m_e = 0.1m_0$.

shown in Fig. 6.14 (b). The values for both types of broadening are consistent with values obtained by previous analysis, where data were plotted versus magnetic field and the broadening was obtained as a function of temperature.

Since neither broadening nor effective mass manifest significant changes in magnetic field up to the 0.5 T (high field limit of the validity of used approximations), we have reduced the number of fitting parameters, and only the field dependence of broadening was

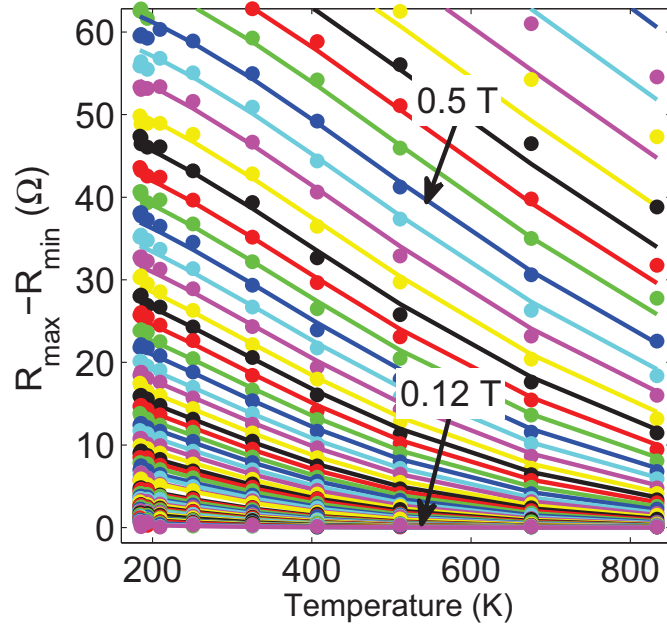


Figure 6.13: Amplitude of SdH oscillations plotted versus temperature for several magnetic fields, distinguished by color. Points are experimental data and curves their fits by formula (6.16).

calculated, as shown in Fig. 6.15. Effective mass of electron was taken to be $m_e = 0.1m_{e0}$, which is in agreement with fitted value and also with the value obtained by far infrared absorption measurements of cyclotron resonance. Again, as in the previous case when using two fitting parameters, also here the field-dependent analysis is consistent with the temperature-dependent analysis.

We comment on a field dependence of the broadening above 0.5 T, thus, beyond the limits of a validity of approximations under which the formula (6.16) for longitudinal conductivity was derived. The broadening exhibits clear maximum at the field of 0.6 T, Fig. 6.15. The spin-splitting appears roughly at this field, but the expression for conductivity (6.16) has been derived without considering the spin splitting. One can expect that at a very small spin splitting, the two spin Landau levels are nearly, but not yet completely separated. Hence, one can describe them still as a one Landau level, but with effectively larger broadening. This is why we believe, that the maximum in broadening is caused by the fact, that spin splitting is not taken into account, what effectively broadens Landau levels.

We conclude, that there is neither significant temperature nor field dependence of both the broadening and the electron effective mass in the range of the fields up to 0.5 T and temperatures from 91 mK to 1200 mK. We have found, that Landau levels are well described by Lorentzian broadening with parameter $\Gamma_e = 110 \mu\text{eV}$, what corresponds to the quantum lifetime $\tau_q = \hbar/2\Gamma_e = (3.0 \pm 0.3)$ ps. We also underline the importance of using the full expression (6.16) instead of approximative formula (6.17).

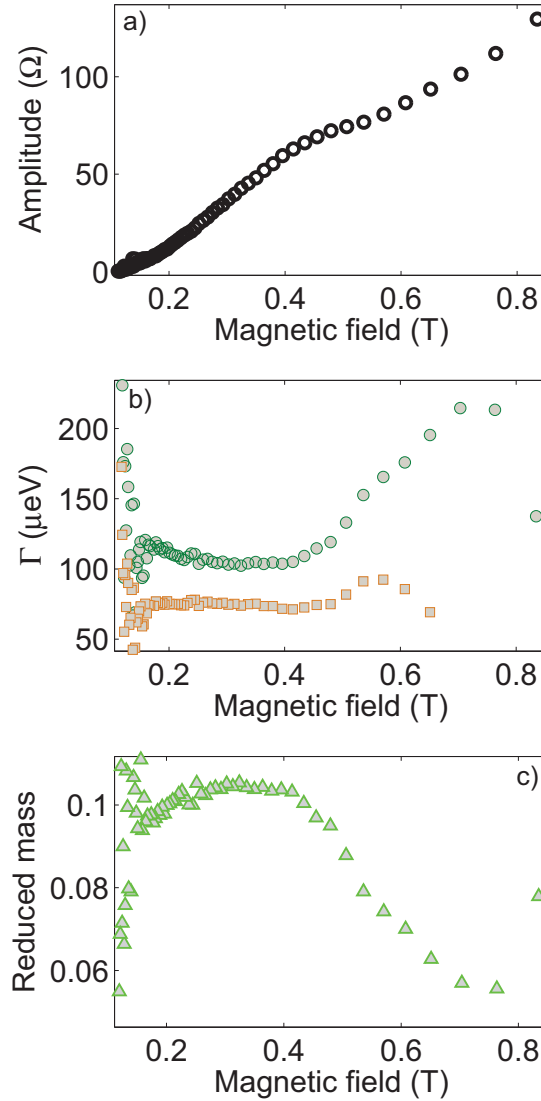


Figure 6.14: Amplitude of SdH oscillations (a) and effective mass of electron (in units of m_0) (c) as a function of magnetic field as obtained by fitting the temperature dependence of SdH oscillations. Fitting parameters (a) and (c) are results of the fitting procedure presented in Fig. 6.13. (b) Broadening Γ_e calculated from the amplitude (a) using formula (6.19) taking Lorentzian (green circles) and Gaussian (orange squares) broadening into account.

6.1.3 Comments on various formulas of SdH oscillations

Finally, we would like to comment on various formulas for SdH oscillations, which are commonly used in the literature. Since 1950's there have been a number of theoretical studies of SdH effect [57, 58, 59, 60] both in 3D and 2D systems. We have already

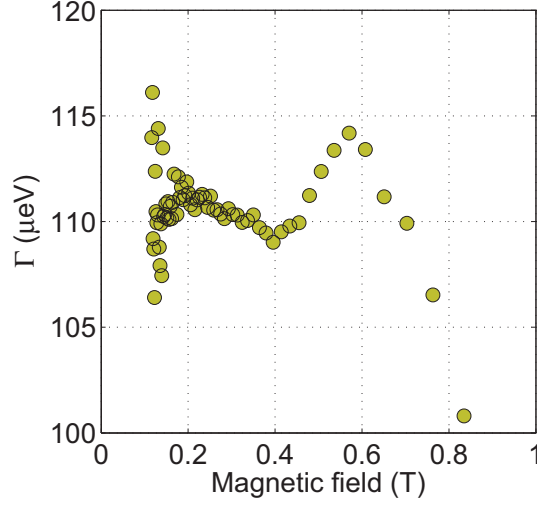


Figure 6.15: Broadening of the Lorentzian-shape Landau levels as a function of magnetic field. Parameter Γ_e obtained by fitting data presented in Fig. 6.13.

considered two possible types of broadening which are usually used [61] and now we look on the origin of two possible numerical prefactors in the conductivity formula. In this thesis we follow the work of Ando [62, 56, 63], who uses the formula (6.14) with a prefactor 2. However, the prefactor 4 is also sometimes used [64, 65, 66]. It was shown [55, 67], that the difference comes from the type of scattering in studied system. The prefactor is equal to 2 (4) if the scattering is of the long-(short-)range type.

Drude conductivity σ_{xx} is given in the diffusion regime ($\omega_e \tau_{tr} \gg 1$) by

$$\sigma_{xx} = \frac{e^2 n_{eff}}{m_e \tau_{tr} \omega_e}, \quad (6.21)$$

where an effective concentration of carriers n_{eff} contributing to the conductivity is proportional to the density of states $g_e(E_F, B)$

$$n_{eff} \propto g_e(E_F, B). \quad (6.22)$$

Hence we have a linear proportionality between conductivity and the density of states

$$\sigma_{xx} \propto g_e(E_F, B). \quad (6.23)$$

If also $1/\tau_{tr}$ is proportional to the density of states

$$\frac{1}{\tau_{tr}} \propto g_e(E_F, B), \quad (6.24)$$

then conductivity is proportional to the square of the density of states

$$\sigma_{xx} \propto g_e^2(E_F, B). \quad (6.25)$$

Taking into account the fact that g_e can be written as $g_e = 1 + \delta g_e$, where δg_e is a small modulation ($\delta g_e \ll 1$), than neglecting the second order term $\delta^2 g_e$,

$$g_e^2(E_F, B) = (1 + \delta g_e)^2 \simeq 1 + 2\delta g_e, \quad (6.26)$$

we obtain the additional prefactor 2. The probability $1/\tau_{tr}$ is proportional to the density of states if the scattering is of the short-range origin. Because our data fit better with the prefactor 2, we guess that there is a dominant role of the long-range scattering. This conclusion can be done also comparing transport ($\tau_{tr} = 15$ ps) and quantum lifetime ($\tau_q = 3$ ps). If the short-range scattering dominates, these times are expected to be equal [65, 68].

The absence of the short-range scattering is another sign of the high quality of our samples, as has been already concluded from the low field onset of SdH oscillations and the spin-splitting in R_{xx} .

A last comment is devoted to the field dependence of the Gaussian and Lorentzian broadening. Comparing expressions for the conductivity (6.14) in the case of Lorentzian (Γ_L) and Gaussian broadening (Γ_G), one gets the relation between these two types of broadening

$$\Gamma_L = \frac{\pi}{\hbar\omega_e} \Gamma_G^2. \quad (6.27)$$

Consequently, the field independent Lorentzian broadening is equivalent to the square-root (\sqrt{B}) field dependence of the Gaussian broadening. Hence, having no further information on the shape of LLs, we can not deduce the field dependence of the broadening. The determination of the LL shape could be done comparing zero field value of resistance R_{xx0} with the experiment. However, without information on the nature of the scattering in the sample (long or short range), this factor would vary by a factor of two and the comparison would be difficult. It seems to us that the best way is to compare the quality of the fit to data plotted versus $1/B$, as done in Fig. 6.9 and Fig. 6.10. If the analysis independent on the shape of Landau levels is required, than plotting data versus temperature is a preferable option.

6.2 Low-field magneto-resistance in CdMnTe QW

For the sake of comparison with the non-magnetic 20 nm wide CdTe QW, we present also low field magneto-resistance measurements in 21.1 nm wide CdMnTe QW. Both QWs contain 2DEG of the similar concentration (4.5 and $4.0 \times 10^{11} \text{ cm}^{-2}$ in CdTe and CdMnTe QW, respectively). The main difference with respect to the non-magnetic CdTe QW is a presence of manganese.

6.2.1 Base temperature measurements

Longitudinal magneto-resistance R_{xx} measured in CdMnTe QW at the base temperature $T = 90$ mK is shown in Fig. 6.16. For better readability, we plot the data as a function of the inverse value of the magnetic field. The same data are also plotted in Fig. 6.19 in linear x-scale (B-dependence). The resistance R_{xx} in CdMnTe QW exhibits SdH oscillations, as well as the resistance R_{xx} in the non-magnetic CdTe QW. The beating pattern of the SdH oscillations is a fingerprint of manganese. The beating has well defined nodes (black arrows in Fig. 6.16) and maxima (red arrows in Fig. 6.16) and the nodes at sufficiently high magnetic fields exhibit doubled frequency of SdH oscillations (see nodes $n = \{0, 1, 2, 3, 4\}$ in Fig. 6.16). The beating is due to manganese induced Giant Zeeman Splitting (GZS) and the character of nodes (zero/non-zero amplitude or doubled frequency of SdH oscillations)

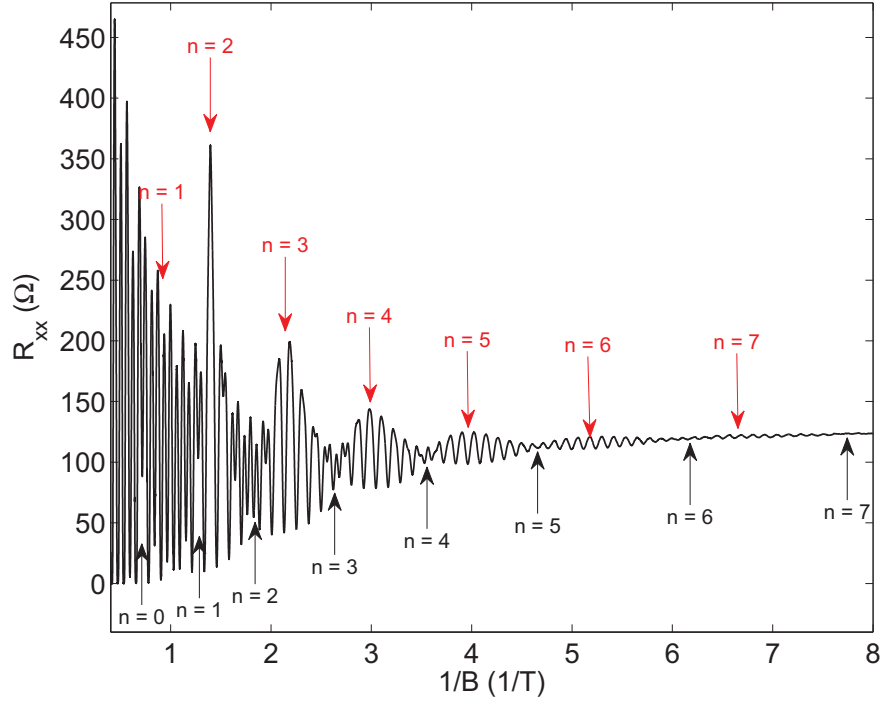


Figure 6.16: Longitudinal magneto-resistance R_{xx} as a function of the inverse value of magnetic field. Measured in 21.1 nm wide CdMnTe QW at the base temperature of 90 mK. Sample was illuminated by laser light at the energy $E_{exc} = 2.41$ eV (Ar^+), power on the sample $P_{illum} = 1.0$ μ W and the laser spot size was ≈ 2 mm. Black (red) vertical arrows show positions of the nodes (maxima of beating) in the beating pattern of R_{xx} , when the condition $\Delta_s = \hbar\omega_e(n + \frac{1}{2})$ ($\Delta_s = n\hbar\omega_e$) is fulfilled.

is governed by the ratio of the broadening of electronic Landau levels Γ_e and the cyclotron energy $\hbar\omega_e$. An electronic configuration of manganese is $[Ar]4s^23d^5$, hence in the equilibrium there are 5 electrons with the same spin in the last partially occupied electronic shell. These 5 electrons described by d-wave functions (spherical harmonics $Y_{l,m} = Y_{2,m}$) give rise to the intrinsic magnetic moment $S_{Mn} = 5/2$. The interaction of these d-electrons with s-electrons from the conduction band is generally called the s-d exchange interaction. The s-d exchange interaction manifests as Giant Zeeman Splitting (GZS). GZS can be understood as a consequence of local magnetic field produced by alignment of magnetic moments of manganese in the direction of the external magnetic field. The stronger external magnetic field is, the more manganese atoms are aligned parallel with each other giving rise to stronger local magnetic field. Such an enhancement of the local magnetic field with respect to the external field leads to a non-linear field dependence of the energy of electrons in the conduction band³ and also to the non-linear increase of the spin splitting which becomes enormously large with respect to the bare Zeeman splitting. This is why such a splitting is called GZS. GZS vanishes at zero magnetic field and it is more than $6\times$ larger than the cyclotron energy $\hbar\omega_e$ already at magnetic field of ≈ 0.25 T in our sample. In order to explain the beating pattern of the SdH oscillations, we follow the work of

³Energy levels of holes are also influenced by the presence of manganese, in this case by p-d exchange interaction, as will be shown in the chapter 7.2.2.

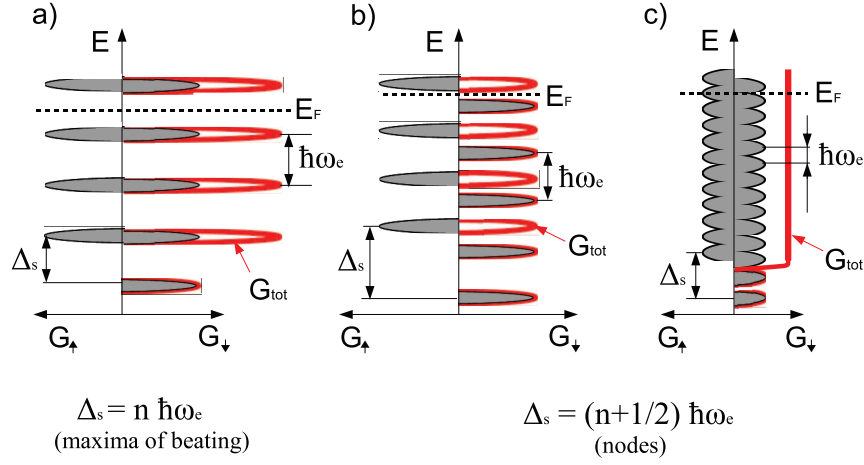


Figure 6.17: Scheme of the relative energy positions of the density of states (G) of electrons with the spin up (G_{\uparrow}) and down (G_{\downarrow}) (grey filled curves). Total, spin unresolved density of states G_{tot} is depicted by the solid red curve. Fermi energy E_F moves in the part of the DOS shown by horizontal dashed line. Part (a) describes the situation when the energy of the total spin splitting of the electronic Landau levels Δ_s is an integer multiple of the cyclotron resonance energy ($\Delta_s = n\hbar\omega_e$, $n = \{0, 1, 2, \dots\}$). When situation (a) occurs, maxima in the beating pattern of the longitudinal magneto-resistance R_{xx} are observed. Parts (b) and (c) describe the situation, when the condition $\Delta_s = \hbar\omega_e(n + \frac{1}{2})$, $n = \{0, 1, 2, \dots\}$ is fulfilled and the nodes are observed in the beating pattern of R_{xx} versus B . Parts (b) and (c) correspond to the situation, when the width of the electronic Landau levels Γ_e is (b) smaller (c) larger than the energy of the cyclotron resonance $\hbar\omega_e$. In the case (b), the total spin unresolved DOS is still modulated (frequency of the modulation is twice higher than the modulation of the spin resolved DOS) and in the case (c) the modulation of the total DOS is smoothed out due to the fulfilled condition $\Gamma_e > \hbar\omega_e$.

Teran [69]. The maxima of the density of states (DOS) of the electrons with spin up (G_{\uparrow}) and down (G_{\downarrow}) become alternatively in- and out- of phase when increasing magnetic field. If the two DOS are in-phase (out-of-phase), maxima (nodes) in the beating pattern are observed. This is because the in-phase alignment of the two DOS keeps the gap between two adjacent Landau levels open, see Fig. 6.17 (a), for this reason the oscillations are observed. Moreover, it maximizes number of states, into which the electrons can scatter, and for this reason maxima in the beating are observed. This situation occurs when the spin gap of the electronic Landau levels Δ_s is an integer (n) multiple of the cyclotron energy $\hbar\omega_e$

$$\Delta_s = n\hbar\omega_e. \quad (6.28)$$

If the DOS G_{\uparrow} and G_{\downarrow} are out-of-phase, it means the condition

$$\Delta_s = \hbar\omega_e(n + \frac{1}{2}) \quad (6.29)$$

is fulfilled, the nodes in the beating pattern are observed. The amplitude of SdH oscillations behaves in this case differently, if the broadening of electronic Landau levels Γ_e is larger/smaller than the cyclotron energy $\hbar\omega_e$. If the Γ_e is much larger than $\hbar\omega_e$, the total, spin unresolved DOS $G_{tot} = G_{\uparrow} + G_{\downarrow}$ is not modulated, it is gapless and it can be approximated by the constant DOS. In such a case, instead of the oscillations, nodes are observed in the beating, see scheme in Fig. 6.17 (c). However, at sufficiently high magnetic

field, when the cyclotron energy is much larger than the LL broadening ($\hbar\omega_e \gg \Gamma_e$), the gap in the total DOS remains open and SdH oscillations are observed. The frequency of the SdH oscillations is twice the frequency at the maxima of the beating, because the spin resolved DOS are out-of-phase and for this reason the total DOS G_{tot} is modulated at twice higher frequency than the spin resolved DOS G_{\uparrow} and G_{\downarrow} , see scheme in Fig. 6.17 (b). The possibility to observe these nodes is due to better sample quality with respect to the samples used in the study of Teran [69], where no such nodes have been observed.

More quantitative analysis of the SdH oscillations is presented in Fig. 6.18. We plot the filling factor versus inverse value of the magnetic field positions of the R_{xx} minima in order to determine the concentration of the 2DEG, $n_e = 4.0 \times 10^{11} \text{ cm}^{-2}$. The minima of the R_{xx} do not correspond alternatively to odd and even filling factors at low magnetic fields, as is usual in non-magnetic QWs. Here, due to the GZS, minima tend to belong to the same parity of the filling factors within the interval of two adjacent nodes and the parity changes at the nodes. If the double frequency of the SdH oscillations is observed in the vicinity of the nodes, then the alternating odd and even filling factors are recovered, as has been shown, and as can be seen in Fig. 6.18. Taking zero field resistance $R_{xx,0} = 132 \Omega$

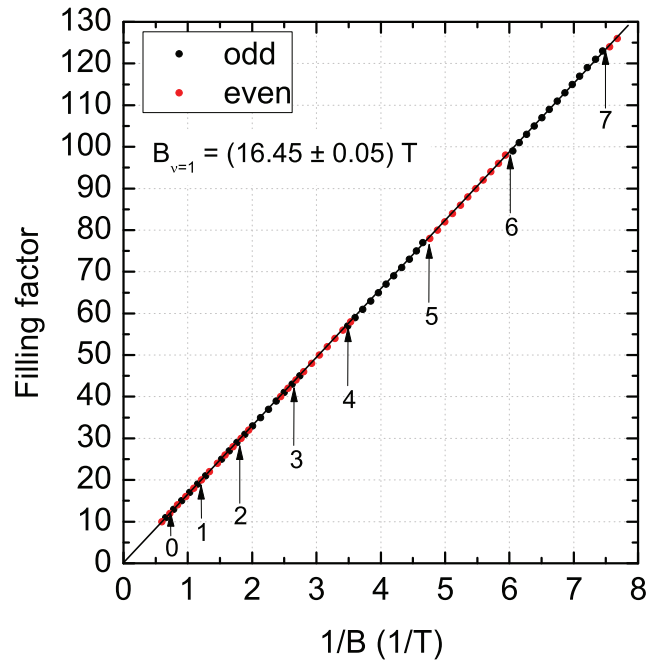


Figure 6.18: Filling factor versus inverse value of the magnetic field to determine concentration of 2DEG. The analysis of the data presented in Fig. 6.16. The fitting of the slope gives magnetic field at the filling factor $\nu = 1$, $B_{\nu=1} = 16.45 \text{ T}$ and the corresponding electron sheet concentration $n_e = 4.0 \times 10^{11} \text{ cm}^{-2}$. Black (red) points correspond to the minima of the longitudinal resistance R_{xx} at odd (even) integer filling factors. Vertical arrows show positions of the nodes in magnetic field and the numbers are indices n in the condition $\Delta_s = \hbar\omega_e(n + \frac{1}{2})$, which has to be fulfilled if nodes are observed.

and the concentration of 2DEG $n_e = 4.0 \times 10^{11} \text{ cm}^{-2}$, one can estimate mobility of 2D electrons $\mu = 120000 \text{ cm}^2\text{V}^{-1}\text{s}^{-1}$, which is twice smaller than the value established in our non-magnetic CdTe QW. The analysis of the damping of SdH oscillations gives the

broadening of electronic Landau levels $\Gamma_e = 130 - 140 \mu\text{eV}$, which is by 20-30 μeV larger than in the CdTe QW. Both the smaller value of the electron mobility and the larger broadening of LLs (shorter scattering time) lead us to the conclusion that the quality of CdMnTe QW is worse than the quality of CdTe QW. Such a conclusion is obvious, when we assume that the in-plane randomly distributed manganese atoms act as additional scattering centers, thus contributing to the shorter scattering time and smaller mobility.

6.2.2 Temperature dependence

In the following paragraph, the temperature dependence of the longitudinal resistance R_{xx} is presented and qualitatively analyzed. Since the detailed analysis of the damping of SdH oscillations as a function of temperature have been presented in the case of CdTe QW, here we focus on the temperature dependence of the beating pattern. The temperature dependence of R_{xx} is shown in Fig. 6.19 in the range of temperatures from 90 mK to 1230 mK. The increasing temperature damps the amplitude of SdH oscillations, as in the case of CdTe QW, and the positions of nodes shift to lower magnetic field. In order to explain such a behavior, we present more quantitative description of GZS and we model the observed temperature dependence of nodes. It can be shown [70, 71] that electron energy levels $E_{C,\uparrow(\downarrow)}$ can be described by the formula (6.30),

$$E_{C,\uparrow(\downarrow)} = \pm \frac{1}{2} N_0 \alpha x \langle S_z \rangle \quad (6.30)$$

where the \pm signs correspond to the two electronic spin states, N_0 is the number of unit cells per unit volume, α is the exchange integral of the interaction of s-electrons in a conduction band and d-electrons of Mn^{2+} atom, x is the averaged mole fraction of manganese and $\langle S_z \rangle$ is the thermal average of z^{th} component of Mn^{2+} spin [70, 72]. The value $\langle S_z \rangle$ is governed, in magnetic field and non-zero temperature, at the first approximation, by Brillouin function, as shown in equation (6.31).

$$\langle S_z \rangle = S_0 B_{5/2} \left(\frac{\frac{5}{2} g_{Mn} \mu_B B}{k_B (T + T_0)} \right) \quad (6.31)$$

The Brillouin function is generally defined [73] as

$$B_J(y) = \frac{2J+1}{2J} \coth \left(\frac{2J+1}{2J} y \right) - \frac{1}{2J} \coth \left(\frac{y}{2J} \right). \quad (6.32)$$

Following the pioneering work of Gaj [70], the parameter S_0 expresses the saturation value of the thermal average of z^{th} spin component $\langle S_z \rangle$, g_{Mn} is the g-factor of manganese ($g = 2$ [70, 74, 75]), T is the lattice temperature and $T + T_0$ is an effective temperature of manganese atoms. The temperature T_0 takes into account anti-ferromagnetic coupling between two manganese atoms. Parameters S_0 and T_0 depend on the concentration of manganese. Mean concentration of manganese is in our QW of about 0.3%, hence the expected values (in bulk CdMnTe) are $S_0 = 2.4$ and $T_0 = 0.09 \text{ K}$ [76]. Exchange interaction parameter $N_0 \alpha = +0.22 \text{ eV}$ does not depend on the concentration of manganese, but it can slightly depend on the quantum confinement [75]. However, quantum confinement changes this parameter of about few percents, therefore we neglect this effect. Within this

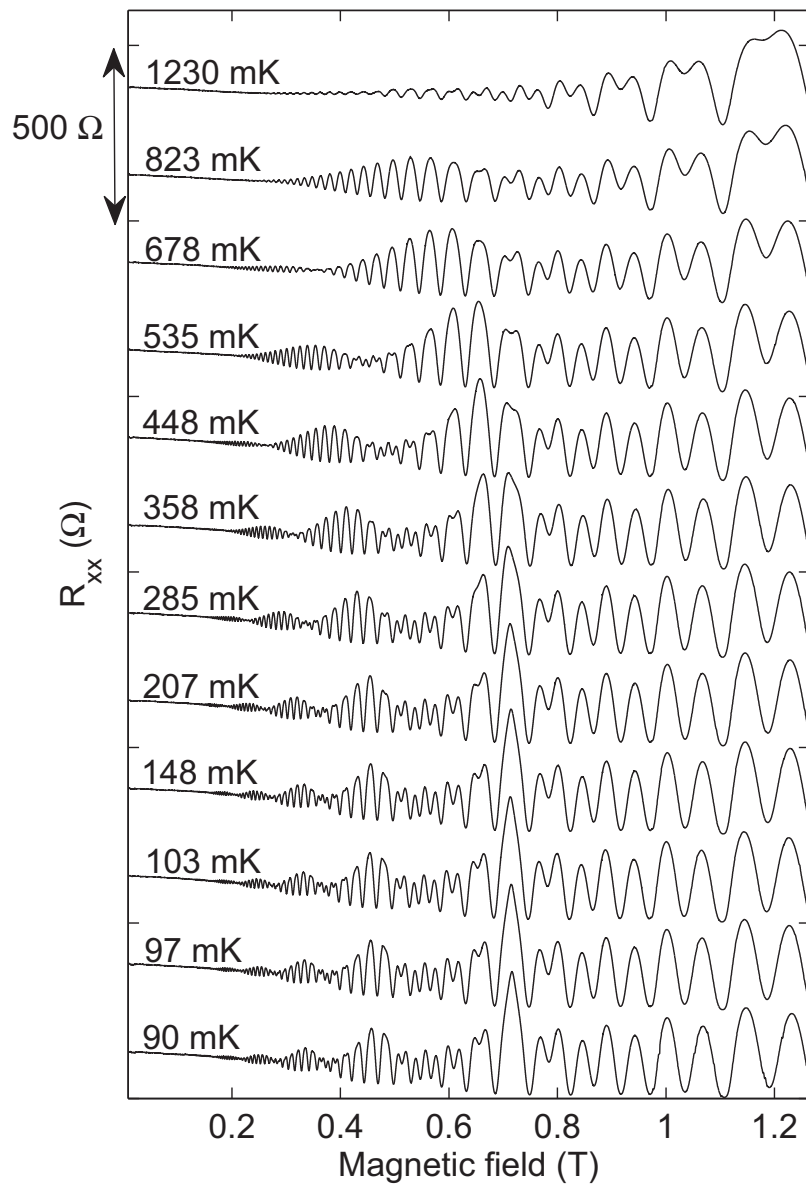


Figure 6.19: Longitudinal magneto-resistance R_{xx} as a function of the magnetic field. Measured in 21.1 nm wide CdMnTe QW in the range of temperatures from 90 mK to 1230 mK. Sample was illuminated by laser light at the energy $E_{exc} = 2.41$ eV (Ar^+), power on the sample $P_{illum} = 1.0$ μW and the laser spot size was ≈ 2 mm. For the sake of clarity, the curves are shifted with respect to each other in the y-direction. The double arrow in the top-left corner denotes 500 Ω unit of the y-scale.

simple model of GZS, one can write for the total spin splitting Δ_s of the electronic Landau

levels

$$\Delta_s = g_e \mu_B B + \Delta_{exch} B_{5/2} \left(\frac{\frac{5}{2} g_{Mn} \mu_B B}{k_B (T + T_0)} \right), \quad (6.33)$$

where $\Delta_{exch} = N_0 \alpha x S_0$. We note that the contribution of the bare Zeeman splitting has a negative sign with respect to the contribution of the polarization of manganese and it tends to close the electronic spin gap at high magnetic field. Taking Eq. (6.33) and the condition for the nodes given by Eq. (6.29), we have calculated the temperature dependence of the field position of the nodes by fitting temperature independent parameters Δ_{exch} and T_0 . In Fig. 6.20, the model (solid red curve), using fitted values $\Delta_{exch} = (1.67 \pm 0.05)$ meV and $T_0 = (60 \pm 10)$ mK, is compared with the experimental data (circles). The agreement between the data and the model is more qualitative than quantitative. The model predicts a shift of the nodes to lower fields with increasing temperature, however, the predicted decrease is too fast.

For this reason, following the work of Teran [77], we have tried to improve the presented model of the GZS by including many-body electron-electron interactions in 2DEG and we have included also an influence of the polarization of the 2DEG on the polarization of manganese. Energy contribution of the electron-electron interaction $\Delta E_{\uparrow\downarrow}$ to the spin splitting Δ_s is in the low field limit proportional to the polarization of 2DEG and it can be described [78] as $\Delta E_{\uparrow\downarrow} = \Delta_0 \mathcal{P}$, where $\Delta_0 = 2.1$ meV in CdTe and \mathcal{P} is the polarization of 2DEG. The polarization can be in the presence of GZS approximated as $\mathcal{P} \simeq \frac{\Delta_s}{2E_F}$, where $E_F = 9.5$ meV is the Fermi energy in our CdMnTe QW. An influence of the polarization of 2DEG on the magnetization of manganese can be included by replacing energy of manganese $E_{Mn} = g_{Mn} \mu_B B$ by $E_{Mn} = g_{Mn} \mu_B B + \frac{1}{2} \alpha n_e^{3D} \mathcal{P}$. The 3D concentration of 2DEG can be approximated by 2D concentration n_e^{2D} and an effective width of the QW d_{QW}^* , $n_e^{3D} \approx n_e^{2D} / d_{QW}^*$. The effective width of the QW is calculated from the real width $d_{QW} = 21.1$ nm as $d_{QW}^* \approx d_{QW} / 2$. As a result, the total spin spin splitting of electronic LLs Δ_s reads

$$\Delta_s = g_e \mu_B B + \Delta_0 \frac{\Delta_s}{2E_F} + \Delta_{exch} B_{5/2} \left[\frac{\frac{5}{2} (g_{Mn} \mu_B B + \frac{1}{2} \alpha n_e^{3D} \mathcal{P})}{k_B (T + T_0)} \right]. \quad (6.34)$$

Because the Eq. (6.34) is an implicit function of Δ_s , we have solved it self-consistently. The model, using $\Delta_{exch} = (1.50 \pm 0.05)$ meV and $T_0 = (64 \pm 10)$ mK as fitting parameters, is plotted in Fig. 6.20 by red dotted line. As can be seen, these two many-body contributions play negligible role on the shape of the observed temperature dependence of the nodes. Although the quality of the fit did not change, many-body effects reduce the exchange energy Δ_{exch} from 1.7 to 1.5 meV, with respect to the first, the simplest model.

In the third model, we take into account more precisely anti-ferromagnetic (AF) exchange interaction between two manganese atoms. The formula (6.31) is derived in the mean-field approximation and takes into account especially the weak, but long-range, carrier mediated exchange interaction between manganese atoms. The direct, stronger, but short-range, anti-ferromagnetic (AF) exchange interaction is considered only phenomenologically by introducing the parameter T_0 [80, 77]. The direct exchange is usually weak in the diluted magnetic semiconductors with very low manganese concentration, because only few of manganese atoms are so close to each other that the direct short-range exchange interaction is efficient. In such a case, the approximation of the direct AF interaction by

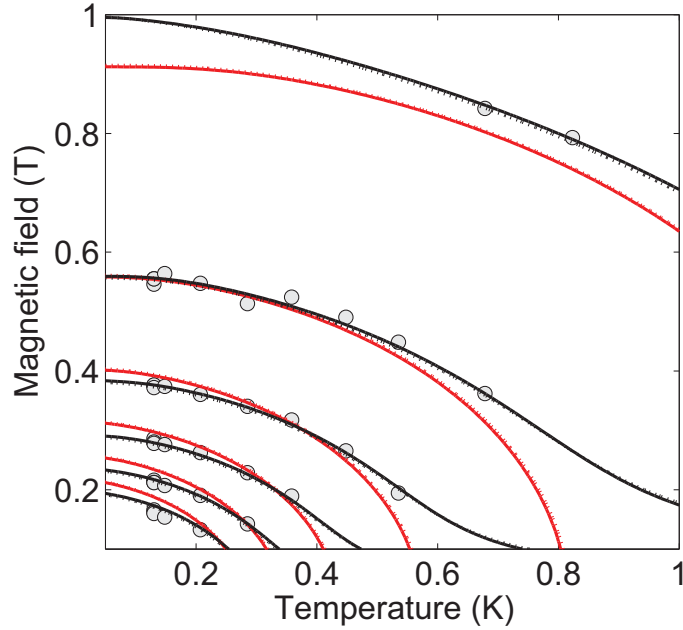


Figure 6.20: Magnetic field position of the nodes in $R_{xx} = R_{xx}(B)$ as a function of the temperature. Circles are experimentally determined positions of nodes. Red solid curve is the expected temperature dependence of the nodes within the most simple model (following the work of Gaj [70]), in which the mean value $\langle S_z \rangle$ is described only by the Brillouin function (direct anti-ferromagnetic Mn-Mn exchange interaction is not taken properly into account). Black solid curve is the model, which properly includes direct anti-ferromagnetic Mn-Mn exchange interaction. In this model, we follow the work of Aggarwal [79]. The dotted curves are the two former models extended by the many-body electron-electron interaction and an influence of the polarization of the 2DEG on the polarization of manganese, as suggested by Teran [77].

the phenomenological parameter T_0 is sufficient. However, although there is enough small average concentration of manganese in our QW ($\approx 0.3\%$), the local manganese concentration is due to the digital doping much higher⁴. Digital doping means that manganese is not homogeneously distributed across the QW, but it resides in only 7 mono-layers out of 65 mono-layers, which compose the whole QW. Therefore, even though the average manganese concentration is low ($\approx 0.3\%$), locally it is much higher ($0.3\% \times 65/7 = 2.8\%$)⁵. At such a concentration, there is already high probability that manganese atoms are gathered into small clusters [81, 82, 76] like pairs, open and closed triangles. For the sake of simplicity, we consider only clustering into the pairs. Following the work of Aggarwal [79],

⁴For details on the structure of our samples, see chapter 3

⁵The local manganese concentration $x_{loc} = 2.8\%$ is only rough estimate, because we do not take into account diffusion of manganese into the neighboring mono-layers. The real concentration is probably still slightly lower

⁶The importance of the local manganese concentration in the heterostructures has been pointed out also by Grieshaber [76]

the average z^{th} component of the Mn spin $\langle S_z \rangle$ is given by the formula

$$\langle S_z \rangle = S_0 B_{5/2} \left(\frac{\frac{5}{2} g_{Mn} \mu_B B}{k_B (T + T_0)} \right) + \frac{1}{2} P_p \sum_{n=1}^5 \frac{1}{\exp \left(\frac{2n J_{NN} - g_{Mn} \mu_B B}{k_B T} \right) + 1} \quad (6.35)$$

and the spin splitting of the electronic LLs reads

$$\Delta_s = g_e \mu_B B + \Delta_{exch} B_{5/2} \left(\frac{\frac{5}{2} g_{Mn} \mu_B B}{k_B (T + T_0)} \right) + \frac{\Delta_{exch} P_p}{2 S_0} \sum_{n=1}^5 \frac{1}{\exp \left(\frac{2n J_{NN} - g_{Mn} \mu_B B}{k_B T} \right) + 1}. \quad (6.36)$$

The parameters P_p and J_{NN} , which describe the magnetization of manganese in the pairs, are the probability of the single manganese to be part of the pair cluster and the short-range exchange energy, respectively. Comparison of this model with the data is shown in Fig. 6.20 (model is plotted by solid black curve). Very good agreement with the experimentally observed temperature dependence of the positions of nodes has been obtained. The probability that manganese is part of the pair cluster is $P_p = (25 \pm 5)\%$ and the short-range exchange energy $J_{NN} = (10 \pm 5) \mu\text{eV}$. The expected probability P_p is in the single monolayer at $x_{loc} = 2.8\%$ roughly $P_p = 10\%$ [76]. However, it has been shown [81] that the number of pairs can be more than doubled at similar manganese concentrations ($x_{loc} = 5\%$) than statistically predicted within the model of random manganese distribution. On the basis of the work of Galazka [81] we also conclude that part of manganese atoms is not distributed randomly in our QW. The short-range exchange energy $J_{NN} = (10 \pm 5) \mu\text{eV}$ is roughly $4\times$ smaller than reported in bulk CdMnTe [81] of similar local manganese concentration ($x_{loc} = 5\%$). We believe that this difference is given by the digital doping of manganese in separate mono-layers, in contrast to the result obtained in bulk CdMnTe [81]. The parameters $\Delta_{exch} = (1.45 \pm 0.05) \text{ meV}$ and $T_0 = (45 \pm 10) \text{ mK}$ do not differ significantly from those obtained in the first two simpler models. Including electron-electron interaction and influence of the polarization of 2DEG on the magnetization of manganese again does not change the quality of the fit (see black dotted curve in Fig. 6.20). However, it changes the value of Δ_{exch} , which is then $\Delta_{exch} = (1.30 \pm 0.05) \text{ meV}$. Corresponding average concentration of manganese is $x = (0.25 \pm 0.4)\%$, which is in good agreement with the expected value 0.3% . The twice smaller value of T_0 than expected is believed to be due to the quantum confinement and digital doping of manganese, because the expected $T_0 = 90 \text{ mK}$ has been reported for bulk CdMnTe. The second reason could be that the AF coupling of manganese in pair clusters is now considered separately. Before, the pairs have been considered effectively only in the temperature T_0 . However, now, we consider pairs separately and therefore the T_0 can be smaller.

To conclude, we have found that both CdMnTe and CdTe QWs exhibit SdH oscillations in the longitudinal resistance. Analysis of the damping of SdH oscillations at base temperature shows that the quality of CdMnTe QW is worse than the quality of CdTe QW. We have assigned the worse quality to the manganese dopants, which play a role of additional scattering centers. The most pronounced manifestation of manganese in the CdMnTe QW is the beating pattern in SdH oscillations. The analysis of the beating pattern has shown the importance of the short-range (also called nearest-neighbor) Mn-Mn anti-ferromagnetic interaction and the presence of non-randomly distributed manganese.

We have shown that the contribution of many-body electron-electron interaction as well as the influence of the polarization of 2DEG on the magnetization of manganese do not improve the quality of the modelling of the temperature dependence of the nodes observed in SdH oscillations. Nevertheless these contributions affect the amplitude of the exchange energy Δ_{exch} .

6.3 High-field magneto-resistivity in CdTe QW

6.3.1 Magneto-resistivity in perpendicular field

In the following section, we present measurements of the high-field longitudinal (R_{xx} , Fig. 6.21) and Hall (R_{xy} , Fig. 6.22) magneto-resistivity in 20 nm wide CdTe QW in order to investigate both integer and possibly fractional quantum Hall states. We have observed well developed integer quantum Hall states (QHS) up to the filling factor $\nu \approx 20$ and two well developed fractional QHS 5/3 and 4/3. Among others, also a signature of fractional QHS at higher Landau level $N = 1$ has been observed, namely fractions 8/3 and 7/3. Around fractional states 5/3 and 4/3 we have observed metal-insulator transition⁷, which is extraordinarily stable up to the highest temperatures achievable (1410 mK). Similar stability of the metal-insulator transition is observed also in the vicinity of the filling factor 8/3, which represents in fact the same filling factor as 5/3, but at higher Landau level.

The Hall resistivity, which was measured simultaneously with the longitudinal resistivity R_{xx} , is plotted in the Fig. 6.22. Well developed plateaux have been observed for all integer filling factors up to $\nu \approx 20$ and fractional states 4/3 and 5/3. Although plateau corresponding to the fractional state 5/3 is well developed, its resistivity is not exactly equal to $(3/5)(h/e^2)$. The expected resistivity $(3/5)(h/e^2)$ is shown in Fig. 6.22 by black dashed horizontal line labelled $\nu(R_{5/3})$. Solid red horizontal line shows the expected Hall resistivity according to the position of the minimum in R_{xx} (filling factor labelled $\nu(R_{min})$). Surprisingly, the resistivity of this Hall plateau best corresponds to the filling factor $\nu(R_{MIT})$, which corresponds in R_{xx} to the magnetic field of metal-insulator transitions (this is why we use the label MIT). The detail of the vicinity of the fractional filling factor 5/3 in the longitudinal resistivity is shown in Fig. 6.23. However, an explanation of such striking observation has not yet been found.

In the temperature dependence of longitudinal resistivity R_{xx} , Fig. 6.21, one can see a gradual disappearance of integer QHS. This is given by thermal activation of the carriers within the Zeeman spin gap for odd filling factors, or within cyclotron gap for even filling factors. We have used the simplest method to describe observed thermal activation by assuming that the resistivity $R_{xx} \propto n_e$, where n_e is a concentration of thermally activated carriers which is given by Fermi-Dirac distribution $n_{FD} = 1/(\exp((E - E_F)/k_B T) + 1)$ approximated by $n_{FD} \approx \exp(-(E - E_F)/k_B T)$. Since Fermi energy is located at integer

⁷Metal-insulator transition is distinguished in the data by minimal temperature dependence of the resistivity R_{xx} . Resistivity of the insulator decreases with increasing temperature, because localized carriers which do not contribute to the conductivity can achieve enough thermal energy to escape their localizing potentials, hence the higher temperature the more carriers can contribute to the conductivity, thus decreasing resistivity. In metals, the presence of free carriers is inherited from the definition of metal. However, at higher temperatures, the influence of scattering of the carriers by lattice vibrations grows, and thus the conductivity decreases (resistivity increases) with growing temperature.

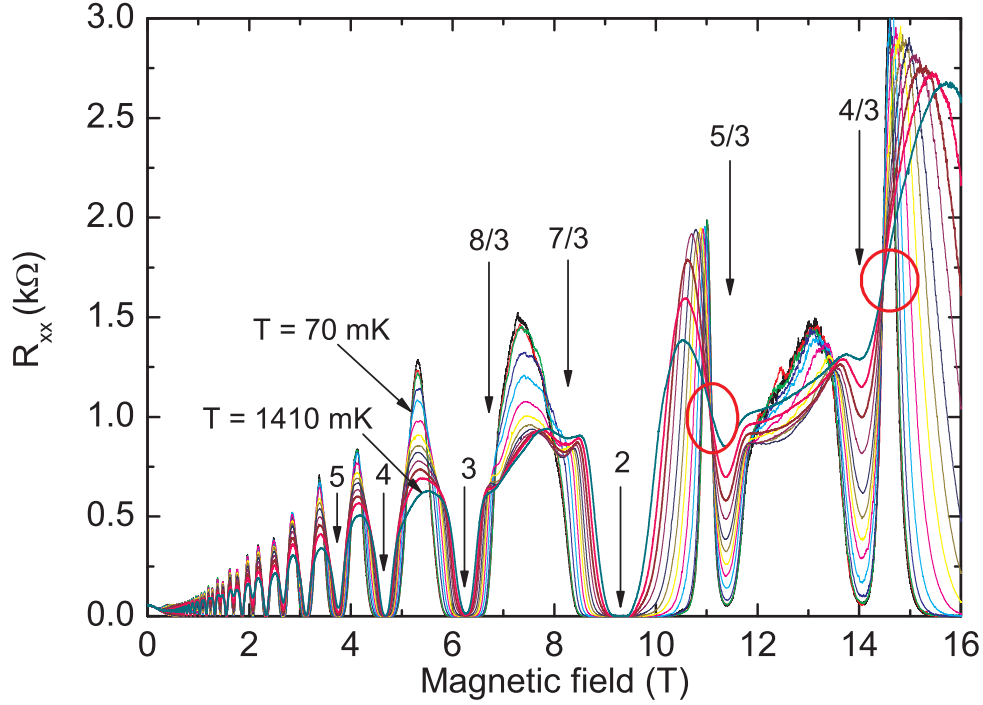


Figure 6.21: Longitudinal resistivity R_{xx} as a function of magnetic field from 0 to 16 T measured in 20 nm wide CdTe/CdMgTe QW in the temperature range from 70 to 1410 mK. The lowest and the highest temperatures are marked by arrows. Sample was illuminated by laser light at the energy $E_{exc} = 2.41$ eV (Ar^+); power on the sample $P_{illum} = 1.0$ μW and the laser spot size ≈ 2 mm. Integer filling factors 2, 3, 4 and 5 together with fractional filling factors $4/3$, $5/3$, $7/3$ and $8/3$ are marked by vertical arrows. The two red circles show the position of metal-insulator transition.

filling factor exactly in the middle of the gap Δ , the energy difference $E - E_F = \Delta/2$ is a half of the measured gap. The resulting expression for the thermal gap activation Δ is

$$R_{xx} \propto e^{-\frac{\Delta}{2k_B T}} \Leftrightarrow \ln(R_{xx}) \propto -\frac{\Delta}{2k_B T}. \quad (6.37)$$

The analysis of the thermal activation of the spin gap is plotted in the Fig. 6.24 and of the cyclotron gap in Fig. 6.25. The data in figures 6.24 and 6.25 are extended by the data measured at temperatures from 1.9 K to 20.6 K. Using equation (6.37) for the thermal activation, one can obtain the size of the spin gap at odd filling factors $\nu = 3, 5, 7, \dots, 19$ and the cyclotron gap at even filling factors 4, 6 and 8. The gap at filling factor 2 can not be properly analyzed, because it is not yet thermally activated at as high temperature as 20.6 K.

The field dependence of the energy gap at both odd and even filling factors is plotted in Fig. 6.26. The data are compared with the field dependence of the energy gap Δ as expected from the single-particle model of the electron motion in magnetic field.

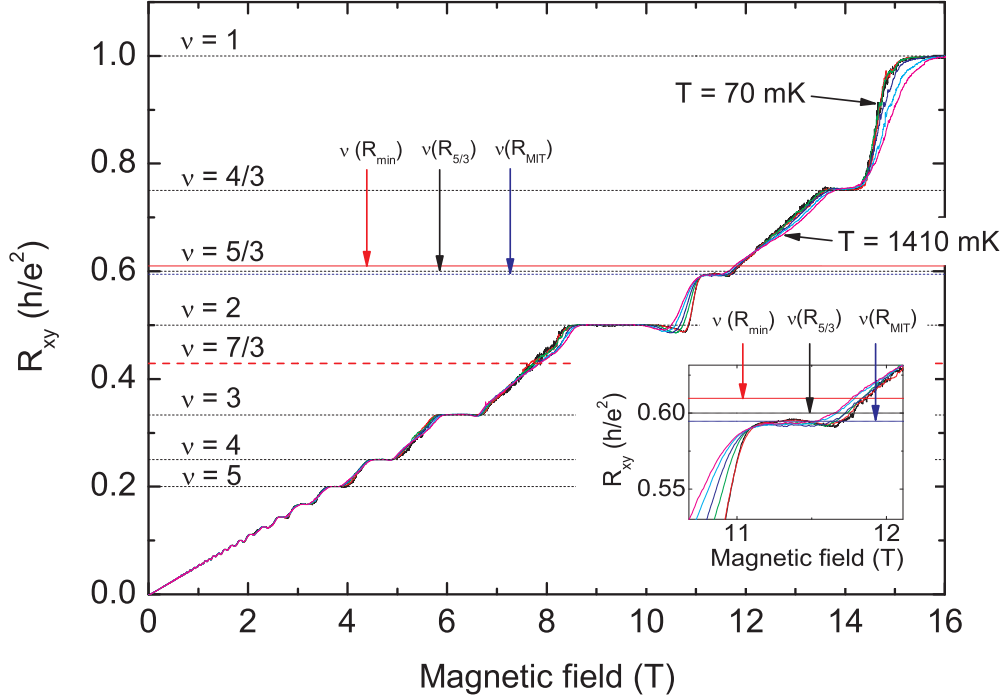


Figure 6.22: Hall resistivity R_{xy} measured simultaneously with longitudinal resistivity R_{xx} presented in Fig. 6.21. Vertical lines mark integer and fractional filling factors. Expected Hall resistivity at Hall plateaux for filling factors $\nu(R_{min})$, $\nu(R_{5/3})$ and $\nu(R_{MIT})$ are also marked. Field dependence of the Hall resistivity R_{xy} in the vicinity of $\nu = 5/3$ is depicted in the inset.

The expected single-particle gaps at odd ($\Delta_{odd}(B) = g_e \mu_B B$) and at even ($\Delta_{even}(B) = \hbar \omega_e - g_e \mu_B B$) filling factors are shown by black ($\Delta_{odd}(B)$) and red ($\Delta_{even}(B)$) straight line in Fig. 6.26, respectively. The higher absolute values of the spin gap (odd ν) are due to the spin gap enhancement at the Fermi energy and the details of this phenomenon will be discussed in the chapter 7.3. The lower values of the cyclotron gap are usually explained either in terms of the, so called, mobility gap, or this discrepancy is explained by not fulfilled assumptions, under which is the formula (6.37) for the thermally activated gap derived. We guess that the mobility gap can not explain the observed disagreement between the data and the experiment, because the mobility gap is driven by the spectral width of the Landau levels, which has been determined in the low-field regime from the damping of the amplitude of the SdH oscillations ($\Gamma = 110 \mu\text{eV}$ for the Lorentzian broadening). We have found that the LL width is constant up to 0.5 T. In order to explain the observed disagreement, this broadening would have to be $\approx 5 \times$ larger already at 2 T. We guess that such a field dependence of the LL broadening is quite unlikely.

The second approach [83] is based on description of the thermal activation of the

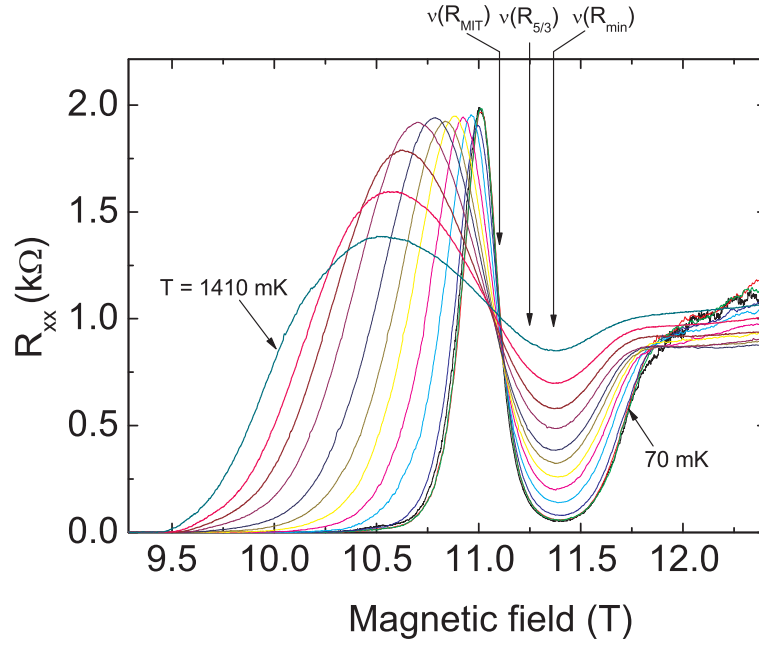


Figure 6.23: Inset of the Fig. 6.21 around fractional filling factor $5/3$. The filling factors $\nu(R_{min})$, $\nu(R_{5/3})$ and $\nu(R_{MIT})$ are marked by vertical arrows.

longitudinal resistance using the formula

$$\frac{R_{max} - R_{min}}{R_{max}} = \frac{AT}{\Delta \sinh(\frac{2\pi^2 k_B T}{\Delta})}. \quad (6.38)$$

Here, R_{min} is the minimal resistance at the given integer filling factor ν (Fig. 6.21). The parameter R_{max} is the local maximum of the R_{xx} in the vicinity of the filling factor ν in the field dependence of R_{xx} . The difference $R_{max} - R_{min}$ therefore determines the amplitude of the oscillations of the longitudinal resistance R_{xx} at the filling factor ν . Parameter A scales the amplitude of the oscillations of R_{xx} and Δ is the unknown energy of the gap. The formula (6.38) is derived on the basis of the relation (6.16), where the density of states is replaced by the harmonic modulation (the first term in the expansion of the DOS into the Fourier series). The cyclotron gap determined using the relation (6.38) agrees well with the expected, single-particle cyclotron gap (reduced by the spin gap), as is shown in Fig. 6.26 by red circles.

6.4 Magneto-resistivity in tilted field

Interacting carriers in certain FQH ground states can have opposite spins provided the Zeeman energy is sufficiently small. This is typically observed in GaAs-based 2D electron gases (2DEGs), where an increase in the Zeeman energy induces a change in the spin polarization of the ground state from unpolarized to fully spin-polarized one. This

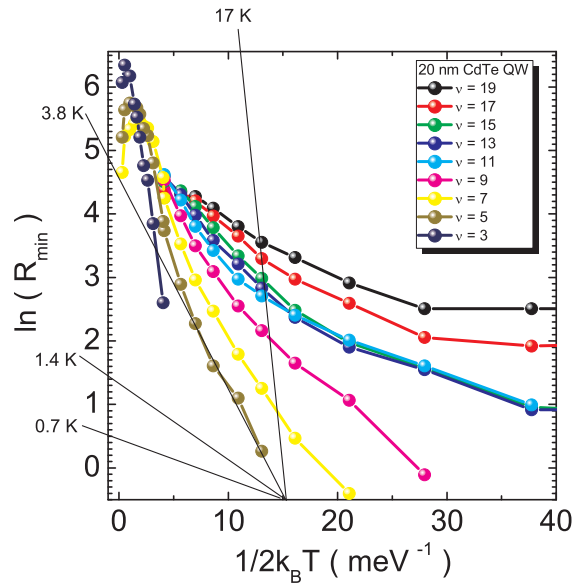


Figure 6.24: Arrhenius plot of the minimal longitudinal resistivity R_{xx} at odd filling factors. Minima analyzed from the data in Fig. 6.21 and from high temperature data up to 20.6 K. Only well developed integer quantum Hall states has been taken into account. Slopes corresponding to certain gaps Δ are plotted by solid black lines and labelled by the gap size in Kelvins.

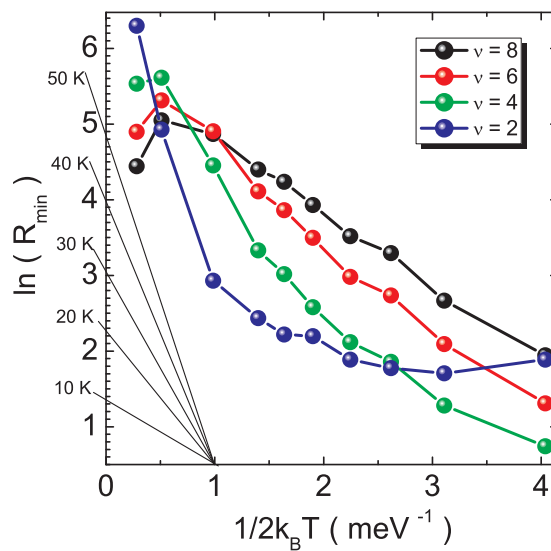


Figure 6.25: The same as Fig. 6.24 but for even filling factors.

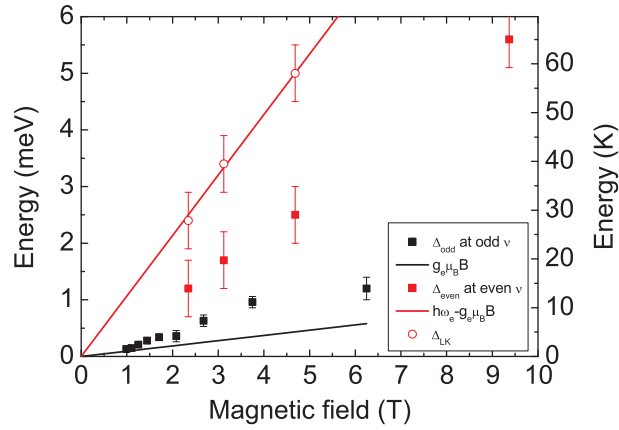


Figure 6.26: Activation energy Δ_{odd} analyzed from the Arrhenius plot in Fig. 6.24 for odd filling factors (black points) and activation energy Δ_{even} analyzed from the Arrhenius plot in Fig. 6.25 for even filling factors (red points). Relation (6.37) was used to analyze the thermal activation of the gaps. Expected single-particle field dependence of the activation energy at odd and even filling factors is plotted by black and red straight line, respectively. Gap at even filling factors determined using formula (6.38) is plotted by red circles.

transition has been reported for the FQH states at filling factors $\nu=4/3$, $\nu=8/5$, $\nu=2/3$, or $\nu=2/5$, [84, 85, 86, 87] as well as in a GaAs 2D hole gas. [88] Subsequently, this behavior was elegantly interpreted within the composite fermions (CF) model [89] for the FQH effect by invoking Zeeman energy-induced crossings between spin-split composite fermion Landau levels, leading to possible changes of the spin configuration of the ground state [90]. More recently, the $\nu=4/3$ FQH state was investigated in a strained Si quantum well, [91] where the associated resistance minimum was found to maintain its strength with increasing Zeeman energy, which was interpreted as the consequence of a spin-polarized ground state. The latter work addresses the interesting question of how the FQH effect manifests itself in a 2D system with an intrinsically larger Zeeman energy than in GaAs. However, the influence of the valley degeneracy inherent in Si is another degree of freedom that may also interfere with the FQH physics.

Here, we study the evolution of FQH states under relatively high intrinsic Zeeman energy in a *single valley* electron system. This is made possible by investigating the FQH effect in a high quality 2D electron gas in CdTe, a single valley direct gap semiconductor in which the bare electronic g-factor is about four times larger than in GaAs. The transport measurements performed at mK temperature reveal *fully-developed* FQH states (i.e. zero longitudinal resistance and exact quantization of the Hall resistance) in the upper spin branch of the lowest ($N=0$) Landau level (LL), which constitutes to our knowledge the first observation of the FQH effect in II-VI semiconductor. Tilted magnetic fields experiments up to 28 Tesla show no significant changes of the FQH gap both at filling factor $4/3$ and $5/3$, which is a behavior typical of spin-polarized ground states for which the lowest energy excitation is not a spin-flip. This can be accounted for by the relatively high intrinsic Zeeman energy which wins over the Coulomb energy to force the spins to align with the magnetic field. This can also be seen as the consequence of energy level crossings in the

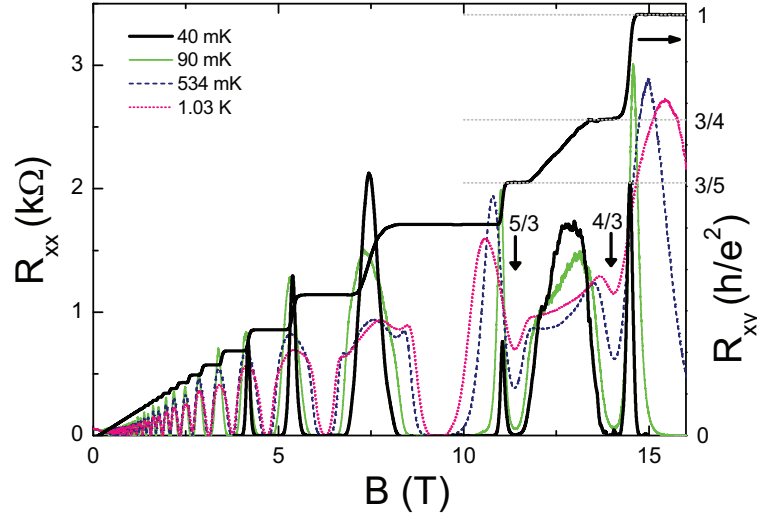


Figure 6.27: Hall resistance R_{xy} and longitudinal resistance R_{xx} versus perpendicular magnetic field for different temperatures.

composite fermion approach for the FQH effect. Significantly, emerging FQH minima at filling factors $7/3$ and $8/3$ are also observed at intermediate temperatures in the first excited ($N=1$) LL, demonstrating the high quality of the 2DEG that it is now possible to achieve in this material. Intriguingly, there is no sign of the $\nu=5/2$ FQH effect down to $T \sim 10$ mK. Future studies of the $\nu=5/2$ FQH state in this high Zeeman energy system could be of great importance to shed light on the long-standing question regarding the spin polarization of this state.

The sample studied here is a 20 nm wide CdTe quantum well, as described in chapter 3. It was cooled down in a $^3\text{He}/^4\text{He}$ dilution fridge to mK temperature in a number of different ways: under continuous illumination with a green laser or a green light emitting diode (LED), under continuous illumination with a yellow LED, and, in the darkness. These types of cooldowns will be referred to as cooldown A, B and C respectively. The resulting electron density for cooldown A, B, and C, are $n_s = 4.50, 4.53$ and $3.80 \times 10^{11} \text{ cm}^{-2}$ respectively, and the electron mobility at $T \sim 600$ mK for cooldown A is around $\mu = 260000 \text{ cm}^2/\text{Vs}$. Transport measurements were performed with a standard low frequency lock-in technique for temperatures between 40 mK and 1.4 K under magnetic fields up to 28 T.

In Fig. 6.27, we plot the longitudinal resistance R_{xx} for cooldown A as a function of the perpendicular magnetic field for different temperatures. Pronounced FQH states are observed at low temperature at filling factor $\nu=4/3$, and $\nu=5/3$, with the resistance falling to zero, together with well defined quantized Hall resistance. The role of illumination in improving the sample quality is critical, as the quantum lifetime τ_q extracted from the low field Shubnikov de Haas (SdH) oscillations is found to increase more than five times, from 0.6 ps in the dark to 3 ± 0.3 ps after illumination. This value of τ_q is comparable to the one which can be observed in GaAs samples with a mobility of the order of $10^6 - 10^7 \text{ cm}^2\text{V}^{-1}\text{s}^{-1}$, despite our moderate measured mobility of $260000 \text{ cm}^2/\text{Vs}$.⁸

⁸This apparent contradiction is due to the fact that in such high mobility GaAs samples, the long-range scattering by remote donors is even more predominant and leads to a higher mobility, for comparable τ_q .

Nevertheless, at low temperature, an important number of electronic states are localized, leading to wide zero resistance states in the integer quantum Hall effect, which prevent the observation of any signs of the FQH effect in the first excited ($N=1$) LL. As the temperature is increased, the fraction of localized states is reduced and weak FQH minima become visible in the $N=1$ LL. These features persist up to relatively high temperature, demonstrating again the quality of the sample.

In Fig. 6.28 we focus on the FQH effect in the $N=0$ Landau level. Fig. 6.28 (a) shows the temperature dependence of the longitudinal resistance at $\nu=5/3$ and $4/3$, for cooldown A and B as a function of the inverse temperature. The difference in sample quality between cooldowns appears clearly when comparing the low temperature behavior of the initially similar resistance at filling factor $4/3$. Arrhenius plots are generally used to extract an activation gap or mobility gap, corresponding to the energy difference between the edge of the delocalized states of the ground and excited states. However, a simple extraction of this activation gap Δ requires the observation of an expanded linear region (typically at least one order of magnitude) where $R_{xx} \sim e^{-\Delta/2k_B T}$, whereas such a region is rather absent in our data. This non-thermally-activated behavior is actually expected when a Gaussian or Lorentzian level shape is taken into account, for which one expects the linear behavior in an activation plot to deviate at low temperature in the presence of a broadening which reduces the mobility gap. This effect becomes important when the particles level broadening is non-negligible compared to the total (spectral) gap. To analyze our data, we therefore use the model proposed in Ref. [92] which includes a disorder-induced Gaussian broadening to calculate the temperature dependence of the resistance. The LL broadening is imposed by the one extracted for electrons via SdH measurements. The results of these simulations are plotted as dotted-lines in Fig. 6.28 (a) and show very good agreement with the experimental behavior. From this model we estimate the *total* FQH gap in cooldown B to be 3.15 K and 3.0K for $\nu=4/3$ and $\nu=5/3$, respectively. In units of Coulomb energy, $e^2/4\pi\epsilon_0\epsilon_r l_B$, where $\epsilon_r=10$ is the relative dielectric constant in CdTe and $l_B = \sqrt{\hbar/eB}$ the magnetic length, the *total* FQH gap corresponds to 0.013 and 0.014, respectively.

Activation data was also collected when tilting the 2DEG plane in the total magnetic field with an in-situ rotation stage at an angle of $\theta = 55^\circ$. This data, also plotted in Fig. 6.28 (a), is very similar to the $\theta = 0^\circ$ behavior for $\nu=4/3$ and $\nu=5/3$. The small difference can be well reproduced for both fractions either by introducing a small increase ($\sim 10\%$) in the level width, while the total gap remains constant, or by using a constant level width and a slightly reduced gap ($\sim 10\%$ also). The total gaps extracted from our analysis at $\theta = 0^\circ$ and $\theta = 55^\circ$ are plotted in the inset of Fig. 6.28 (a) as a function of the total field at fixed perpendicular field (filling factor), the vertical error bar representing the possible gap decrease at $\theta = 55^\circ$. Starting with the measured gap value for $\theta = 0^\circ$, we show how the gap should evolve as a function of total magnetic field (Zeeman energy) in three different configurations: a spin-polarized ground state with single particle spin-reversed excitation ($\Delta S = -1$, where ΔS is the spin change during the excitation), a spin-polarized ground state without spin flip excitations ($\Delta S = 0$), and a spin-unpolarized ground state ($\Delta S = +1$). The bare g-factor $g^* = -1.6$ is taken from Raman scattering measurements performed on the same sample.

The fact that the $\nu=5/3$ gap remains nearly constant at $\theta = 55^\circ$ suggests, as observed in GaAs, a spin-polarized ground state with a lowest energy excitation which is not a spin-flip, since no increase is observed despite of a significant variation (nearly a factor of 2) of

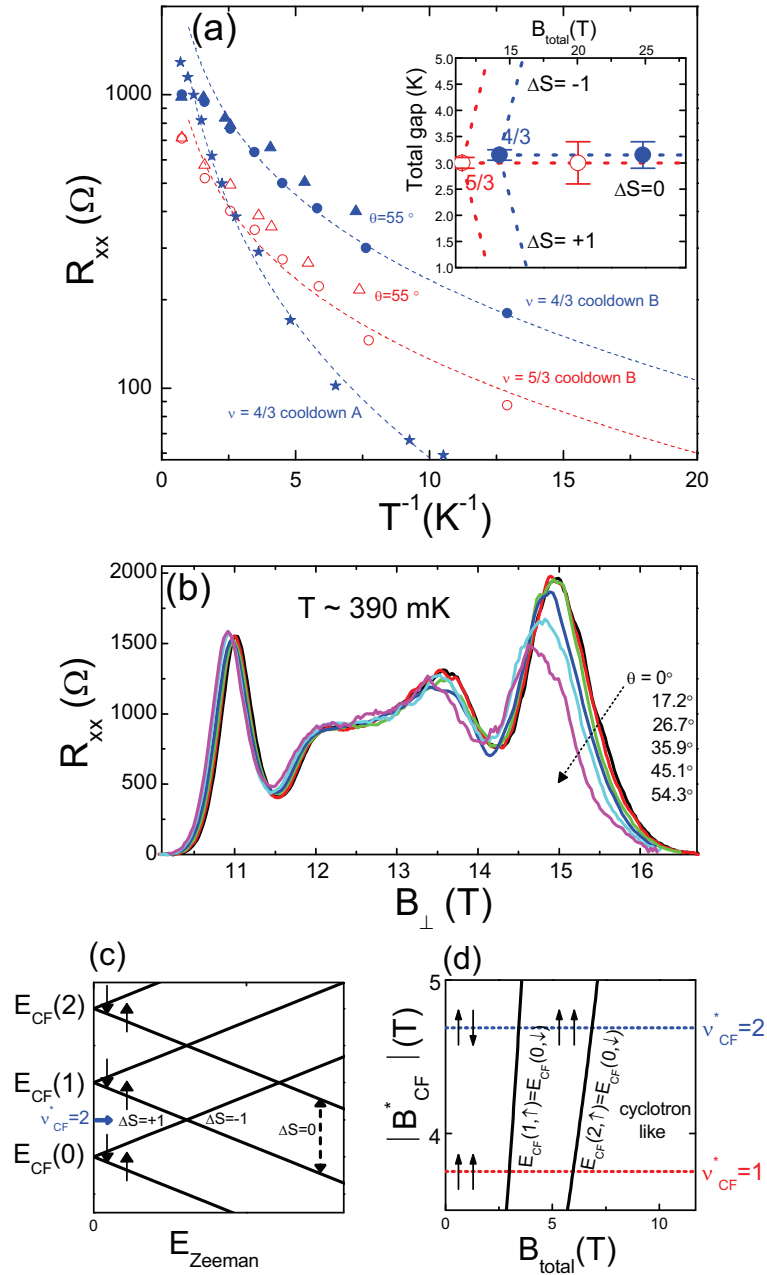


Figure 6.28: (a) Longitudinal resistance R_{xx} at $\nu=4/3$ as a function of inverse temperature for cooldown A (stars) and for cooldown B at $\theta = 0^\circ$ (circles) and $\theta = 55.6^\circ$ (triangles). The same data for cooldown B at $\nu=5/3$ (open symbols). Simulations of the thermally activated resistance (dashed lines) (see text). Inset: Corresponding total FQH gaps at $\nu=4/3$ and $\nu=5/3$ as a function of the total field B_{total} . Expected evolution of the gaps for different ground states (dotted lines) (see text). (b) Angular dependence of the longitudinal magneto-resistivity R_{xx} in the upper spin branch of the $N=0$ LL at fixed temperature $T \sim 390$ mK. Data plotted as a function of the component B_{\perp} of the total field B_{tot} ; $B_{\perp} = B_{tot} \cos(\theta)$. Increasing tilting angle θ indicated by the arrow. (c) Schematic representation of the CF fan diagram at fixed CF cyclotron energy, as a function of the Zeeman energy (see text). $E_{CF}(N)$ is the energy of the N^{th} CF level. The arrows depict the spin orientation of each sub-band. (d) Position of the CF level crossings in the $(|B_{CF}^*|, B_{total})$ plane (see text). The arrows depict the spin polarization of the ground state in different region.

the Zeeman energy. If the $\nu=4/3$ state was to be unpolarised, one would expect a sharp decrease of the gap or even its disappearance, here around $B_{total} = 16\text{T}$, before reentrance at higher fields due to a change in the ground state polarization. This transition has been observed in GaAs 2DEG at low electron density, [84, 90] and also for higher densities close to the one of our CdTe sample. In Refs. [84, 93], the $\nu=4/3$ FQH gap for sample G71 with initial electron density $\sim 2.7 \times 10^{11}\text{cm}^{-2}$ decreases as the density (total field) is increased and is close to vanishing for magnetic fields of about 12 T. Our observation of a quasi-unchanged gap at $\theta = 55^\circ$ shows the $\nu=4/3$ FQH state is spin-polarized in CdTe. The fact that this gap is *not increasing* further suggests that the lowest energy excitations in this state do not involve spin flip excitation.

The qualitative behavior of the gap at different tilt angles between $\theta = 0^\circ$ and $\theta = 55^\circ$ can be inferred from a detailed angular dependence of R_{xx} measured for a fixed intermediate temperature of $T \sim 390$ mK. At this temperature the gap variation can efficiently be probed as observed when comparing the resistance values at $\nu=4/3$ and $\nu=5/3$ for cooldown A and B (Fig. 6.28 (a)). This angular dependence plotted in Fig. 6.28 (b). shows only a very weak variation of the resistance at $\nu=5/3$ and $\nu=4/3$ over the entire θ range studied ($0 < \theta < 55^\circ$). This demonstrates that no significant changes in the $\nu=4/3$ and $\nu=5/3$ FQH gaps are observed upon tilting, as expected for a spin-polarized state with no spin-flip excitation.

This behavior can actually be understood more quantitatively using the CF theory for FQH effect, where FQH for electron is mapped onto the integer quantum Hall effect for composite fermions. In the upper spin branch of the $N = 0$ LL, around $\nu=3/2$, these CF see an effective magnetic field $B_{CF}^* = 3(B_\perp - B_{\perp 3/2})$, where $B_{\perp 3/2}$ is the magnetic field corresponding to $\nu=3/2$. [94, 90] In this case the $\nu=4/3$ ($5/3$) FQH effect for electrons is the $\nu_{CF}^* = 2(1)$ integer quantum Hall effect for CF. The scale of the CF cyclotron gap between two CF levels is then given by $\hbar e|B_{CF}^*|/m_{CF}^*$, where m_{CF}^* is the CF effective mass. When the Zeeman energy is added to this simple picture, which is schematically depicted in Fig.6.28.c, the lower spin branch of the $N=1$ CF level ($(1, \uparrow)$) may have a lower energy than the upper spin branch of the $N=0$ CF level ($(0, \downarrow)$). In this situation the ground state at $\nu_{CF}^* = 2$, initially formed by $(0, \uparrow)$ and $(0, \downarrow)$ CF levels for small Zeeman energies, is now formed by the $(1, \uparrow)$ and $(0, \uparrow)$ CF levels and therefore spin-polarized. This picture can be applied to our 2DEG in CdTe, with a g-factor of $g^* = -1.6$ and the composite fermions effective mass experimentally determined in Ref. [95] as a function of B_{CF}^* ($m_{CF}^* = 0.51 + 0.074|B_{CF}^*|$)⁹. In Fig.6.28.c, we plot in a $(|B_{CF}^*|, B_{total})$ plane the position of the crossing points of the $(0, \downarrow)$ CF level with the $(1, \uparrow)$ and $(2, \uparrow)$ levels. For $\nu = 4/3$ ($\nu_{CF}^* = 2$), these crossings occur for $B_{total} \sim 3.4$ T and $B_{total} \sim 6.8$ T respectively, explaining why the $\nu=4/3$ FQH ground state is spin-polarized with no spin-reversed excitations for the total magnetic field range investigated ($14 < B_{total} < 25$ T). The excitation gap in this domain corresponds to a CF cyclotron gap (referred to as “cyclotron-like” in Fig. 6.28 (c)). The same conclusions are drawn for the $\nu = 5/3$ ($\nu_{CF}^* = 1$) FQH state, provided $B_{total} > 3$ T. We note that the CF cyclotron gap used in these calculations is larger than the experimentally measured FQH gap discussed above, meaning that the transition to “cyclotron-like” excitations should occur at even smaller magnetic field.

⁹The CF effective mass in our sample may differ from the one extracted in Ref. [95], because of different ϵ_r , LL mixing and finite thickness of the QW.

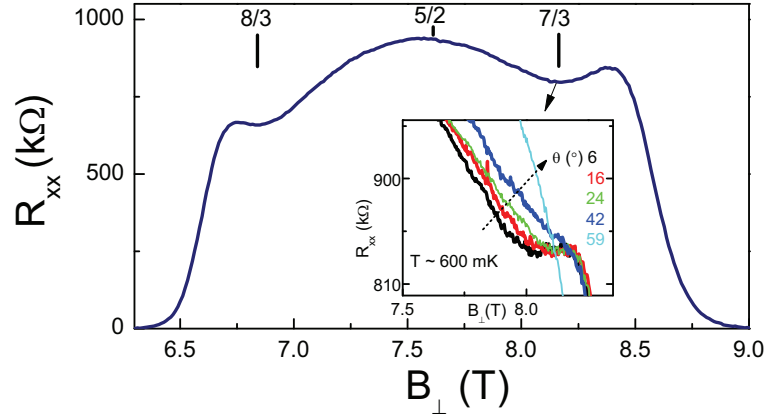


Figure 6.29: Magneto resistance R_{xx} in the lower spin branch of the $N=1$ LL at $T = 534$ mK. Corresponding filling factors are indicated on top. Inset: angular dependance of the $\nu=7/3$ minimum at $T = 600$ mK.

Finally, we turn to the description of the emerging FQH effect in the $N = 1$ LL which can be observed in our sample at intermediate temperatures. As can be seen in Fig. 6.27, weak minima are emerging at filling factors $\nu=7/3$ and $\nu=8/3$ for temperatures above 400-500 mK. At lower temperatures, the increasing number of localized states leads to the FQH effect being masked by the integer quantum Hall effect. The $T = 534$ mK perpendicular field data of Fig. 6.27 are inserted for clarity in Fig. 6.29. In the inset of Fig. 6.29, we focus on the evolution of the local minimum at $\nu=7/3$ and $T = 600$ mK for different tilt angles. The minimum maintains its strength at low angles, before starting to weaken around $\theta = 24^\circ$ and finally disappearing for $\theta > 42^\circ$. The relative initial stability with respect to tilt angle is similar to the one observed in the $N = 0$ LL, and suggests that, as for $\nu=5/3$ and $\nu=4/3$, the $\nu=7/3$ state is already in a regime where the ground state is spin-polarized with a lowest energy excitation which is not a spin flip. However, the observation of a $\nu=7/3$ state at lower temperatures (not possible because of localization) would be necessary to validate this hypothesis. At higher angles however, the minimum clearly disappears and the resistance at the broad maximum in R_{xx} associated with the $N = 1$ LL starts to increase. Depending on the orientation between the parallel magnetic field and the current flow, the transport was found to be anisotropic, somewhat reminiscent of the anisotropy observed at low temperature in high mobility GaAs-based 2DEG. [96, 97]

In contrast to FQH states $\nu=7/3$ and $\nu=8/3$, no minimum is observed at filling factor $\nu=5/2$. This remains true at ultra-low temperature ($T \sim 10$ mK), where we still have delocalized electrons around $\nu=5/2$. The absence of a $\nu=5/2$ FQH minimum could primarily be attributed to insufficient sample quality. However, it is also possible that the high Zeeman energy in CdTe plays a particular role in the formation of the $5/2$ FQH state. Despite of a great deal of theoretical evidence for the $\nu=5/2$ FQH state, there is still no direct experimental observation of the *full* spin polarization of $\nu = 5/2$ FQH state, as expected [98]. Instead, recent optical measurements [99] point toward a spin unpolarized state. In our samples ($g_e = -1.6$), $\nu=5/2$ occurs at $B = 7.6$ T, thus the Zeeman energy is about ~ 8 K, which is more than one order of magnitude larger than the very weak energy gap usually associated with the $5/2$ FQH state (even in the highest mobility GaAs

samples). Under such conditions, the stabilization of an unpolarized ground state is very unlikely. Whether this is the reason or not for the “missing” minimum at $\nu=5/2$ in our CdTe sample is a fundamental question which could only be decisively answered by further significant improvement of sample quality.

In conclusion, we have shown that the 2DEG in a CdTe quantum well can have a high quality, leading to the observation of pronounced FQH states in the upper spin branch of the $N = 0$ LL, as well as emergent FQH minima in the $N = 1$ LL. The physics of these FQH states is strongly influenced by the intrinsic Zeeman energy, resulting in the complete spin polarization of the FQH ground states $4/3$ and $5/3$, in agreement with a CF approach for FQH effect and the low energy excitations of composite fermions at $\nu = 4/3$ and $\nu = 5/3$ do not undergo the spin-flip.

Chapter 7

Magneto-photoluminescence

7.1 Spectral properties of zero field PL

7.1.1 Introduction

An experimental investigation of photoluminescence (PL) and magneto-photoluminescence was one of our main techniques to explore the properties of 2DEG. Therefore it is important to know, what are the main contributions to the spectral line shape of PL. Among other things, the spectral line shape provides wide range of quantitative and qualitative information on different properties of investigated QWs such as a type of the radiative recombination (excitonic, free-electron-free-hole, donor-acceptor, etc.), shape and spectral width of broadening of energy levels, effective temperature of holes and electrons or spectral position of the forbidden gap [100].

We will start the description of the PL line shape from the simplest model based on Fermi golden rule and an ideal band structure. As a second step, we introduce broadening of energy levels. Two types of broadening will be investigated, Gaussian and Lorentzian. Further on, we compare our simplified model with experimental data of PL at zero magnetic field. At the end, we will discuss contributions of the broadening of valence and conduction band to the total broadening determined in the PL line shape analysis. Because in the whole presented work, we have paid special attention to the 20 nm wide QW (for the reasons which will be shown in chapter 7.3), we will focus also here on this sample.

Electron concentration in 20 nm wide QW reaches value of $4.5 \times 10^{11} \text{ cm}^{-2}$, which is high enough with respect to metal-insulation transition (MIT), above which the excitonic effects should be negligibly weak¹. The electron concentration in our samples corresponds to the dimensionless parameter $r_s = 1.6$ ². Such a small value of the parameter r_s implies also negligible binding energy of excitons [102]. The recombination is not even of the acceptor- or donor-related origin, because in such a case, as will be shown in following chapters, field dependence of the energy of PL emission (Landau level quantization) would not exhibit contributions of both free electrons and free holes. Therefore we assume that the radiative recombination is due to free-electron-free-hole recombination process. The electrons of a 2DEG occupy the lowest electronic subband up to the Fermi energy

¹MIT occurs at $\approx 2 \times 10^{11} \text{ cm}^{-2}$ in 10 nm wide single-side doped CdTe QWs, see [101]

²Parameter r_s describes an average distance between electrons. The average distance is measured in the units of an effective Bohr radius a_0^* , for definitions of r_s and a_0^* , see chapter 4

$E_F = 10.8$ meV from the bottom of the conduction band. The corresponding Fermi wave vector $k_F = \sqrt{2m_e E_F}/\hbar = 168 \times 10^6 \text{ m}^{-1}$ determines the range of wave vectors around Γ point, in which the electron-hole recombination takes place. The largest wave vector of emitted photon $k_\gamma \approx 8 \times 10^6 \text{ m}^{-1}$ is roughly 20 times smaller than k_F . Hence, we neglect wave vector of emitted photon with respect to k_F and thus we consider that wave vector is conserved during the radiative recombination process.

7.1.2 Description of the PL spectrum

Intensity of PL is given in the first order of the perturbation theory (dipole approximation), by Fermi golden rule (7.1),

$$I_{PL}(h\nu) \propto J_{CV} n_{FD}^e n_{FD}^h |M|^2 \quad (7.1)$$

where J_{CV} is a joint density of states of conduction electrons and valence band holes, n_{FD}^e and n_{FD}^h are Fermi-Dirac distributions of electrons and holes and $|M|^2$ is a matrix element of the optical transition, also called the oscillator strength. Joint density of states of electrons and holes is given in an ideal 2DEG by step-like function (7.2)

$$J_{CV} = \frac{1}{\pi\hbar^2} \frac{m_e m_h}{m_e + m_h} \theta(E - E_g) \quad (7.2)$$

where m_e and m_h are effective masses of electrons and holes and E_g is the band gap energy.

One of the procedures to describe the non-ideal 2DEG is to consider that band gap energy E_g changes across the sample. These variations are caused by an inhomogeneous width of the quantum well, interface roughness, non-homogeneous internal electric field and other effects which can generally shift the band gap energy. We can write then, that E_g is a random variable with a statistical distribution given by a function $f_g = f_g(\Gamma_g)$, where Γ_g accounts for the variation of the band gap E_g across the sample. The two experimentally most often considered situations are, if the distribution function posses Lorentzian, Eq. (7.3), or Gaussian line shape, Eq. (7.4).

$$f_g = \frac{1}{\pi\Gamma} \frac{1}{1 + \left(\frac{E}{\Gamma}\right)^2} \quad (7.3)$$

$$f_g = \frac{1}{\sqrt{2\pi}\Gamma} e^{-\frac{E^2}{2\Gamma^2}} \quad (7.4)$$

The probability that the gap occurs in the interval $(E_g, E_g + dE_g)$ is $f_g(E - E_g)dE_g$. States inside this interval contribute to the broadened joint density of states $J_{CV,\Gamma}$ by $f_g(E - E_g)dE_g\theta(E)$. Total broadened joint density of states $J_{CV,\Gamma}$ is then simply a sum of all such contributions over all possible values of band gap energy E_g , see Eq. (7.5).

$$J_{CV,\Gamma} = \int_{-\infty}^{\infty} f_g(E - E_g) \frac{1}{\pi\hbar^2} \frac{m_e m_h}{m_e + m_h} \theta(E), dE \quad (7.5)$$

Formula (7.5) is from a mathematical point of view a convolution of the distribution function f_g and ideal joint density of states J_{CV} , $J_{CV,\Gamma} = f_g * J_{CV}$.

The resulting expression of the spectral line shape of a free-electron-free-hole recombination is given by formula (7.6).

$$I_{PL}(h\nu) \propto J_{CV,\Gamma} \frac{m_r}{\pi \hbar^2} n_{FD}^e n_{FD}^h |M|^2 \quad (7.6)$$

For the sake of simplicity, we consider matrix element $|M|^2$ to be independent on the energy. Under these particular assumptions we can write the analytical expression for the PL line shape of free-electron-free-hole recombination, considering wave vector conservation and Gaussian (7.7), resp. Lorentzian (7.8) broadening of both conduction and valence band.

$$I_{PL}(h\nu) = \frac{I_0}{2} \left[1 + \operatorname{erf} \left(\frac{h\nu - E_g}{\sqrt{2}\Gamma_g} \right) \right] \frac{1}{\exp \left(\frac{E_e - E_{F,e}}{k_B T_e} \right) + 1} \left[1 - \frac{1}{\exp \left(\frac{E_h - E_{F,h}}{k_B T_h} \right) + 1} \right] \quad (7.7)$$

$$I_{PL}(h\nu) = \frac{I_0}{2} \left[1 + \frac{2}{\pi} \arctan \left(\frac{h\nu - E_g}{\Gamma_g} \right) \right] \frac{1}{\exp \left(\frac{E_e - E_{F,e}}{k_B T_e} \right) + 1} \left[1 - \frac{1}{\exp \left(\frac{E_h - E_{F,h}}{k_B T_h} \right) + 1} \right] \quad (7.8)$$

$E_{F,e}$, $E_{F,h}$, T_e and T_h are Fermi energies and temperatures of electrons in the conduction band and photo-excited holes in the valence band. Energies E_e and E_h stand for single particle energies of electron and hole, which participate in the recombination process of the emission of $h\nu$ photon. In our situation of the parabolic band structure, the electron and hole energies E_e and E_h are given by the relations (7.9) and (7.10).

$$E_e = E_g + \frac{m_h}{m_e + m_h} (h\nu - E_g) \quad (7.9)$$

$$E_h = -\frac{m_e}{m_e + m_h} (h\nu - E_g) \quad (7.10)$$

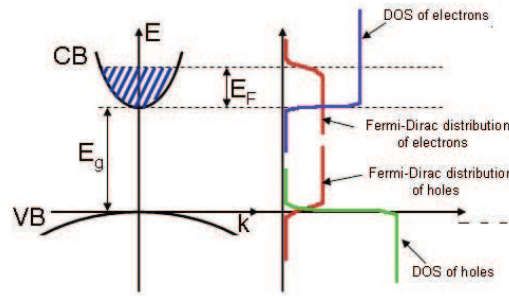


Figure 7.1: Schematic band structure (left panel) and density of states of electrons and holes together with occupation factors on the right side.

The parameter I_0 scales the amplitude of PL intensity. In Fig. 7.1, we sketch schematically Fermi-Dirac distributions of electrons and holes. Joint density of states is a two-particle property and it cannot be plotted in this single particle scheme. Therefore we sketch only single-particle density of states of electrons and holes. Roughly speaking, broadening Γ_g determines the width of the low energy tail of PL spectrum. Temperature

of holes is reflected in the width of the high energy tail from the maximum of PL to approximately Fermi energy. Band gap energy E_g defines the position of PL emission in the spectrum. Temperature of electrons T_e is responsible for how quickly intensity of PL emission decreases in the vicinity of the Fermi energy.

7.1.3 Fitting procedure

We used formulas (7.7) and (7.8) to fit PL spectrum of the 20 nm wide QW measured at five selected temperatures 0.08, 2.66, 7.90, 16.0 and 20.6 K. One set of parameters required by the model of PL line shape has been obtained from other experiments than zero-field PL [effective mass of electrons $m_e = 0.1m_0$ (Far infrared absorption), effective mass of holes $m_h = 0.5m_0$ (field dependence of PL), Fermi energy of electrons $E_F^e = 10.8$ meV (magneto-resistance and photoluminescence-excitation)]. Temperature of electrons was difficult to extract from our PL spectra due to very weak PL intensity at high energy tail of PL spectra even at high temperatures. This is due to small concentration of holes, which could recombine with electrons from the vicinity of Fermi energy. Therefore temperature of electrons was assumed to be the same as a lattice temperature. The set of other five parameters was unknown: band gap energy E_g , total broadening of joint density of states Γ_g , temperature of holes T_h , Fermi energy of holes $E_{F,h}$ and scaling parameter I_0 . These parameters should be used as fitting parameters.

In order to reduce number of fitting parameters, we have eliminated the scaling amplitude I_0 by normalizing both measured PL spectra and functions (7.7) and (7.8) per unite amplitude. Fermi energy of holes $E_{F,h}$ was eliminated by two methods. The first possibility is based on the fact that the concentration of photo-excited holes is very small, hence, we assume that Fermi energy $E_{F,h}$ lies deeply in the forbidden gap. Therefore it is possible to replace Fermi-Dirac distribution of holes by Boltzmann distribution. This approximation is suitable for the case of Gaussian broadening, however fails in the case of Lorentzian broadening. The reason is that we replace Fermi-Dirac distribution of holes, which has finite limit at high energies, by the Boltzmann distribution, which grows at high energies exponentially, as $e^{E/k_B T}$. If considering Gaussian broadening, then density of states in the forbidden gap decreases as $e^{-E^2/2\Gamma^2}$, thus number of occupied states decreases exponentially as $e^{-E^2/2\Gamma^2} e^{E/k_B T} \propto e^{-E}$. However, when we do the same approximation for the Lorentzian broadening, a number of states in the forbidden gap diminishes only as $1/E^2$ and thus a number of occupied states states in the forbidden gap increases as e^E/E^2 . This non-physical behavior is caused by the fact that Lorentzian function decreases much slower than exponentially growing Boltzmann distribution. Hence, by this first method, fitting parameter E_F was excluded only in the case of Gaussian broadening. This approximation tends more likely to fail in the case of Lorentzian broadening.

The second method of excluding Fermi energy of holes from the set of fitting parameters is to find the relation between $E_{F,h}$ and one of the remaining parameters E_g and(or) Γ_g . A good candidate to do this is a broadening Γ_g of joint density of states $J_{CV,\Gamma}$. We will discuss here only the case of Gaussian broadening, because, as will be explained later, this method again fails for the case of Lorentzian line shape. Broadening Γ_g is given by the convolution of distribution functions describing broadening of a valence and conduction band. If one finds the relation between Γ_g and broadening of the valence band Γ_V , it is possible to calculate Fermi energy $E_{F,h}$ from the known concentration of photo-excited

holes ($n_{ph} \approx 10^8 \text{ cm}^{-2}$). For the sake of simplicity, we will assume that valence and conduction bands possess the same type of (Gaussian) broadening. Moreover, as we have shown in the analysis of low-field magneto-resistance, although Lorentzian broadening is more suitable for conduction band, Gaussian broadening is, in the first approximation, also good description of low-field broadening of electronic Landau levels and will be a sufficient approximation for the moment. We have concluded in chapter 6.1 that in such a case, the broadening of electronic Landau levels is $\Gamma_e = 0.07 \text{ meV}$ and we have shown that it does not depend neither on temperature (from 91 mK to 1.2 K) nor on magnetic field (from 0.12 to 0.5 T). We extrapolate this value to the zero magnetic field, and assume that the width Γ_C of a distribution function describing broadening of the electronic conduction band is $\Gamma_C = \Gamma_e = 0.07 \text{ meV}$. It follows from the properties of a convolution of two gaussian functions that the relation between Γ_g , Γ_C and Γ_V is given as:

$$\Gamma_g^2 = \Gamma_V^2 + \Gamma_C^2 \quad (7.11)$$

Thus, having parameter Γ_g from the fitting of the spectral line shape of PL, having Γ_C from the analysis of low-field magneto-resistance and concentration of holes as a parameter given by the concentration of photo-excited carriers $n_h = n_{ph} = 10^8 \text{ cm}^{-2}$, we can calculate Fermi energy of holes from the equation for their concentration n_h .

$$n_h = \int_{-\infty}^{\infty} \frac{m_h}{\pi \hbar^2} \frac{1}{2} \left[1 + \operatorname{erf} \left(\frac{E}{\sqrt{2}\Gamma_V} \right) \right] n_{FD}^h(E, E_{F,h}, T_h) dE \quad (7.12)$$

Equation (7.12) is an integral of zero-field density of states and Fermi-Dirac distribution of holes n_{FD}^h given by Fermi energy $E_{F,h}$ and temperature of holes T_h . Hence, the fitting of the PL spectrum has to be done self-consistently by fitting expression (7.7) and solving equation (7.12) at the same time.

This method is not applicable to the case, when broadening of energy levels is described by a Lorentzian line shape. It is again due to slowly vanishing high-energy tails of Lorentzian distribution, which gives infinite number of hole states above top of the valence band (e.g. towards forbidden gap). Infinite number of states above the top of the valence band causes non-physical shift of the Fermi energy of holes to the infinitely high energies and makes it impossible to treat such a problem numerically. There are two ways, how to eliminate this divergency. The first is to cut the density of states at certain, arbitrarily chosen energy, or to fix Fermi energy at a given level. We have chosen the second method, and fixed the Fermi energy of holes at the top of the valence band. The expressions (7.7) and (7.8) which we are using to fit the spectral line shape of zero-field PL are non-linear functions of all three remaining fitting parameters E_g , Γ_g and T_h . As a consequence, the result of fitting depends on initial values of fitting parameters, which are used as a starting points for the method of least squares. In order to stabilize the solution and make it less dependent on the initial values of E_g , Γ_g and T_h , we have solved the minimization problem self-consistently. Good convergence was achieved usually after 3-5 iterations and such a solution was much more robust with respect to the change of the initial fitting parameters.

The results of the fitting procedure are compared with a data in the figure 7.2 and obtained parameters E_g , Γ_g and T_h are shown for both types of energy level broadening and selected lattice temperatures in the table 7.1.3.

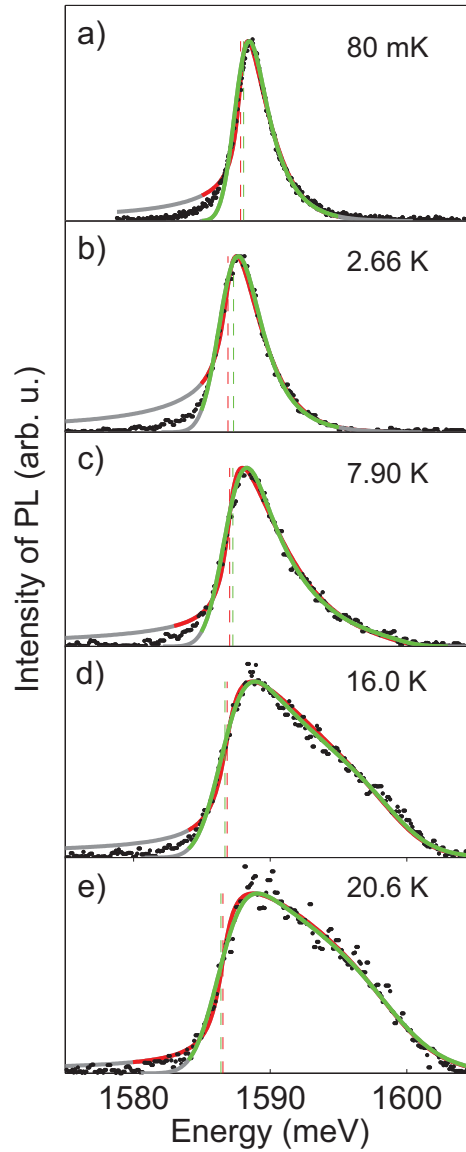


Figure 7.2: Measured PL spectra (black points) compared with the models of PL line shape using Gaussian broadening (green curve) and Lorentzian broadening (red curve) for the temperatures (a) 80 mK, (b) 2.66 K, (c) 7.90 K, (d) 16.0 K and (e) 20.6 K. Grey curves are continuations of both models in the range of the experimental data, which was not used in the fitting procedure. PL was excited by green Argon laser ($E_{exc} = 2.41$ eV), excitation power was of about $0.5 \mu W/cm^2$ and a diameter of an area illuminated by laser was ≈ 2 mm. Positions of the band gap edge is shown by red (green) vertical dashed lines for energy levels described by lorentzian (gaussian) distribution function.

7.1.4 Discussion

For the case of gaussian energy level broadening, we have compared both methods of excluding Fermi energy of holes from the set of fitting parameters and concluded that

T_{bath} (K)	$k_B T$ (meV)	Gaussian broadening			Lorentzian broadening		
		E_g (meV)	Γ_V (meV)	T_h (K)	E_g (meV)	Γ_V (meV)	T_h (K)
0.08	0.007	1588.1	0.8	3.2	1587.8	0.3	2.9
2.66	0.2	1587.3	1.1	3.5	1586.9	0.5	3.3
7.90	0.7	1587.3	1.2	6.7	1587.0	0.4	5.8
16.0	1.4	1586.7	1.4	21.5	1586.8	0.6	13.8
20.6	1.8	1586.4	1.5	38.0	1586.5	0.6	21.6

Table 7.1: Parameters of band gap energy E_g , broadening of joint density of states Γ_g and temperature of holes T_h as obtained by fitting the zero-field PL spectrum using model of broadened energy levels by gaussian and lorentzian distribution functions. The results of the spectral line shape analysis at five selected lattice temperatures T are presented. For the sake of comparison, also corresponding energy $k_B T$ is shown.

both methods lead to the same values of E_g , Γ_g and T_h within uncertainty smaller than ± 0.3 meV, ± 0.1 meV and ± 1 K, respectively. In the case of Lorentzian broadening, as has been already mentioned, the Fermi energy of holes was fixed at the top of valence band.

The values of the band gap energy are equal within an error ± 0.3 meV for both types of broadening and they are depicted by vertical dashed lines in Fig. 7.2. The band gap energy has a decreasing tendency as a function of growing temperature. Such a behavior is in agreement with theoretically expected band gap temperature dependence in CdTe [103].

The width of the broadening Γ_g is systematically larger for Gaussian broadening. The reason is that Gaussian function has exponentially diminishing high-energy tails in comparison to the Lorentzian energy level broadening, which diminishes only as $1/E^2$. Hence, in order to spread Gaussian density of states in roughly the same interval of energies as in the case of similar Lorentz distribution, larger Gaussian broadening is needed.

Broadening Γ_g tends to increase with increasing temperature and its amplitude scales with $k_B T$ at high temperatures above 8 K. As has been already mentioned, when assuming the same type of broadening for both conduction and valence band, we can calculate broadening of the energy levels of the valence band Γ_V . The relation between Γ_g (broadening of joint density of states $J_{CV,\Gamma}$, obtained by the analysis of the PL spectrum), Γ_C and Γ_V (broadening of the conduction band and valence band, respectively) is,

$$\Gamma_g^l = \Gamma_C^l + \Gamma_V^l \quad (7.13)$$

where index $l = 1$ ($l = 2$) stands for Lorentzian (Gaussian) shape of energy levels. Due to the small value of $\Gamma_C = 0.07$ meV with respect to Γ_g in the case of Gaussian broadening, one can write $\Gamma_V \approx \Gamma_g$. In the case of Lorentzian broadening, $\Gamma_V = \Gamma_g - 0.11$ meV³, see Tab. 7.1.3 for temperature dependence of Γ_g .

Temperature of holes T_h tends to saturate at low bath temperatures $T_{bath} \rightarrow 0$. This is common behavior with the temperature of electrons, as concluded from the analysis of Shubnikov-de Haas oscillations (see chapter 6.1, page 44). In contrast to the electronic temperature T_e , which gets saturated at 200 mK, temperature of holes saturates at much higher temperature of 3 K (measured at the lattice temperature 80 mK).

³Parameter $\Gamma_C = 0.11$ meV was analyzed from the low field Shubnikov-de Haas oscillations using Lorentzian line shape of Landau levels, and parameter $\Gamma_C = 0.07$ meV using Gaussian line shape. See chapter 6.1 for more details.

We interpret the higher temperature of holes T_h at low bath temperatures to be due to the fact that holes recombine before they establish thermal equilibrium. In order to get thermalized, every hole has to cover an average distance in 2D plane $l_{th} = 1/\sqrt{n_{ph}} \approx 1\mu\text{m}$, where n_{ph} is a concentration of photo-excited carriers, which is the same as a concentration of holes. This is an average distance between two tail states in the hole DOS, which are supposed to be occupied in thermal equilibrium. The mean path covered by holes during their lifetime is in average $l_{rec} \approx 4\mu\text{m}$ (PL decay time is in CdTe QWs $\tau_{PL} \approx 0.3\text{ ns}$ [104] at 2 K, which is in the same time as lifetime of holes. Thermal speed of holes is $v_{th} = \sqrt{2k_B T_h/m_h} \approx 13\text{ km/s}$ ($T_h = 3\text{ K}$), therefore $l_{rec} = v_{th}\tau_{PL} = 4\mu\text{m}$). This seems to be enough in order to find thermal equilibrium for every hole. However, we are talking here in average values. Hence, although majority of holes will find their thermalized position in disordered potential during their lifetime, some part of holes will not and these could contribute to the higher effective temperature T_h .

We are aware that high temperature of holes T_h at the limit $T_{bath} \rightarrow 0$ could be also due to partial localization of holes. The influence of the localization should be weakened at higher temperatures, therefore one would expect narrowing of the PL spectrum in the range of bath temperature from 0 K to the $T_{bath} = T_{h,sat} \cong 3\text{ K}$. Narrowing of PL spectrum should be reflected in the lower value of T_h . The only temperature at which we could observe such a narrowing is $T_{bath} = 2.66\text{ K}$. However, we have observed rather increasing T_h ($T_h = 3.3 - 3.5\text{ K}$), therefore we guess that holes are rather free than localized.

Last comment will be devoted to the behavior of T_h at the limit of high lattice temperatures T_{bath} . Fast increase of T_h above $T_{bath} = 16\text{ K}$ ($T_h > T_{bath}$ in this limit) is caused by thermal occupation of the first light hole subband lh_1 . Subband lh_1 is 4.7 meV below ground heavy hole state hh_1 at $\mathbf{k} = 0$, hence it starts to get populated at temperatures $T_{lh_1} \geq 4.7\text{ meV}/5k_B = 11\text{ K}$. Light hole band lh_1 is mixed with heavy hole band hh_1 at $\mathbf{k} \neq 0$, hence we can expect, that transition $e_1 - lh_1$ is also radiative. However, it contributes to the PL spectrum at energies 4.7 meV and higher above band gap (band gap position depicted in Fig. 7.2 by vertical lines). Because we have taken into account only first heavy hole subband in our analysis, enhanced intensity of PL at high energy tail of PL spectrum will be reflected in higher temperature of holes T_h . The same considerations can be done for the case of second heavy hole subband hh_2 , which is at the energy 8.5 meV below ground heavy hole subband at $\mathbf{k} = 0$ and thus it gets thermally populated at the temperatures $T_{hh_2} \geq 20\text{ K}$. The fitting parameter T_h is therefore hassled by the systematic error for lattice temperatures higher than 11 K.

7.2 An overview of the experimental results in magnetic field

The major part of this thesis was devoted to the experimental study of the magneto-photoluminescence. Here, we introduce the typical magneto-PL data of both CdTe and CdMnTe QWs measured at low temperatures of about 80-90 mK and basic analysis of the spectra is presented here. Magneto-photoluminescence studies were performed using an experimental set-up based on optical fibers. The photoluminescence was excited by continuous wave green Ar⁺ ion laser line at the energy $E_{exc} = 2.41$ eV, which is high enough above the band gap energy of the Cd_{0.74}Mg_{0.26}Te barrier. PL signal was detected always in one given circular polarization (σ^+ or σ^-) and the detected polarization was changed by changing the polarity of magnetic field. Left-handed circular polarization σ^+ correspond to the recombination of electrons with spin $s = -1/2$ and heavy holes with an angular momentum $j_z = +3/2$ and right-handed circular polarization σ^- correspond to the recombination of electrons $s = +1/2$ and holes $j_z = -3/2$ (we follow convention of Born and Wolf [7]). Signal was guided by the optical fiber into the grating spectrometer with a spectral resolution of about 100 μ eV and the signal was detected by nitrogen cooled CCD camera.

7.2.1 CdTe QWs

In the first part of this introduction, we present the data of the magneto-photoluminescence of CdTe QWs measured at the temperature of 80 mK. The data measured for 20 nm (30 nm) wide QW are shown in the Fig. 7.3 (Fig. 7.4). The parts (a) of the Fig. 7.3 and Fig. 7.4 correspond to the magneto-PL measured in σ^+ circular polarization and parts (b) to the polarization σ^- . The main difference between these two samples is, beside the width of QW, the concentration of the 2DEG. The smaller the electron concentration is, the narrower band of the PL emission is observed in the spectrum. The emission band in the 20 nm wide QW spreads over the interval ≈ 11 meV (at $B = 0$ T from ≈ 1.585 to ≈ 1.596 eV). This range is in a good agreement with the Fermi energy 10.8 meV deduced from the analysis of the magneto-transport experiments. In the case of the 30 nm wide QW, the width of the emission band is ≈ 7 meV (it spreads from ≈ 1.590 to ≈ 1.597 eV at $B = 0$ T), what is also in agreement with the expected electron concentration in this QW. At first sight, the magnetic field evolution of the PL emission exhibits linearly B -dependent transitions. Linear B -dependence is caused by the Landau level quantization of both conduction and valence band free-electron and free-hole states. The optically allowed transitions can be described in a single-particle approximation by energies $E_{N,s}$,

$$E_{N,s} = E_0 + \hbar e B \left(\frac{1}{m_e} + \frac{1}{m_h} \right) \left(N + \frac{1}{2} \right) + s(|g_e| - |g_h|)\mu_B B, \quad (7.14)$$

where N is a quantum number of the Landau levels between which the transitions occur, E_0 is the energy of the PL emission at zero magnetic field, $s = +1/2$ ($s = -1/2$) stands for the circular polarization σ^+ (σ^-), m_e , m_h , g_e and g_h are effective masses of electrons, holes and g-factors of electrons and holes, respectively. The origin of these transitions are depicted in a Fig. 7.5 by vertical arrows.

It can be seen, in the case of a field evolution of the PL in the 20 nm wide CdTe QW, that there is a duplet and triplet structure of the optical transitions corresponding

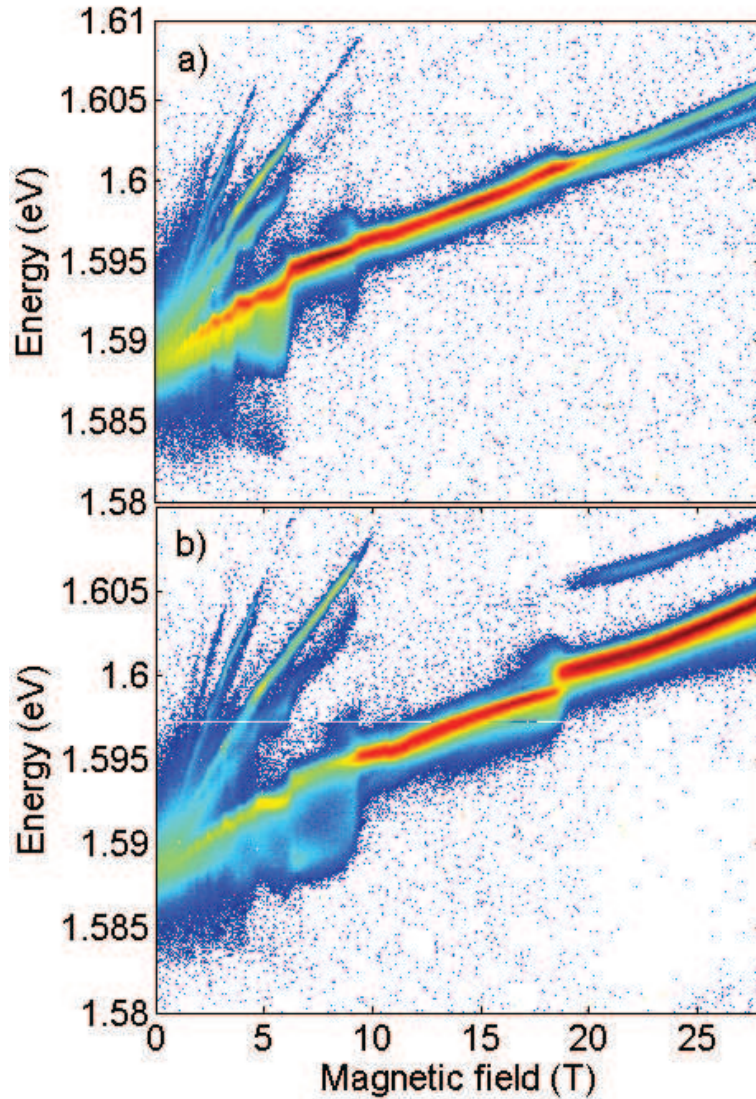


Figure 7.3: Magneto-photoluminescence of 20 nm wide CdTe QW measured at $T = 80$ mK in (a) σ^+ and (b) σ^- circular polarization. Blue (red) color corresponds to the low (high) PL intensity. Concentration of the 2DEG corresponds to the filling factor $\nu = 1$ at magnetic field $B_{\nu=1} = 18.74$ T.

to Landau levels $N = 1$ and $N = 2$. This doublet and triplet structure is also shown in the PL spectrum measured at the filling factor $\nu = 6$ in the Fig. 7.6. At the same time, we have observed no such a duplet or triplet structure of the recombination spectrum in the 30 nm wide QW. Although both QWs are asymmetrically doped, the internal electric field is smaller in the wider QW, as has been also shown by the calculations of the band structure in chapter 4. Therefore, we suggest that the internal electric field allows transitions between electron and hole LLs with the quantum numbers $N_h = N_e - 1$, $N_h = N_e - 2$, etc. These are additional transitions, beside the only allowed transitions

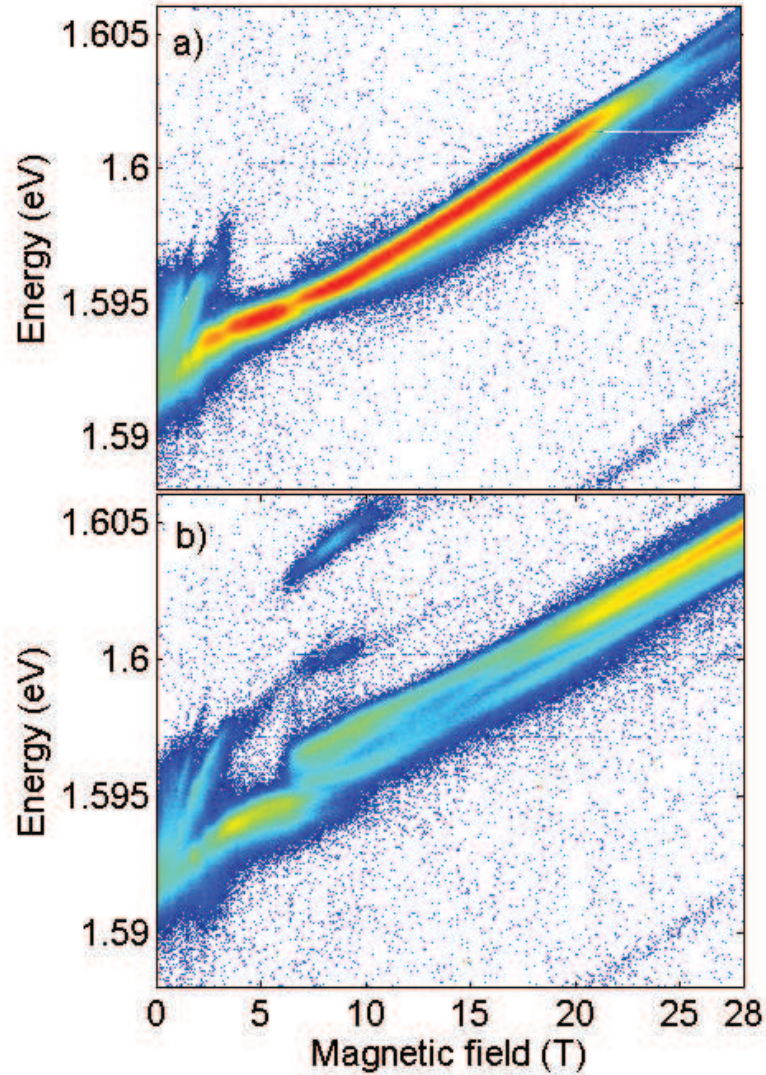


Figure 7.4: The same as Fig. 7.3, but for 30 nm wide CdTe QW. Concentration of the 2DEG corresponds to the filling factor $\nu = 1$ at magnetic field $B_{\nu=1} = 12.0$ T.

$N_e = N_h$ in the QWs with zero internal electric field (see chapter 2 for more details). This is also reason, why we have observed only single transition for each LL in the wider (30 nm wide) QW, in which the internal electric field is weaker, QW is more symmetrical, and in which only transitions $N_e = N_h$ are allowed. Therefore, we interpret the doublet structure in the 20 nm wide QW at the LL $N_e = 1$ as the recombination between electronic and hole LLs $N_h = N_e$ and $N_h = N_e - 1$. The triplet structure at the LL $N_e = 2$ is due to the set of transitions $N_h = N_e$, $N_h = N_e - 1$ and $N_h = N_e - 2$. These transitions are depicted in the inset in the Fig. 7.6. The energy distance between the neighbor components of these

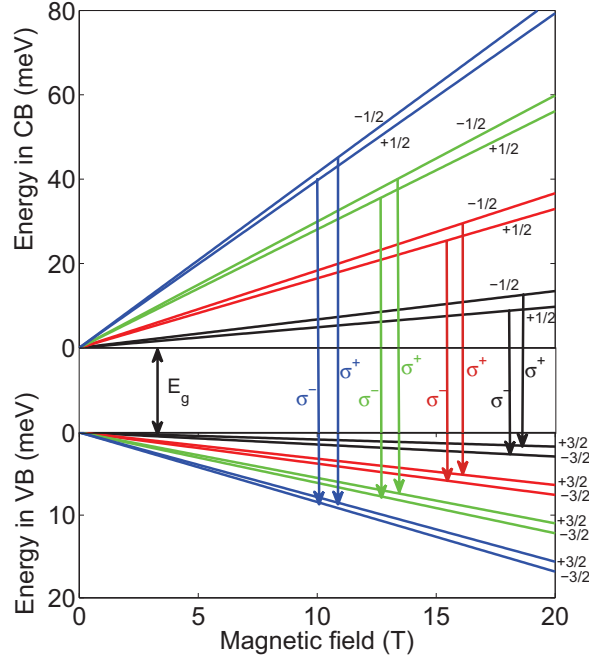


Figure 7.5: Magnetic field evolution of the Landau levels in the conduction band (CB) and in the valence band (VB) in CdTe QWs. Electronic Landau levels $N_e = \{0, 1, 2, 3\}$ (upper part) and hole Landau levels $N_h = \{0, 1, 2, 3\}$ (lower part) depicted by black, red, green and blue colors, respectively. Allowed optical interband transitions sketched by vertical arrows. The polarization of emitted photons is marked. Every Landau level is spin split. For the sake of clarity, the spin splitting was taken $2\times$ larger than the real spin splitting in both conduction and valence band.

doublets and triplets correspond to the cyclotron energy of holes with an effective mass $m_h \approx 0.2-0.3m_0$. This interpretation is consistent with the experimental observation that the transition from the LL $N_e = 0$ consists of only one single line because there is no hole LL with negative quantum number N_h . Analogously, we expect, however much weaker, quadruplet, quintuplet etc. radiative transitions corresponding to the LLs $N_e = \{3, 4, \dots\}$. Although the presented interpretation can explain the experimental data, the mechanism, why parallel electric and magnetic fields couple is not clear. Therefore, more detailed experimental and theoretical study is needed in order to justify the presented explanation.

We focus now only on the main transitions $N_e = N_h$. The energy of the PL emission exhibits, especially in the 20 nm wide QW, the oscillatory field dependence, which correlates with the integer filling factor. Electron-electron interactions, combined with different perturbations induced by the presence of the valence band hole, are almost certainly at the origin of these features [105]. The understanding these features is far from universal [106, 107, 105, 108] and a detailed analysis of the energy of each individual magneto-PL transitions is not in the scope of this thesis. However, we have found simple description of the difference of these energies measured in the two circular polarizations and the details will be discussed in the following chapter 7.3.

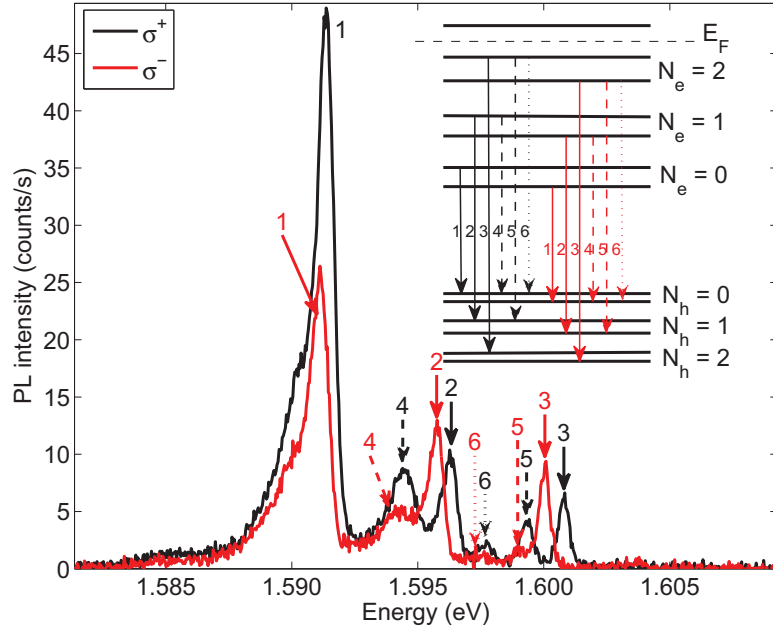


Figure 7.6: Photoluminescence spectra measured in 20 nm wide CdTe QW at $T = 80$ K and at the filling factor $\nu = 6$ ($B_{\nu=1} = 18.74$ T) in σ^+ (black curve) and σ^- (red curve) polarization. Excitation by Ar^+ laser at $E_{exc} = 2.41$ eV. Inset depicts electronic ($N_e = \{0, 1, 2\}$) and hole ($N_h = \{0, 1, 2\}$) Landau levels. The transitions are labelled by black (σ^+) and red (σ^-) numbers and arrows. The transitions $N_h = N_e$, $N_h = N_e - 1$ and $N_h = N_e - 2$ are depicted by solid, dashed and dotted arrows, respectively.

Analysis of the effective mass of holes

Field evolution of the energy position of the PL emission described in a single-particle model by the formula (7.14) allows to extract the effective mass of holes. There are few possible approaches. The first is to analyze directly the field evolution of the energy of PL in a certain polarization (σ^+ or σ^-). This approach is principally correct, however, one has to take into account also effective g -factor of electrons and holes $g_{eff} = |g_e| - |g_h|$, what is another fitting parameter, which increases uncertainty of the obtained effective mass of holes. We have chosen another method, which is based on the fact, that in the single particle model, the spin splitting contributes in the σ^+ (σ^-) polarization by a factor of $\pm g_{eff} \mu_B B$. Therefore it is possible to eliminate the effective g -factor g_{eff} as a fitting parameter by taking the average $E_{ave} = 1/2(E_{N,+1/2} + E_{N,-1/2})$ of the energy positions in both circular polarizations. The average energy $E_{ave,N}$ for the PL emission from the Landau level N

$$E_{ave,N} = E_0 + \hbar e B \left(\frac{1}{m_e} + \frac{1}{m_h} \right) \left(N + \frac{1}{2} \right) \quad (7.15)$$

consists of only two fitting parameters, E_0 and m_h . The effective mass of electrons was determined in the FIR measurements. The average positions of PL emission $E_{ave,N}$ together with their description by the single particle model, Eq. (7.15) are shown in Fig. 7.7. We have obtained zero field energy of PL emission $E_0 = (1588.4 \pm 0.3)$ meV and effective

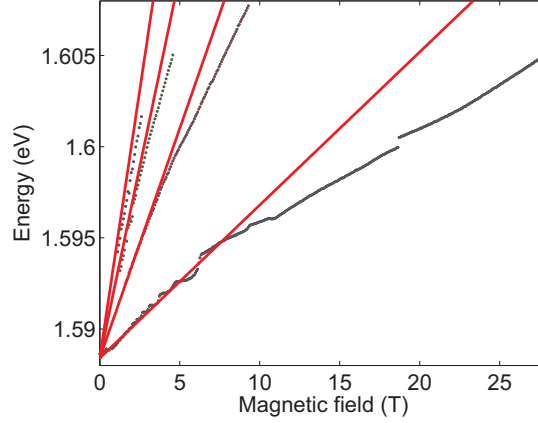


Figure 7.7: The average energy position of σ^+ and σ^- of PL emission from CdTe QW at $T = 80$ mK. Experimental data (black points) are compared with the fitting by the single-particle model, Eq. (7.15).

mass of holes $m_h = (0.3 \pm 0.1)m_0$. The mean value of E_0 is within an experimental error 0.3 meV the same as a value of the band gap energy E_g , which was determined from the analysis of the zero field shape of the PL emission. The effective mass of holes is slightly smaller than the mass assumed in the analysis of the zero-field PL spectra, however, it well agrees with our calculations of the valence band structure, which show that the in-plane effective mass of heavy holes is in the near vicinity of the Γ point $\approx 0.3m_0$. The disagreement between the single-particle model (red curves in Fig. 7.7) and the data at higher energies is explained in terms of the increasing role of excitonic effects in partially occupied Landau levels.

7.2.2 CdMnTe QWs

In the following we deal with 21.1 nm wide QW based on diluted magnetic semiconductor, CdMnTe. The magneto-PL data measured in CdMnTe QW at the temperature $T = 90$ mK are shown in Fig. 7.8. The PL transitions exhibit again Landau level quantization of the energy levels and Landau levels $N = \{1, 2\}$ show similar doublet and triplet structure as has been observed in 20 nm wide CdTe QWs. In chapter 6.2, we have shown, how manganese influences electronic energy levels. Energy levels of holes $E_{V,\uparrow(\downarrow)}$ are given in the presence of manganese by

$$E_{V,\uparrow(\downarrow)} = \pm \frac{1}{2} N_0 \beta x \langle S_z \rangle, \quad (7.16)$$

where β is an exchange integral between p-holes in a valence band and d-electrons of Mn^{2+} atoms ($N_0 \beta = -0.88$ eV). For the sake of simplicity, we neglect the nearest neighbor Mn-Mn anti-ferromagnetic interaction and we describe the average z^{th} component $\langle S_z \rangle$ of the manganese spin by the simplest model given by Eq. (6.31). As a result of sp-d electron-hole-manganese exchange interaction⁴, we have GZS of the conduction and valence band

⁴Because the inter-band recombination concerns both conduction band s-electrons and valence band p-holes, it is common to discuss influence of manganese in terms of s-pd exchange interaction, which takes

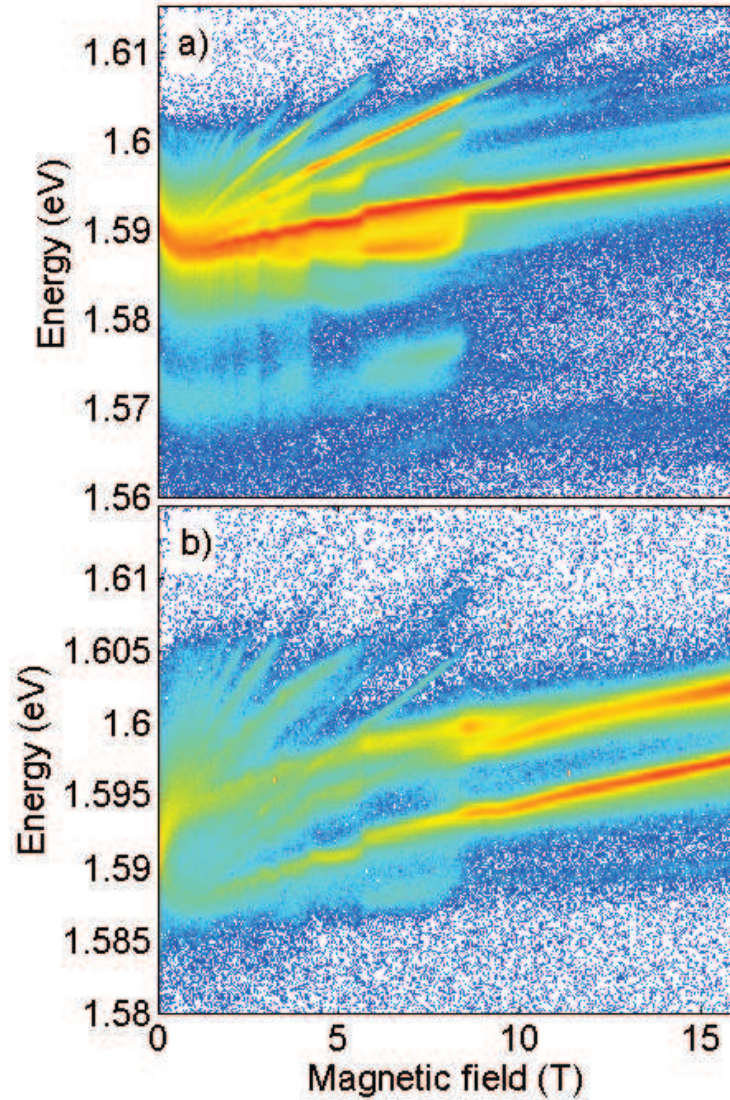


Figure 7.8: Magneto-photoluminescence of 21.1 nm wide CdMnTe QW measured at $T = 90$ mK in (a) σ^+ and (b) σ^- circular polarization. Blue (red) color corresponds to the low (high) PL intensity. Concentration of the 2DEG corresponds to the filling factor $\nu = 1$ at magnetic field $B_{\nu=1} = 17.2$ T.

ΔE_C and ΔE_V , respectively. Since the exchange integral β is 4-times bigger than α , GZS of the valence band will be 4-times larger than the GZS of the conduction band ($\Delta E_V = 4\Delta E_C$). Because we focus on the magneto-optical studies of our heterostructures, the selection rules are essential to understand the radiative recombination processes. It is well known that due to the presence of manganese, the g -factor of electrons changes sign with respect to the sign in non-magnetic CdTe. This leads to the selection rules similar to into account both s-d and p-d interactions together.

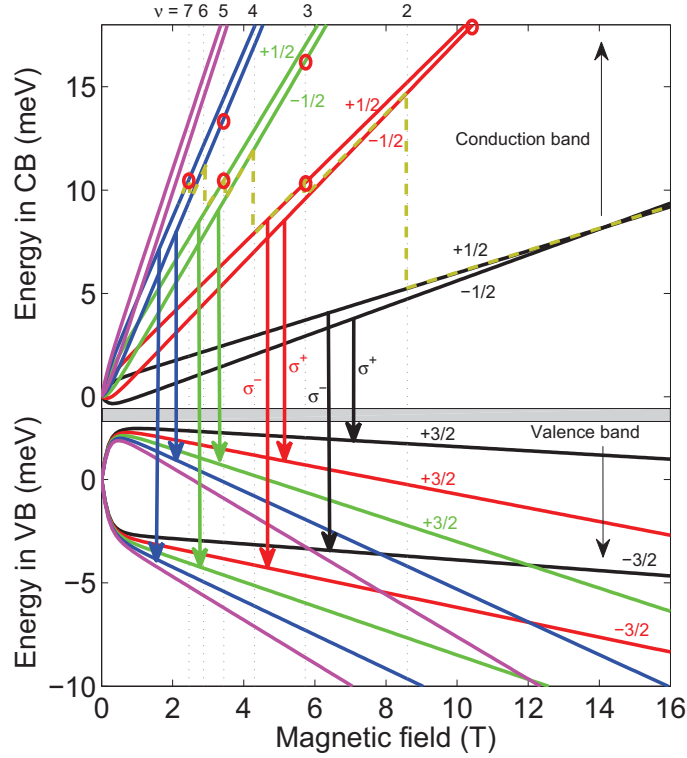


Figure 7.9: Magnetic field evolution of first five electronic (upper curves) and hole (lower curves) Landau levels. Black, red, green, blue and magenta colors correspond to the indices of Landau levels 0, 1, 2, 3 and 4. Arrows depict allowed optical transitions, dotted lines integer filling factors 2, 3, 4, 5, 6 and 7, dark yellow dashed line is a Fermi energy at $T = 0$ K and red circles show the maximum field up to which the PL emission from a given Landau level was observed.

those in GaAs. Selection rules in CdMnTe are depicted in Fig. 2.2 and Fig. 7.9 where the GZS is also considered, hence the spin-resolved Landau levels do not scale linearly with magnetic field, but they follow field dependence given by Brillouin function (6.32). As a consequence, it is expected to observe Giant Zeeman splitting of the amplitude ΔE_{PL}

$$\Delta E_{PL} = 5\Delta E_C = 5N_0\alpha x S_0 B_{5/2} \left(\frac{\frac{5}{2}g\mu_B B}{k_B(T + T_0)} \right). \quad (7.17)$$

Field dependence of the energy of PL emission from the Landau level $N = 0$ in CdMnTe QW measured up to 16 T at the temperature of 90 mK is shown in Fig. 7.10. The data show clear evidence of GZS, which is a fingerprint of the presence of manganese. The energy position of PL emission exhibits blue shifts, which are of the same origin as in CdTe QW. Since these well-defined shifts of the PL energy correlate with the integer filling factor, see vertical lines in Fig. 7.10, we have used them to determine magnetic field at the filling factor $\nu = 1$. The inverse values of magnetic fields at which PL energies show discontinuities are plotted in Fig. 7.11 as a function of an integer (filling factor). The slope of this dependence gives a concentration of a two-dimensional electron gas in CdMnTe QW, $n_e = 4.2 \times 10^{11} \text{ cm}^{-2}$.

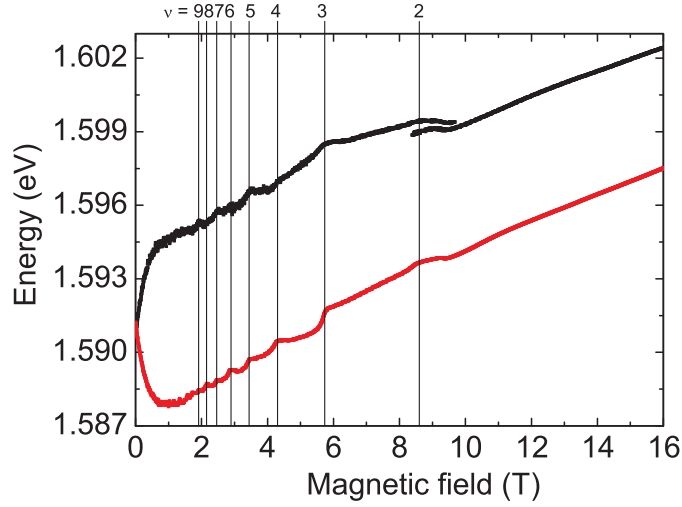


Figure 7.10: Energy position of magneto-PL emission in σ^+ (red dots) and σ^- (black dots) circular polarization. PL excited by the Ar^+ laser at the energy of $E_{exc} = 2.41$ eV, excitation power was $P_{exc} \approx 1.4 \mu\text{W}$ and laser spot size of about 0.5-1 mm. Measured at the temperature $T = 90$ mK.

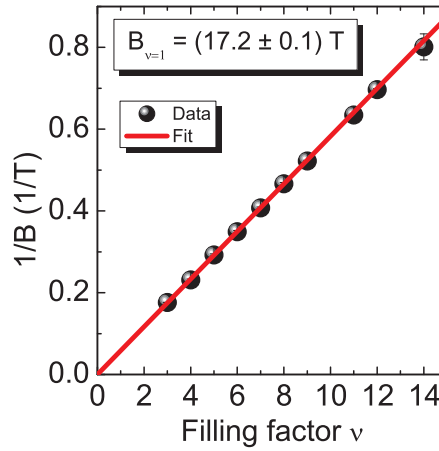


Figure 7.11: Inverse value of the magnetic field versus filling factor to determine concentration of 2DEG. Fitting the slope gives magnetic field at the filling factor $\nu = 1$, $B_{\nu=1} = 17.2$ T and the corresponding electron sheet concentration $n_e = 4.2 \times 10^{11} \text{ cm}^{-2}$.

As can be seen in the magneto-PL data in Fig. 7.10, the energy of the PL emission is not given only by GZS, but also other phenomena contribute. These are Landau level quantization, bare Zeeman splitting of CdTe and electron-electron interaction. In the framework of the single particle picture, average E_{ave} of PL energies in σ^+ and σ^- polarization ($E_{ave} = (E_{\sigma^+} + E_{\sigma^-})/2$) should be spin independent and given simply by $E_{ave} = E_0 + \hbar\omega_c/2$, as has been already shown in the analysis of the CdTe magneto-PL data. E_0 is the energy of PL emission at zero magnetic field and $\hbar\omega_c = eB/\mu_r$, where

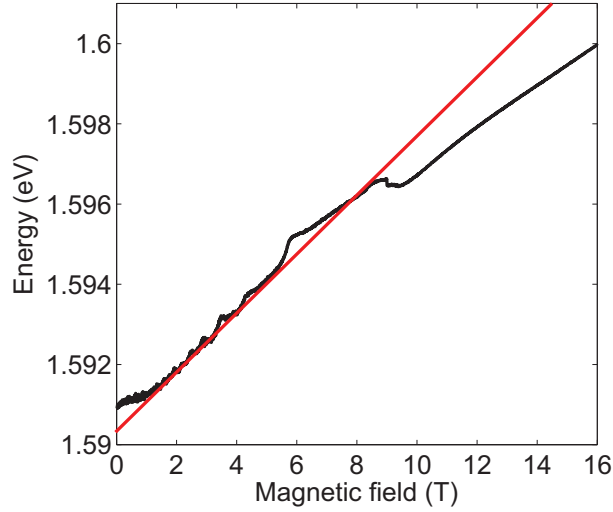


Figure 7.12: Average E_{ave} of the energy positions of PL emission in σ^+ and σ^- polarization ($E_{ave} = (E_{\sigma^+} + E_{\sigma^-})/2$). In the framework of a single particle picture, value E_{ave} is spin independent and the slope of its field dependence is given by $\hbar\omega_c/2$. Fitting procedure gives $\hbar\omega_c/2 = (0.7 \pm 0.1)$ meV/T and the corresponding effective mass of holes is $m_h = (0.5 \pm 0.1)m_0$ (using an effective mass of electrons $m_e = 0.1m_0$).

μ_r stands for reduced mass $\mu_r^{-1} = m_e^{-1} + m_h^{-1}$. Field dependence of E_{ave} is plotted in Fig. 7.12 and the fitting parameters we have obtained are $\hbar\omega_c = (1.4 \pm 0.2)$ meV/T and $E_0 = (1.5908 \pm 0.0003)$ eV. Assuming effective mass of electrons $m_e = 0.1m_0$ leads to the effective mass of holes $m_h = (0.5 \pm 0.1)m_0$, which is in a good agreement with values in non-magnetic CdTe QWs.

Spin dependent contributions are convenient to analyze by taking difference of the emission energies $E_{diff} = E_{\sigma^-} - E_{\sigma^+}$, because such a quantity do not involve spin independent part given by the Landau level quantization $\hbar\omega_c(n + 1/2)$ and thus such an operation reduces one fitting parameter. Difference E_{diff} is plotted in Fig. 7.13. The three spin-dependent contributions are apparent. The oscillations of the spin gap are due to electron-electron interactions, which will be discussed in the case of CdTe QWs in the chapter 7.3. The second contribution is the bare Zeeman splitting, giving rise to the negative slope of total spin splitting at high magnetic fields. The bare Zeeman splitting is fitted taking into account only the local minima of the spin gap, because only these minima are not influenced by the electron-electron interaction. The slope (-0.08 ± 0.03) meV/T reproduces an effective electron-hole g-factor $|g_{eh}| = |g_e| - |g_h| = (1.4 \pm 0.5)$, which agrees with reported values of an effective g-factor of electrons and holes [27]. Third, we discuss the strongest contribution to the Giant Zeeman Splitting, given by the saturation of the magnetization of manganese atoms, which is saturated at low magnetic field of about 1 T and it reaches value of (6.8 ± 0.2) meV. From the saturation at (6.8 ± 0.2) meV one can deduce concentration of manganese in the sample. Saturation value is given according to the equation (7.17) by $E_{sat} = 5N_0\alpha xS_0 = 1.1$ eV $\times xS_0$. Parameter S_0 depends also on the manganese concentration x . However, we expect manganese concentration of about 0.3% and in this low concentration regime S_0 can be approximated by constant [70, 76],

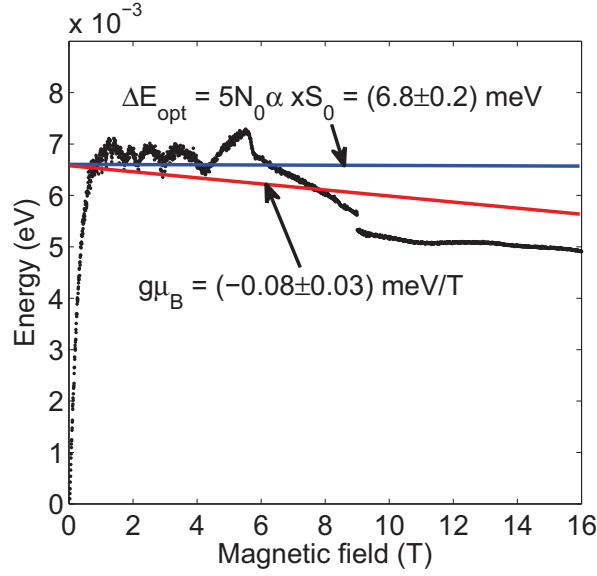


Figure 7.13: Spin gap $E_{diff} = E_{\sigma-} - E_{\sigma+}$ of Landau level $N = 0$ in CdMnTe/CdMgTe QW. Concentration of electron gas $n_e = 4.2 \times 10^{11} \text{ cm}^{-2}$, manganese concentration 0.3%. Blue horizontal line depicts the saturated contribution to the Giant Zeeman Splitting (6.8 meV) given by the saturation of the magnetization of manganese atoms at low (≈ 1 T) magnetic field. The red curve denotes the total spin splitting including bare Zeeman splitting of CdTe and saturation of the magnetization of Mn atoms. The electron-electron interaction is not taken into account as well as low field regime for magnetic fields $B < 1$ T. The slope of the red line denotes the bare g-factor of CdTe ($|g_e| = 1.6$).

$S_0 = 2.4$. The resulting manganese concentration is then $x = 0.25$ %, which is also in agreement with the value obtained from the low-field magneto-resistance data analysis.

Taking into account all the former discussed single or two-particle contributions⁵ to the energy position of PL emission $E_{\sigma+}$ and $E_{\sigma-}$ in both circular polarizations as a function of magnetic field, one can write single-particle expression

$$E_{\sigma\pm} = E_0 + \hbar\omega_c(N + 1/2) \mp \frac{1}{2}g_{eh}\mu_B B \pm \frac{1}{2}N_0(\beta - \alpha)xS_0B_{5/2} \left(\frac{\frac{5}{2}g\mu_B B}{k_B(T + T_0)} \right) \quad (7.18)$$

for the transition energies $E_{\sigma+}$ and $E_{\sigma-}$ from the Landau level $N = 0$. A comparison of this expression with the data is shown in the Fig. 7.14. The parameters used to describe data are summarized in Tab. 7.2. One can see a fairly good agreement with the experimental data. Both data and the model show an important feature of CdMnTe-based QWs. It can be seen at high magnetic fields that the spin gap has a tendency to close, see Fig. 7.13. The observed gap closing is caused by interplay of the saturated giant Zeeman splitting and the bare Zeeman splitting of CdTe (not influenced by the presence of manganese) and it is the manifestation of the fact that electronic g-factor in CdMnTe has an opposite sign with respect to the sign in non-magnetic CdTe. The expected magnetic field at which the energy of the spin gap should be zero is of about 14 T.

⁵The two-particle contributions are the electron-hole effective g -factor and s-d manganese-electron and p-d manganese-hole interaction. The many-body term responsible for the oscillations of the spin gap is omitted and discussed in the chapter 7.3 in the simpler case of non-magnetic CdTe QWs.

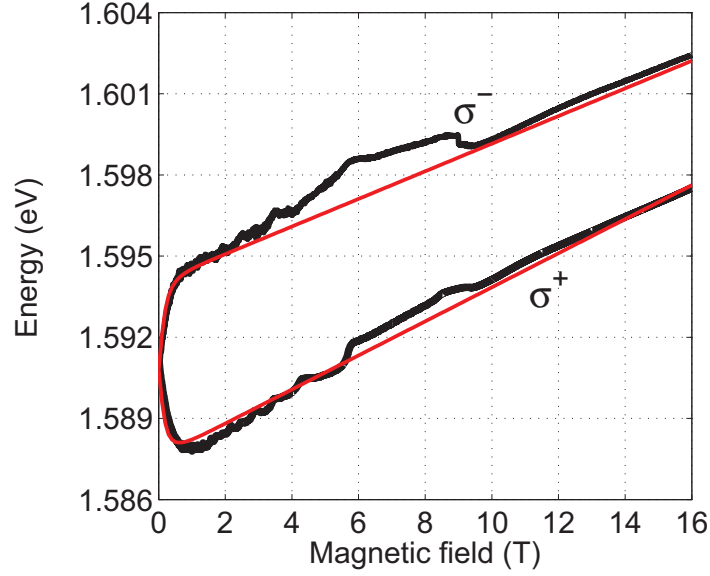


Figure 7.14: Energies of the PL emission from CdMgTe/CdMnTe QW measured as a function of magnetic field up to 16 T. Black points are data in both circular polarizations and red curves show theoretical fit to the data. The parameters used to model the data are following: zero-field energy of PL $E_0 = 1.5908$ eV, effective mass of electron $m_e = 0.1m_{e,0}$, electron-hole g-factor $g_{eh} = -1.6$, strength of the electron-manganese interaction $N_0\alpha = +220$ meV, strength of hole-manganese $N_0\beta = -880$ meV, manganese concentration $x = 0.3\%$, lattice temperature $T = 88$ mK, effective manganese temperature $T + T_0 = 378$ mK and manganese g-factor $g = 2.0$

Parameter	Value
Energy of zero-field PL emission	$E_0 = (1.5908 \pm 0.0003)$ eV
Effective mass of electron	$m_e = 0.1m_{e,0}$
Effective mass of hole	$m_h = (0.5 \pm 0.1)m_0$
Index of the Landau level	$N = 0$
Electron-hole g-factor	$g_{eh} = (-1.4 \pm 0.5)$
Strength of electron-manganese interaction	$N_0\alpha = 220$ meV
Strength of hole-manganese interaction	$N_0\beta = -880$ meV
Manganese concentration	$x = 0.25\%$
Saturation value of manganese spin projection into z-axis	$S_0 = 2.4$
Effective g-factor of manganese	$g = 2.0$
Lattice temperature	$T = 90$ mK
Effective manganese temperature	$T + T_0 = 380$ mK

Table 7.2: Table of parameters used to fit the energy of PL emission from CdMgTe/CdMnTe QW, data shown in Fig. 7.10 and compared with the model in Fig. 7.14.

7.3 Spin gap enhancement

7.3.1 Introduction

In the following chapter, we present the study of magnetic field and temperature dependence of the energy of spin splitting in fully populated electronic Landau levels. Spin

splitting ΔE can be calculated in a single-particle band structure model to be equal to Zeeman splitting $\Delta E_Z = g_e \mu_B B$, where g_e is effective g -factor of electrons, μ_B is Bohr magneton and B is magnetic field. Zeeman splitting thus grows linearly with magnetic field. However, a number of experimental [109, 92, 110, 111] and theoretical [112, 113, 114] works show that the spin splitting can be much larger at certain filling factors in a 2DEG, than would be the expected single particle energy ΔE_Z . This phenomenon, referred to in the literature as g factor or spin gap enhancement (SGE), is here in the scope of our interest. Spin gap enhancement is usually observed at odd integer filling factors (ν), hence it is thought to be driven by the spin polarization of a 2DEG and is a primary manifestation of the interactions between two-dimensional electrons in the integer quantum Hall effect (QHE) regime. It is a result of the specific character of the spin-excitation spectra of a 2DEG at odd integer ν -QHE states [115, 28]. More simplified approach can be also used, where SGE can be seen as arising from the contribution of Coulomb interactions (including exchange terms) to the energy which is required to remove, or inject, an electron from, or to, a given spin resolved Landau level (LL). We use this simplified approach to describe SGE and we discuss conditions under which such an approach is justified.

The experimental study of the spin-gap enhancement has been generally limited to experiments which probe the spin splitting at the Fermi level [109, 92, 111, 116, 117, 118], for QHE states at exactly odd filling factors. This limitation has been thought to be overcome with spectroscopic methods such as, for example, interband optics [119, 120, 121] or tunnelling experiments [122], which, within their trivial description, permit to investigate the processes of removing/adding an electron from/to a 2DEG, at arbitrary energy, filling factor and temperature. Among the different spectroscopic methods, magneto-luminescence measurements has been widely invoked to investigate electron-electron correlation in the QHE regime, however, measurements to probe the spin-gap enhancement are rather sporadic [119, 122].

Here, we show that the enhancement of the spin splitting is not only a property of spin excitations at the Fermi level, but that it is also relevant for fully occupied spin Landau levels, located well below the Fermi energy. We have measured the many body contribution to the spin gap for fully populated spin Landau levels over a wide range of filling factors and temperatures, and show that it is driven by Coulomb interaction, apparent via the spin polarization of the investigated 2DEG with its relatively large bare Zeeman splitting.

In the following paragraph, we first point out the main advantages of a 2DEG embedded in CdTe-based heterostructures with respect to the most studied heterostructures based on III-V semiconductor, GaAs. The increasingly high quality of GaAs/GaAlAs structures has been driving advances in the physics of interacting 2D electrons last three decades. Notably, 2D electrons in a GaAs matrix are characterized by a relatively small bare g factor (-0.44) and therefore by a small value of the interaction parameter $\eta = E_z/\mathcal{D}$, where $E_z = g\mu_B B$, $\mathcal{D} = e^2/\epsilon l_B$, and, $l_B = \sqrt{\hbar/eB}$ is the magnetic length. The small value of η is responsible for the rich physics exhibited by interacting 2D electrons in the QHE regime, for example the occurrence of competing spin polarized/unpolarized many body ground states [84] or Skyrmion-type spin texture excitations [123, 124, 125]. However, this complex physics often masks the appearance of simpler and basic many body effects, which should emerge more clearly when η is sufficiently large. Disorder is an additional source of complications in ascertaining the spin polarization in systems with small g factors. While

high electron mobilities are obviously advantageous, GaAs-based structures are also rather fragile, displaying, for example, metastable effects upon illumination, with an associated decrease in mobility and homogeneity, which frequently prevents the simultaneous basic characterization of such structures using magneto-optics and magneto-transport. A 2DEG in a CdTe matrix [126], used in our experiments, is characterized by relatively large (bare) g factor (-1.6) and the η -parameter in this system exceeds by a factor of ≈ 3 its value in GaAs structures (the dielectric screening $\epsilon = 9$ is slightly less efficient in CdTe). CdTe, which has a conduction band as simple as the one in GaAs, appears at the present time to be an almost ideal model system to study the QHE physics of the primary spin-polarized states.

7.3.2 Samples

In order to have a comparison of the spin gap enhancement obtained by means of magneto-PL with the one derived from usually employed techniques of activated magneto-transport, it was crucial to measure both magneto-PL and magneto-transport simultaneously. However, this was difficult in the case of 30 nm wide CdTe QW, where the correlation between both experiments was very poor. Therefore we have focused our interest on the 20 nm wide CdTe QW, for which the magneto-PL and magneto-transport data were well correlated. Experiments have been carried out using either a $^3\text{He}/^4\text{He}$ dilution refrigerator or a variable temperature ^4He cryostat, in magnetic fields supplied by a resistive (28 T) or superconducting (11 T) magnets. A standard, low frequency (≈ 10 Hz) lock-in technique has been applied for the resistance measurements. Polarization resolved, σ^+ and σ^- photoluminescence (PL) spectra have been measured using a single 600 μm -diameter optical fiber to transmit the excitation beam (514 nm-line of Ar^+ laser) and to collect the photoluminescence signal for the spectrometer equipped with a nitrogen cooled CCD camera. Special attention has been paid to assure a low level of laser excitation ($\approx 50 \mu\text{W}/\text{cm}^2$), to precisely calibrate the magnetic field, and to measure the spectra at small intervals (down to 5 mT) of the magnetic field. Under our experimental conditions (continuous laser illumination), the 2DEG density of $\approx 4.5 \times 10^{11} \text{ cm}^{-2}$ and mobility of $\mu = 2.6 \times 10^5 \text{ cm}^2/\text{Vs}$ were well reproduced in different experimental runs.

7.3.3 Experimental results

The characteristic result of simultaneous magneto-PL and magneto-resistivity measurements of our sample are shown in Fig. 7.15. Magneto-PL spectra reflect typical Landau level fan chart in both circular polarizations and energy positions of PL emission exhibit commonly observed abrupt blue shifts at every integer filling factor, as has been already discussed in the introduction of this chapter. In transport, Fig. 7.15(b), the investigated 2DEG shows all typical attributes of the QHE in a system with fairly high mobility and relatively high electron concentration; well developed integer QHE states and the appearance of 5/3, 4/3 and 2/3 fractional states, which are discussed in chapter 6.1. Good correlation between abrupt changes in energy positions of PL emission, plateaux in Hall resistance and minima in longitudinal resistance can be clearly seen in Fig. 7.15. In the chapter 6.1 we have presented the detailed quantitative analysis of low-field magneto-transport (also shown in Fig. 7.15 (e)) and a Dingle analysis of the SdH oscillations gave a quantum lifetime

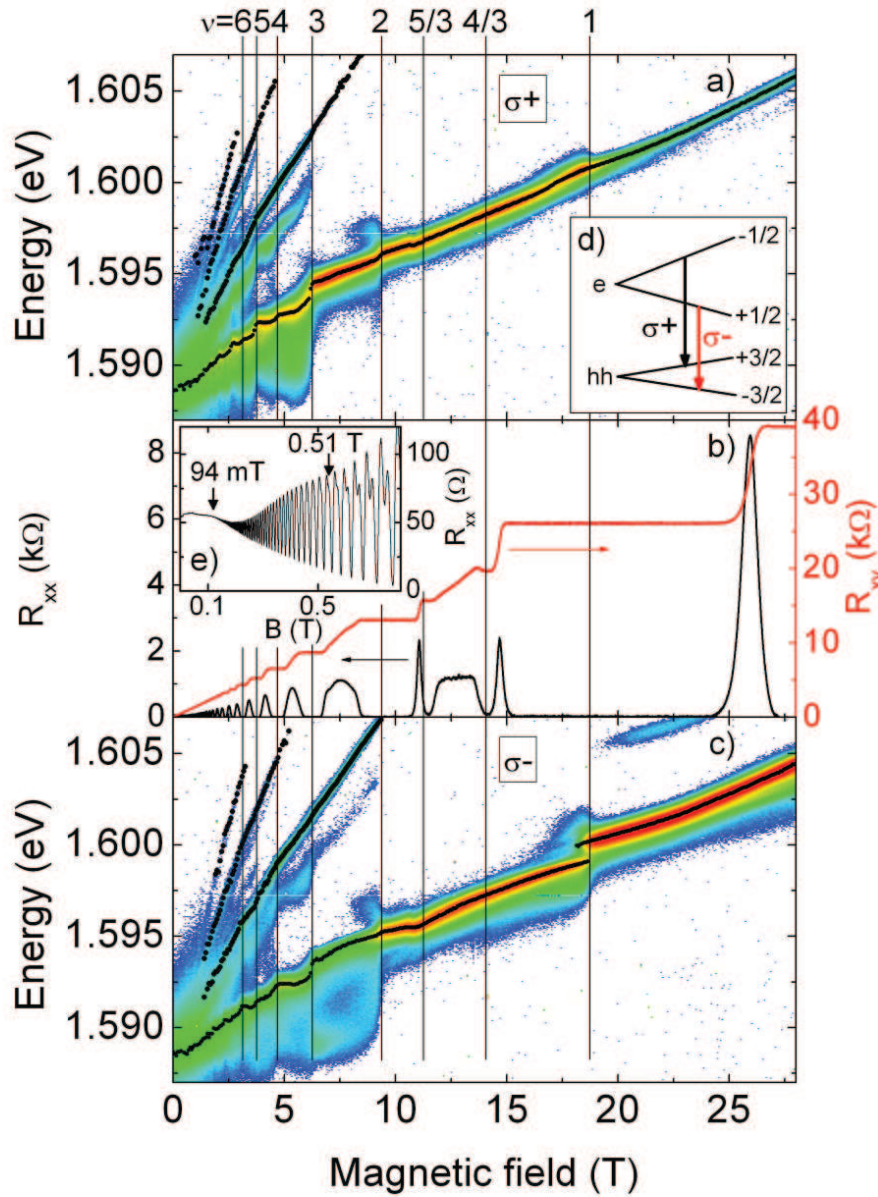


Figure 7.15: (a) and (c) Color plot of σ^+ and σ^- magneto-PL of a 2DEG in a 20 nm wide CdTe QW, measured at 80 mK, under low power ($\approx 0.5\text{W}/\text{m}^2$), $\lambda = 514\text{ nm}$ -Ar $^+$ excitation. Black points indicate the energy of the main peaks. Inset (d) shows the the optical selection rules. (b) Results of the simultaneous magneto-transport measurements showing the longitudinal (R_{xx}) and Hall (R_{xy}) resistance. Vertical lines indicate the Landau level filling factor. Inset (e) shows an expanded view of R_{xx} at low magnetic fields.

$\tau_q = \hbar/2\Gamma = (3.0 \pm 0.3)\text{ ps}$ (broadening of Lorentzian Landau levels $\Gamma \approx 110\text{ }\mu\text{eV}$) as compared to the transport lifetime $\tau_\tau \approx 15\text{ ps}$ (derived from the measured mobility). From the

field at which the Shubnikov de Haas (SdH) oscillations ($B_1 \approx 94$ mT), and spin-splitting appears ($B_2 \approx 0.51$ T), we obtain a first estimate of the enhanced g factor, $g^* \approx 3.7$ using the condition ($\hbar e B_1 / m^* \approx g^* \mu_B B_2$) where the electron effective mass $m^* = 0.1 m_e$ was derived from cyclotron resonance absorption measured on a parent sample. As has been already mentioned, although the description of the absolute energy position of PL emission in a given polarization is far from being universal [106, 107, 105, 108], we have found, however, that information on the effects of electron-electron interactions can be relatively simply extracted from the relative positions of polarization-resolved PL peaks arising from different LL spin components.

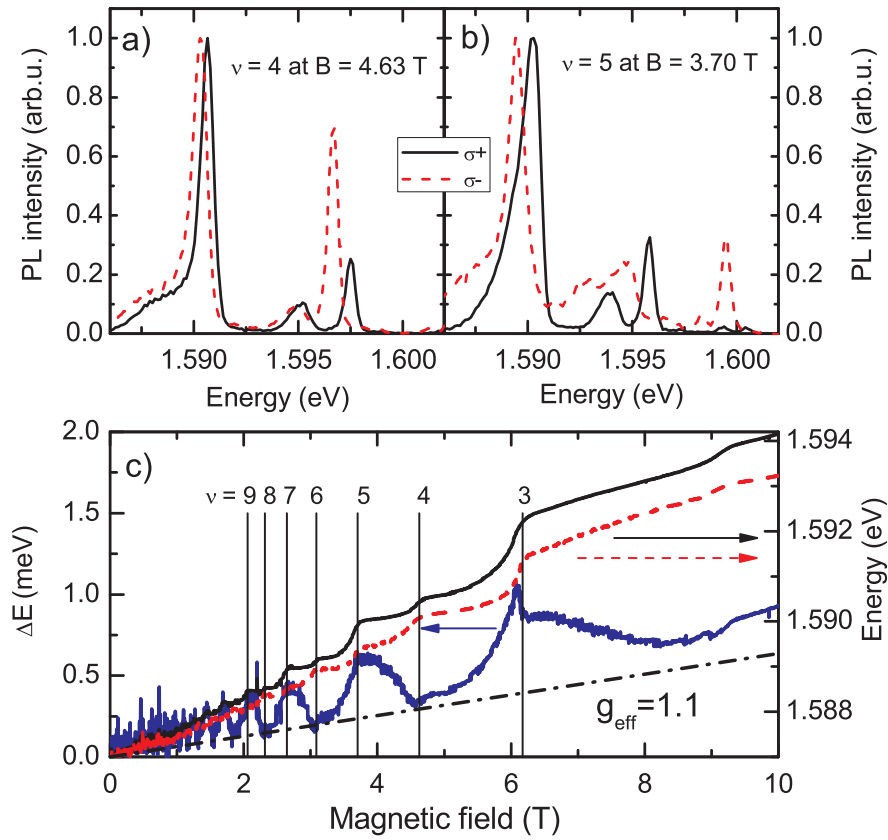


Figure 7.16: Normalized σ^+ (black curves) and σ^- (red curves) PL spectra at magnetic fields corresponding to filling factors $\nu = 4$ (a) and $\nu = 5$ (b) ($T = 80$ mK, $E_{\text{exc}} = 2.41$ eV, $P_{\text{exc}} = 0.5$ W/m²). (c) Field evolution of the energy of PL emission in σ^+ (solid black curve) and σ^- (dashed red curve) circular polarization. Difference is shown by blue curve and contribution of the bare Zeeman splitting is depicted by black dashed dotted line with the label $|g_{\text{eff}}| = 1.1$ of an effective g -factor of electrons and holes.

7.3.4 Spin splitting of fully populated Landau levels

We concentrate on the energy positions of σ^+ and σ^- magneto-PL transitions (Fig. 7.15) which are, beside $3 - 5\times$ smaller contribution of holes⁶, mainly due to electrons, with different spins, recombining from the fully populated lowest lying LLs (L_0, L_1, L_2, L_3). While the energy of each of these peaks displays a non-trivial dependence on the magnetic field, here we analyze the evolution of the energy separation ΔE between the σ^+ and σ^- transitions. The effect of SGE is apparent already in a raw data, as can be seen in Fig. 7.16 (a) and (b). Total spin splitting at LL L_0 is bigger at smaller magnetic field (3.70 T) than at higher magnetic field (4.63 T). The field evolution of both energy of PL emission from LL L_0 in σ^+ polarization E_{σ^+} (solid black curve) and in σ^- polarization E_{σ^-} (red dashed curve) are plotted in Fig. 7.16 (c). The difference of these two quantities ($E_{\sigma^+} - E_{\sigma^-}$) gives the total spin gap as a function of magnetic field at $T = 80$ K as is shown in Fig. 7.16 (c) (blue curve). Two contributions to the field dependence of spin gap ΔE are apparent. Linear background (dashed dotted black line in Fig. 7.16 (c)) is attributed to the single particle Zeeman energy (ΔE_Z) and non-monotonic oscillatory part ($\Delta E_{\uparrow\downarrow}$) is assigned to the many body effects. Many-body oscillatory part has maxima at odd integer filling factors ν and zeros at even integer filling factors. The linear term can be extracted from the splitting at even integer ν and it is in agreement with the ordinary Zeeman effect expected in our structure. Taking into account the selection rules depicted in inset (d) of a Fig. 7.15, the splitting $\Delta E_Z = (|g| - |g_h|)\mu_B B = g_{eff}\mu_B B$, which requires $g_{eff} = 1.1$ to fit the data in agreement with the reported values of $g = -1.6$ and $g_h \approx 0.5$, for electronic and valence hole g factors in CdTe QWs [127]. Temperature dependence in Fig. 7.17 further shows, that bare Zeeman splitting does not change considerably with temperature. On the other hand, the enhanced part $\Delta E_{\uparrow\downarrow}$ totally disappears at high temperatures. Moreover, disappearing of spin gap enhancement is faster at lower magnetic fields. So far, we have discussed the behavior of SGE in the lowest lying LL, L_0 . The analysis of energy positions of PL emission from higher LLs (L_1, L_2, L_3) allows us to determine the dependence of the SGE on the index N of LL, see Fig. 7.18. Spin gap enhanced part is plotted as a function of the filling factor. We note, that filling factor was changed by magnetic field in our samples. Electron sheet concentration was determined using simultaneous magneto-resistance measurements and it was found to be constant during all experiments presented here ($n_e = 4.5 \times 10^{11} \text{ cm}^{-2}$). Filling factor ν and magnetic field B are then in direct relation; $\nu = B_{\nu=1}/B$, where $B_{\nu=1} = 18.5$ T is the magnetic field at the filling factor $\nu = 1$. In Fig. 7.18 we present only many-body contribution $\Delta E_{\uparrow\downarrow}$ to the total spin splitting for four lowest lying Landau levels (L_0, L_1, L_2 and L_3). The data has been measured at base temperature of 80 mK and they clearly show, that spin gap enhancement $\Delta E_{\uparrow\downarrow}$ is of the same amplitude for all experimentally attainable Landau levels.

7.3.5 Data modelling

Results presented in Fig. 7.17 and Fig. 7.18 suggest that $\Delta E_{\uparrow\downarrow}$ is ruled by the spin polarization $\mathcal{P} = \frac{n_{\downarrow} - n_{\uparrow}}{n_{\downarrow} + n_{\uparrow}}$ of the 2DEG. The same assumption comes from first-principle calculations of SGE [112, 113, 114]. Many-body contribution is then given by $\Delta E_{\uparrow\downarrow} = E_{\Delta} \frac{n_{\downarrow} - n_{\uparrow}}{n_{\downarrow} + n_{\uparrow}}$. Pre-

⁶Ratio of the effective mass of holes and electrons $m_h/m_e \approx 3 - 5$, therefore the energy position of the PL emission is driven mainly by the electrons.

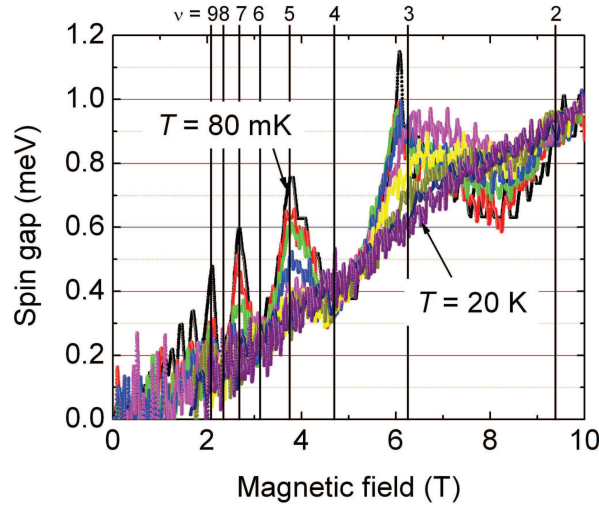


Figure 7.17: Total spin gap as a function of magnetic field for several temperatures. The lowest (80 mK) and the highest (20 K) temperatures are marked by arrows and labels.

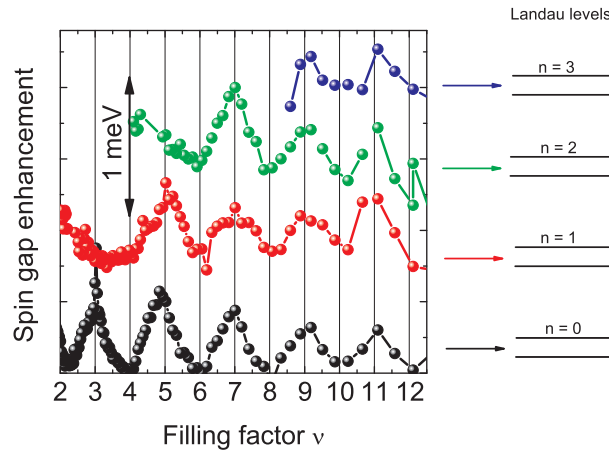


Figure 7.18: Enhanced (many-body) part of the total spin splitting as a function of the filling factor. Enhanced part was extracted from the PL emission of LLs $N = 0, 1, 2, 3$ (black, red, green and blue curve) at base temperature of 80 mK.

factor E_{Δ} is expected to depend on magnetic field as \sqrt{B} in high field limit and it should be constant when field approaches zero⁷. Both low- and high-field limits of the pre-factor E_{Δ} are plotted in Fig. 7.19. Since our data are in wide range of magnetic fields, we consider, that E_{Δ} depends on magnetic field as $\sqrt[4]{B^2 + B_0^2}$. This semi-phenomenological field

⁷Coulomb interaction scales with the inverse value of the magnetic length at high fields [114, 115, 28] but rather with the inverse of the mean inter-electron distance when B tends to zero [113, 110, 114].

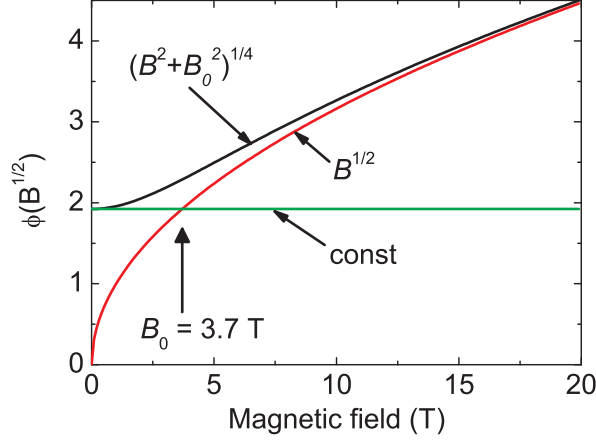


Figure 7.19: Low-field (green curve) and high-field (red curve) limit of magnetic field dependence of the pre-factor $\phi(B)$. Black curve given by field dependence $\phi(B) = \sqrt[4]{B^2 + B_0^2}$ phenomenologically joins both low- and high-field limits.

dependence is plotted in Fig. 7.19 as a black curve and it joins both low- and high-field limits of E_Δ behavior. The last element to describe the total spin gap is the scaling of many-body contribution $\Delta E_{\uparrow\downarrow}$ and its possible dependence on the index N of LL. As shown in a data, see Fig. 7.18, SGE is of the same amplitude for 4 lowest lying LLs, therefore we assume/extrapolate, that SGE is of the same amplitude for all LLs up to the LL in the vicinity of the Fermi energy. To sum up, we can write the resulting expression for total spin splitting ΔE as:

$$\Delta E = |g|\mu_B B + \Delta E_{\uparrow\downarrow} = |g|\mu_B B + \Delta'_0 \varphi(B) \cdot \frac{n_\downarrow - n_\uparrow}{n_\downarrow + n_\uparrow}. \quad (7.19)$$

In the equation (7.19), the parameter Δ'_0 is the scaling of the SGE amplitude and the function $\varphi(B) = \sqrt[4]{B^2 + B_0^2}$ denotes phenomenologically the field dependence of the pre-factor E_Δ . To compare the suggested model with the experiment, we need to calculate concentration of electrons with spin up (n_\uparrow) and down (n_\downarrow). These quantities are generally given by integral of density of states $G(E, B)$ and Fermi-Dirac distribution $n_{FD}(E, E_F)$, $n_{\downarrow(\uparrow)} = \int G^{\downarrow(\uparrow)}(E, B) n_{FD}(E, E_F) dE$. Since broadening of LLs ($\Gamma \approx 110 \mu\text{eV}$, from low-field magneto-transport analysis) is smaller than spin gap even at the lowest magnetic field of 2 T ($g_e \mu_B B|_{2\text{ T}} = 190 \mu\text{eV}$), we neglect overlap of LLs and density of states can be replaced in such a case by a sum of δ -functions. This leads to set of equations (7.20) and (7.21),

$$n_{\downarrow(\uparrow)} = \frac{eB}{h} \sum_{N=0}^{\infty} n_{FD}(E_{N,s=\downarrow(\uparrow)}, E_F) \quad (7.20)$$

$$n_e = n_\downarrow + n_\uparrow \quad (7.21)$$

where equation (7.21) is to preserve constant electron concentration $n_e = 4.5 \times 10^{11} \text{ cm}^{-2}$ and $E_{N,s=\downarrow(\uparrow)} = \hbar\omega_c(N + 1/2) + s|g|\mu_B B + s\Delta'_0 \sqrt[4]{B^2 + B_0^2} \cdot \frac{n_\downarrow - n_\uparrow}{n_\downarrow + n_\uparrow}$ is the energy position

of the Landau level L_N with a spin s . Finally, we self-consistently calculate $\Delta E_{\uparrow\downarrow}$ (and \mathcal{P}) and obtain agreement with the data, see Fig. 7.20 and 7.21, by adjusting the two fitting parameters, $\Delta_0 = \Delta'_0 \sqrt{B_0} = 2.1$ meV and $B_0 = 3.7$ T.

7.3.6 Discussion

In spite of the fact that we have assumed many approximations, our model describes experimental data fairly well in wide range of magnetic fields (2-10 T) and temperatures (80 mK-20 K), see Fig. 7.20 and Fig. 7.21. Temperature range covers two important limits; a) low-temperature limit, when temperature has no influence on the polarization of 2DEG ($k_B T \ll \Delta E$) and b) high-temperature limit, when polarization (and SGE) tends to zero ($k_B T \gg \Delta E$). The discrepancy at the filling factors $\nu = 3$ (and $\nu = 1$) is due to more complex [105] recombination processes, which cannot be explained by our simplified model of looking at the electron-hole recombination as a process of adding/removing electron into/out from the 2DEG. Proper treatment of these filling factors should consider final-state interactions, final-state excitations and their dispersion relations. However this approach is more correct, such calculations are neither disposable these days for arbitrary filling factor, magnetic field and temperature nor they are in the scope of our simplified approach. We guess that our simplification might be well justified in the limit of low magnetic fields, when $\beta = \frac{\hbar\omega_c}{e^2/\epsilon l_B} < 1$ (in CdTe QWs: $\beta = 1$ at $B \approx 30$ T) and at high electron concentrations (high filling factors). On the other hand, for the dilute systems and at high magnetic fields, a more appropriate picture of the PL process consists of considering the recombination between the interband magneto-excitons in the initial state and spin or charge excitation of a 2DEG in the final state [128, 107, 129, 130, 131, 105, 132]. Considering this approximation, we expect the same behavior at even filling factors, when polarization of 2DEG vanishes. But, the analysis of σ^+ and σ^- PL will be more complex in the vicinity of low odd filling factors (e.g., $\nu = 1, 3$). This alternative approach might be more appropriate for GaAs-based structures, for which the high field limit is reached at lower magnetic fields (in GaAs QWs $\beta = 1$ at $B = 8$ T). It should be emphasized, that in this sense CdTe-based QWs are quite unique and more suitable for SGE studies rather than GaAs-based QWs. In this study, we are in the regime of the field-strength parameter $\beta = (0.36 - 0.57) \text{ T}^{1/2}$. To reach the same field regime in GaAs heterostructures, one has to work in the magnetic fields from 1 to 3 T and electron sheet concentration has to be of about $1 \times 10^{11} \text{ cm}^{-2}$ (to study the same range of filling factors from 2 to 10 as in this presented work). Although the quality of GaAs QWs is high these days, it will be still very difficult to observe well separated LLs in magnetic fields as low as 1 T.

The assumption that SGE does not depend on the index N of LL is based on three distinct findings. (a) We have already discussed experimental data (Fig. 7.18) and the analysis of SGE at high LLs. (b) Supplementary measurements of the activation energy deduced from thermally activated magneto-resistance show (within an experimental error) the same values of the total spin splitting at odd filling factors $\nu = 5, 7, 9$ as the values obtained from our magneto-optical data, see Fig. 7.17 and Fig. 7.22. Since magneto-transport probes vicinity of the Fermi energy and magneto-PL probes lowest lying LLs, we conclude on the constant SGE within all LLs. (c) Our model, even though we analyse only lowest lying LLs, depends on the total spin splitting of LLs in the vicinity of the Fermi energy. The smaller spin splitting at the Fermi energy E_F is, the faster and sooner it disappears with

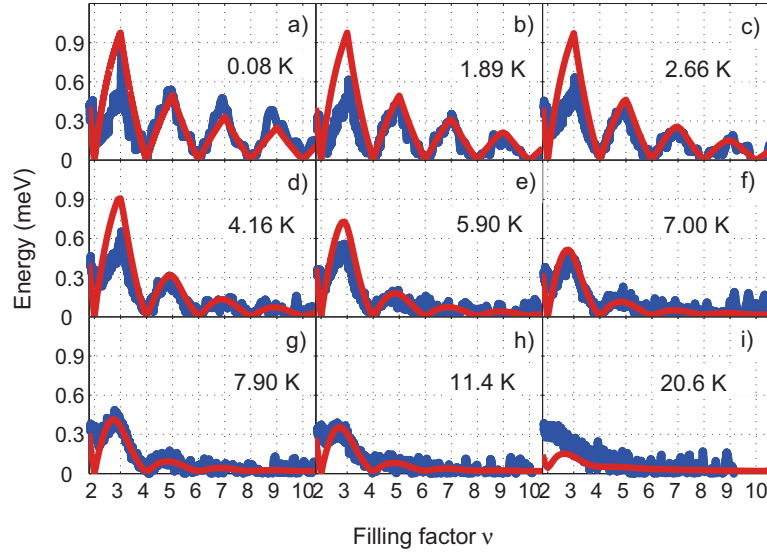


Figure 7.20: Enhanced part of the total spin gap as a function of the filling factor for temperatures a) 80 mK, b) 1.89 K, c) 2.66 K, d) 4.16 K, e) 5.90 K, f) 7.00 K, g) 7.90 K, h) 11.4 K and i) 20.6 K. Experimental data are plotted by black points and self-consistent model of SGE is plotted by red curves. Data correspond to spin gap enhancement extracted from PL emission from $N = 0$ Landau level. Spin gap enhanced part was obtained from total spin splitting subtracting temperature independent Zeeman splitting with effective g -factor 1.1.

increasing temperature. We have tested various scenarios of SGE dependence on the LL index N , but the constant dependence was found to be the most suitable. We should note here, that this conclusion, even though according to us correct, is in disagreement with a work of Dial [122], who has found that SGE has decreasing amplitude with increasing N . We speculate about physical meaning of such a conclusion and about explanation given by Dial [122]. We guess this tendency is given mainly by incorrect energy calibration in tunnelling or scanning tunnelling spectroscopy (STS) experiments. Many of the spectrally resolved data obtained by these experiments exhibit similar effect of energy spectra distortion, see for example [133, 134, 135], and therefore we guess that tunnelling spectroscopy can give wrong energy dependence of SGE in 2DEG or, also for example, different Fermi velocity in graphene samples [136, 137].

Physical meaning of the two fitting parameters Δ_0 and B_0 is the following. The parameter $\Delta_0 = 2.1$ meV scales the amplitude of SGE and it takes into account effectively all the phenomena which reduce many-body electron-electron interaction (finite quantum well width, disorder, etc.). Magnetic field $B_0 = 3.7$ T denotes the intermediate region of magnetic fields where low-field limit of the pre-factor E_Δ , see equation (7.19), switches into the high-field limit, see also Fig. 7.19. There is, according to our estimates, a non-trivial connection between magnetic field (B_0) and Landau level broadening Γ .

We discuss also two limiting cases of our model. Low field limit ($B \rightarrow 0$) and magnetic fields around filling factor $\nu = 1$. When magnetic field tends to zero (in the limit of $T = 0$ K), equation (7.19) for total spin gap becomes linear in field; $E_\Delta = |g|\mu_B B + \Delta_0/\nu =$

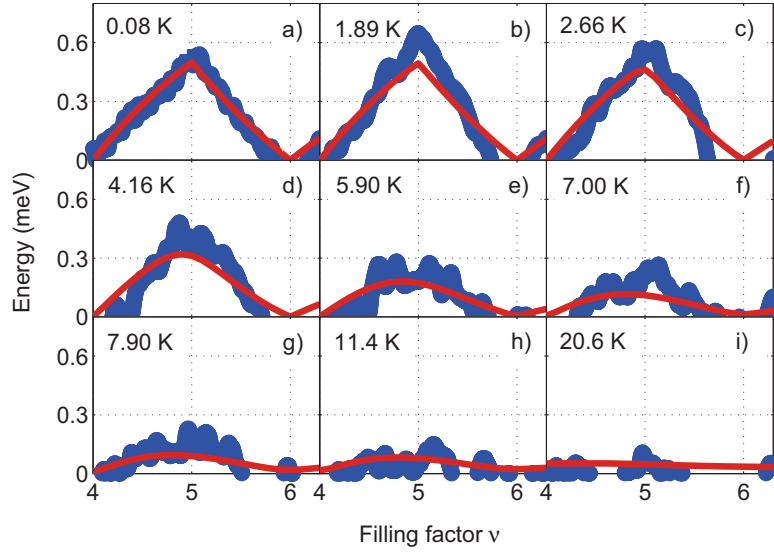


Figure 7.21: The same as Fig. 7.20, but the SGE corresponds to $N = 1$ Landau level.

$(|g| + \Delta_0/\mu_B B_{\nu=1})\mu_B B = g^* \mu_B B$, where $B_{\nu=1}$ is the magnetic field for $\nu = 1$. With $B_{\nu=1} = 18.5$ T ($n = 4.5 \times 10^{11}$ cm $^{-2}$) and $\Delta_0 = 2.1$ meV we extract $g^* = 3.6$ for the enhanced g factor in good agreement with the estimation of $g^* \sim 3.7$ from the low field onset of spin splitting in the SdH oscillations in magneto-resistivity measurements. Limit around filling factor $\nu = 1$ is more discussible and difficulties at this low filling factor were already sketched. However, a quantitative comparison with GaAs will be carried out here. At the filling factor $\nu = 1$, the polarization of the 2DEG is $\mathcal{P} = 1$ and we can extrapolate in Eq. (7.19) $E_\Delta = |g|\mu_B B + \Delta_0 \sqrt{1 + B_{\nu=1}^2/B_0^2}$ and calculate $E_\Delta = 6.4$ meV. This value is $\sim 4\times$ smaller than its limit of $\sqrt{\pi/2}e^2/\epsilon l_B$ [115, 28] but in good agreement with the reported values in GaAs structures from optical and capacitance measurements [120, 116].

Final note will be dedicated to the magneto-optical experimental method itself. We would like to emphasize here, that in contrast to usually employed thermodynamical probes, method of magneto-PL is capable to directly measure spin gap at arbitrary magnetic field (filling factor) and temperature. This is in contrast to, for example, magneto-transport activation energy experiments, where spin gap determination is restricted to only integer filling factors and wide range of temperatures necessary to deduce spin gap automatically embarrasses spin gap determination as a function of temperature, hence, assumptions about temperature independent spin gap are usually considered. This assumption need not to be necessarily fulfilled, as has been shown in the presented study.

7.3.7 Conclusions

To conclude, we have employed spectroscopic polarization-resolved magneto-PL technique to study two-dimensional electron gas confined in CdTe quantum well. Clear many-body electron-electron contributions to the spin splitting of the fully occupied two-dimensional

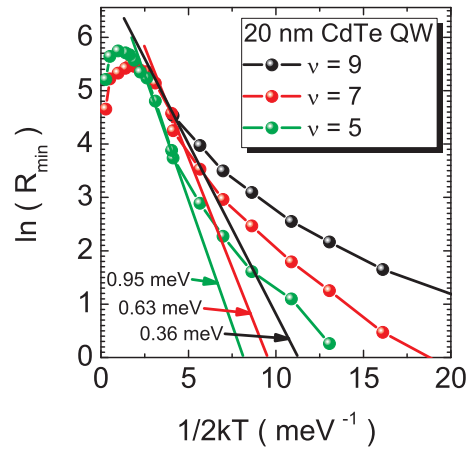


Figure 7.22: Arrhenius plot to extract activation gap at odd filling factors $\nu = 5, 7, 9$ (black, red and green curve). Corresponding slopes and extracted activation energies are 0.95 meV, 0.63 meV and 0.36 meV.

Landau levels are revealed. These many-body contributions, which express themselves as a spin gap enhancement at odd filling factors, are mainly driven by the spin polarization of the two-dimensional gas, since it is maximized at odd filling factors and vanishes at even filling factors and high temperatures. We conclude, that at every odd filling factor (and its surroundings), a whole ladder of fully occupied Landau levels undergoes rigid shift up- or downwards (depending on the electron spin state). This simple picture of the many body spin-gap enhancement emerges from magneto-PL studies of a 2DEG with relatively large (single particle) g -factor.

7.4 Intensity changes of PL

7.4.1 Introduction

Intensity of the photo-luminescence carries a wide spectrum of information on the properties of energy levels and on optically active transitions in semiconductor heterostructures. In the chapter 7.1 we have shown description of the spectral properties of PL emission at zero magnetic field. Here we focus on the modulations of the intensity of PL emission as a function of magnetic field.

7.4.2 Relative strength of the radiative and non-radiative recombination channel

Modulation of the PL intensity can have many reasons. As a first point, it carries an information on mutual strengths of radiative and non-radiative electron-hole recombination channels [138]. It is convenient to define the PL efficiency $\eta_q = p_r / (p_r + p_{nr})$ as a ratio of the probability of the radiative recombination p_r and the total probability of recombination. The later is given by the sum of the probability of the radiative p_r and non-radiative

p_{nr} recombination. Intensity of the radiative recombination I_r is thus related to the intensity of the excitation I_{exc} by the PL efficiency; $I_r = \eta_q I_{exc}$. If the radiative channel is much stronger than the non-radiative one ($p_r \gg p_{nr}$), then the PL efficiency $\eta_q \rightarrow 1$ is close to 1 and the intensity of the radiative recombination will be given only by the intensity of the excitation I_{exc} and therefore no intensity changes of PL can be observed in such a case (unless the intensity of the excitation I_{exc} changes). However, if the non-radiative recombination channel is dominant over the radiative one ($p_{nr} \gg p_r$), then the PL efficiency can be approximated as $\eta_q \approx p_r/p_{nr}$ and intensity I_r is $I_r = \eta_q I_{exc} \approx p_r/p_{nr} I_{exc}$. In this case, if the probability of the radiative (p_r) or non-radiative (p_{nr}) recombination changes, it will be reflected in the intensity of PL emission in spite of the fact that the intensity of the excitation is constant ($I_{exc} = \text{const.}$).

We present the total intensity of PL emission in Fig. 7.23. The data clearly show the evolution of the intensity of the PL emission as a function of magnetic field, therefore we conclude that the non-radiative channel of recombination is dominant in our QWs.

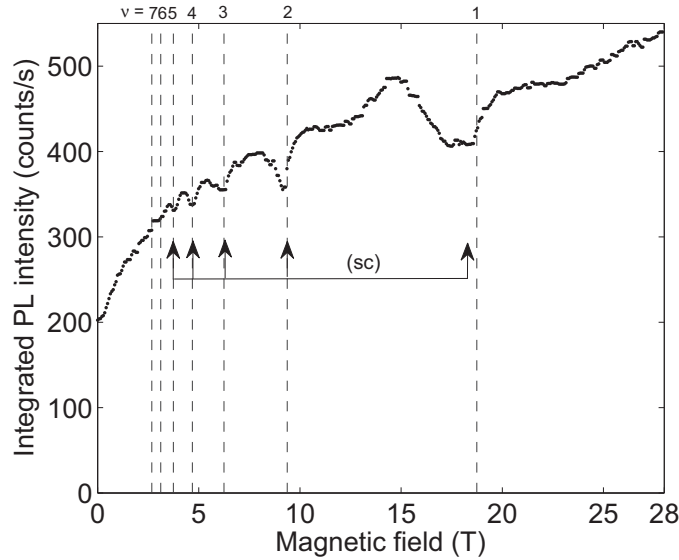


Figure 7.23: Integrated intensity of the PL emission in 20 nm wide CdTe QW (sum of the PL intensity in σ^+ and σ^- polarization). Data measured at the temperature of 80 mK. Excitation by Ar^+ laser line at $E_{exc} = 2.41$ eV. Labels (sc) denote minima of the total intensity at integer filling factors (effects of the oscillatory efficiency of screening). Integer filling factors depicted by dashed vertical lines.

7.4.3 Effect of occupancy, degeneracy and selection rules

We present the polarization resolved integrated PL intensity from the Landau level $N = 0$ in the Fig. 7.24. The field dependence reveals the increase of the PL intensity in the low field regime, labelled (i) for both circular polarizations in the Fig. 7.24. This is a manifestation of increasing degeneracy of the Landau levels in magnetic field. Increasing degeneracy in the fully occupied Landau level means linearly increasing concentration of electrons and therefore increasing intensity of PL. However, the intensity of the PL in σ^-

polarization stays soon almost unchanged, interval labelled (ii). This is due to the interplay of still increasing electron concentration in the electronic LL $N_e = 0$ and decreasing concentration of holes $j_z = -3/2$ in the hole LL $N_h = 0$. Decreasing concentration of holes $|N_h, j_z\rangle = |0, -3/2\rangle$ is due to the small concentration of photo-excited carriers and spin splitting of hole Landau levels. At high magnetic fields, holes tend to occupy only the lowest energy hole level $|0, +3/2\rangle$, which is at the expense of the occupation of the hole state $|0, -3/2\rangle$, responsible for the intensity of the PL in σ^- polarization. The region of high magnetic fields above filling factor $\nu = 1$ (label (iii)) is a manifestation of the selection rules in CdTe. At filling factors smaller than 1, the electronic LL $|0, -1/2\rangle$ gets empty, therefore only the PL in σ^- polarization remains. The schematic drawing of this phenomenon in CdTe is presented in Fig. 7.25. The PL intensity at intermediate magnetic fields between filling factors $\nu = 2$ and $\nu = 1$ are influence by both low- and high-field mechanisms (as discussed above) and they can not be easily separated here. The intensity minima and maxima are in this range of filling factors probably due to the

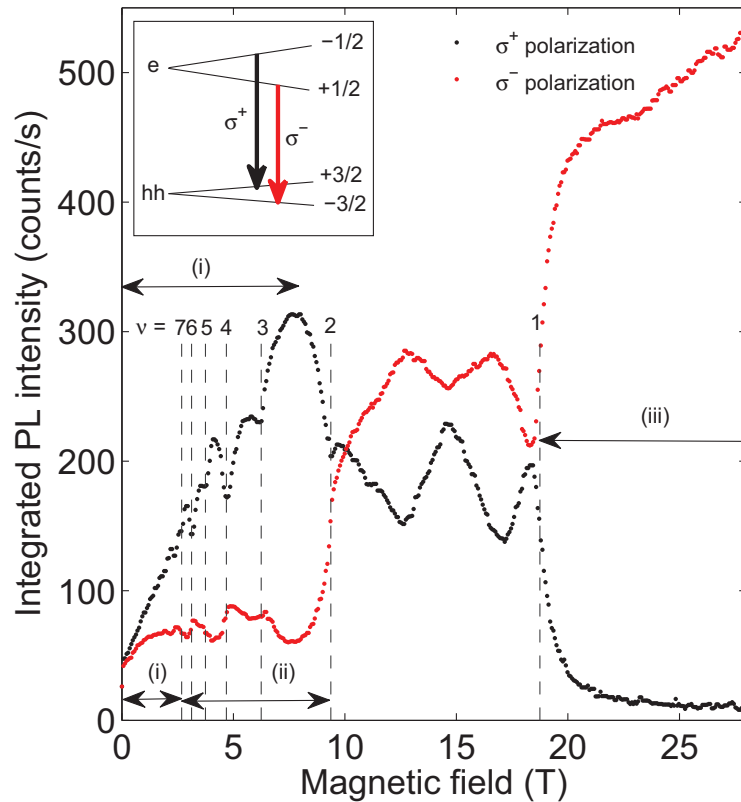


Figure 7.24: Integrated intensity of PL from Landau level $N = 0$ in σ^+ (black points) and σ^- (red points) circular polarization. Data measured in 20 nm wide CdTe QW at the temperature of 80 mK. Excitation by Ar^+ laser line at $E_{exc} = 2.41$ eV. Following labels denote the characteristic field evolution of the intensity of PL discussed in the text: (i) - increase of the intensity in both σ^+ and σ^- polarization, label (ii) - interval of weak B -dependence of the intensity in σ^- polarization and (iii) - switching of the relative intensity of the PL in σ^+ and σ^- polarization. The inset depicts the selection rules in CdTe for inter-band transitions between electron and hole LLs.

FQHE. However, the detail study of this phenomenon will be presented elsewhere.

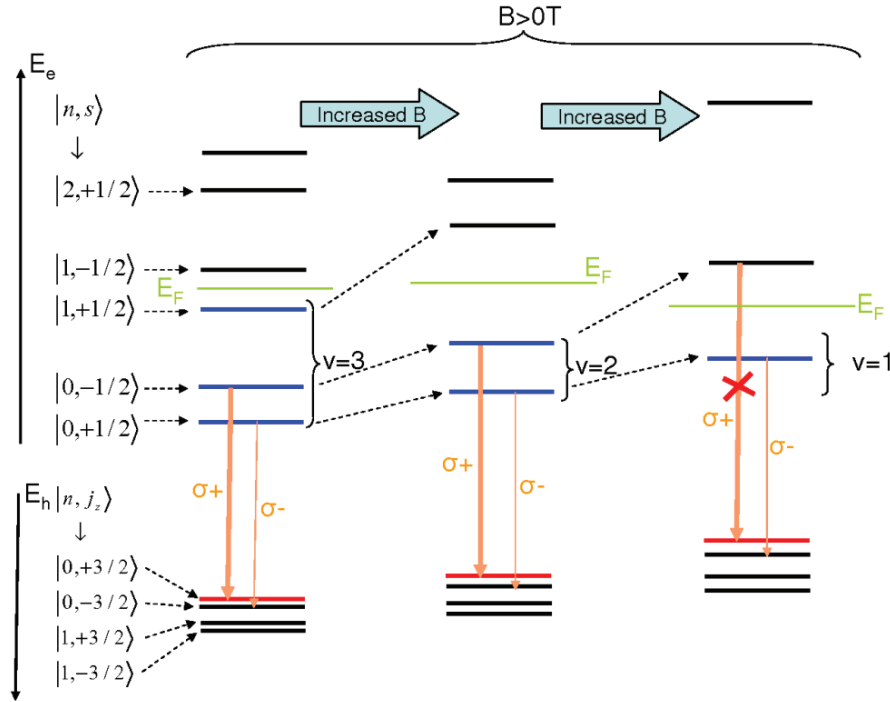


Figure 7.25: Scheme of electron and hole Landau levels for 3 gradually increasing magnetic fields (from left to right). Black and blue colored electron levels correspond to empty and occupied states, respectively. Concentration of holes is too small to fully occupy any hole Landau level in the range of considered magnetic fields, therefore we only marked by red color the hole Landau level which is the most occupied. Dipole allowed optical transitions are depicted by orange arrows and their mutual strength is shown by the thickness of the arrow. In spite of the fact that at the filling factor $\nu = 1$ the transition σ^+ is allowed, it is in fact very weak because there are no electrons on the LL $|0, -1/2\rangle$.

7.4.4 Screening

Another significant feature of the integrated PL intensity are sharp minima at every integer filling factor, labelled (sc) in Fig. 7.23 and minima in the integrated σ^+ PL having origin in the recombination from LL $N = 0$, black curve in Fig. 7.24.

These minima at integer filling factors are interpreted to be due to the oscillatory efficiency of the screening. Effect of the screening on the efficiency of the radiative emission in 2DEG was studied both theoretically [139] and experimentally [140, 121, 138]. The effect of screening acts differently on the various kinds of processes of electron-hole recombination. Depending on excitonic [141], acceptor related [139, 121], donor related [142, 143] or free-electron-free-hole [138] recombination, we can find different mechanisms of PL intensity modulations. Due to high electron concentration in our samples, we observe only free-electron-free-hole recombination. It was shown [138], that this type of recombination can be seen as a kind of acceptor-like recombination [139], where valence-band hole is not bound to acceptors (no acceptors are presented in our QWs) but it undergoes certain degree of localization. Such a localization can occur on, for example, quantum well width

fluctuations, lattice defects or on the random fluctuations of the electrostatic potential of positively charged donors. The fact that holes are weakly localized in magnetic field is not in contrast with our previous conclusion, in which we have stated that holes are free at zero magnetic field. The reason is that magnetic field squeezes hole wave function and it can cause field induced localization of holes. In such a case, if the screening of the electrons is efficient, the potential fluctuations are well smoothed out and hole wave function is spread across large area. If the screening of electrons is very poor, they feel deeper localization potential and wave function of holes is more squeezed and occupies smaller area. Since the probability of the radiative recombination of holes is proportional to the area over which holes are localized [138], it is apparent, that the more efficient screening the stronger radiative recombination. The screening is very efficient, if electrons have enough degrees of freedom to redistribute. Hence, screening is efficient when Fermi energy lies inside Landau level and it is inefficient, when Fermi energy lies in between of two well-separated LLs. In other words, when LLs are well separated then screening is weak at integer filling factors (Fermi energy lies between the two LLs) and this leads to the minima of the integrated PL intensity.

However, in the integrated intensity of σ^- PL from LL $N = 0$ we have observed maxima at integer filling factors, red curve in Fig. 7.24. These maxima are observed also in the PL emission (in both polarizations) from all higher Landau levels $N = \{1, 2, 3, \dots\}$, see Fig. 7.26. Explanation can be given in terms of intra-subband scattering where holes from $N_h = 0$ LL scatter due to unscreened scattering potential into higher LLs (of the same hole subband), thus enhancing radiative recombination [144, 145] from higher LLs at the expense of the σ^+ radiative recombination from the ground LL $N_h = 0$. Such scattering processes correlate with oscillations of the screening efficiency and therefore also with an integer filling factor. The experimental evidence of the intensity minima in σ^+ PL from LL $N = 0$ and maxima of the PL intensity from all higher LLs at integer filling factors reflects the presence of the strongest scattering channel of holes. The biggest amount of holes is therefore scattered from the ground LL of holes $|N_h, j_z\rangle = |0, +3/2\rangle$ into all LLs with higher energy.

7.4.5 Field-induced optical spin pumping

In the following part, we present mechanism, which manifests in a B -dependence of polarization resolved PL intensity from LL $N = 0$. The PL exhibits decrease (increase) of the intensity in σ^+ (σ^-) polarization in the intervals of filling factors labelled (I.) in Fig. 7.26. These filling factors are characterized by the presence of the Fermi energy of electrons in the LL $s = -1/2$ (the higher energy electron spin state in CdTe, see the left part of the scheme in Fig. 7.27).

In order to explain such a behavior, we make two assumptions. The first is that the photo-excited carriers are depolarized. Although the excitation light of the energy $E_{exc} = 2.41$ eV passes through polarizer and quarter wave plate, these are optimized for the energy of PL (≈ 1.6 eV), but they work poorly at the energy E_{exc} . In the case of small remaining polarization, the carriers will be efficiently depolarized during the thermalization process. During the thermalization, every electron has to lose more than 800 meV of energy ($E_{exc} = 2.41$ eV, $E_g \approx 1.6$ eV, $E_{exc} - E_g \approx 800$ meV), which usually goes along with an emission of acoustical and optical phonons. This energy relaxation

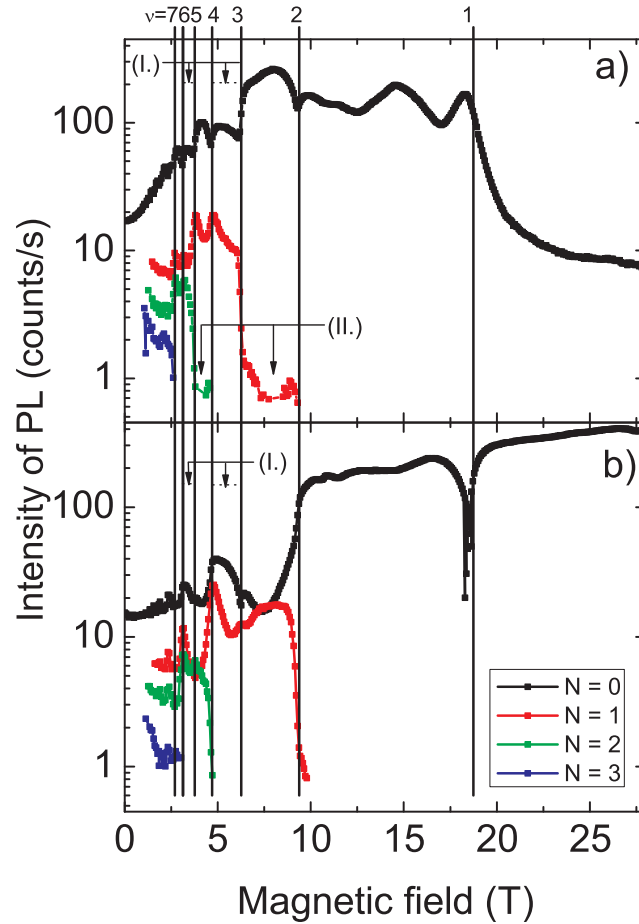


Figure 7.26: Intensity of the polarization resolved PL from the 20 nm wide CdTe/CdMgTe QW containing 2DEG of the electron sheet concentration $4.5 \times 10^{11} \text{ cm}^{-2}$. Data measured under the same conditions as in the Fig. 7.24. PL intensities in (a) σ^+ and (b) σ^- polarization. Vertical lines show positions of integer filling factors. Intensity of PL corresponding to the recombination of electrons and holes from LLs $N = 0, 1, 2, 3$ are depicted gradually by black, red, green and blue colors. Labels (I.) and (II.) denote the the intensity oscillations discussed in the text.

also tends to dissipate the initial spin polarization before the electrons relax down to the Fermi energy in the conduction band.

The second assumption is that the major changes of PL intensity are caused by the concentration of photo-excited holes in the valence band. This is because concentration of photo-excited electrons n_{ph} is at least three orders of magnitude smaller than the concentration of 2DEG n_e , therefore any change of the electron concentration by photo-excited electrons leads only to weak relative changes in PL intensity of the order of roughly $n_{ph}/n_e \approx 10^{-3}$. The observed increase (decrease) of the PL intensity in σ^- (σ^+) polarization is then interpreted as an increase (decrease) of the concentration of holes with angular momentum $j_z = -3/2$ ($j_z = +3/2$). In order to explain both experimental observations, we propose that holes undergo spin-flip $j_z = +3/2 \rightarrow j_z = -3/2$.

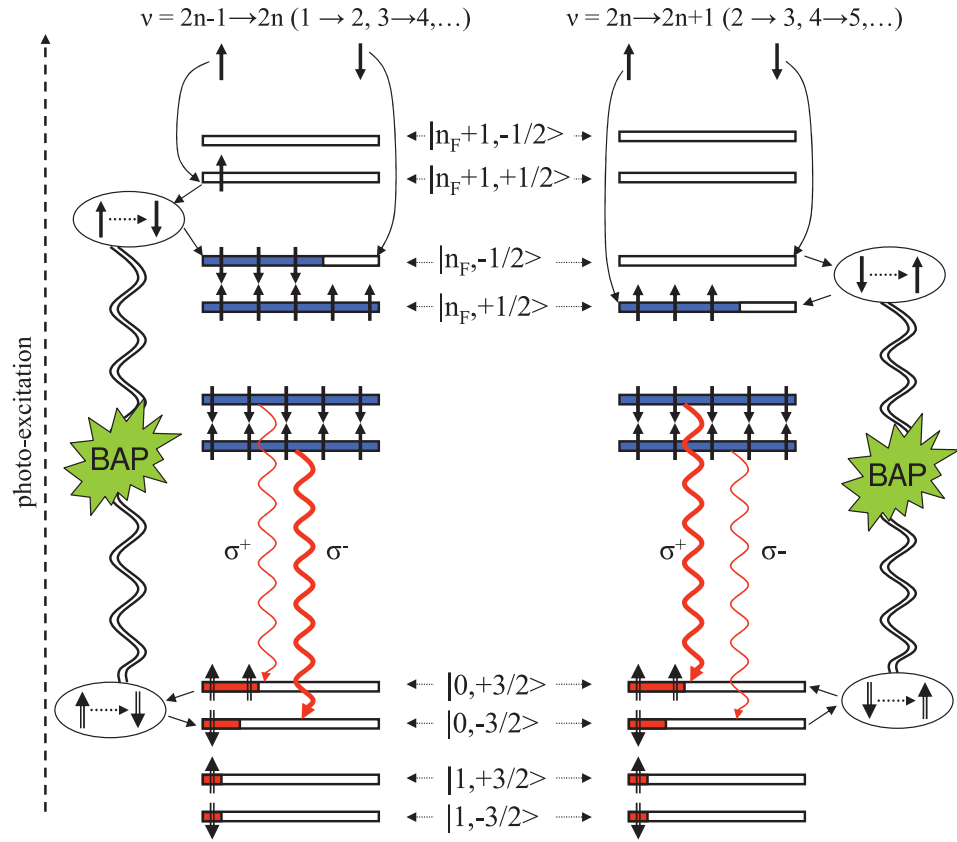


Figure 7.27: Schematic drawing illustrating mechanism of intensity modulations in the LL $N = 0$. When the Fermi energy lies within the electronic LL of a spin $s = -1/2$ ($s = +1/2$) see left scheme (right scheme), electron spin-flips $|+1/2\rangle \rightarrow |-1/2\rangle$ ($|-1/2\rangle \rightarrow |+1/2\rangle$) have to take place in order to get photo-excited electrons thermalized. These spin-flips of electrons go along with spin-flips of holes $|+3/2\rangle \rightarrow |-3/2\rangle$ ($|-3/2\rangle \rightarrow |+3/2\rangle$). The spin-flip processes depicted in the right part of the scheme are weak due inefficient energy relaxation caused by small density of phonon states. Dashed line on the left side shows photo-excitation of electrons of from the valence band high into a conduction band. Full(empty) electronic Landau levels are depicted by blue(white) rectangles. Partial occupation of hole levels is marked by red color. Suggested electronic transitions are shown by thin arrows and observed radiative transition (PL) is depicted by wavy red lines according to the selection rules in CdTe and their thickness correspond to intensity enhancement(thick line) or reduction(thin line) caused by simultaneous electron and hole spin-flip. Quantum number n_F denotes index of the Landau level where Fermi level lies.

At the same time, all the photo-excited unpolarized electrons have to relax on the lowest lying unoccupied or partially occupied LL. This is the LL where the Fermi energy is located. The spin state of this LL is $s = -1/2$, in the considered intervals of filling factors $\nu = 1 - 2, 3 - 4, 5 - 6, etc.$, labelled (I.) in the Fig. 7.26. Half of the unpolarized photo-excited electrons are already in the spin state $s = -1/2$, but the half of them is in the state $s = +1/2$. Therefore in order to get on the lowest partially occupied LL, they have to flip the spin. We have thus electronic spin-flip $s = +1/2 \rightarrow s = -1/2$, which goes along with the hole spin-flip $j_z = +3/2 \rightarrow j_z = -3/2$ and both are sketched schematically in the Fig. 7.27 (left part).

The mechanisms responsible for the simultaneous spin-flip of electrons and holes is the so called Bir-Aharonov-Pikus spin relaxation mechanism (BAP). The process of the spin flip of holes induced by the spin flip of electrons is analogy with so called Dynamical Nuclear Polarization (DNP) [146], where electrons interact with nuclei of the atom and the spin-flip of electrons is capable to induce spin-flip of nuclei. In our case, the spin polarization of electrons is not transferred to the polarization of nuclei, but to the polarization of holes, and thus changing intensity of magneto-PL.

7.4.6 Lattice relaxation

The presented mechanism of the simultaneous electron and holes spin-flip is active only if the electronic Fermi energy lies in the LL $s = -1/2$ (the higher energy spin state in CdTe), as we have sketched in the left part of the Fig. 7.27. The reason is the efficiency of the energy dissipation. The electron spin-flip $s = +1/2 \rightarrow s = -1/2$ is a relaxation across the cyclotron gap. The cyclotron gap is in CdTe $\approx 3.5-11$ meV in the range of magnetic fields 3-10 T. Such an energy can be dissipated by means of longitudinal acoustical phonons (LA-phonons) into the lattice, because there are many available phonon states in this range of energies, as can be seen in the density of phonon states in Fig. 7.28. On the other hand, the electron spin flip $s = -1/2 \rightarrow s = +1/2$ within LL N is a relaxation across the Zeeman gap, which is only 0.3-0.9 meV in the considered range of magnetic fields. Such an energy is difficult to dissipate by means of phonons, because there is only negligibly small density of phonon states, see Fig. 7.28. Because an angular momentum is not conserved during these phonon-assisted simultaneous spin-flip processes of electrons and holes, we assume that they are allowed due to the light-hole heavy-hole valence band mixing.

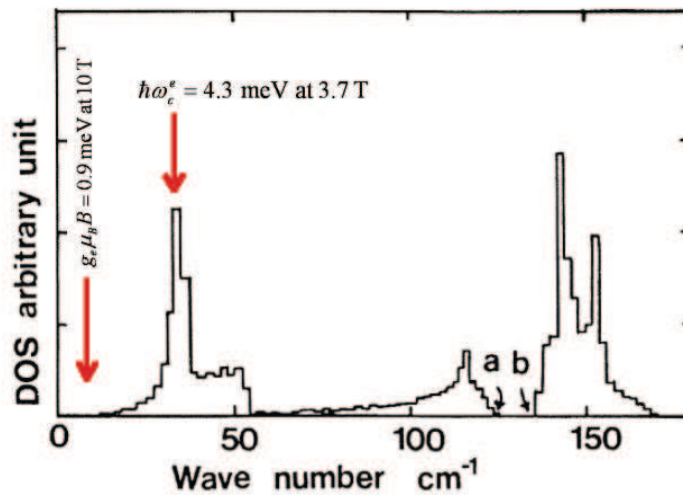


Figure 7.28: Density of phonon states in CdTe, taken from [21]. Left red arrow shows energy of Zeeman splitting at 10 T and right red arrow shows electron cyclotron gap at 3.7 T.

The small efficiency of the phonon-assisted spin-flip processes $s = -1/2 \rightarrow s = +1/2$ across the spin gap (right part of the scheme in Fig. 7.27) is manifested also in the data. In Fig. 7.26, we present the intensities of polarization resolved PL from all experimentally observable LLs. According to the selection rules in CdTe, the PL in σ^+ polarization

from the LL $N = 1$ should disappear at the filling factor $\nu < 3$. This is because at the filling factors smaller than 3, the LL $|1, -1/2\rangle$ should be empty. However, we can observe a residual PL from the LL $|1, -1/2\rangle$ even at filling factors $\nu < 3$, as shown in the Fig. 7.26 by the label (II.). This experimental observation shows that the phonon-assisted electron spin-flip relaxation $s = -1/2 \rightarrow s = +1/2$ across the spin gap is really inefficient. This is why LL $|1, -1/2\rangle$ stays partially occupied and weak PL is observed from this LL at $\nu < 3$, although it should not be already observed in the case that electrons were completely thermalized. In Fig. 7.29, we present analysis of the same magneto-PL data as in Fig. 7.26, but instead of the intensities, energy positions of the PL emission are depicted. The red circles show the expected disappearing of the σ^+ polarization in the case of thermalized electrons. Non-thermalized electrons due to non-efficient electron relaxation $s = -1/2 \rightarrow s = +1/2$ across the spin gap cause the observation of the σ^+ polarization to the higher fields (lower filling factor) than expected in the case of efficient thermalization.

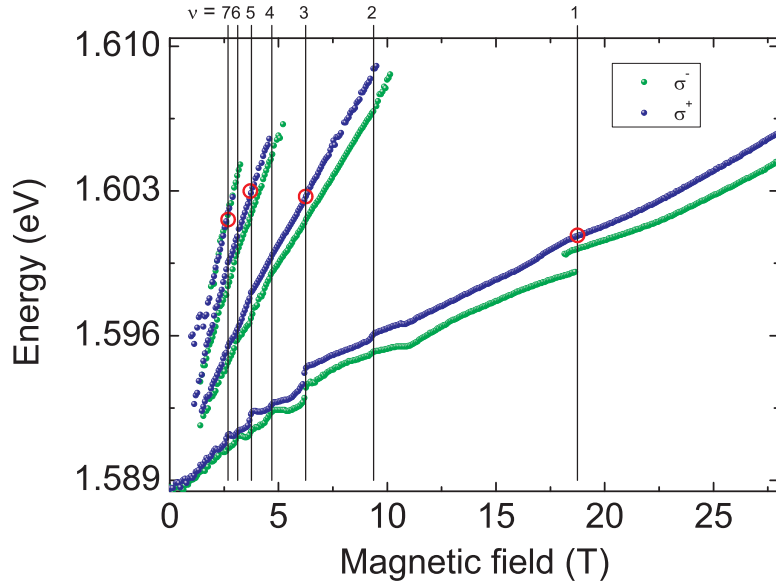


Figure 7.29: Energy position of PL from 20 nm wide CdTe QW, electron sheet concentration $n_e = 4.5 \times 10^{11} \text{ cm}^{-2}$. PL measured in σ^+ (blue dots) and σ^- (green dots) circular polarization. Red circles show, at which magnetic field the PL from σ^+ polarization is expected to disappear if electrons in the conduction band would be thermalized and the energy relaxation processes would be always efficient.

7.4.7 Comparison with CdMnTe QWs

In order to further support our interpretation of the simultaneous electron and hole spin spin-flip, we have measured field dependence of the PL intensities in CdMnTe QWs. CdMnTe QW has very similar parameters as the CdTe QW; width of the CdMnTe QW embedded in CdMgTe barrier is 21.1 nm and electron concentration of about $4.2 \times 10^{11} \text{ cm}^{-2}$ is

almost the same as the concentration in CdTe QW ($4.5 \times 10^{11} \text{ cm}^{-2}$). The main difference between these two heterostructures is the presence of manganese. As we have shown in the chapter 7.2.1, already small amount of manganese changes the sign of the electronic g-factor due to the electron-manganese sd-interaction. Therefore the electronic LL with the spin $s = +1/2$ will be at higher energy as compared to the LL with the spin $s = -1/2$. This is in contrast to CdTe QW, where the ordering of the spin LLs is opposite.

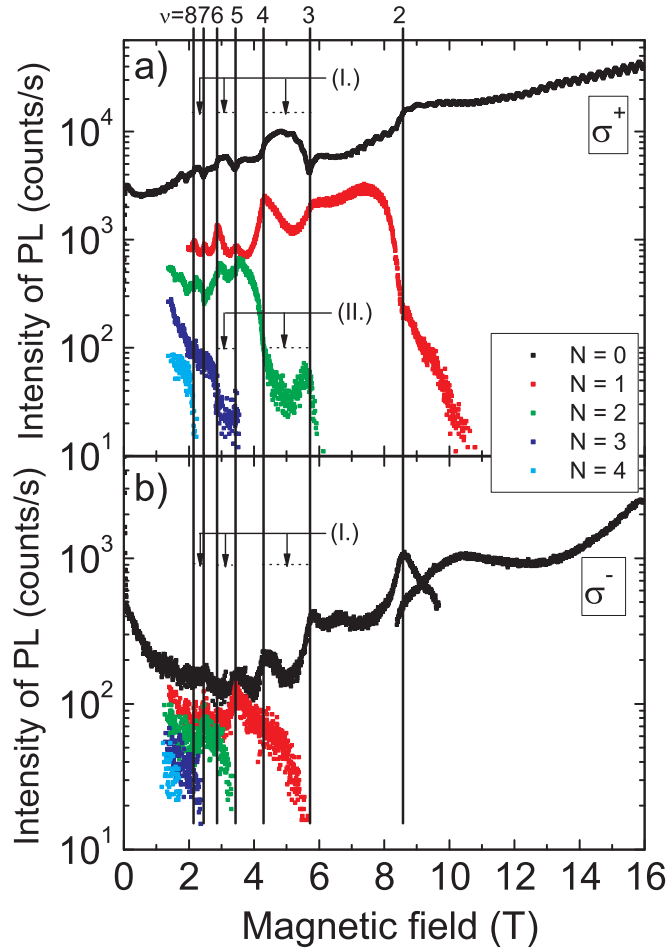


Figure 7.30: Intensity of magneto-PL emission in (a) σ^+ (b) and σ^- circular polarization. PL intensities from LLs $N = \{0, 1, 2, 3, 4\}$ are depicted by black, red, green, blue and light blue curves, respectively. PL excited by green Argon laser line at the energy of $E_{exc} = 2.41 \text{ eV}$, excitation power was $P_{exc} \approx 1.4 \mu\text{W}$ and laser spot size was in the range 0.5-1 mm. Measured at the bath temperature $T = 90 \text{ mK}$. Vertical lines show positions of integer filling factors. Labels (I.) and (II.) denote the intervals of the filling factors discussed in the text.

The polarization resolved PL intensity from the lowest LLs in CdMnTe QW is depicted in Fig. 7.30. The data show many similar features as PL measured in CdTe QW. The occurrence of the intensity modulations itself shows again on the dominant non-radiative recombination channel. Due to the Giant Zeeman splitting, hole LLs $j_z = -3/2$ are deeply in the valence band, therefore holes occupy primarily the valence band states $j_z = +3/2$.

This is why the polarization σ^+ is dominant in CdMnTe QWs. The dips in the intensity of σ^+ polarization at integer filling factors in the PL emission from Landau level $N = 0$ originate in the oscillatory efficiency of the screening and maxima of PL intensity from all higher LLs show on intra-subband scattering of holes as in CdTe QWs.

The intervals of the filling factors, which are in the scope of our interest are labelled (I.) in the Fig. 7.30 and Fig. 7.31. We directly compare the B -dependence of PL intensities in both CdTe and CdMnTe QWs in the Fig. 7.31. In CdMnTe, the intensity of PL from LL $N = 0$ in σ^+ polarization increases at these intervals of filling factors. This is in contrast to the observation in CdTe QWs, where decrease of the PL intensity was observed. However, we will show that this is in agreement with the proposed simultaneous electron and hole spin-flip and the only difference is the reversed ordering of the LLs with the spin $s = \pm 1/2$ in CdMnTe with respect to their ordering in CdTe QWs.

Since we observe the increase of the PL intensity in σ^+ polarization, the concentration of holes $j_z = +3/2$ has to increase. Therefore, the hole spin flips $j_z = -3/2 \rightarrow j_z = +3/2$ are expected. Because we are at such filling factors, where the Fermi energy of electrons is located within electronic LL $s = +1/2$, half of the unpolarized photo-excited electrons have to flip their spin from the state $s = -1/2$ to the state $s = +1/2$. As a matter of fact, we observe simultaneous electron and hole spin-flip $s = -1/2 \rightarrow s = +1/2$ for electrons and $j_z = -3/2 \rightarrow j_z = +3/2$ for holes. This process is efficient, because the electron relaxes across the cyclotron gap, therefore having enough phonon states in order to dissipate the released energy. However, its efficiency is limited by the concentration of holes in the spin state $j_z = -3/2$. Concentration of these holes is small due to Giant Zeeman splitting, therefore considerable part of electrons remains on the electronic LL $s = -1/2$ instead of relaxing on the lowest partially occupied LL $s = +1/2$, where Fermi energy is located in thermal equilibrium. This gives rise, for example, to the PL emission from LL $N = 2$ in σ^+ polarization at filling factors $\nu < 4$, where no PL is expected if electrons were thermalized. Intervals of the filling factors where this hot luminescence appears are labelled (II.) in Fig. 7.30.

When Fermi energy is located within LL $s = -1/2$ (the lower energy spin state in CdMnTe), the electron spin-flip $s = +1/2 \rightarrow s = -1/2$ is inefficient, because the released energy of electron would be too small to be dissipated by phonons into the lattice due to the negligible density of phonon states at these energies. Low efficiency of this electron spin-flip process should be accompanied by the hot luminescence in σ^- polarization. For example, hot PL from LL $N = 1$ in σ^- polarization is expected between filling factors 2 and 3, Fig. 7.30. However, we have observed no such hot PL. This is because its intensity is expected to be much weaker with respect to the PL of thermalized carriers and therefore experimentally unavailable due to a generally weaker σ^- PL in CdMnTe QWs.

Comparing the conclusions from the experiments on CdTe and CdMnTe QWs, we have found simultaneous electron and hole spin flip relaxation. Electron spin-flip $s = +1/2 \rightarrow s = -1/2$ goes along with the hole spin flip $j_z = +3/2 \rightarrow j_z = -3/2$ in CdTe QWs, thus reducing (enhancing) PL intensity from the LL $N = 0$ in the σ^+ (σ^-) polarization. In the case of CdMnTe QWs, the electron spin-flip $s = -1/2 \rightarrow s = +1/2$ goes along with the hole spin flip $j_z = -3/2 \rightarrow j_z = +3/2$, thus reducing (enhancing) PL intensity from the LL $N = 0$ in the σ^- (σ^+) polarization. We have found that the efficiency of the simultaneous electron and hole spin-flip process is governed by both electrons and holes. If the electrons relax across the Zeeman spin gap (cyclotron gap), efficiency is low

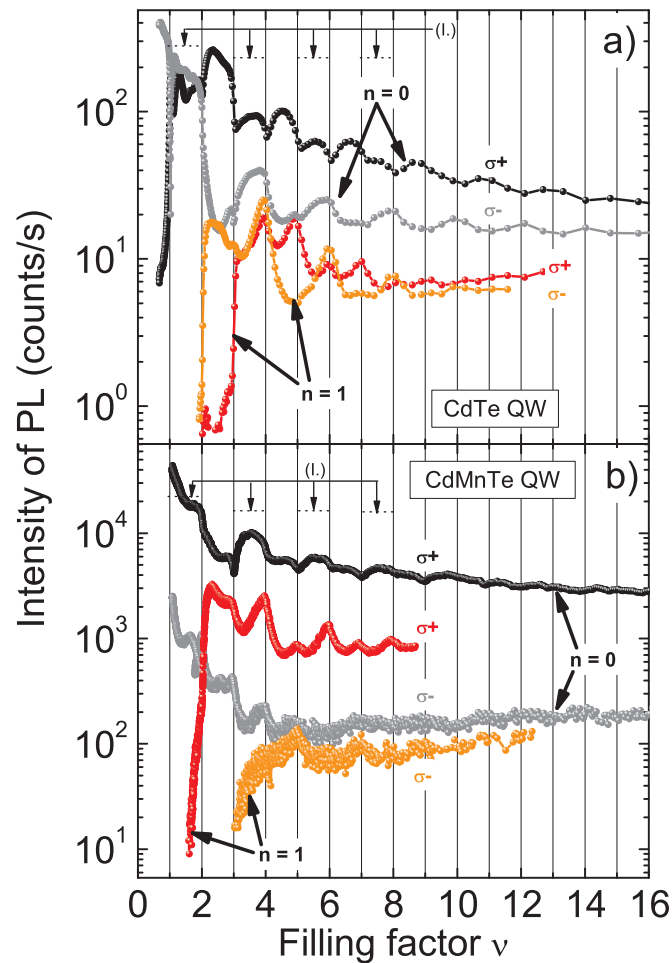


Figure 7.31: Intensity of PL emission from LL $n = 0$ (black and grey curve) and $n = 1$ (red and orange curve) from (a) CdTe and (b) CdMnTe QW plotted as a function of the filling factor. Data has been measured at (a) 80 mK (b) 90 mK, excited with Argon laser line at 514 nm and excitation power was of about $50 \mu\text{W}/\text{cm}^2$. Labels (I.) show intervals of the filling factors discussed in the text.

(high) and it is governed by the density of phonon states, into which the released energy can be dissipated. The holes influence the efficiency too, but in the sense that if their concentration is too small, certain part of the electrons do not thermalize in spite of the fact that with respect to the density of phonon states they could. Therefore we conclude that the experimentally observed simultaneous electron and hole spin-flip processes are not two independent events but they influence and depend on each other. We attribute this simultaneous electron and hole spin-flip process to the phonon assisted Bir-Aharonov-Pikus spin relaxation mechanism.

Chapter 8

Photoluminescence excitation

8.1 Brief introduction

Photoluminescence excitation is a complementary experimental technique to the photoluminescence (PL). While PL probes inter-band transitions between occupied conduction and unoccupied valence band states, PLE is sensitive to the transitions between occupied valence and empty conduction band states. In other words, PLE is capable to probe electronic states above Fermi energy of electrons E_F , and PL below E_F ¹.

PLE spectrum is a dependence of PL intensity on the energy E_{exc} of the excitation photon [147]. The PL intensity can be measured either at the maximum of PL emission or taken as an average in a given spectral range around maximum or it can be taken as an integral of whole PL spectrum. The larger is this interval, the more is noise reduced. On the other hand, too large interval embarrasses observation of PLE spectra beyond resonant excitation due to the presence of laser scattered light in the taken spectral window. We use an averaging in the interval given by FWHM² of PL emission spectrum. FWHM is determined in such a PL spectrum, which is excited high above (40 meV and more) the energy of PL emission. Choosing this interval was a good compromise between noise level and possibility to observe PLE in close surroundings, beyond the resonant excitation. The total absorbed intensity I_{abs} , Eq. (8.1), of the excitation laser beam

$$I_{abs}(E_{exc}) = I_0(1 - e^{-\alpha(E_{exc})d_{QW}}) \quad (8.1)$$

in the QW is governed according to the Lambert-Beer law by the incident intensity I_0 , absorption coefficient $\alpha(E_{exc})$ and a width of the QW d_{QW} . The intensity I_0 does not equal to the incident intensity on the sample. Relation between these two quantities is given by the transmission of the air-barrier, barrier-QW interface, which are given by Fresnel relations and by the absorption in a barrier. The transmission of the air-barrier and transmission through barrier are assumed to be spectrally independent, because excitation energy E_{exc} is well below band gap of Cd_{0.74}Mg_{0.26}Te barrier. The absorption coefficient $\alpha(E_{exc})$ depends on the energy of the excitation photons E_{exc} and its value is

¹Strictly speaking, we should talk about quasi-Fermi energy of electrons, which is different from the Fermi energy of electrons in equilibrium. However, the difference is given by the concentration of photo-excited carriers, which is in our case more than $10^3 \times$ smaller than the equilibrium concentration of 2DEG, hence the difference between Fermi and quasi-Fermi energy of electrons is negligible.

²Full width at half maximum.

$\approx 25000 \text{ cm}^{-1}$ [148] in a bulk CdTe in the spectral region above the band gap energy at a temperature of liquid helium $T = 4.2 \text{ K}$. Since widths of our QWs are 20 and 30 nm, $\alpha(E_{exc})d \ll 1$ and expanded exponential function around zero gives a linear proportionality between absorbed intensity and absorption coefficient $\alpha(E_{exc})$, Eq. (8.2).

$$I_{abs}(E_{exc}) = I_0 \alpha(E_{exc})d \quad (8.2)$$

Because the PL intensity $I_{PL}(E_{exc})$ is proportional, via the quantum efficiency η , to the intensity of the absorbed light $I_{abs}(E_{exc})$, it is possible to study absorption $\alpha(E_{exc})$ of the QW by means of PL intensity, $\alpha(E_{exc}) \propto I_{PL}(E_{exc})$. Such a result is easy to understand in a common sense, saying the more system absorbs, the more luminescence it gives. This is also why the PLE spectra are sometimes called quasi-absorption. The other reason for this is that the PLE spectrum is not influenced only by the absorption, but also by the efficiency of the relaxation processes of the photo-excited carriers.

8.2 Zero field photoluminescence excitation

We have used PLE excitation technique to study both 20 and 30 nm wide QWs. First, we focus on PLE at zero magnetic field and in the second part, we present field evolution of PLE. The essence of PLE experiment is, as formerly mentioned, to measure PL as a function of energy E_{exc} of photons used to excite PL. The result of such an experiment is shown in Fig. 8.1 for 20 nm wide QW at $T = 4.2 \text{ K}$ and $B = 0 \text{ T}$. The straight diagonal line is an elastically scattered light, or also called Rayleigh resonant scattering, from the laser excitation beam. Energy of the excitation photons E_{exc} was tuned from $\approx 1.575 \text{ eV}$ (left down corner in a map on a Fig. 8.1) up to the energy $\approx 1.7 \text{ eV}$. The broad horizontal line is a PL spectrum (red color depicts high PL intensity, blue color means no signal). Thus every vertical cut of the map of PLE is one single PL spectrum as taken by CCD camera. Onset of the PL is expected in 2DEG when energy of the excitation is tuned above Fermi energy (e.g. $E_{exc} > 1.602 \text{ eV}$ in Fig. 8.1)³. However, we have found an absorption resonance already when exciting below Fermi energy, where no absorption and therefore no PL emission is expected. This emission occurs at 1.594 eV in PL spectrum and is labeled “X” in Fig. 8.1. The band-to-band recombination occurs, as expected, when energy of the excitation is above Fermi energy (e.g. above $\approx 1.603 \text{ eV}$ in PL spectrum). In order to explain the origin of the unexpected absorption below Fermi energy, we follow the interpretation of Teran [101], who assumes non-homogeneous spatial distribution of 2DEG, therefore coexistence of the regions where QW contains 2DEG and where QW is almost empty. In the empty regions, PL emission is a radiative recombination of bound electron-hole pair (exciton). Due to the absence of 2DEG, the electron-hole interaction is not screened and thus the interaction is not weakened as compared to the regions where 2DEG is. In the regions of 2DEG, excitons are screened [149, 102] and only band-to-band free-electron-free-hole recombination at the energy $\approx 1.588 \text{ eV}$ takes place. The red shift of the later recombination process with respect to the excitonic one at 1.594 eV is explained by a band gap renormalization [101] caused by electron-electron interaction in the regions with 2DEG.

³Fermi energy 1.602 eV is introduced here in the absolute energy scale as measured in a PL spectrum. When we measure the Fermi energy from the bottom of the conduction band of a ground electronic state confined in a 20 nm wide QW, then $E_F = 10.8 \text{ meV}$.

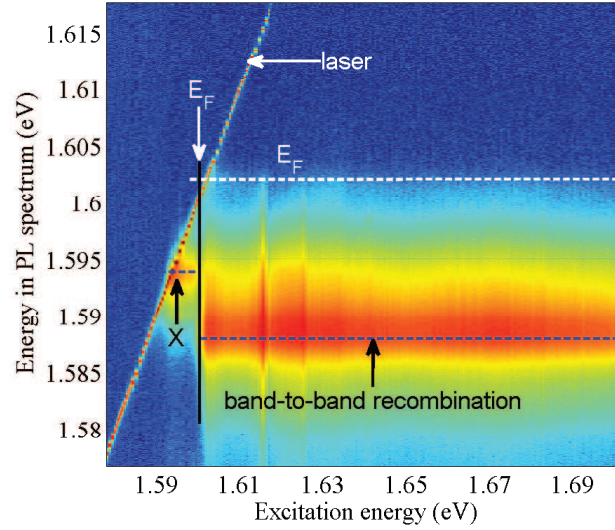


Figure 8.1: PL spectrum of 20 nm wide QW at $T = 4.2$ K and zero magnetic field as a function of excitation energy E_{exc} . Red (blue) color means high (zero) intensity of detected light. Excitation performed by σ^- circularly polarized light and PL detected at the same polarization. Fermi energy E_F marked in both PL and PLE spectrum, excitonic (X) and band-to-band PL transitions marked by horizontal dashed lines.

PLE spectra have been obtained by taking intensity profile following band-to-band PL transition (dashed line in Fig. 8.1) averaging PL intensity in the spectral range determined by FWHM of the PL emission peak. Absorption spectra of both 20 and 30 nm wide QWs are plotted in Fig. 8.2 and Fig. 8.3, respectively. Two contributions to the PLE spectra of both QWs are clearly observed. The step-like spectrum reflects the nature of the 2-dimensional density of states and the blue-shifted onset of the absorption with respect to the PL is determined by the presence of the electron gas which fills the conduction band up to the Fermi energy E_F and by parabolic dispersion relation of the electron and hole bands which both together give rise to the Moss-Burstein shift $\Delta_{MB} = E_F(1+m_e/m_h) \approx 1.25E_F$ of the absorption onset [101]. In our case the Moss-Burstein shift is 13.5 meV and 8.8 meV in the case of the 20 and 30 nm wide QW which contain an electron gas of the concentration 4.5 and $2.9 \times 10^{11} \text{ cm}^{-2}$, respectively. The data are compared with the calculations of the subband energy structure presented in the chapter 4. The calculations agree well with a data in the low energy part of the spectra. However, in higher energy part, instead of expected increase of absorption and consequently also increase of PL intensity, the inverse behavior is observed. We interpret this discrepancy by stronger non-radiative channels when exciting into higher subbands. In other words, we assume that the quantum efficiency of PL decreases at higher energies. This is an example, that even though the proportionality between absorption and PL intensity is usually valid, there are violations of this rule, hence attribution of quasi-absorption instead of absorption is more correct.

The second contribution to the absorption spectra is composed of the peak-like structure, which is, except of the peak on the Fermi energy, usually explained in terms of absorption into the excitonic states bound to the higher electronic subbands. These excitons do not undergo the metal-insulator-transition [150, 101] to the band-to-band recombina-

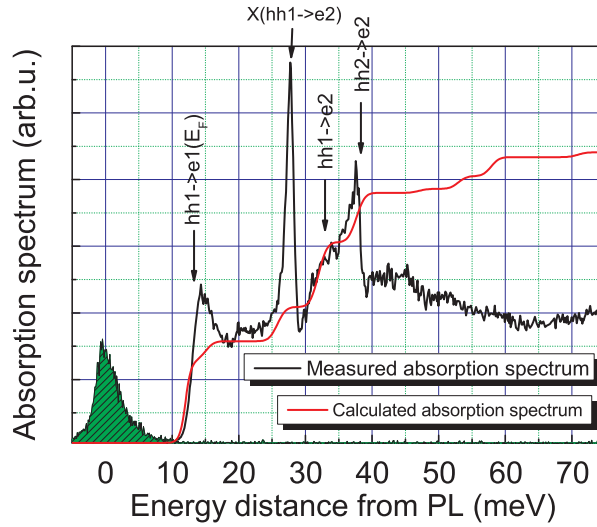


Figure 8.2: PLE spectrum (black curve) of 20 nm wide QW at $T = 4.2$ K compared to the calculated absorption (red curve) and photoluminescence spectrum (green filled peak). Excitation performed by σ^- circularly polarized light and PL detected at the same polarization. Energy scale was related to the energy of PL emission. Onsets of $hh_1 - e_1(E_F)$, $hh_1 - e_2$ and $hh_2 - e_2$ inter-subband transitions marked by arrows. Absorption into the excitonic state $X(hh_1 - e_2)$ bound below the second subband is also labelled.

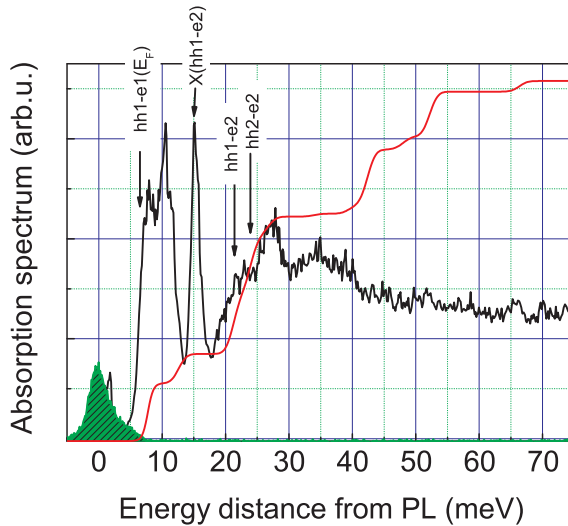


Figure 8.3: The same as in Fig. 8.2, but measured for 30 nm wide QW.

tion. It has been shown by many authors, that these excitations, bound to higher unoccupied subbands, are stable not only in empty QWs [151, 152, 153, 154], but also in the electron-hole plasma [155] and in a hole [156, 157] and electron gas. The later was studied both theoretically [158, 159, 160, 153] and experimentally [161, 162, 163]. We give a comment

on the two excitons bound to the second electronic subband e_2 . Because we interpret these two excitons according to our band structure calculations as a bound state of the electron from the second electronic subband e_2 and heavy hole from the ground heavy hole subband hh_1 , we labelled them $X(hh_1 - e_2)$ in both Figs. 8.2 and 8.3. The binding energy of these two excitons is ≈ 3.7 and ≈ 6.0 meV in 20 and 30 nm wide QW, respectively. There are two reasons for this. The first is the screening of the electron-hole interaction by the 2DEG, which occupies the ground electronic subband. The concentration of a 2DEG is lower in 30 nm wide QW, therefore the binding energy is less screened and consequently the exciton binding energy is higher than in 20 nm wide QW. The second reason is the strength of an internal electric field inside the QWs caused by single-side doping. As has been already shown by our calculations in the chapter 4, the internal electric field is higher in 20 nm wide QW, because the width of a well is smaller and moreover the concentration of positively charged donors is higher. Both these two contributions lead to the higher internal electric field in 20 nm wide QW. This electric field tends to separate the electron and hole apart, thus leading to the reduction of the excitation binding energy in 20, with respect to the 30 nm wide QW.

The last comment on the zero-field PLE spectra is devoted to the quasi-absorption resonance at the Fermi energy, labelled $hh_1 \rightarrow e_1(E_F)$ in both Figs. 8.2 and 8.3. This absorption resonance has no common interpretation so far. Some authors explain it as a band non-parabolicity in the valence band at the Fermi wave vector k_F [164] in a 2DEG, or as a non-parabolicity of light hole levels at the Γ point in a 2DHG [165]. Also an explanation by many-body Fermi edge singularity is often accepted [166, 167, 168, 169]. We do not treat this resonance and leave the question of its origin opened.

8.3 Field evolution of PLE

We will focus now on a study of PLE in magnetic field perpendicular to the plane of 2DEG. An example of PL spectrum as a function of the energy of excitation is shown in Fig. 8.4 for 20 nm wide QW measured at $T = 4.2$ K and magnetic field $B = 14$ T. As in the case of PLE at zero magnetic field, the most intense straight diagonal line is a spectrum of scattered laser light being tuned from 1.584 eV to ≈ 1.7 eV. The thick red horizontal line in Fig. 8.4 depicts PL from the electronic Landau level $N = 0$. In contrast to the map of PLE taken at zero magnetic field, set of four replicas of a laser scattered light spectrum is observed. The energy distance between these replicas and spectrum of scattered laser light is always integer multiple of LO-phonon energy, as depicted in Fig. 8.4 by vertical yellow double-arrow. Up to 4 LO-phonon replicas have been observed in PL spectra, which shows on the importance of LO-phonon assisted energy relaxation channel.

Field dependences of PLE spectra for 20 and 30 nm wide QW are shown in Fig. 8.5 and Fig. 8.6, respectively. The lowest energy signal (starting at ≈ 1.59 eV) is a spectral position of PL from the lowest lying Landau level ($N=0$). The gap between PL emission and absorption (depicted by blue color) is due to the presence of 2DEG, thus forbidding absorption below Fermi energy. Here, we plot PLE spectra determined from narrow spectral region around the maximal PL intensity (averaged data in the range of FWHM of the most intense PL peak), hence the absorption below Fermi level, as discussed in the section about zero field PLE, is not visible here. The most intense peaks in PLE spectrum above

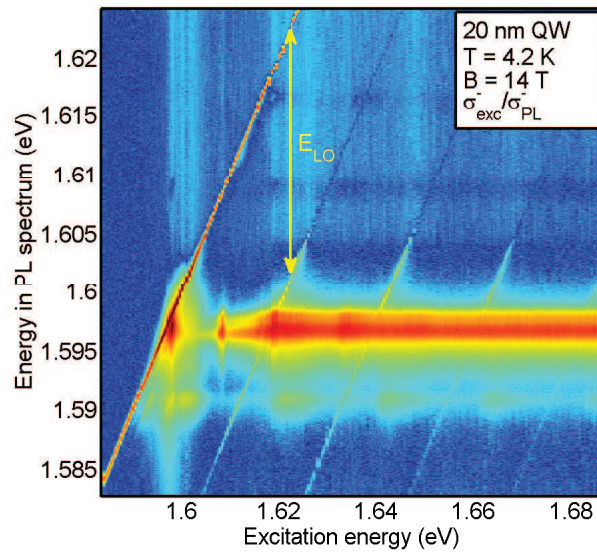


Figure 8.4: PL spectrum of 20 nm wide QW at $T = 4.2$ K and $B = 14$ T as a function of excitation energy E_{exc} . Excitation performed by σ^- circularly polarized light and PL detected at the same polarization. Energy of LO-phonon shown by yellow arrow.

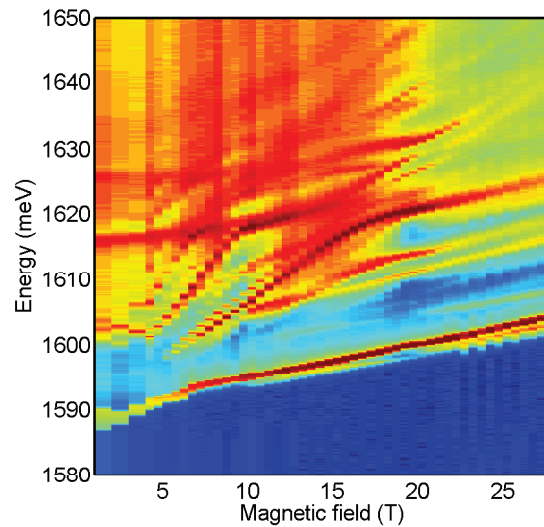


Figure 8.5: PLE of 20 nm wide QW versus magnetic field up to 28 T. Measured under the same conditions as described in Fig. 8.1 and Fig. 8.2

Fermi energy, linearly growing with magnetic field, are caused by unoccupied electronic Landau levels.

The nature of the anticrossing in 20 nm wide QW (Fig. 8.5) at roughly 18 T will be

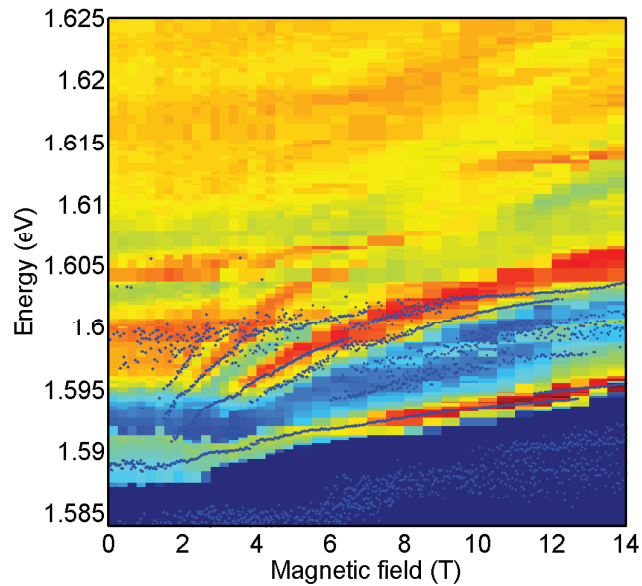


Figure 8.6: PLE of 30 nm wide QW versus magnetic field up to 28 T. Measured under the same conditions as described in Fig. 8.2. Blue crosses show positions of PL emission peaks.

a matter of further investigation. We suggest few possible interpretations at the moment. First, we propose magneto-polaron effect, since such an avoided anticrossing is expected in CdTe QW at this magnetic field and FIR cyclotron resonance absorption data show similar behavior. On the other hand, it could be also demonstration of light-hole-heavy-hole mixing in the valence band or some other interaction effect between e_1 and e_2 subbands.

For the sake of illustration, we have plotted PLE (absorption) and PL (emission) together for the 30 nm wide QW, see Fig. 8.6. The PL is plotted by blue crosses, which mark the positions of PL peaks. The data well illustrate the complementarity of PL and PLE experiments. PL, as has been mentioned in the introduction of this chapter, is sensitive to the occupied electronic Landau levels only and PLE on empty electronic Landau levels. This is why PL is visible only in a narrow band above PL emission from $N = 0$ LL. The width of a band where PL is visible is determined by the Fermi energy. Above Fermi energy, electronic LLs are empty, thus only PLE probes these states.

Chapter 9

Conclusions

9.1 Conclusions (English)

We have presented an experimental study of two-dimensional electron gas (2DEG) embedded in a single side modulation n-doped CdTe/CdMgTe and magnetic CdMnTe/CdMgTe quantum wells. The experimental investigation has been done by means of magnetophotoluminescence, photoluminescence excitation, longitudinal and Hall resistance measurements and complementary techniques of far infrared cyclotron resonance absorption and Raman inelastic scattering. Experimental results have been subjected to the detailed analysis and compared with theoretical models based on both simple single particle models, more complex models of electron-electron many-body interactions and some data has been compared with numerical calculations of confined states in a QW.

The knowledge of the energy spectrum of confined states in our QWs was essential in order to properly interpret the experimental data. Therefore, as a first step, we have done numerical calculations of the confined states and their energies. The electron-electron interactions have been taken into account in the Local Density Approximation (LDA) and electronic and hole wave functions have been calculated in the Envelope Function Approximation (EFA).

Basic characterization of the samples by means of far infrared absorption and inelastic Raman scattering helped us to determine the effective mass and effective g-factor of electrons, which are the two key parameters in a single particle description of spin resolved Landau level quantization of the energy levels of 2DEG in magnetic field.

The low-field magneto-conductivity showed that the semi-classical Drude term represents the most important contribution to the longitudinal conductivity. Weaker contributions, by roughly three orders of magnitude, have been also found. They are due to effects of weak localization, electron-electron interaction and Shubnikov-de Hass oscillations. Many-body electron-electron contribution has been also successfully explained by semi-classical model of circling electrons. Analysis of the amplitude of Shubnikov-de Hass oscillations in the longitudinal resistance revealed further information on the Landau level structure, namely the shape of Landau levels and the size of their broadening. The difference between transport scattering time ($\tau_{tr} = 15$ ps) and quantum life time ($\tau_q = 3$ ps) led us to conclude on the presence of dominant long-range scattering mechanism. In the studied CdTe QWs, we have found no significant changes of Landau level broadening and

electron effective mass as a function of temperature from 90 mK to 1.2 K and magnetic field up to 0.5 T. The high magnetic field magneto-transport has shown well developed fractional quantum Hall states in the Landau level $N = 0$ ($\nu = 5/3, 4/3$) and $N = 1$ ($\nu = 7/3, 8/3$). The fractional quantum Hall (FQH) states $5/3$ and $4/3$ have been subjected to the magneto-transport studies in a tilted magnetic field. We have found that the properties of these FQH states are strongly influenced by the intrinsic Zeeman energy, resulting in the complete spin polarization of the ground state of both FQH states $5/3$ and $4/3$, in agreement with a composite fermion approach for FQH effect.

Spin gap enhancement of the fully occupied Landau levels has been studied by means of magneto-PL in wide range of magnetic fields and temperatures. The observed field and temperature dependence has been successfully described by simple phenomenological model. We have concluded that the spin gap enhancement does not occur only in the vicinity of the Fermi energy, as has been known so far, but it occurs at all occupied Landau levels and its magnitude is the same for all Landau levels up to the Fermi energy.

Magnetic field induced modulations of the polarization resolved PL intensity revealed several mechanisms influencing the efficiency of the radiative recombination. We have shown that the dominant role in the recombination of electrons and holes is played by non-radiative recombination channels. Other phenomena influencing an efficiency of the radiative recombination have been also recognized, like degeneracy of Landau levels, occupation of Landau levels, selection rules and oscillatory efficiency of the screening. The pivotal conclusion of our PL intensity studies is an identification of the simultaneous electron and hole spin-flip, mediated by phonon-assisted Bir-Aharonov-Pikus spin-relaxation mechanism.

Manifestation of the two-dimensional density of states has been revealed in the photoluminescence excitation spectra. We have found also an importance of the screening and internal electric field in the single side modulation doped QWs, which influence the binding energy of excitons bound to the unoccupied Landau levels $N = 1$.

Although we have presented an extensive magneto-optical and magneto-transport experimental study of a 2DEG, many phenomena have been successfully interpreted and the data interpretation has been often supported by numerical calculations and data modelling, many questions remained unsolved and some other appeared. Among those questions, which remained unsolved, let's mention for example the doublet Landau level structure in both circular polarizations which can be well seen at higher Landau levels in both photoluminescence and photoluminescence excitation. Even though we have presented a simple model to describe oscillations of the spin gap, there is no generally accepted explanation for the oscillatory behavior of the absolute position of the PL emission (if any exists). The reason, why longitudinal resistance shows large plateaux and energy of photoluminescence sharp jumps at certain magnetic field is also not clear so far. An avoided anticrossing observed in quasi-absorption (PLE) at every such a magnetic field, when any of the Landau levels from the ground electronic subband crosses absorption resonance of an exciton below the first excited electronic subband is also striking, as well as peaks in the quasi-absorption at the Fermi energy. The interpretation of the absorption below Fermi energy in PLE spectra at zero magnetic field should be probably also reexamined. So far, we have interpreted this absorption as an excitonic one and we have argued by non-homogeneous distribution of 2DEG. However, it seems to us, that the electron gas is not so inhomogeneous as would be required by the proposed explanation. We have shown,

that the spin gap enhancement appears not only in the Landau levels in the vicinity of the Fermi energy, but also in the fully occupied Landau levels. However, the question has risen, whether the spin gap enhancement occurs also in completely empty Landau levels. Analysis of the thermally activated magneto-transport measurements revealed great inadequacies in the satisfactory description of the experimental data. Therefore, we invoke more theoretical effort to properly describe this kind of experiments.

To summarize, we have shown number of new experimental results, some of them have been successfully interpreted and led to the conclusions of the fundamental character. However, also many questions remained unanswered and new have risen. Therefore, further both experimental and theoretical investigations of a two-dimensional electron gas will be certainly of a future interest of many forthcoming effort of many research groups and we hope, that our work will contribute to a correct understanding of the properties of a 2DEG and generally to the understanding of many-body strongly interacting systems.

9.2 Résumé (En français)

Nous avons présenté une étude expérimentale de gaz d'électrons bidimensionnel (GE-2D) confiné dans des puits quantiques de CdTe/CdMgTe et des puits quantiques magnétiques de CdMnTe/CdMgTe. La recherche expérimentale a été faite au moyen de magnétophotoluminescence, de spectroscopie d'excitation de la photoluminescence, de mesures de résistance longitudinale et de résistance Hall et de techniques complémentaires, comme l'absorption de résonance cyclotron infrarouge et la diffusion Raman inélastique. Les résultats expérimentaux ont été soumis à une analyse détaillée et comparés à des modèles théoriques basés sur des modèles simples de mono-particules, à des modèles plus complexes d'interactions multi-corps électron-électron. Quelques résultats ont été comparés aux calculs numériques des états confinés dans des boîtes quantiques.

La connaissance du spectre d'énergie des états confinés dans nos boîtes quantiques était essentielle afin d'interpréter correctement les résultats expérimentaux. C'est pourquoi nous avons d'abord effectué des calculs numériques des états confinés et de leurs énergies respectives. Les interactions électron-électron ont été considérées dans l'approximation de densité locale (Local Density Approximation - LDA) et les fonctions d'onde d'électron et de trou ont été calculées dans l'approximation de fonction enveloppe (Envelope Function Approximation - EFA).

La caractérisation élémentaire au moyen d'absorption infrarouge et de diffusion Raman nous ont aidés à déterminer la masse des électrons et leur facteur g effectif, qui sont les deux paramètres principaux dans une description de mono-particule dans le champ magnétique. La magnéto-conductivité à bas champ a indiqué que la contribution de la conductivité longitudinale la plus importante est la contribution semi-classique de Drude. Des contributions d'approximativement trois ordres de grandeur plus faibles ont été également trouvées. Elles sont dues aux effets de la localisation faible (Weak Localization - WL), d'interaction électron-électron et d'oscillations Shubnikov-de Hass. La contribution de l'interaction électron-électron a été expliquée également avec succès avec le modèle semi-classique des électrons tournants. L'analyse de l'amplitude des oscillations Shubnikov-de Hass dans la résistivité longitudinale a donné des informations supplémentaires sur la structure des niveaux de Landau, comme leur forme et la taille de leur élargissement. La différence entre le temps de transport ($\tau_{tr} = 15$ ps) et le temps quantique ($\tau_q = 3$ ps) nous a menés à la conclusion de la présence du mécanisme de dispersion d'origine longue portée. Dans les études des puits quantiques de CdTe, nous n'avons trouvé aucun changement des élargissements des niveaux de Landau ni de la masse effective de l'électron en fonction de la température (entre 90 mK et 1.2 K) et du champ magnétique (jusqu'à 0.5 T). Le magnéto-transport dans les champs magnétiques intenses a mis en évidence des états Hall quantiques fractionnaires bien identifiés dans les niveaux de Landau $N = 0$ ($\nu = 5/3, 4/3$) et $N = 1$ ($\nu = 7/3, 8/3$). Les états fractionnaires $5/3$ et $4/3$ ont été soumis à des études de magnéto-transport dans un champ magnétique incliné. Nous avons constaté que les propriétés de ces états sont fortement influencées par l'énergie Zeeman, et que leur l'état fondamental est complètement polarisé, en accord avec une approche de fermions composites décrivant l'effet Hall quantique fractionnaire.

Le gap de spin amplifié dans les niveaux Landau entièrement occupés a été étudié au moyen de magnéto-photoluminescence dans un grand intervalle de champs magnétiques et de températures. La dépendance en champ et en température a été décrite avec succès

par un modèle phénoménologique simple. Nous avons conclu que le gap de spin amplifié n'apparaît pas seulement à proximité de l'énergie de Fermi, comme décrit jusqu'ici, mais que le phénomène se produit à tous les niveaux de Landau occupés et que son amplitude est la même pour tous les niveaux de Landau jusqu'à l'énergie de Fermi.

Le modulation par le champ magnétique de l'intensité de la photoluminescence résolue en polarisation a indiqué que plusieurs mécanismes influencent l'efficacité de la recombinaison radiative. Nous avons prouvé que le rôle dominant dans la recombinaison des électrons et des trous est joué par un processus non-radiatif. D'autres phénomènes influençant l'efficacité de la recombinaison radiative ont été également identifiés, comme la dégénérescence des niveaux de Landau, leur taux d'occupation, les règles de sélection et l'efficacité de l'écrantage. La conclusion principale de notre étude de l'intensité de la photoluminescence est une identification du processus mis en jeu, processus au cours duquel le spin de l'électron et le spin du trou se renversent en même temps. Ce processus est contrôlé par le mécanisme Bir-Aharonov-Pikus, qui est le mécanisme de la relaxation de spin assistée par les phonons.

Les spectres obtenus par la spectroscopie d'excitation de la photoluminescence reflètent la densité d'états caractéristique des systèmes bidimensionnels. Les résonances excitoniques, qui sont observées aux bords des sous-bandes électriques inoccupées, illustrent l'importance de l'écrantage et des champs électriques intrinsèques dans les puits asymétriquement dopés.

Nous avons présenté des études magnéto-optiques et de magnéto-transport approfondies d'un gaz électronique bidimensionnel. Les phénomènes identifiés ont été interprétés avec succès et l'interprétation a été souvent confirmée par des calculs numériques. Cependant, beaucoup de questions restent non résolues et d'autres sont apparues. Parmi ces questions non résolues, nous voudrions mentionner par exemple la structure en doublet de niveaux de Landau dans les deux polarisations circulaires, qui peut être observée clairement à des niveaux de Landau plus élevés par photoluminescence et par excitation de photoluminescence. Même si nous avons présenté un modèle simple pour décrire les oscillations de gap de spin, il n'y a pas d'explication communément admise pour les oscillations de la position absolue de l'émission de la photoluminescence (s'il en existe). La raison pour laquelle la résistance longitudinale présente de grands plateaux et pour laquelle l'énergie de photoluminescence change pour certaines intensités de champ magnétique n'est pas encore éclaircie. L'origine du croisement des niveaux de Landau observé par spectroscopie d'excitation de la photoluminescence ainsi que des maxima dans la quasi-absorption à l'énergie de Fermi reste aussi inconnue. L'interprétation de l'absorption au-dessous de l'énergie de Fermi dans des spectres de photoluminescence d'excitation en champ magnétique nul devrait être probablement réexaminée. Jusqu'ici, nous avons interprété cette absorption comme l'absorption des excitons et nous avons discuté la distribution non homogène du gaz électronique bidimensionnel. Cependant, il nous semble que le gaz d'électrons n'est pas si inhomogène que suggéré par l'explication proposée. Nous avons montré que le gap de spin amplifié concerne non seulement les niveaux de Landau à proximité de l'énergie de Fermi, mais également les niveaux de Landau entièrement occupés. Cependant, la question se pose si le gap de spin amplifié existe également dans les niveaux de Landau complètement vides. L'analyse du magnéto-transport thermiquement activé a montré de grandes limites dans la description théorique. Par conséquent, un effort d'interprétation théorique est nécessaire afin de décrire correctement ce genre d'expériences.

Pour conclure, nous avons décrit plusieurs de nouveaux résultats expérimentaux. Certains d'entre eux ont été interprétés avec succès et ont menés à des conclusions de caractère fondamental. Cependant, beaucoup de questions restent sans réponse et de nouvelles ont été posées. Nous espérons que ce travail constituera une base pour de futures investigations expérimentales et théoriques sur les gaz d'électrons bidimensionnels et contribuera à une compréhension correcte de ses propriétés. Nous espérons également que ce travail permet de mieux comprendre la physique des systèmes multi-corps présentant une interaction électron-électron forte.

9.3 Závěr (Česky)

V předložené práci jsme prezentovali výsledky experimentálního studia dvou - dimenzionálního elektronového plynu (2DEP) v asymetricky n-dopovaných kvantových jamách CdTe/CdMgTe a semi-magnetických kvantových jamách CdMnTe/CdMgTe. Experimentální studium bylo provedeno metodami měření magneto-fotoluminiscence, excitační luminescence, podélného a Hallova odporu a pomocí doplňkových technik infračervené absorpce a Ramanova rozptylu. Experimentální výsledky byly podrobeny detailní analýze a srovnány s teorií, kde byly použity jak jednoduché, jednočásticové modely, tak komplexnější modely zahrnující mnoha-částicové, elektron-elektronové interakce.

Znalost energetického spektra vlastních stavů 2DEP je esenciální pro správnou interpretaci experimentálních dat. Proto byly v prvním kroku provedeny numerické výpočty kvantových vlastních stavů a jejich energií v kvantových jamách CdTe. Elektron-elektronová interakce v 2DEP byla započtena v aproximaci lokální elektronové hustoty (Local Density Approximation - LDA) a elektronové a děrové vlnové funkce byly spočteny v aproximaci obáلكové funkce (Envelope Function Approximation - EFA).

Metodami infračervené absorpce a Ramanova rozptylu byla určena efektivní hmoty a efektivní g-faktor elektronu, což jsou dva klíčové parametry v jednočásticovém popisu pohybu elektronu v magnetickém poli, a tedy popisu spinově rozlišených Landauových hladin. Analýza elektrické vodivosti v nízkém magnetickém poli ukázala na dominantní roli semi-klasického Drudeho příspěvku. Dále bylo nalezeno několik slabších příspěvků, které byly identifikovány jako vliv slabé lokalizace, elektron-elektronové interakce a Shubnikov-de Haasových oscilací. Příspěvek mnoha-částicové elektron-elektronové interakce byl taktéž úspěšně vysvětlen semi-klasickým model cirkulujících elektronů. Z analýzy Shubnikov-de Haasových oscilací byl určen tvar a šířka Landauových hladin. Z rozdílu mezi transportní dobou života ($\tau_{tr} = 15$ ps) a kvantovou dobou života ($\tau_q = 3$ ps) bylo usouzeno na dominantní přítomnost daleko-dosahového rozptylového mechanismu. Ve studovaných kvantových jamách CdTe jsme nenalezli žádné význačné změny rozšíření Landauových hladin a změny efektivní hmoty elektronu v rozmezí teplot od 90 mK do 1.2 K a magnetických polí do 0.5 T. V magneto-transportních měřeních ve vysokém magnetickém poli byly identifikovány zlomkové kvantové Hallovy stavy v Landauových hladinách $N = 0$ ($\nu = 5/3, 4/3$) a $N = 1$ ($\nu = 7/3, 8/3$). Zlomkové kvantové Hallovy stavy $5/3$ a $4/3$ byly podrobeny detailnímu studiu v nakloněném magnetickém poli. Bylo zjištěno, že oba stavy jsou značně ovlivněny velikostí energie Zeemanovského štěpení, což vede k úplné polarizovanosti těchto stavů, ve shodě s teorií kompozitních fermionů pro zlomkový kvantový Hallův jev. Spinové štěpení plně obsazených Landauových hladin bylo studováno v širokém rozsahu teplot a magnetických polí metodou magneto-fotoluminiscence. Vliv elektron-elektronové interakce a její teplotní a polní závislost byla úspěšně popsána jednoduchým modelem. Bylo zjištěno, že k zesílení spinového štěpení vlivem elektron-elektronové interakce nedochází jen v Landauových hladinách v okolí Fermiho meze, jak bylo známo doposud, ale že k zesílení spinového štěpení dochází ve všech plně obsazených Landauových hladinách a míra štěpení je ve všech hladinách stejná. Dále bylo určeno několik mechanismů ovlivňujících intenzitu fotoluminiscence 2DEP v magnetickém poli. V první řadě byl zjištěn dominantní vliv nezářivých elektron-děrových rekombinačních procesů. Mezi dalšími parametry ovlivňujícími intenzitu magneto-luminiscence jmenujme degeneraci Landauových hladin, jejich obsazení, výběrová pravidla a v magnetickém

poli oscilující efektivitu stínění. Stěžejní závěr studia intenzity luminiscence je identifikace simultánního spinového relaxačního procesu elektronů a děr, který je zprostředkován BAP (Bir-Aharonov-Pikus) relaxačním mechanismem doprovázeným emisí longitudinálních akustických fononů. Projev dvou-dimenzionální hustoty stavu byl zjištěn při studiu 2DEP metodou excitační luminiscence. Taktéž byla zjištěna důležitost stínění a vnitřního elektrického pole v asymetricky dopované kvantové jámě, kde obojí ovlivňuje vazebnou energii excitonu vázaného u neobsazené Landauovy hladiny $N = 1$.

Přestože se předkládaná práce zabývá širokou řadou vlastností 2DEP, spousta jevů byla úspěšně interpretována a interpretace dat byla často podpořena srovnáním dat s teorií a numerickými modely, spousta problémů zůstala nedořešena a nové otázky vyvstaly. Mezi těmi nezodpovězenými otázkami zmiňme například multiplenní strukturu Landauových hladin pozorovanou v obou kruhových polarizacích jak v datech fotoluminiscence tak excitační luminiscence. Přestože jsme prezentovali jednoduchý fenomenologický model objasňující zesílení spinového štěpení, doposud neexistuje jednoznačně přijímaný model popisující oscilující chování absolutní hodnoty energie luminiscence (pokud takový model vůbec existuje). Důvod, proč podélný odpor vykazuje v magnetickém poli široká plata a energie luminiscence ostré schody taktéž není znám. Podstata interakce při křížení Landauových hladin ze základního elektronového podpásu s excitonovým stavem vázaným u prvního neobsazeného elektronového podpásu taktéž není známa, stejně tak původ píků v kvazi-absorpci na Fermiho mezi. Interpretace absorpce pod Fermiho mezí bude muset být patrně přezkoumána. Doposud byla tato absorpce identifikována jako excitonová v nehomogenním elektronovém plynu. Avšak, dle našeho názoru, nehomogenita studovaného elektronového plynu není natolik velká, jak by bylo vyžadováno pro vytvoření oblastí bez 2DEP, a tedy oblastí s přítomností excitonu. Při studiu zesíleného spinového štěpení jsme ukázali, že k tomuto mnoha-částicovému jevu dochází ve všech plně obsazených Landauových hladinách až po Fermiho mez. Další otázka vyvstává, zda by bylo možné toto zesílené spinové štěpení pozorovat i v neobsazených hladinách nad Fermiho mezí. Při analýze dat teplotně aktivovaného magneto-transportu jsme odhalili značné nedostatky v dostupném a adekvátním popisu dat. Proto bychom rádi v tomto směru apelovali na další teoretické snahy.

V této práci jsme prezentovali široké spektrum experimentálních výsledků, část z nich byla úspěšně interpretována a vedla k závěrům fundamentálního charakteru. I přesto, spousta otázek zůstala otevřena a nové vyvstaly. Proto věříme, že budoucí, jak experimentální, tak teoretické snahy studia dvou-dimenzionálního elektronového plynu budou jistě naplní mnoha nadcházejících prací řady výzkumných týmů a doufáme, že tato práce přispěje ke správnému porozumění vlastností 2DEP a obecně k hlubšímu porozumění mnoha-částicových systémů.

Chapter 10

List of publications

- [1] Piot B. A., Kunc J., Potemski M., Maude D. K., Betthausen C., Vogl A., Weiss D., Karczewski G., Wojtowicz T., Fractional quantum Hall effect in CdTe, *Phys. Rev. B* **82**, 081307 (2010).
- [2] Kunc J., Kowalik K., Teran F. J., Płochocka P., Piot B. A., Maude D. K., Potemski M., Kolkovsky V., Karczewski G., Wojtowicz T., Enhancement of the spin gap in fully occupied two-dimensional Landau levels, *Phys. Rev. B* **82**, 115438 (2010).
- [3] K. Kowalik, F. J. Teran, P. Plochocka, J. Kunc, D. K. Maude, M. Potemski, K. J. Friedland, R. Hey, K. Ploog, G. Karczewski and T. Wojtowicz, Exchange driven spin splitting of fully occupied Landau levels measured using polarization resolved photoluminescence spectroscopy, *Physics of Semiconductors, AIP Conference Proceedings* **1199**, 249-250 (2009).
- [4] L. F. dos Santos, Y. Galvão Gobato, M. D. Teodoro, V. Lopez-Richard, G. E. Marques, M. J. S. P. Brasil, M. Orlita, J. Kunc, D. K. Maude, M. Henini, R. J. Airey, Circular Polarization in a Non-magnetic Resonant Tunneling Device, *Nanoscale Research Letters*, (accepted for publication).
- [5] Sprinzl D., Kunc J., Ostatnický T., Horodyský P., Grill R., Franc J., Malý P., Němec P., Dephasing of free carriers and excitons in bulk CdTe, *phys. stat. sol. b* **244**, 1612-1617 (2007).
- [6] Franc J., Babentsov V., Feychuk P., Kunc J., Hlídek P., Semiconductor-polymer composite with strong nonlinear optical properties - art. no. 65821K, *Nonlinear Optics and Applications II, Book Series: Proceedings of the society of photo-optical instrumentation engineers (SPIE)* **6582**, K5821-K5821 (2007).

References

- [1] W. T. Sommer, Phys. Rev. Lett. **12**, 271 (1964).
- [2] A. B. Fowler, F. F. Fang, W. E. Howard, and P. J. Stiles, Phys. Rev. Lett. **16**, 901 (1966).
- [3] K. v. Klitzing, G. Dorda, and M. Pepper, Phys. Rev. Lett. **45**, 494 (1980).
- [4] D. C. Tsui, H. L. Stormer, and A. C. Gossard, Phys. Rev. Lett. **48**, 1559 (1982).
- [5] C. Kittel, *Introduction to Solid State Physics, seventh edition*, John Wiley sons, inc., New York, 1996.
- [6] G. A. Bastard, *Wave Mechanics Applied to Semiconductor Heterostructures*, Halsted, New York, 1991.
- [7] M. Born and E. Wolf, *Principles of Optics*, Cambridge University Press, 1997.
- [8] G. Karczewski, J. Jaroszyński, A. Barcz, M. Kutrowski, T. Wojtowicz, and J. Kosut, Journal of Crystal Growth **184/185**, 814 (1998).
- [9] T. Suntola, Materials Science Reports **4**, 265 (1989).
- [10] J. N. Schulman and Y.-C. Chang, Phys. Rev. B **24**, 4445 (1981).
- [11] Y.-C. Chang and J. N. Schulman, J. Vac. Sci. Technol. **21**, 540 (1982).
- [12] J. N. Schulman and Y.-C. Chang, Phys. Rev. B **31**, 2056 (1985).
- [13] M. G. Burt, J. Phys.: Condensed Matter **9**, R53 (1999).
- [14] P. Harrison, *Quantum wells, wires and dots, Theoretical and computational physics of semiconductor nanostructures*, Wiley, United Kingdom, 2009.
- [15] I. Galbraith and G. Duggan, Phys. Rev. B **38**, 10057 (1988).
- [16] L. Hedin, Phys. Rev. **139**, A796 (1965).
- [17] S. K. Lyo and E. D. Jones, Phys. Rev. B **38**, 4113 (1988).
- [18] D. Huang and S. K. Lyo, Phys. Rev. B **59**, 7600 (1999).
- [19] M. Orlita, R. Grill, P. Hlídek, M. Zvára, G. H. Döhler, S. Malzer, and M. Byszewski, Phys. Rev. B **72**, 165314 (2005).

- [20] L. R. Ram-Mohan, *Finite element and boundary element applications in quantum mechanics*, Oxford university press, United Kingdom, 2007.
- [21] U. Rössler and A. Adachi, *Electronic, transport, optical and other properties, Landolt-Börnstein series: Numerical data and functional relationships in Science and Technology (Condensed matter)*, Springer, United Kingdom, 2009.
- [22] B. Kuhn-Heinrich, W. Ossau, H. Heinke, F. Fischer, T. Litz, A. Waag, and G. Landwehr, *Appl. Phys. Lett.* **63**, 2932 (1993).
- [23] E. Oh, C. Parks, I. Miotkowski, M. D. Sciacca, A. J. Mayur, and A. K. Ramdas, *Phys. Rev. B* **48**, 15040 (1993).
- [24] P. Redliński and B. Jankó, *Phys. Rev. B* **71**, 113309 (2005).
- [25] J. M. Rowe *et al.*, *Phys. Rev. B* **10**, 671 (1974).
- [26] Q. X. Zhao, N. Magnea, and M. Willander, *Journal of Crystal Growth* **184/185**, 835 (1998).
- [27] Q. X. Zhao, M. Oestereich, and N. Magnea, *Appl. Phys. Lett.* **69**, 3704 (1996).
- [28] C. Kallin and B. I. Halperin, *Phys. Rev. B* **30**, 5655 (1984).
- [29] R. Romestain and C. Weisbuch, *Phys. Rev. Lett.* **45**, 2067 (1980).
- [30] H. C. A. Oji and A. H. MacDonald, *Phys. Rev. B* **34**, 1371 (1986).
- [31] L. Wendler and V. G. Grigoryan, *Solid State Communications* **71**, 527 (1989).
- [32] L. Wendler and R. Pechstedt, *J. Phys.: Condens. Matter* **2**, 8881 (1990).
- [33] L. V. Kulik, I. V. Kukushkin, V. E. Kirpichev, K. v. Klitzing, and K. Eberl, *Phys. Rev. B* **61**, 12717 (2000).
- [34] S. N. Klimin and J. T. Devreese, *Phys. Rev. B* **68**, 245303 (2003).
- [35] E. Abrahams, P. W. Anderson, D. C. Licciardello, and T. V. Ramakrishnan, *Phys. Rev. Lett.* **42**, 673 (1979).
- [36] P. W. Anderson, *Phys. Rev.* **109**, 1492 (1958).
- [37] M. I. Dyakonov, *Solid State Communications* **92**, 711 (1994).
- [38] W. Knap, C. Skierbiszewski, A. Zduniak, E. Litwin-Staszewska, D. Bertho, F. Kobbi, J. L. Robert, G. E. Pikus, F. G. Pikus, S. V. Iordanskii, V. Mosser, K. Zekentes, and Y. B. Lyanda-Geller, *Phys. Rev. B* **53**, 3912 (1996).
- [39] A. Zduniak, M. I. Dyakonov, and W. Knap, *Phys. Rev. B* **56**, 1996 (1997).
- [40] S. McPhail, C. E. Yasin, A. R. Hamilton, M. Y. Simmons, E. H. Linfield, M. Pepper, and D. A. Ritchie, *Phys. Rev. B* **70**, 245311 (2004).

-
- [41] A. P. Dmitriev, V. Y. Kachorovskii, and I. V. Gornyi, *Phys. Rev. B* **56**, 9910 (1997).
- [42] A. V. Germanenko, G. M. Minkov, A. A. Sherstobitov, and O. E. Rut, *Phys. Rev. B* **73**, 233301 (2006).
- [43] I. Garate, J. Sinova, T. Jungwirth, and A. H. MacDonald, *Phys. Rev. B* **79**, 155207 (2009).
- [44] A. Zduniak, M. I. Dyakonov, and W. Knap, *Phys. Rev. B* **56**, 1996 (1997).
- [45] G. M. Minkov, A. V. Germanenko, O. E. Rut, A. A. Sherstobitov, V. A. Larionova, A. K. Bakarov, and B. N. Zvonkov, *Phys. Rev. B* **74**, 045314 (2006).
- [46] M. A. Paalanen, D. C. Tsui, and J. C. M. Hwang, *Phys. Rev. Lett.* **51**, 2226 (1983).
- [47] K. H. Gao, W. Z. Zhou, Y. M. Zhou, G. Yu, T. Lin, S. L. Guo, J. H. Chu, N. Dai, Y. Gu, Y. G. Zhang, and D. G. Austing, *Appl. Phys. Lett.* **94**, 152107 (2009).
- [48] W. Poirier, D. Mailly, and M. Sanquer, *Phys. Rev. B* **57**, 3710 (1998).
- [49] I. V. Gornyi and A. D. Mirlin, *Phys. Rev. B* **69**, 045313 (2004).
- [50] T. A. Sedrakyan and M. E. Raikh, *Phys. Rev. Lett.* **100**, 106806 (2008).
- [51] E. M. Baskin, L. N. Magarill, and M. V. Entin, *Sov. Phys. JETP* **48**, 365 (1978).
- [52] A. Dmitriev, M. Dyakonov, and R. Jullien, *Phys. Rev. B* **64**, 233321 (2001).
- [53] A. V. Bobylev, F. A. Maaø, A. Hansen, and E. H. Hauge, *Phys. Rev. Lett.* **75**, 197 (1995).
- [54] R. M. Hill, *J. Phys. C: Solid State Phys.* **9**, L381 (1976).
- [55] P. T. Coleridge, H. Hayne, P. Zawadzki, and A. S. Sachrajda, *Surface Science* **361/362**, 560 (1996).
- [56] T. Ando, A. B. Fowler, and F. Stern, *Rev. Mod. Phys.* **54**, 437 (1982).
- [57] E. M. Lifshits and A. M. Kosevich, *J. Phys. Chem. Solids* **4**, 1 (1958).
- [58] E. M. Lifshits, *J. Phys. Chem. Solids* **4**, 11 (1958).
- [59] P. N. Argyres, *J. Phys. Chem. Solids* **4**, 19 (1958).
- [60] R. W. Shaw and D. E. Hill, *Phys. Rev. B* **1**, 658 (1970).
- [61] A. Endo and Y. Iye, *Journal of Phys. Soc. Japan* **77**, 064713 (2008).
- [62] T. Ando, *J. Phys. Soc. Japan* **37**, 1233 (1974).
- [63] M. Razeghi, *Fundamentals of solid state engineering, 2nd Edition*, Springer, 2006.
- [64] A. Isihara and L. Smrčka, *J. Phys. C: Solid State Phys.* **19**, 6777 (1986).

- [65] P. T. Coleridge, R. Stoner, and R. Fletcher, Phys. Rev. B **39**, 1120 (1989).
- [66] M. Hayne, A. Usher, J. J. Harris, and C. T. Foxon, Phys. Rev. B **46**, 9515 (1992).
- [67] P. T. Coleridge, P. Zawadzki, and A. S. Sachrajda, Phys. Rev. B **49**, 10798 (1994).
- [68] P. T. Coleridge, Phys. Rev. B **44**, 3793 (1991).
- [69] F. J. Teran, M. Potemski, D. K. Maude, T. Andrearczyk, J. Jaroszynski, and G. Karczewski, Phys. Rev. Lett. **88**, 186803 (2002).
- [70] J. A. Gaj, R. Planel, and G. Fishman, Solid State Commun. **29**, 435 (1979).
- [71] S.-K. Chang, A. V. Nurmikko, J.-W. Wu, L. A. Kolodziejski, and R. J. Gunshor, Phys. Rev. B **37**, 1191 (1988).
- [72] B. Kuhn-Heinrich, M. Popp, W. Ossau, E. Bangert, A. Waag, and G. Landwehr, Semicond. Sci. Technol. **8**, 1239 (1993).
- [73] M. I. Darby, Brit. J. Appl. Phys. **18**, 1415 (1967).
- [74] J. A. Gaj, W. Grieshaber, C. Bodin-Deshayes, J. Cibert, G. Feuillet, Y. Merle d'Aubigné, and A. Wasiela, Phys. Rev. B **50**, 5512 (1994).
- [75] B. König, I. A. Merkulov, D. R. Yakovlev, W. Ossau, S. M. Ryabchenko, M. Kutrowski, T. Wojtowicz, G. Karczewski, and J. Kossut, Phys. Rev. B **61**, 16870 (2000).
- [76] W. Grieshaber, A. Haury, J. Cibert, Y. M. d'Aubigné, A. Wasiela, and J. A. Gaj, Phys. Rev. B **53**, 4891 (1996).
- [77] F. J. Teran, M. Potemski, D. K. Maude, D. Plantier, A. K. Hassan, A. Sachrajda, Z. Wilamowski, J. Jaroszynski, T. Wojtowicz, and G. Karczewski, Phys. Rev. Lett. **91**, 077201 (2003).
- [78] J. Kunc, K. Kowalik, F. J. Teran, P. Plochocka, B. A. Piot, D. K. Maude, M. Potemski, V. Kolkovsky, G. Karczewski, and T. Wojtowicz, Phys. Rev. B **82**, 115438 (2010).
- [79] R. L. Aggarwal, S. N. Jasperson, P. Becla, and R. R. Galazka, Phys. Rev. B **32**, 5132 (1985).
- [80] J. König and A. H. MacDonald, Phys. Rev. Lett. **91**, 077202 (2003).
- [81] R. R. Galazka, S. Nagata, and P. H. Keesom, Phys. Rev. B **22**, 3344 (1980).
- [82] Y. Shapira, S. Foner, D. H. Ridgley, K. Dwight, and A. Wold, Phys. Rev. B **30**, 4021 (1984).
- [83] B. Piot, *Levée de dégénérescence de spin dans le régime Hall quantique*, PhD thesis, Université Joseph Fourier-Grenoble I., France, 2006.
- [84] R. G. Clark *et al.*, Phys. Rev. Lett. **62**, 1536 (1989).

- [85] J. P. Eisenstein, H. L. Stormer, L. Pfeiffer, and K. W. West, *Phys. Rev. Lett.* **62**, 1540 (1989).
- [86] L. W. Engel, S. W. Hwang, T. Sajoto, D. C. Tsui, and M. Shayegan, *Phys. Rev. B* **45**, 3418 (1992).
- [87] W. Kang, J. B. Young, S. T. Hannahs, E. Palm, K. L. Campman, and A. C. Gossard, *Phys. Rev. B* **56**, R12776 (1997).
- [88] A. G. Davies, R. Newbury, M. Pepper, J. E. F. Frost, D. A. Ritchie, and G. A. C. Jones, *Phys. Rev. B* **44**, 13128 (1991).
- [89] J. K. Jain, *Phys. Rev. Lett.* **63**, 199 (1989).
- [90] R. R. Du, A. S. Yeh, H. L. Stormer, D. C. Tsui, L. N. Pfeiffer, and K. W. West, *Phys. Rev. Lett.* **75**, 3926 (1995).
- [91] K. Lai, W. Pan, D. C. Tsui, and Y.-H. Xie, *Phys. Rev. B* **69**, 125337 (2004).
- [92] A. Usher *et al.*, *Phys. Rev. B* **41**, 1129 (1990).
- [93] R. G. Clark, J. R. Mallett, A. Usher, A. M. Suckling, R. J. Nicholas, S. R. Haynes, Y. Journaux, J. J. Harris, and C. T. Foxon, *Surface Science* **196**, 219 (1988).
- [94] B. I. Halperin, P. A. Lee, and N. Read, *Phys. Rev. B* **47**, 7312 (1993).
- [95] D. R. Leadley, R. J. Nicholas, C. T. Foxon, and J. J. Harris, *Phys. Rev. Lett.* **72**, 1906 (1994).
- [96] M. P. Lilly, K. B. Cooper, J. P. Eisenstein, L. N. Pfeiffer, and K. W. West, *Phys. Rev. Lett.* **82**, 394 (1999).
- [97] W. Pan, R. R. Du, H. L. Stormer, D. C. Tsui, L. N. Pfeiffer, K. W. Baldwin, and K. W. West, *Phys. Rev. Lett.* **83**, 820 (1999).
- [98] G. Moore and N. Read, *Physics B* **360**, 362 (1991).
- [99] M. Stern, P. Plochocka, V. Umansky, D. K. Maude, M. Potemski, and I. Bar-Joseph, *Phys. Rev. Lett.* **105**, 096801 (2010).
- [100] J. Christen and D. Bimberg, *Phys. Rev. B* **42**, 7213 (1990).
- [101] F. J. Teran, Y. Chen, M. Potemski, T. Wojtowicz, and G. Karczewski, *Phys. Rev. B* **73**, 115336 (2006).
- [102] D. V. Kulakovskii, S. I. Gubarev, and Y. E. Lozovik, *JETP Letters* **74**, 118 (2001).
- [103] P. Horodyský and P. Hlídek, *phys. stat. sol. b* **243**, 494 (2006).
- [104] E. A. Zhukov, D. R. Yakovlev, M. Bayer, M. M. Glazov, E. L. Ivchenko, G. Karczewski, T. Wojtowicz, and J. Kossut, *Phys. Rev. B* **76**, 205310 (2007).

- [105] See, for example K. Asano and T. Ando, Phys. Rev. B **65**, 115330 (2002), and references therein.
- [106] T. Tsuchiya *et al.*, Physica B **256-258**, 577 (1998).
- [107] P. Hawrylak and M. Potemski, Phys. Rev. B **56**, 12386 (1997).
- [108] W. Zawadzki, S. Bonifacie, S. Juillaguet, C. Chaubet, A. Raymond, Y. M. Meziani, M. Kubisa, and K. Ryczko, Phys. Rev. B **75**, 245319 (2007).
- [109] R. J. Nicholas *et al.*, Phys. Rev. B **37**, 1294 (1988).
- [110] D. R. Leadley *et al.*, Phys. Rev. B **58**, 13036 (1998).
- [111] D. K. Maude *et al.*, Physica B **249-251**, 1 (1998).
- [112] F. F. Fang and P. J. Stiles, Phys. Rev. **174**, 823 (1968).
- [113] J. F. Janak, Phys. Rev. **178**, 1416 (1969).
- [114] T. Ando and Y. Uemura, J. Phys. Soc. Japan **37**, 1044 (1974).
- [115] Yu. A. Bychkov *et al.*, Pis'ma Zh. Eksp. Teor. Fiz. **33**, 152 (1981).
- [116] V. T. Dolgoplov *et al.*, Phys. Rev. Lett. **79**, 729 (1997).
- [117] J. K. Wang *et al.*, Phys. Rev. B **45**, 4384 (1992).
- [118] S. A. J. Wieggers *et al.*, Phys. Rev. Lett. **79**, 3238 (1997).
- [119] I. V. Kukushkin *et al.*, Europhys. Lett. **22**, 287 (1993).
- [120] I. V. Kukushkin and V. B. Timofeev, Adv. Phys. **45**, 147 (1996).
- [121] M. Potemski, Physica B **256-258**, 283 (1998).
- [122] O. E. Dial *et al.*, Nature **448**, 176 (2007).
- [123] S. L. Sondhi *et al.*, Phys. Rev. B **47**, 16419 (1993).
- [124] A. Schmeller *et al.*, Phys. Rev. Lett. **75**, 4290 (1995).
- [125] D. K. Maude *et al.*, Phys. Rev. Lett. **77**, 4604 (1996).
- [126] G. Karczewski *et al.*, J. Crystal Growth **184/185**, 814 (1998).
- [127] Q. X. Zhao *et al.*, Appl. Phys. Lett. **69**, 3704 (1996).
- [128] N. R. Cooper and D. B. Chklovskii, Phys. Rev. B **55**, 2436 (1997).
- [129] O. Volkov, V. Zhitomirskii, I. Kukushkin, K. von Klitzing, and K. Eberl, JETP Letters **65**, 38 (1997).
- [130] F. Plentz, D. Heiman, L. N. Pfeiffer, and K. W. West, Phys. Rev. B **57**, 1370 (1998).

- [131] L. Gravier, M. Potemski, P. Hawrylak, and B. Etienne, Phys. Rev. Lett. **80**, 3344 (1998).
- [132] M. Byszewski *et al.*, Nat. Phys. **2**, 239 (2006).
- [133] W. B. Su, S. M. Lu, C. L. Jiang, H. T. Shih, C. S. Chang, and T. T. Tsong, Phys. Rev. B **74**, 155330 (2006).
- [134] S. Ogawa, S. Heike, H. Takahashi, and T. Hashizume, Phys. Rev. B **75**, 115319 (2007).
- [135] K. Suzuki, K. Kanisawa, C. Janer, S. Perraud, K. Takashina, T. Fujisawa, and Y. Hirayama, Phys. Rev. Lett. **98**, 136802 (2007).
- [136] D. L. Miller *et al.*, Science **324**, 924 (2009).
- [137] G. Li, A. Luican, and E. Y. Andrei, Phys. Rev. Lett. **102**, 176804 (2009).
- [138] M. Potemski, Physica B **256-258**, 283 (1998).
- [139] K. Meimberg, M. Potemski, P. Hawrylak, Y. H. Zhang, and K. Ploog, Phys. Rev. B **55**, 7685 (1997).
- [140] J. Rubio, H. P. van der Meulen, J. M. Calleja, V. Härle, R. Bergmann, and F. Scholz, Phys. Rev. B **55**, 16390 (1997).
- [141] C. Y. Hu, W. Ossau, P. H. Tan, T. Wojtowicz, G. Karczewski, and J. Kossut, Phys. Rev. B **63**, 045313 (2001).
- [142] J.-P. Cheng, Y. J. Wang, B. D. McCombe, and W. Schaff, Phys. Rev. Lett. **70**, 489 (1993).
- [143] P. Hawrylak, Phys. Rev. Lett. **72**, 2943 (1994).
- [144] R. J. Haug, J. Kucera, P. Streda, and K. von Klitzing, Phys. Rev. B **39**, 10892 (1989).
- [145] Y. Kawano and T. Okamoto, Phys. Rev. B **70**, 081308 (2004).
- [146] A. W. Overhauser, Phys. Rev. **92**, 411 (1953).
- [147] I. Pelant and J. Valenta, *Luminiscenční spektroskopie, I. Objemové krystalické polovodiče*, Academia, 2006.
- [148] P. Horodyský, *Optical properties of Cd_{1-x}Zn_xTe*, PhD thesis, Charles University, Faculty of mathematics and physics, Prague, 2006.
- [149] J. A. Reyes and M. del Castillo-Mussot, Phys. Rev. B **56**, 14893 (1997).
- [150] V. Huard, R. T. Cox, K. Saminadayar, A. Arnoult, and S. Tatarenko, Phys. Rev. Lett. **84**, 187 (2000).
- [151] D. S. Chemla and D. A. B. Miller, Journal of Opt. Soc. Am. B **2**, 1155 (1985).

-
- [152] M. Matsuura and Y. Shinozuka, *Journal of Physical Society of Japan* **53**, 3138 (1984).
- [153] G. D. Sanders and K. K. Bajaj, *Phys. Rev. B* **35**, 2308 (1987).
- [154] M. Matsuura and T. Kamizato, *Phys. Rev. B* **33**, 8385 (1986).
- [155] S. Schmitt-Rink and C. Ell, *Journal of Luminescence* **30**, 585 (1985).
- [156] M. Kemerink, P. M. Koenraad, P. C. M. Christianen, R. van Schaijk, J. C. Maan, and J. H. Wolter, *Phys. Rev. B* **56**, 4853 (1997).
- [157] L. Gravier, M. Potemski, A. Fisher, and K. Ploog, *Solid State Electronics* **40**, 697 (1996).
- [158] S. I. Gubarev, O. V. Volkov, V. A. Koval'skii, D. V. Kulakovskii, and V. I. Kukushkin, *Solid State Electronics* **40**, 697 (1996).
- [159] A. B. Henriques, *Superlattices and Microstructures* **12**, 527 (1992).
- [160] A. B. Henriques, *Phys. Rev. B* **44**, 3340 (1991).
- [161] D. Huang, H. Y. Chu, Y. C. Chang, R. Houdré, and H. Morkoç, *Phys. Rev. B* **38**, 1246 (1988).
- [162] R. Stepniewski, M. Potemski, H. Buhmann, D. Toet, J. C. Maan, G. Martinez, W. Knap, A. Raymond, and B. Etienne, *Phys. Rev. B* **50**, 11895 (1994).
- [163] A. B. Henriques, E. T. R. Chidley, R. J. Nicholas, P. Dawson, and C. T. Foxon, *Phys. Rev. B* **46**, 4047 (1992).
- [164] M. H. Meynadier, J. Orgonasi, C. Delalande, J. A. Brum, G. Bastard, M. Voos, G. Weimann, and W. Schlapp, *Phys. Rev. B* **34**, 2482 (1986).
- [165] M. Kemerink, P. M. Koenraad, and J. H. Wolter, *Phys. Rev. B* **54**, 10644 (1996).
- [166] S. A. Brown, J. F. Young, Z. Wasilewski, and P. T. Coleridge, *Phys. Rev. B* **56**, 3937 (1997).
- [167] D. A. Abanin and L. S. Levitov, *Phys. Rev. Lett.* **94**, 186803 (2005).
- [168] T. Mélin and F. Laruelle, *Phys. Rev. Lett.* **85**, 852 (2000).
- [169] M. S. Skolnick, J. M. Rorison, K. J. Nash, D. J. Mowbray, P. R. Tapster, S. J. Bass, and A. D. Pitt, *Phys. Rev. Lett.* **58**, 2130 (1987).

High mobility two-dimensional electron gas in CdTe quantum wells: High magnetic field studies

Experimental studies of two-dimensional electron gases confined in CdTe and CdMnTe quantum wells are presented. The data analysis is supported by numerical calculations of the band structure of confined states, using the local density and envelope function approximations. Four by four, k.p calculations have been performed to justify the parabolic approximation of valence bands. Samples were characterized by Raman scattering spectroscopy and far infrared cyclotron resonance absorption measurements. Low-field magneto-transport shows the dominant contribution of the semi-classical Drude conductivity and three orders of magnitude weaker contributions of weak localization, electron-electron interaction and Shubnikov-de Haas oscillations. The contribution of electron-electron interactions is explained within a semi-classical model of circling electrons. The shape of Landau levels, broadening, transport and quantum lifetimes and dominant long-range scattering mechanism have been determined. High-field magneto-transport displays fractional quantum Hall states at Landau levels $N = 0$ and $N = 1$. The ground states $5/3$ and $4/3$ have been determined to be fully spin polarized, in agreement with the approach of composite fermions for the fractional quantum Hall effect. The form of the photoluminescence at zero magnetic field and its evolution with temperature have been described by simple analytical model. Magnetic field and temperature dependence of the photoluminescence has been found to display the enhanced spin splitting of fully occupied Landau levels. This many body enhanced spin gap has been successfully described by a numerical model. The intensity of the photoluminescence demonstrated the importance of the non-radiative recombination channel, degeneracy of Landau levels, their occupation, selection rules and screening. The mechanism of the simultaneous electron and hole spin-flip was recognized and attributed to the longitudinal acoustical phonon assisted Bir-Aharonov-Pikus spin relaxation mechanism. Photoluminescence excitation spectra embody the characteristic density of states of two-dimensional systems. The excitonic resonances, which are observed at the edges of unoccupied electric subbands, illustrate the importance of screening and internal electric fields in asymmetrically doped quantum wells.

Keywords: Two-dimensional electron gas, integer and fractional quantum Hall effect, electron-electron interaction, optical spectroscopy and electronic transport at high magnetic fields and low temperatures.

Gaz électronique bidimensionnel de haute mobilité dans des puits quantiques de CdTe: Etudes en champ magnétique intense

Une étude expérimentale de gaz d'électrons bidimensionnel confiné dans des puits quantiques de CdTe et de CdMnTe est présentée. L'analyse des données est soutenue par des calculs numériques de la structure de bande des états confinés, utilisant l'approximation de densité locale et de fonction enveloppe. Un calcul de type k.p a été utilisé pour justifier l'approximation parabolique appliquée aux bandes de valence. Les échantillons ont été caractérisés par spectroscopie Raman et par spectroscopie d'absorption de la résonance cyclotron infrarouge. Le magnéto-transport à bas champ est dominé par la contribution semi-classique de Drude et révèle trois contributions plus faibles, qui sont la localisation faible, l'interaction électron-électron et les oscillations Shubnikov-de Haas. La contribution des interactions électron-électron est expliquée dans un modèle semi-classique à trajectoire circulaire. La forme des niveaux de Landau, leur élargissement, les temps de vie transport et quantique et le mécanisme dominant de diffusion à longue portée ont été déterminés. Le magnéto-transport sous champs magnétiques intenses révèle la présence d'états de Hall quantiques fractionnaires dans les niveaux de Landau $N = 0$ et $N = 1$. Nous avons montré que les états $5/3$ et $4/3$ étaient complètement polarisés en spin, en accord avec l'approche des fermions composites pour l'effet Hall quantique fractionnaire. La forme de la photoluminescence à champ magnétique nul et son évolution avec la température sont décrites par un modèle analytique simple. La dépendance en champ magnétique et en température de la photoluminescence indique que le gap de spin est amplifié dans les niveaux de Landau entièrement occupés. Ces effets multi-corps de l'amplification du gap de spin ont été décrits avec succès par un modèle numérique simple. L'intensité de la photoluminescence a mis en évidence l'importance des processus non-radiatifs pendant la recombinaison, la dégénérescence des niveaux de Landau, leur taux d'occupation, les règles de sélection et l'influence de l'écrantage. Le mécanisme de la relaxation parallèle des spins d'électron et de trou a été identifié et attribué au mécanisme Bir-Aharonov-Pikus, assisté par les phonons acoustiques. Les spectres obtenus par la spectroscopie d'excitation de la photoluminescence reflètent la densité d'états caractéristique des systèmes bidimensionnels. Les résonances excitoniques, qui sont observées aux bords des sous-bandes électriques inoccupées, illustrent l'importance de l'écrantage et des champs électriques intrinsèques dans les puits asymétriquement dopés.

Mots Clés: Gaz électronique bidimensionnel, effets Hall quantiques entier et fractionnaire, interaction électron-électron, spectroscopie optique et transport électronique en champ magnétique intense et a basse température.

Dvourozměrný elektronový plyn v kvantových jamách CdTe: studie ve vysokých magnetických polích

Tato práce se zabývá experimentálním studiem dvou-dimenzionálního elektronového plynu v kvantových jamách CdTe a CdMnTe. Interpretace dat je podpořena numerickými výpočty pásové struktury kvantově omezených stavů použitím aproximace lokální elektronové hustoty a aproximace obálkové funkce. Řešení vlastních stavů Kohn-Luttingerova 4×4 k.p hamiltoniánu vedlo k potvrzení správnosti parabolické aproximace valenčních pásů. Základní charakterizace vzorků proběhla metodami Ramanovy spektroskopie a infračervené absorpce. Magneto-transport v nízkém magnetickém poli ukazuje na dominantní vliv semi-klasické Drudeho vodivosti a taktéž byly pozorovány o tři řády slabší efekty slabé lokalizace, elektron-elektronové interakce a Shubnikov-de Haasových oscilací. Příspěvek elektron-elektronové interakce byl také vysvětlen semi-klasickým modelem cirkulujících elektronů. Mimo jiné byl určen tvar a rozšíření Landauových hladin, transportní a kvantová doba života a dominantní rozptylový mechanismus vodivostních elektronů. Magneto-transport ve vysokém magnetickém poli vykazuje formování zlomkových kvantových Hallových stavů v Landauových hladinách $N = 0$ a $N = 1$. Bylo zjištěno, že základní zlomkové stavy $5/3$ a $4/3$ jsou plně polarizované, v souladu s teorií kompozitních fermionů pro zlomkový kvantový Hallův jev. Teplotní závislost tvaru spektrální čáry fotoluminiscence v nulovém magnetickém poli byla popsána jednoduchým analytickým modelem a byl prokázán nezanedbatelný vliv vyšších děrových podpásů. Studium zesíleného spinového štěpení v širokém rozsahu teplot a magnetických polí ukázalo, že k tomuto mnoha - částicovému jevu nedochází jen v okolí Fermiho meze, ale i v plně obsazených Landauových hladinách a tento jev byl úspěšně popsán numerickým modelem. Intenzita luminiscence v magnetickém poli ukázala dominantní vliv nezářivé rekombinace elektron-děrových párů a dále vliv degenerace Landauových hladin, jejich obsazení, výběrových pravidel a stínění. Taktéž byl identifikován proces současné spinové relaxace elektronů a děr, zprostředkovaný BAP (Bir-Aharonov-Pikus) relaxačním mechanismem doprovázeným emisí podélných akustických fononů. Spektra excitační luminiscence vykazují vliv hustoty stavů dvou-dimenzionálního systému s parabolickou disperzí. Excitonové rezonance pozorované na hraně druhého elektronového podpásu ukazují na důležitost stínění a vnitřního elektrického pole v asymetricky dopovaných kvantových jamách.

Klíčová slova: Dvourozměrný elektronový plyn, celočíselný a zlomkový kvantový Hallův jev, elektron-elektronová interakce, optická spektroskopie a elektronový transport ve vysokém magnetickém poli a nízkých teplotách.